Springer Proceedings in Energy

Gagan Anand
Jitendra Kumar Pandey
Sarvendra Rana *Editors*

Nanotechnology for Energy and Water

Proceedings of the International Conference NEW-2017

Springer

Springer Proceedings in Energy

More information about this series at http://www.springer.com/series/13370

Gagan Anand · Jitendra Kumar Pandey
Sarvendra Rana
Editors

Nanotechnology for Energy and Water

Proceedings of the International Conference NEW-2017

Springer

Editors
Gagan Anand
University of Petroleum and Energy Studies
Dehradun
India

Sarvendra Rana
University of Petroleum and Energy Studies
Dehradun
India

Jitendra Kumar Pandey
University of Petroleum and Energy Studies
Dehradun
India

ISSN 2352-2534 ISSN 2352-2542 (electronic)
Springer Proceedings in Energy
ISBN 978-3-319-63084-7 ISBN 978-3-319-63085-4 (eBook)
https://doi.org/10.1007/978-3-319-63085-4

Library of Congress Control Number: 2017947023

Printed on acid-free paper

This Springer imprint is published by Springer Nature
The registered company is Springer International Publishing AG
The registered company address is: Gewerbestrasse 11, 6330 Cham, Switzerland

Contents

Chapter 1
Application of Nano Particle/Fluid in Performance Enhancement of Solar Still: A Review

Anil Kumar, Perapong Tekasakul and Prashant Singh Chauhan

Abstract Water is fundamental need to survive life and the origin of human being is based on water only. The delivery of drinking water is fetching a key issue in many regions of the world. Among the non-conventional techniques to desalinate hard water or brine, is sun based refining i.e. solar desalination. The solar still is the most efficient approach to achieve this target. Solar still has low yield, however it is safe and pure, and it can be used to supply the drinking water in remote areas. Improvement of the design of conventional solar stills to improve the productivity has always been the concern of researchers and engineers in the field of solar energy. In this review article nanoparticle/fluids based solar still is discussed in brief. Heat transfer improvement in solar still is one of the challenging issues of compact designs and energy saving techniques, and the use of nanoparticles/fluids greatly improves the rate of evaporation.

Keywords Solar still · Distillation · Nano particles/fluids

1.1 Introduction

Water is the most important necessity for human life. The need for fresh water is increasing day by day due to rapid increase in population and industrial development. Water desalination is one of the simple method to get drinkable freshwater from the saline water using solar energy and the setup is known as solar stills [1]. In the solar still, brackish water is filled inside the insulated basin and enclosed by crystal clear glass on the top.

A. Kumar (✉) · P. Tekasakul
Energy Technology Research Center and Department of Mechanical Engineering, Prince of Songkla University, Hat Yai 90112, Songkhla, Thailand
e-mail: anilkumar76@gmail.com

A. Kumar · P.S. Chauhan
Department of Energy (Energy Centre), Maulana Azad National Institute of Technology, Bhopal 462 003, India

G. Anand et al. (eds.), *Nanotechnology for Energy and Water*,
Springer Proceedings in Energy, https://doi.org/10.1007/978-3-319-63085-4_1

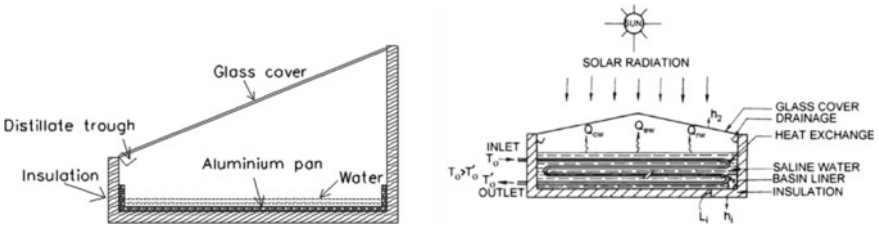

(a) Single slope **(b) Double slope**

Fig. 1.1 Conventional solar stills [2, 5]

Solar radiation transmitted through the glass and reach to the black absorber surface at the bottom, therefore, heating of the water starts. The hot water gets evaporated due to the difference in partial vapor pressure at water surface and just above it. Vapors comes in contact with lower side of glass, get condensed and collected using a drain channel [2–5]. Solar still can be mostly classified as single and double slope still [2, 5]. Figure 1.1 shows conventional solar stills.

Many research work had been conducted to increase the still yield for example asymmetric greenhouse type solar still with mirrors [4], black rubber and black gravel [16, 17], capillary film [12], double and single slope solar still [19], electrical blower [20], phase change materials [21–23], reflectors and absorbers [5], regenerative solar desalination unit [3], solar water purifier [2], solar still with thermal storage [13], solar water collector [14, 15], triple-basin still [11], water plat collectors [6–8], wick still [9, 10], sponge cubes [18], and suspended absorber [24].

In addition, the glass and water temperature difference is a key factor that can affect the yield of the solar still. To maintain maximum possible temperature difference, numerous researchers had examined the systems of flowing water over the glass cover. The condensation rate can be enhanced by increasing the flow rate of glass cooling water and decreasing the inlet cooling water temperature hence, the yield can be enhanced [25–27]. Cooling water flow over the glass cover has many advantages like continuous self-cleaning of glass and results of high still efficiency. Still efficiency can be improved up to 20% by the water cooling film technique [28].

Nano particle/fluids has several special properties compared to its base liquid, such as high thermal conductivity and high solar radiation absorptivity which can help to enhance the still yield [29, 30]. In this research article, various nanoparticle/fluids and its effect on yield and performance of still has been discussed in detail.

1.2 Nano Particle/Fluids Based Solar Still

In this section, single and double slope solar still with nanoparticle/fluids are discussed:

Sharshir et al. used the graphite and copper oxide micro-flakes with different concentrations at different basin water depths and different film cooling flow rates to

improve the performance of a solar still. The micro-flakes concentration was varied from 0.125–2%. The glass cooling flow rate was varied between 1 and 12 kg/h. The results illustrate that the solar still productivity was enhanced by 44.91% and 53.95% using the copper oxide and graphite micro-flakes, respectively as compared with the conventional solar still. On the other hand, when water flows over the glass cover, the output yield was improved by 47.80% and 57.60% using copper oxide and graphite particles, respectively. In another experiment the daily efficiency was found 38% and 40% more using copper oxide and graphite, respectively, when there was not glass film cooling [31].

Sahota and Tiwari presented an analytical expression of the characteristic equation for passive double slope solar still for three different nanofluids ($Al2O_3$, TiO_2 and CuO). The investigation was carried out for optimized concentration as 0.25% for metallic nanoparticles. Higher thermal efficiency was obtained such as 50.34% ($Al2O_3$); 46.10% (TiO_2); and 43.81% (CuO) for nanofluids as compared to 37.78% (base fluid). The thermal exergy was found higher for nanofluids which are 14.10% for $Al2O_3$; 12.38% for TiO_2; and 9.75% for CuO as compared to base fluid 4.92% [32].

Elfasakhany examined the performance of a simple-type solar still integrated with paraffin wax (PW) nanocomposite energy storage system. Three different cases namely case-1 without PW; case-2 with PW, and case-3 with copper-PW nanocomposite (NCPW) was investigated and compared to each other. The yield improved by about 119% and 125% for cases 2 and 3, respectively, as compare to case 1. The designed system working time was extended during the night by 5 h and 6 h by applying PW and NCPW, respectively. The results also represent that addition of nanomaterials to PW can enhance its thermal conductivity and thermal storage capacity [33].

Gupta et al. studied the thermal characteristics of modified still with CuO nanoparticles. The productivity and efficiency of solar still was increased by using nanoparticles. The experiments were conducted at water depth of 5 and 10 cm with nanoparticles addition of 0.12% by weight. Modified solar still with nanoparticles produced 3445 and 3058 ml/m^2 per day at water depth of 5 and 10 cm respectively, whereas conventional solar still 2814 and 2351 ml/m^2 per day for respective water depth. Productivity of modified still was found 22.4% and 30% higher than conventional still at water depth of 5 and 10 cm, respectively. The estimated cost was INR (₹) 0.61 and 0.53 per liter for conventional and modified still respectively at 10 cm water depth whereas for 5 cm water depth it was ₹ 0.51 and 0.40 per liter for conventional still for modified still respectively [34].

Singh and Singh introduced a single basin solar still and conducted experiments for with and without nanofluid conditions. Alumina powder ($Al2O_3$) was used as nanoparticles which is insoluble in water. The nanofluid increased the thermal conductivity of the water up to 20% and the distillation process was also become 20% faster than the normal water. The overall efficiency of the solar still with nanofluid was found 5% more as compared to without nanofluid [35].

Omara et al. designed and constructed new hybrid solar still and analyzed its performance. It contains corrugated, wick absorbers and incorporated with an

external condenser. The performance of corrugated wick still was compared with conventional still. The performance of corrugated wick still with internal reflectors, integrated with external condenser and using different types of nanomaterials was investigated and also individually compared.

Solar still with external condenser, corrugated wick and reflectors improves the productivity of the modified solar still. The output of corrugated wick still with reflectors was enhanced up to 180% as compared to conventional still by applying vacuum. Yield of solar still was intensified using aluminum oxides and cuprous nanoparticles by 255% and 285%, respectively [36].

Kabeel et al. performed the experimental work on modified solar still with different nanomaterials (aluminum oxides and cuprous) at various weight fraction concentrations of nanoparticles with and without providing vacuum. This work was carried out for the concentration range of 0.02–0.2% with increment of 0.02%. Highest yield was attained for the cuprous oxide nanoparticles with 0.2% concentration and using vacuum fan. Output was increased by 133.64% and 93.87% for with and without fan, respectively. Conversely, aluminum oxide nanoparticles application improved the distillation by 125% and 89% with and without fan, respectively [37].

Further, Kabeel et al. examined the effect of external condenser with still basin and using Alumina nanofluids (Al_2O_3). Experimentations were conducted for performance evaluation of modified solar still in Kafrelsheikh City Egypt climatic conditions. A small fan with photovoltaic panels was used to improve the condensation rates. The highest performance was achieved at 1350 rpm fan speed throughout the day. The productivity was 53% higher as compared to conventional still. The mixing of nanofluids with water improved the solar still yield. 116% and 76% solar still yield were increased for with and without operating fan, respectively [38].

Gnanadason et al. fabricated and tested a single basin solar slope still made of aluminium sheet with and without nano particles/fluids. Output of solar still can improve with the change in design, salt concentrations, absorbing material and water depth inside solar still. Thermal efficiency of solar still was increased 15% by mixing of nano particles/fluids with saline water. Nano particles/fluids mixing with the brackish water increase the 40% thermal conductivity which increases the 60% efficiency. The system was sufficient for a family having 4 members. It can produce the 7.5 litres/day/m^2 [39].

Koilraj et al. designed and tested a single basin vacuum type solar still fabricated using copper sheet with and without nano particles/fluids (Multiwalled carbon nanotubes). Distill water production rate could vary with the design, absorbing material, salt concentration, and water depth. The efficiency was higher for still fabricated with copper and further it was improved by mixing nano particles/fluids with the basin water. Accumulated nano particles/fluids at the basin bottom rises the water temperature with increment of heat transfer rate and result of improved evaporation rate. The proposed designed system was sufficient to fulfill the drinking water requirements of 5-person family. Total water consumption was found approximately 7.5 litre per day [40].

1.3 Conclusions

Fresh water demand is rising gradually due to industrial development and fast growth in population. The solar desalination is globally well known most economical way to produce distilled water from saline water. This work critically analyses application of nanoparticles/fluids in performance enhancement of the of solar still. There is significant effect of nanoparticles/fluids in solar still performance. Nanoparticles/fluids used in the still basin increase the water temperature, heat transfer rate, thermal conductivity and evaporation rate. Hence, it improves efficiency and productivity of conventional systems. This review article will be helpful to researcher in deciding suitable nanoparticles/fluids for energy efficient design of solar stills.

Acknowledgements This research was supported by Postdoctoral Fellowship of Dr. Anil Kumar from Prince of Songkla University, Hat Yai, Thailand. Corresponding author is highly grateful to PSU, Hat Yai, Thailand for their support.

References

1. H. Panchal, P.K. Shah, Investigation on solar stills having floating plates. Int. J. Energy Environ. Eng. **3**, 3–8 (2012)
2. J. Ward, A plastic solar water purifier with high output. Sol. Energy **75**, 433–437 (2003)
3. Y.H. Zurigat, M.K. Abu-Arabi, Modelling and performance analysis of a regenerative solar desalination unit. Appl. Therm. Eng. **24**, 1061–1072 (2004)
4. I. Al-Hayeka, O.O. Badran, The effect of using different designs of solar stills on water distillation. Desalination **169**, 121–127 (2004)
5. M. Hermann, J. Koschikowski, M. Rommel, Corrosion-free solar collectors for thermally driven seawater desalination. Sol. Energy **72**, 415–426 (2002)
6. A.A. Badran, I.A. Al-Hallaq, I.A. Eyal Salman, M.Z.A. Odat, Solar still augmented with a flat-plate collector. Desalination **172**, 227–234 (2005)
7. C. Tiris, M. Tiris, Y. Erdalli, M. Sohmen, Experimental studies on a solar still coupled with a flat-plate collector and a single basin still. Energy Convers. Manage. **39**, 853–865 (1998)
8. K. Voropoulos, E. Mathioulakis, V. Belessiotis, Experimental investigation of a solar still coupled with solar collectors. Desalination **138**, 103–110 (2001)
9. S.W. Sharshir, M.O.A. El-Samadony, G. Peng, N. Yang, F.A. Essa, M.H. Hamed, A.E. Kabeel, Performance enhancement of wick solar still using rejected water from humidification-dehumidification unit and film cooling. Appl. Therm. Eng. **108**, 1268–1278 (2016)
10. K.K. Matrawy, A.S. Alosaimy, A.F. Mahrous, Modeling and experimental study of a corrugated wick type solar still: comparative study with a simple basin type. Energy Convers. Manage. **105**, 1261–1268 (2015)
11. A.A. El-Sebaii, Thermal performance of a triple-basin solar still. Desalination **174**, 23–37 (2005)
12. B. Bouchekima, A small solar desalination plant for the production of drinking water in remote arid areas of southern Algeria. Desalination **159**, 197–204 (2003)
13. G. Mink, L. Horvath, E. Evseev, A. Kudish, Design parameters, performance testing and analysis of a double-glazed, air-blown solar still with thermal energy recycle. Sol. Energy **64** (265–27), 7 (1998)

14. K. Voropoulos, E. Mathioulakis, V. Belessiotis, Solar stills coupled with solar collectors and storage tank—analytical simulation and experimental validation of energy behavior. Sol. Energy **75**, 199–205 (2003)
15. K. Voropoulos, E. Mathioulakis, V. Belessiotis, Experimental investigation of the behavior of a solar still coupled with hot water storage tank. Desalination **156**, 315–322 (2003)
16. A.S. Nafey, M. Abdelkader, A. Abdelmotalip, A. Mabrouk, Solar still productivity enhancement. Energy Convers. Manage. **42**, 1401–1408 (2001)
17. A.S. Nafey, M. Abdelkader, A. Abdelmotalip, A. Mabrouk, Enhancement of solar still productivity using floating perforated black plate. Energy Convers. Manage. **43**, 937–946 (2002)
18. H.M. Rababah, Experimental study of a solar still with sponge cubes in basin. Energy Convers. Manage. **44**, 1411–1418 (2003)
19. A.J. Khalifa, A. Al-Jubouri, M. Abed, An experimental study on modified simple solar stills. Energy Convers. Manage. **40**, 1835–1847 (1999)
20. G.N. Tiwari, H. Singh, R. Tripathi, Present status of solar distillation. Sol. Energy **75**, 367–373 (2003)
21. Samuel Harris, D.G., Nagarajan, P.K., Sathyamurthy, R., El-Agouz, S.A., Kannan, E.: Improving the yield of fresh water in conventional solar still using low cost energy storage material. Energy Convers. Manage. **112**, 125–134 (2016)
22. A.E. Kabeel, M. Abdelgaied, Improving the performance of solar still by using PCM as a thermal storage medium under Egyptian conditions. Desalination **383**, 22–28 (2016)
23. A.E. Kabeel, M. Abdelgaied, M. Mahgoub, The performance of a modified solar still using hot air injection and PCM. Desalination **379**, 102–107 (2016)
24. A. El-Sebaii, S. Aboul-Enein, E. El-Bialy, Single basin solar still with baffle suspended absorber. Energy Convers. Manage. **41**, 661–675 (2000)
25. A. Abdullah, Improving the performance of stepped solar still. Desalination **319**, 60–65 (2013)
26. B.A. Abu-Hijleh, Enhanced solar still performance using water film cooling of the glass cover. Desalination **107**, 235–244 (1996)
27. A. Kabeel, M. Rayan: Theoretical and experimental investigation on the influence of still glass cover cooling on water productivity. Mansoura Univ. J. (MEJ) Fac. Eng. **25**, 55–66 (2000)
28. T.K. Sherwood, R.L. Pigford, C.H. Wilke, *Mass Transfer* (McGraw Hill, New York, 1975)
29. A. Ghozatloo, A. Rashidi, M. Shariaty-Niassar, Convective heat transfer enhancement of graphene nanofluids in shell and tube heat exchanger. Exp. Therm. Fluid Sci. **53**, 136–141 (2014)
30. T. Elango, A. Kannan, K.K. Murugavel, Performance study on single basin single slope solar still with different water nanofluids. Desalination **360**, 45–51 (2015)
31. S.W. Sharshir, P. Guilong, L. Wu, N. Yang, F.A. Essa, A.H. Elsheikh, I.T Showgi, A.E. Kabeel, Enhancing the solar still performance using nanofluids and glass cover cooling: experimental study. Appl. Therm. Eng. **113**, 684–693 (2017)
32. L. Sahota, G.N. Tiwari, Effect of nanofluids on the performance of passive double slope solar still: a comparative study using characteristic curve. Desalination **388**, 9–21 (2016)
33. A. Elfasakhany, Performance assessment and productivity of a simple-type solar still integrated with nanocomposite energy storage system. Appl. Energy **183**, 399–407 (2016)
34. B. Gupta, P. Shankar, R. Sharma, P. Baredar, Performance enhancement using nano particles in modified passive solar still. Procedia Technol. **25**, 1209–1216 (2016)
35. A.K. Singh, H.K. Singh, Performance evaluation of solar still with and without nanofluid. Int. J. Sci. Eng. Technol., 1093–1101 (2015)
36. A.E. Omara, A.E. Kabeel, F.A. Essa, Effect of using nanofluids and providing vacuum on the yield of corrugated wick solar still. Energy Convers. Manag. **103**, 965–972 (2015)
37. A.E. Kabeel, Z.M. Omara, F.A. Essa, Improving the performance of solar still by using nanofluids and providing vacuum. Energy Convers. Manag. **86**, 268–274 (2014)

38. A.E. Kabeel, Z.M. Omara, F.A. Essa, Enhancement of modified solar still integrated with external condenser using nanofluids: an experimental approach. in *Seventeenth International Water Technology Conference, IWTC17 Istanbul, 5–7 November* (2013), pp 1–9
39. M.K. Gnanadason, P.S. Kumar, V.H. Wilson, G. Hariharan, Vinayagamoorthi NS design and performance analysis of an innovative single basin solar nano still. Smart Grid Renew. Energy **4**, 88–98 (2013)
40. M.K. Gnanadason, P.S. Kumar, G. Jemilda, S.S. Jasper, Effect of nanofluids in a modified vacuum single basin solar still. Int. J. Sci. Eng. Res. **3**(1) (2012)

Chapter 2
Comparative Analysis of Floating Aerogenerators

Amit Kumar Mondal, Ravi Kumar Patel, Abhishek Sharma, Vindhya Devalla and Surajit Mondal

Abstract This paper presents and compares several concepts of higher altitude wind energy exploitation. This new generation of systems employs tethered wings, aircrafts, multi-copters, balloons in order to harness the higher atmospheric winds. The comparison in this paper covers generators placed in ground as well as in air. From available concepts from literature, the most promising concepts were reproduced on the basis of moving mass (wings and tether), design, operational issues, techno- economic comparison. Key design and operational issues in developing and operating these systems are highlighted. A comparative analysis of floating type aerogenerators has been shown in this paper.

Keywords High altitude wind energy · Airborne wind energy · Floating aero-generator · Magenn air rotor system

2.1 Introduction

To date, major part of energy used by our society has originated from fossil and nuclear fuels, which are presently confronting extreme issues, for example, security of supply, economic affordability, ecological sustainability and disaster risks [1]. To address these issues, world is enacting towards energy policies which are concerned towards expansion of sustainable energy sources. In this context, in the last few decades there has been growth and considerable spread in renewable energy sector [2]. Among the available renewable energy sources wind energy is one of the promising widespread sustainable power sources. Due to non-availability of land resources for further harnessing of wind energy through wind turbines, now the current research is focused towards enhancing the power capacity per unit of land

A.K. Mondal (✉) · R.K. Patel · V. Devalla · S. Mondal
University of Petroleum and Energy Studies, 248007 Dehradun, India
e-mail: akmondal1603@gmail.com

A. Sharma
Ariel University, Ariel, Israel

G. Anand et al. (eds.), *Nanotechnology for Energy and Water*,
Springer Proceedings in Energy, https://doi.org/10.1007/978-3-319-63085-4_2

area. This has globally acted on the single wind turbines by increasing the nominal power (up to 5 MW) which results in increased blade length (for swept area), height of the turbine axis (to capture strong winds), gears, weight, design, material used etc. [3], but this has a limitation as the overall cost of the fixed type wind turbine is proportional to the fifth power of its height [4].

In this scenario, a new way of tapping the high altitude wind energy (HAWE) using floating aerogenerators shows promising future, this principle was first introduced by Loyd [5]. Wind power density is variable in nature due to Earth's boundary-layer-like effect i.e. wind speed generally increases with the increase in altitude, same has been studied by Archer and Caldierain [6] in 2009 for altitudes between 500 m and 12,000 m, shown in Fig. 2.1. Due to wind shear, lower layers of wind retards the layers above them [7]. Wind become steadier, more persistent and of high speed at higher altitudes [8]. Researcher's round the world are working on this sector, and during the last decade we have seen few promising prototypes.

The major motivation behind harnessing HAWE is from the climate models, which predicts heavy drag forces against wind flows, the same has also been shown by Marvel et al. [9] and Miller et al. [10]. In this paper an attempt to provide detailed study of floating type wind generators has been done in terms of different concepts, systems used.

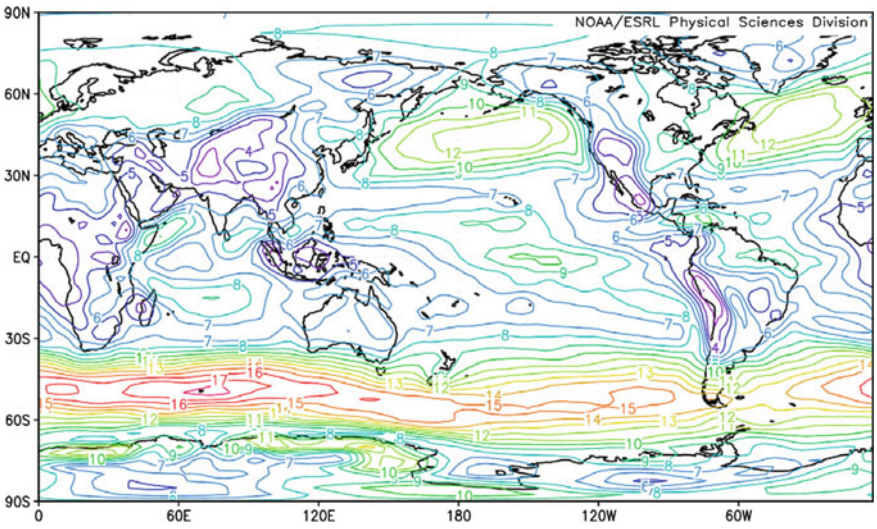

Fig. 2.1 Wind magnitude on pressure level of 850 mbar [11]

2.2 On Going Research

For harnessing HAWE, several techniques are adopted but they can be broadly classified on the basis of the mechanism used for floating, which can be further classified as power generation at ground or sky.

2.2.1 Kite or Airfoil Type

There are different types of floating aerogenerators available on the basis of the type of mechanism used for floating like kite, airfoil, balloon type, rotorcraft type etc. Kite or airfoil type [12–14] floating aerogenerators produces electricity by using the aerodynamic forces into tensile forces via the ropes to the ground station (moving or fixed). The ropes/tethering also provide the desired controlled lift to sustain in sky with the help of the continuous motion of the kite or airfoil. Few of the working prototypes of kite or airfoil based floating aerogenerators are shown in Fig. 2.2, apart the other prototypes using the same concept are as follows:

i. KiteGEN program [15–18]
ii. Peter Lynn Guerilla Kite [19]
iii. Multiple- kite [20]
iv. Laddermill [21, 22]
v. Pumping mill [23]
vi. Axial-Mode Linear Wind Turbine by Gary Dean Ragner [24]
vii. Method of utilization a flow energy and power installation for it by Alexander Bolonkin [25]
viii. Wind Driven Power Generator by Yasunobu Toneaki [26]
ix. Multi-tether cross-wind kite power by Benjamin Tigner [27]
x. Guided wind kite by Franklin F K Chen [28]
xi. Controlling power extraction for wind power generation by Saul Griffith et al. [29]

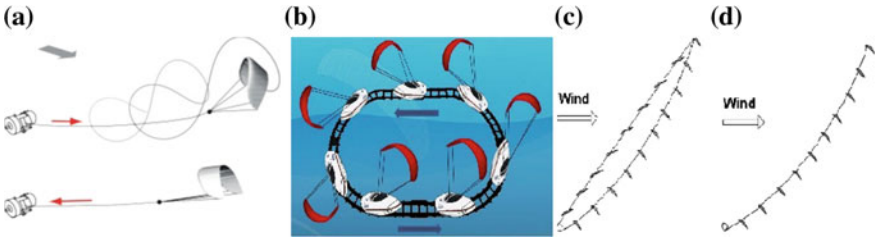

Fig. 2.2 **a** Pumping cycle of parafoil based floating aero generators [14]; **b** Schematic representation of NTS Energie prototype [32]; **c** Working of Laddermill [21, 22]; **d** Working of Pumping mill [23]

xii. Wind drive apparatus for an aerial wind power generation system by Gaylord G. Olson [30, 31]
xiii. NTS Energie prototype [32]
xiv. Wind Energy Device by Norbert L. Osborn [33].
xv. Apparatus for extracting energy from winds at high altitudes by David H. Shepard, Rye [34]
xvi. Apparatus for extracting energy from winds at significant height above the surface by Lambros Lois [35]
xvii. Kite Ground Station and System Using Same by Damon Vander Lind [36]
xviii. Wind energy recovery device and wind power generation device by Toshiyuki Takasaki [37]
xix. Tethered autonomous air vehicle with wind turbines by Eric Blumer et al. [38]
xx. SkySails Power [39]

Kite or airfoil based floating aerogenerators works properly when there is a good amount wind movement, but fails under low or no wind movement cases. Also dynamic modelling corresponding to controlling of these is not linear as it dependent on wind speed, hence it's difficult to model as well as control.

2.2.2 *Balloon Type*

Balloon type floating aerogenerators [40] are comparatively stable and works during low or no wind movement cases. In these balloon acts as a support body for the hanging or embedded wind turbines and the energy produced is transmitted to the ground station via ropes or tethers. Balloons are lighter than air hollow gas filled support structures, because of this they remain in air and are also easy to control during take-off, landing, maintaining altitude etc.

Apart from the above shown prototypes in Fig. 2.3, other prototypes using the same concept are as follows:

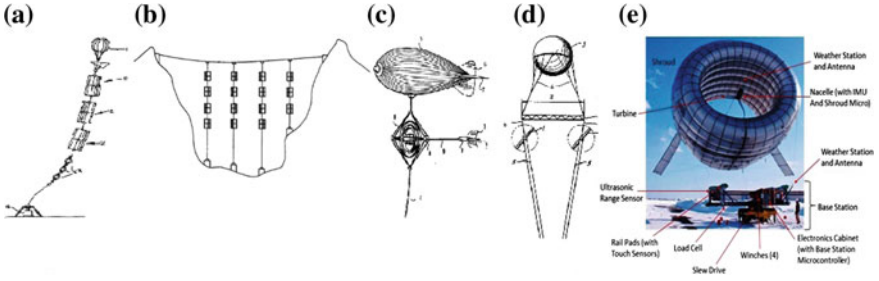

Fig. 2.3 **a** Schematic representation of C M Fry et al. design [41]; **b** Schematic representation of C.M. Fry et al. design [41, 42] using Beldimano's design [43]; **c** Schematic representation of Alberto's Kling's design [44]; **d** Schematic representation of Airship- Windmill [45]; **e** System diagram of Altaeros Energies horizontal axis airborne wind generator [46]

i. William K. Watson's "Airship-floated wind turbine" [47],
ii. Nykolai Bilaniuk's "Airborne wind powered generator" [48].

Although balloon type floating aerogenerators are considered the most stable type floating aerogenerators, but the gas (lighter than air) used for filling these balloons are hydrogen which is sensitive to ignition and helium which is limited and costly [49].

2.2.3 *Multi-copter or Rortorcraft Type*

Multi-copter or rotorcraft type exploits the aerodynamic forces into tensile forces by wind turbines to produce electricity. Flying along controlled path, wings produces aerodynamic and aerostatic lift, which sustains the structure. Due to the rotors, its easy for take-off and landing and during ow or no wind motion these rotors from the ground station power, sustains the structure in air. Few of the available prototypes apart from the one shown in Fig. 2.4, are as follows:

i. Flying Electric Generator [50, 51]
ii. Peter R. Payne et. al's "Self-Erecting Windmill" [52].
iii. Airborne Cyclically controlled power generation using autorotation [53]
iv. Power generation from High Altitude Winds [54]
v. Aleandro Soares Macedo "Hovering wind turbine" [55].

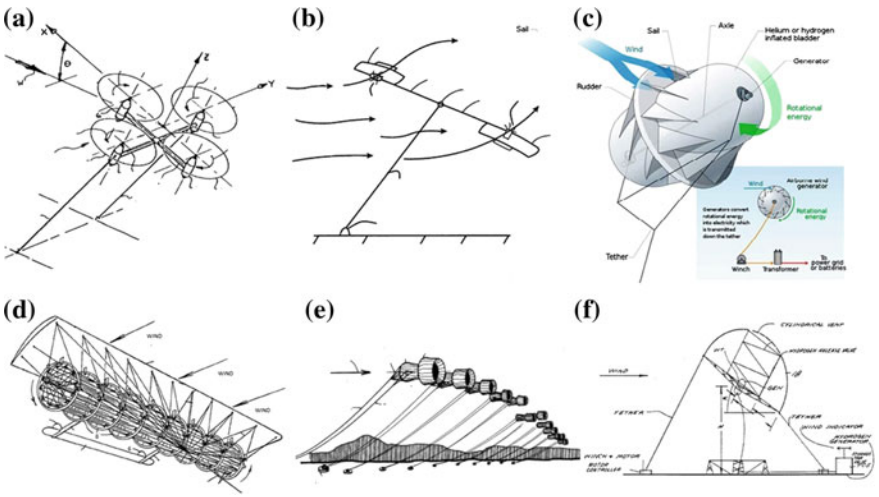

Fig. 2.4 **a** Schematic representation of Flying Electric Generator [50, 51]; **b** Schematic representation of Airborne cyclically controlled power generation using autorotation [53]; **c** Schematic representation of MARS [57]; **d** Schematic representation of David H. Shepard design [54]; **e** Schematic representation of Air Ship Power Turbine [59]; **f** Schematic representation of Tethered Airfoil Wind Energy Conversion System [60]

vi. Magenn Air Rotor System (MARS) [56–58]
vii. Air Ship Power Turbine [59]
viii. Tethered Airfoil Wind Energy Conversion System [60]

2.3 Discussion

Above mentioned HAWE techniques are still under prototype stage and it will take considerable amount of time to make it commercially viable. Although there are several industrial players who are working in this sector like Mahenn Power Inc., Sky WindPower, Joby Energy [61], Makani Power [62], Windlift, Swiss Kite Power, Skysails GmbH, which indeed is a promising fact and will boost confidence of other investors to invest in this sector. Summary of the HAWE harnessing floating aerogenerator prototype classification has been presented in Table 2.1. As per the available literature, a comparative analysis among the different prototypes of floating aerogenerators has been shown in Table 2.2.

HAWE based floating aerogenerators should possess the following attributes [63]:

i. Light weight of the system, which includes generator, wings, blades, balloon etc. [64, 65]
ii. Tethers used for floating aerogenerators have to be rigid enough to sustain the tensile strength and in the same time should have the best power to weight ratio (P/W) [66].

Table 2.1 Summary of floating aerogenerators [67]

General system description	Company	Flying principle	Type	Energy generation system
Turbines on a tethered aircraft	Makani Power	Wings lift	Crosswind	6/8 turbines
	Joby Energy	Wings lift	Crosswind	Several turbines
Tethered Quadcopter	Sky Windpower	Rotors Thrust	Non-Crosswind	4 turbines
Turbines on a lighter than air balloon	Altaeros Energies	Buoyancy	Non-Crosswind	1 turbine
Magnus Effect Turbine	Omnidea	Buoyancy	Non-Crosswind	Buoyant Wind turbine

Table 2.2 Comparative analysis of floating aerogenerators

Floating aerogenerators	Production cost	Wind operability	Mass (kg)/Area
Magenn Air Rotors	20 cents/kWh[a]	3–28 m/s	
Fagiano L M et al. [13, 68] (HAWE)	20 $/MWh	4–25 m/s	500 m^2
Altaeros Energies BAT		Can sustain 44.7 + m/s [69]	
Peter Lynn Guerilla Kite		14–24 mph	
Laddermill [21]	4.38 cents/kWh[c]	4–25 m/s [23]	
Flying Electric Generator by Bryan W Roberts et al. [70]	20 $/MWh	10–35 m/s [d]	9500 kg
Magenn Air Rotor System (MARS)	124 $/MWh [71]	2.5–30 m/s [72] Sustain up to 40 m/s [56]	159 kg [56]

[a]Compared with diesel
[b]Considering Capacity Factor (CF) approximately 0.6
[c]Based on Netherlands Energy Research Foundation (ECN) Simulation model
[d]At an altitude of 4600 m

2.4 Conclusion and Future Perspective

Floating aerogenerators are promising source of HAWE harnessing and conceptually proved their stability. In the last decade, considerable amount of work has been done in the form of patents, prototypes and investment from private and governmental bodies. Depending upon the investment and risk associated with floating aerogenerators, fixed type, small scale floating aerogenerators should be used. Technologies used in floating aerogenerators are at very nascent stage and it will go through with research in perspective of design, material, power electronics to make it viable in long run. Kenny Phan et al. [73] has forecasted a consisted growth of wind energy harnessing in coming decades.

References

1. E.A. Wrigley, Energy and the English industrial revolution. Philos. Trans. R. Soc. Lond. A Math. Phys. Eng. Sci. **371**(1986), 20110568 (2013)
2. W.E.C. Global, *Global Wind statistics 2013* (Belgium, Brussels, 2014)
3. J. Peeringa et al., UpWind 20 MW Wind Turbine Pre-Design. ECN, Paper No. ECN-E–11-017 (2011)
4. J. Kim, C. Park, Wind power generation with a parawing on ships, a proposal. Energy **35**(3), 1425–1432 (2010)
5. M.L. Loyd, Crosswind kite power (for large-scale wind power production). J. Energy **4**(3), 106–111 (1980)
6. C.L. Archer, K. Caldeira, Global assessment of high-altitude wind power. Energies **2**(2), 307–319 (2009)

7. C.L. Archer, M.Z. Jacobson, Evaluation of global wind power. J. Geophys. Res. Atmos. **110** (D12) (2005)
8. P.S. Arya, *Introduction to Micrometeorology*, vol. 79 (Academic Press, 2001)
9. K. Marvel, B. Kravitz, K. Caldeira, Geophysical limits to global wind power. Nat. Clim. Change **3**(2), 118–121 (2013)
10. L. Miller, F. Gans, A. Kleidon, Jet stream wind power as a renewable energy resource: little power, big impacts. Earth Syst. Dyn. **2**(2), 201–212 (2011)
11. L. Perković et al., Harvesting high altitude wind energy for power production: the concept based on Magnus' effect. Appl. Energy **101**, 151–160 (2013)
12. M. Milanese, F. Taddei, S. Milanese, Design and testing of a 60 kW yo-yo airborne wind energy generator, in *Airborne Wind Energy* (Springer, Berlin, 2013), pp. 373–386
13. L. Fagiano, M. Milanese, D. Piga, High-altitude wind power generation. IEEE Trans. Energy Convers. **25**(1), 168–180 (2010)
14. U. Fechner, R. Schmehl, Design of a distributed kite power control system, in *IEEE International Conference on Control Applications (CCA), 2012*, (IEEE, 2012)
15. M. Canale, L. Fagiano, M. Milanese, Power kites for wind energy generation. IEEE Control Syst. Mag. **27**(6), 25–38 (2007)
16. M. Canale, L. Fagiano, M. Milanese, High Altitude Wind Energy Generation Using Controlled Power Kites. IEEE Trans. Control Syst. Technol. **18**(2), 279–293 (2010)
17. M. Ippolito, *Infrastructure for driving and assisting take-off of airfoils for tropospheric aeolian generator*, Google Patents (2014)
18. S. Griffith et al., *Controlling power extraction for wind power generation*, Google Patents (2009)
19. J. Krenciszek et al., *Mathematical Modeling of the Pumping Kite Wind Generator: optimization of the Power Output.* (2008)
20. B. Houska, M. Diehl, Optimal control of towing kites. in *45th IEEE Conference on Decision and Control,* (IEEE, 2006)
21. W.J. Ockels, Laddermill, a novel concept to exploit the energy in the airspace. Aircr. Des. **4** (2), 81–97 (2001)
22. J. Meijaard, W. Ockels, A. Schwab, Modelling of the dynamic behaviour of a Laddermill, a novel concept to exploit wind energy, in *Proceedings of the III Symposium on Cable Dynamics*. (1999)
23. B. Lansdorp, W. Ockels, Comparison of concepts for high-altitude wind energy generation with ground based generator, in *Proceedings of the NRE 2005 Conference, Beijing, China*. (2005)
24. G.D. Ragner, Axial-mode linear wind-turbine, Google Patents (2003)
25. A.Bolonkin, Method of utilization a flow energy and power installation for it, Google Patents (2003)
26. Y. Toneaki, Wind driven power generator, Google Patents (2013)
27. B. Tigner, Multi-tether cross-wind kite power, Google Patents (2011)
28. F.F. Chen, Guided wind kite for increased wind turbine power output, Google Patents (2011)
29. S. Griffith et al., Controlling power extraction for wind power generation, Google Patents (2010)
30. G.G. Olson, Wind drive apparatus for an aerial wind power generation system, Google Patents (2007)
31. G.G. Olson, Aerialwind power generation system and method, Google Patents (2007)
32. Energie, N. *X-Wind*. 2015 [cited 2016 8/1]. https://www.x-wind.de/en/our-project.html
33. N.L. Osborn, Wind energy device, Google Patents (1996)
34. D.H. Shepard, Apparatus for extracting energy from winds at high altitudes, Google Patents (1986)
35. L. Lois, Apparatus for extracting energy from winds at significant height above the surface, Google Patents (1978)
36. D.Vander Lind, Kite Ground Station and System Using Same, Google Patents (2013)

37. ▲高崎▼利之, T. Takasaki, Wind energy recovery device and wind power generation device, Google Patents (2013)
38. E. Blumer, et al., Tethered autonomous air vehicle with wind turbines, Google Patents (2012)
39. Power, S. *SkySails Powe: The next generation of Wind Power*. 2015. http://www.skysails.info/fileadmin/user_upload/Power/Presse/EN_SkySails_Power_Wind_Power_Next_Level.pdf
40. J.W. Kolar et al., Conceptualization and multiobjective optimization of the electric system of an airborne wind turbine. IEEE J. Emerg. Sel. Top. Power Electron. **1**(2), 73–103 (2013)
41. C.M Fry, H.W. Hise, Wind driven, high altitude power apparatus, Google Patents (1978)
42. C.M. Fry, H.W. Hise, Wind driven, high altitude power apparatus, Google Patents (1979)
43. A. Beldimano, Alexander beldimano, Google Patents (1932)
44. A. Kling, Wind driven power plant, Google Patents (1978)
45. G.J. Engelsman, Airship-windmill, Google Patents (1984)
46. C. Vermillion et al., Model-based plant design and hierarchical control of a prototype lighter-than-air wind energy system, with experimental flight test results. IEEE Trans. Control Syst. Technol. **22**(2), 531–542 (2014)
47. W.K. Watson, Airship-floated wind turbine, Google Patents (1985)
48. N. Bilaniuk, Airborne wind powered generator, Google Patents (2011)
49. J. Adhikari, S. Panda, Overview of high altitude wind energy harvesting system, in *5th International Conference on. Power Electronics Systems and Applications (PESA),* (IEEE 2013)
50. B.W. Roberts, D.H., Shepard, Precisely controlled flying electric generators III, Google Patents (2006)
51. B.W. Roberts, D.H. Shepard, Precisely controlled flying electric generators, Google Patents (2007)
52. P.R. Payne, C. McCutchen, Self-erecting windmill, Google Patents (1976)
53. J. Bevirt, L. Kroo, System and method for airborne cyclically controlled power generation using autorotation, Google Patents (2009)
54. D.H. Shepard, *Power generation from high altitude winds*, Google Patents (1987)
55. A.S. Macedo, Hovering wind turbine, Google Patents (2006)
56. K.N Shelke, M.D. Duraphe, *Magenn Air Rotor System (Mars)*
57. Q. Zhao, *A Feasibility Study on High-altitude Wind Power Generation*
58. C. Vermillion, B. Glass, A. Rein, Lighter-than-air wind energy systems, in *Airborne Wind Energy,* (Springer,Berlin, 2013), pp. 501–514
59. W.J. Mouton Jr, D.F. Thompson, Airship power turbine, Google Patents (1979)
60. L.I. Biscomb, Tethered airfoil wind energy conversion system, Google Patents (1982)
61. Energy, J. [cited 2015 12/12/2015]. http://www.jobyenergy.com/tech
62. Power, M. [cited 2015 12/12/2015]. https://www.google.com/makani/technology/
63. A.K. Mondal et al., Advances in floating aerogenerators: Present status and future. Int. J. Precis. Eng. Manuf. **17**(11), 1555–1568 (2016)
64. P. Ragot, M. Markovic, Y. Perriard, Optimization of electric motor for a solar airplane application. IEEE Trans. Ind. Appl. **42**(4), 1053–1061 (2006)
65. T. Wang, Q. Wang, Optimization design of a permanent magnet synchronous generator for a potential energy recovery system. IEEE Trans. Energy Convers. **27**(4), 856–863 (2012)
66. J. Adhikari, S.K. Panda, Generation and Transmission of Electrical Energy in High-Altitude Wind Power Generating System. IEEE J. Emerg. Sel. Top. Power Electron. **3**(2), 459–470 (2015)
67. A. Cherubini et al., Airborne Wind Energy Systems: A review of the technologies. Renew. Sustain. Energy Rev. **51**, 1461–1476 (2015)
68. L. Fagiano, Control of tethered airfoils for high–altitude wind energy generation, Politecnico di Torino (2009)
69. Energies, A. Frequently asked questions. [cited 2016 2/6/2016]. http://www.altaerosenergies.com/faq.html

70. B.W. Roberts et al., Harnessing high-altitude wind power. IEEE Trans. Energy Convers. **22** (1), 136–144 (2007)
71. G. Civalier, et al., Comparative analysis of three concepts for aerostat based electrical power generation system, in *11th AIAA Aviation Technology, Integration, and Operations (ATIO) Conference, including the AIAA Balloon Systems Conference and 19th AIAA Lighter-Than*. (2011)
72. J. Seifert, A review of the Magnus effect in aeronautics. Prog. Aerosp. Sci. **55**, 17–45 (2012)
73. K. Phan, T. Daim, Forecasting the maturity of alternate wind turbine technologies through patent analysis, in *Research and Technology Management in the Electricity Industry* (Springer, Berlin, 2013), pp. 189–211

Chapter 3
Development of Environment Friendly Superhydrophobic Polystyrene/SiO_2 Coatings via Sol-gel Route

Sachin Mahato, Amit Gupta, Joel Justin, Abhishek Tiwari, Amrita Hooda, R.K. Singh, M.S. Goyat, Rajeev Gupta, Abhijit Biswas and Megha Agrawal

Abstract Development of superhydrophobic coatings, motivated by nature (lotus plant) is one of the emerging technologies. The water repellent surface coatings are highly desired in day to day life and engineering applications for example to avoid corrosion, moisture, biofouling and air drag etc. In the present study, environment friendly superhydrophobic polystyrene/SiO_2 coatings retaining average roughness <100 nm has been produced on glass substrate by spin coating method. The estimated ordered roughness has been achieved using 3-mercaptopropyltrimethoxy silane as an accumulating agent. The roughness was characterized by atomic force microscopy (AFM). Chlorotrimethylsilane was used as SiO_2 nanoparticle surface functionalization agent in order to develop superhydrophobic coating. The functionalization of nanoparticles was established by Fourier transform infrared spectroscopy (FTIR). The contact angles were determined using Drop Shape Analyser.

S. Mahato · A. Gupta · J. Justin · A. Tiwari
Department of Mechanical Engineering, University of Petroleum and Energy Studies, Dehradun 248007, Uttarakhand, India

A. Hooda
Department of Electronics and Communication Engineering, University of Petroleum and Energy Studies, Dehradun 248007, Uttarakhand, India

R.K. Singh
Department of Electronics and Communication Engineering, Bipin Tripathi Kumaon Institute of Technology, Dwarahat, Uttarakhand, India

M.S. Goyat · R. Gupta (✉)
Department of Physics, University of Petroleum and Energy Studies, Dehradun 248007, Uttarakhand, India
e-mail: rajeev@ddn.upes.ac.in

A. Biswas
USA Prime Biotech LLC, 1121 S Dixie FWY, New Smyrna Beach FL 32168, USA

M. Agrawal
Department of Bioengineering, University of Illinois at Chicago, Chicago, USA

G. Anand et al. (eds.), *Nanotechnology for Energy and Water*,
Springer Proceedings in Energy, https://doi.org/10.1007/978-3-319-63085-4_3

The composition of polystyrene and nanoparticles was varied to derive a high contact angle approaching super hydrophobic nature.

Keywords Superhydrophobic coating · Nano SiO_2 · Polystyrene · Sol-gel

3.1 Introduction

Surfaces possessing water contact surface angle (CA) of 120^o or more than, it has an interesting feature by which the water rolls off from the surface thus cleaning the surface off dust particles and various other contaminants. This has become quite interesting for the development of water repellent surface which can be used for the enhancement of surface properties of windows, glass, various automotive parts, textiles, pipe-lines (oil and water) and many other industrial and maritime applications. It can also be for bio-medical purposes. This coating can be sprayed onto objects to make them waterproof, anti-corrosive and anti-icing and can be used to protect electronic circuits and grids. Super hydrophobic or hydrophobic feature was seen on lotus leaves. The leaves of the lotus always remain clean because they have the feature in which the water droplets easily roll off from its surface thus cleansing the leaves from contaminants and other dust particles. Therefore, the effect of self-cleaning by water droplets is often termed as "Lotus Effect" [1]. Hydrophobic or Super hydrophobic and hydrophilic surfaces differ with each other on the fact that the previous has zero affinity for water; tending to repel water or be wetted by water or commonly be said to be afraid of water whereas hydrophilic surfaces has an affinity towards water, tendency to get dissolved in, mix with, or be wetted by water. The hydrophobic behaviour is due to the combination of surface roughness and low surface free energy. Nowadays, Super-hydrophobic or (ultra-hydrophobicity) can be obtained by various methods and further new methods or technologies are being invented and the knowledge is transferred for the manufacture of hydrophobic surfaces for various industrial applications and many other applications as mentioned above. Last few years has seen a development in this aspect and an increasing number of research papers have appeared. The water contact angle (CA) largely depends on the surface roughness, surface composition and surface free energy. After the effects of these properties were studied, it was concluded that lesser the surface free energy, better the water contact angle (CA) of that surface. The proper combination of surface structure and surface free energy leads to the effect that water droplets cannot penetrate into the grooves of a rough surface filled with air [1]. Dettre and Johnson in 1964 discovered that the super-hydrophobic phenomenon was related to rough hydrophobic surfaces and they developed a model based on experiments with glass beads coated with paraffin. The earliest work on this coating was done by Wenzel and Cassie and Baxter [2]. Till date various methods for developing super-hydrophobic surfaces have been employed including particle deposition, sol-gel techniques, plasma treatments, vapour deposition [3], etc. Present-day opportunity for research effect lies mainly in vigorous research and practical

engineering [4]. Most of these methods are very expensive as in the case of Plasma treatments [5]. Arguments have recently arisen concerning the applicability of the Wenzel and Cassie-Baxter examples. Experiments showed that the surface properties and geometry at the contact surface affected the contact angle and hysteresis angle.

3.2 Experiment

3.2.1 Materials

Polystyrene (PS) having molecular weight of 104.1 g mol^{-1} was used supplied by Hi Media Laboratories Pvt. Ltd. Silicon-dioxide (SiO_2) having molecular weight of 60.083 g mol^{-1} was also used supplied by Rankem Pvt. Ltd. Tetra-hydro furan (THF) was supplied by Sisco Research Laboratories Pvt. Ltd. All the reagents used in this study were used directly without any refining. The nanoparticles were functionalized by chlorotrimethylsilane (TMCS).

3.2.2 Preparation of the Coating

Several coatings of different compositions were prepared. The reagents used are referred to as PS (polystyrene), SiO_2 (silicon dioxide), THF (tetra hydro furan). Initially, 0.4 g of PS and 0.01 g of SiO_2 were taken and mixed in 12 ml of THF sol. The concentrations of PS and SiO_2 were varied from 1–5 wt% to obtain coating of different thickness on the surface of the glass slides. The solutions were allowed to react at room temperature for a few moments or for a certain interval of time, and then were ultrasonically mixed with the help of Ultrasonic Probe Sonicator. Prior to ultrasonic mixing, a magnetic stirrer was used for the mixing. Clean glass slides were used as a substrate to develop coating by the spin coating technique. Spin-coating of the solution was then carried out on the surface of glass slides using spin coating machine provided by Apexic india Pvt. Ltd. with a spin rate of 1000 RPM for 60 s with an acceleration time of 10 s. The layer, deposited on the surface was then air–dried at room temperature (30 °C) for 2 min. Multi-layer samples were prepared by varying the composition of the reagents time to time by the same process.

3.2.3 Characterization

The morphology of nanocomposite coatings was characterized by atomic force microscopy (AFM, NT-MDT, Ntegra) using tapping mode. Fourier transform infrared (FTIR) spectra of SiO_2 nanoparticles before and after surface functionalization was recorded on Thermonicolet (Anexus) 1600 series. The contact angle in terms of surface wettability of the coatings was determined using drop shape analyzer (DSA 100, Krüss GmbH, Germany).

3.3 Results and Discussion

AFM 2D and 3D images of PS/SiO_2(1%) and PS/SiO_2(5%) coatings are shown in Fig. 3.1. The AFM image of PS/SiO_2(1%) coating (Fig. 3.1a) showing average roughness of about 5 nm. However, the AFM image of PS/SiO_2(5%) (Fig. 3.1b) affirmed the arrangement of nanostructure covering involving the uniform dispersion of firmly settled small agglomerates of the nanoparticles. 3D AFM picture uncovered a satisfactory harsh surface with countless knocks remain on the covering, showing the progressive harshness of PS/SiO_2(5%) coating. The surfaces can be hydrophobic or hydrophilic until the surface is not legitimately treated by a low surface energy material. Therefore, the increase in average roughness of a low surface energy modified surface enhances the contact angle but up to a certain limit [6]. Thus, it can be concluded that the TMCS-functionalized silica nanoparticles reinforced PS coatings are responsible for the progressive roughness, and the superhydrophobicity.

The variation in water contact angle with increasing concentration of SiO_2 nanoparticles in PS is summarized in Table 3.1. The PS and THF concentration was fixed while the content of nanoparticles was varied to synthesize PS/SiO_2 coatings. A steady increase in the contact angle was observed with the increase in

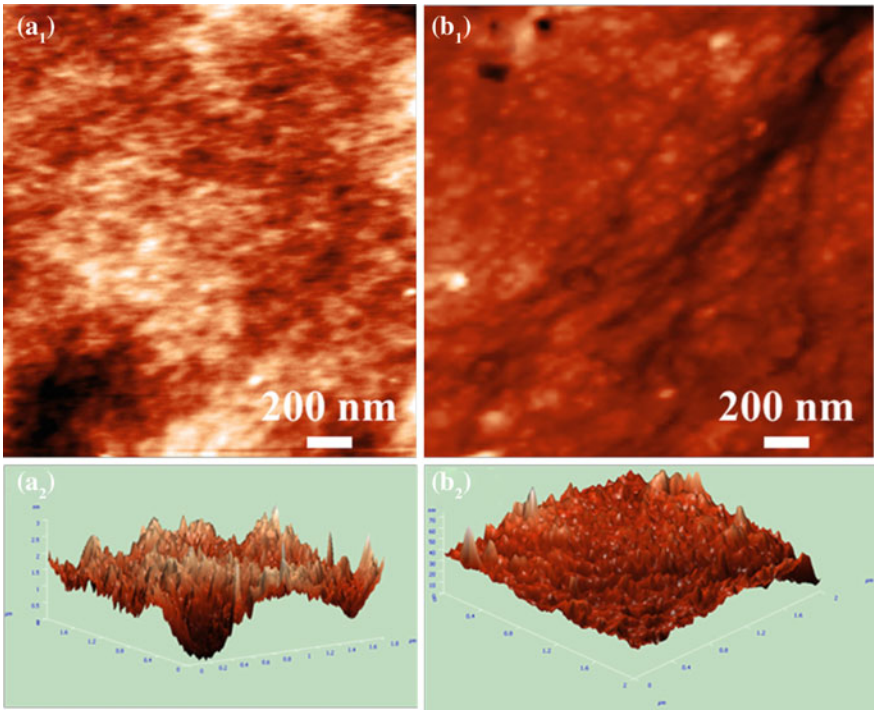

Fig. 3.1 AFM 2D and 3D images of (**a**) PS/SiO_2(1%) and (**b**) PS/SiO_2(5%) coatings

Table 3.1 Wetting properties of the coated glass substrates

S. No.	Conc. of PS (g)	Conc. of SiO_2 (g)	Vol. of THF (ml)	Contact angle		Variance
				Left	Right	
1	0.0	0.0	0.0	44.8	48.3	±5
2	0.4	0.01	12	98.5	102.4	±5
3	0.4	0.02	12	110.8	108.1	±5
4	0.4	0.03	12	120.2	123.0	±5
5	0.4	0.05	12	139.6	141.1	±5

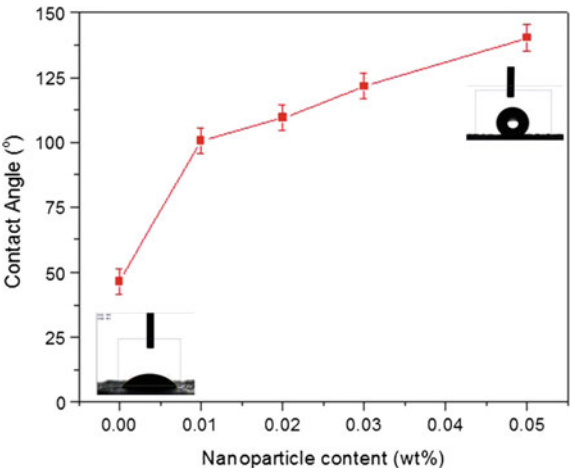

Fig. 3.2 The variation in contact angle with respect to nanoparticle concentration

concentration of nanoparticles up to 5 wt%. That may happened because of increasing surface roughness of the coating with the increase of nanoparticle content. The variation in contact angle with respect to nanoparticle concentration is shown in Fig. 3.2. The wetting properties of the coated glass substrates are shown in Table 3.1.

In the present study, the surface of SiO_2 particles was modified by chlorotrimethylsilane (TMCS) in which the surface hydroxyl groups are replaced by hydrophobic hydrocarbon chains. The surface-capping agent can effectively stop the uncontrolled agglomeration of particles. Additionally, the surface hydrophobicity of nanocoating can also be significantly promoted. Figure 3.3 shows the FTIR spectra of bare and functionalized SiO_2 coating. The absorption peaks around 1600 and 3400 cm^{-1} are because of the Si-OH groups [7]. After the interaction functionalizing agent, the new peaks at 2916 cm^{-1} generate, representing the presence of CH_2 groups [8], and thus they verified the presence of TMCS on the surface of SiO_2. The other bands indicates the siloxane network, at 800–1150 cm^{-1} [8] and band observed at 1710 cm^{-1} attributed to CF_2-CF_2 stretching vibration [9].

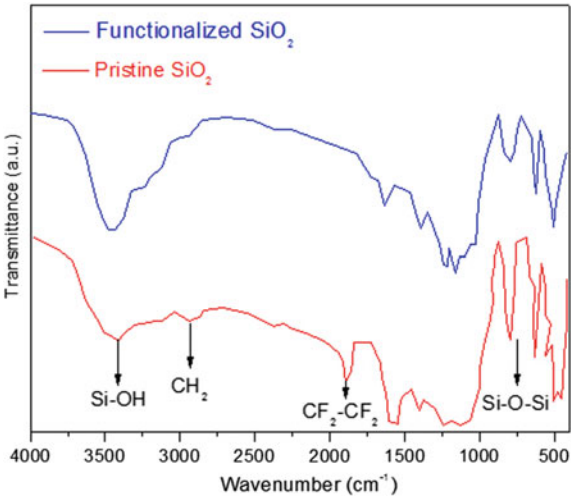

Fig. 3.3 FTIR spectra of pristine and modified SiO_2

3.4 Conclusions

The superhydrophobic polystyrene/SiO_2 nanocoating possessing average roughness <100 nm, with a high contact angle >140° has been successfully synthesized via sol–gel method. This reported technique has prodigious potential to develop superhydrophobic surfaces for various industrial applications.

Acknowledgements The authors acknowledge Inter-university Accelerator Centre (IUAC), New Delhi [Sanction Order No.: UFR-51307, dated: 04.01.2012] for the financial support.

References

1. S. Nagappan, J.J. Park, S.S. Park, C.-S. Ha, Nano Converg. **1**, 30 (2014)
2. J.A. Howarter, J.P. Youngblood, Adv. Mater. **19**, 3838–3843 (2007)
3. S.A. Mahadik, D.B. Mahadik, M.S. Kavale, V.G. Parale, P.B. Wagh, H.C. Barshilia et al., J. Sol-Gel. Sci. Technol. **63**, 580–586 (2012)
4. Y. Rahmawan, L. Xu, S.M. Yang, C. Neinhuis, W. Barthlott, N.J. Shirtcliffe et al., Mater. Chem. A. **1**, 2955–2969 (2013)
5. J. Li, L. Shi, Y. Chen, Y. Zhang, Z. Guo, B. Su et al., J. Mater. Chem. **22**, 9774 (2012)
6. K.L. Cho, I.I. Liaw, A.H.-F. Wu, R.N. Lamb, J. Phys. Chem. C **114**, 11228–11233 (2010)
7. L.H. Yan, H.B. Lv, C.C. Wang, X.D. Yuan, Optics Laser Technol. **43**, 232–236 (2011)
8. N. Saleema, M. Farzaneh, Appl. Surf. Sci. **254**, 2690–2695 (2008)
9. B. Barua, S. Boruah, G. Bhattacharyya, Baruah. Pramana **60**, 47–52 (2003)

Chapter 4
Development of Polystyrene/SiO_2 Superhydrophobic Coating on Metal Substrates for Corrosion Protection

Sachin Mahato, Amit Gupta, Joel Justin, Abhishek Tiwari, Amrita Hooda, Rajeev Gupta, Piyush Kuchhal, Charu Pant and M.S. Goyat

Abstract Corrosion is a key concern for metal industries. Metallic oxidation due to the environment results in a major loss of metal over a span of time. Therefore, a protective coating such as hydrophobic coating is highly desired to avoid moisture in order to provide longevity of the metal. Superhydrophobic surfaces can be produced by controlling the surface roughness of numerous materials and their surface chemistry. In this study, a facile, eco-friendly and low cost sol-gel method for producing superhydrophobic coating on aluminium metal substrates has been reported. The aluminium metal surface was initially roughened using abrasive paper of appropriate grade. Then etching of metal surface was performed using a mixture of de-ionized water, HCl and Acetic Acid respectively in the ratio 20:8:1. The etching time was varied to control the surface roughness of the substrate. Subsequently polystyrene/SiO_2 superhydrophobic coating on aluminium metal substrate was produced. The contact angle was directly measured on the sample surfaces using drop shape analyser. The roughness was characterized by atomic force microscopy (AFM).

Keywords Super-hydrophobicity · Aluminium · Nanocoating · SiO_2

S. Mahato · A. Gupta · J. Justin · A. Tiwari
Department of Mechanical Engineering, University of Petroleum and Energy Studies, Dehradun 248007, Uttarakhand, India

A. Hooda
Department of Electronics & Communication Engineering, University of Petroleum and Energy Studies, Dehradun 248007, Uttarakhand, India

R. Gupta · P. Kuchhal · M.S. Goyat (✉)
Department of Physics, University of Petroleum and Energy Studies, Dehradun 248007, Uttarakhand, India
e-mail: msgoyat@ddn.upes.ac.in

C. Pant
Institute of Nanoscience and Nanotechnology, University of Petroleum and Energy Studies, Dehradun 248007, Uttarakhand, India

G. Anand et al. (eds.), *Nanotechnology for Energy and Water*,
Springer Proceedings in Energy, https://doi.org/10.1007/978-3-319-63085-4_4

4.1 Introduction

Any surface which exhibits a direct angle of contact of 150° or more for water is termed as superhydrophobic surface and the phenomenon is expressed as superhydrophobicity. Some of such examples found in nature are that of a lotus and *Salvinia molesta* leaves. They have a characteristic ultra-low water adhesion and self-cleaning properties [1]. Hydrophobic and superhydrophobic surface modification methods have a very high potential for applications in various industries and day-to-day materials such as various metals where protection against water, corrosion and ice is a matter of concern. This phenomenon can be applied in several major industrial problems; one of which being prevention of corrosion on metallic surfaces. The phenomenon of superhydrophobicity was subjected to extensive study over the years and as a result of which several development methods of surface modifications were made available including spin coating [2, 3], anodic oxidation [4], sol–gel processing [5], etching and lithography [6]. The metallic substrate used in this work is aluminium. Due to its high strength-to-weight ratio and good electrical conductivity, this metal can be utilized for highly stressed structural parts that of commercial aircraft, aerospace and defence equipment and components. So, the protection of this metal against corrosion is obligatory. The method of surface modification using spin coating and chemical etching can be used to achieve hydrophobic nature on the metallic surface. The major contributing factors towards hydrophobic nature of a surface it's the virtue of its low surface energy, surface composition and appreciable surface roughness.

4.2 Experimental

Silicon dioxide (SiO_2) nanoparticles (purity ~99%) with diameters in the range 20–30 nm were purchased from Reinste Nano Ventures Pvt. Ltd. Delhi. The nanoparticles were functionalized by chlorotrimethylsilane (TMCS) with molecular weight (Mw) ~108.64 by following our previous reported work [7]. All the reagents and chemicals such as Polystyrene (PS) with average Mw ~35,000, and tetrahydrofuran (THF) with Mw ~72.11 were procured from Sigma Aldrich, India. A suitable etchant for aluminium metal was prepared using a mixture of de-ionized water, HCl and Acetic Acid in the ratio of 20:8:1. The functionalized SiO_2 was added to PS (50 wt%) and THF (12 mL) followed by stirring of 30 min. The final mixture was spin coated on etched aluminium substrate with 2000 rpm for 20 s. The contact angle was directly measured on the sample surfaces using drop shape analyser (DSA 100, Krüss GmbH, Germany) at ambient conditions. The surface morphology and roughness was characterized by atomic force microscopy (Nanosurf, Naino AFM).

4.3 Results and Discussion

The variation in contact angle and roughness with increasing amount of functionalized SiO_2 nanoparticles in PS is shown in Fig. 4.1. A monotonic increase in the contact angle as well as in the roughness was realized with the increase in amount of nanoparticles up to 7 wt% in PS. However, a further increase in nanoparticle content up to 10 wt% reveal decline in both the roughness as well as the contact angle. Initially, the contact angle on aluminium surface was about 80 °C. But, after the PS coating consisting 7 wt% functionalized nano SiO_2, the contact angle increased to 153 °C. That may have happened due to increased surface roughness of the coating with the increase of nanoparticle amount.

AFM 3D images of PS/SiO_2(1%), PS/SiO_2(5%) and PS/SiO_2(7%) coatings are shown in Fig. 4.2. The AFM image of PS/SiO_2(1%) coating shows an average roughness of about 12 nm. However, the AFM images of PS/SiO_2(5%) and PS/SiO_2(7%) coatings increases average roughness to ~26 nm and ~39 nm respectively. This happened due to the arrangement of nanostructure covering consisting uniformly dispersed and firmly settled small agglomerates of SiO_2. The uniform roughness at nano scale leads the formation of air packets because water droplets of micron size cannot pierce through these nano gaps. Also due to low surface energy of the coated surface, the water droplets converted into spherical balls and can easily roll off the surface by slightly changing the angle of inclination of the solid surface. Therefore, it can be inferred that the incorporation of TMCS-functionalized silica nanoparticles in PS is responsible for the increased nano-roughness and the superhydrophobicity.

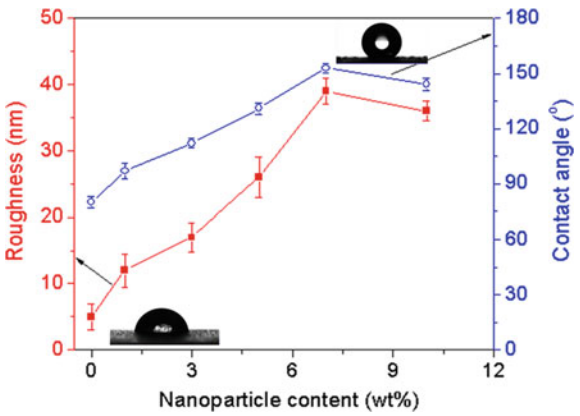

Fig. 4.1 The variation in contact angle and roughness with respect to nanoparticle content

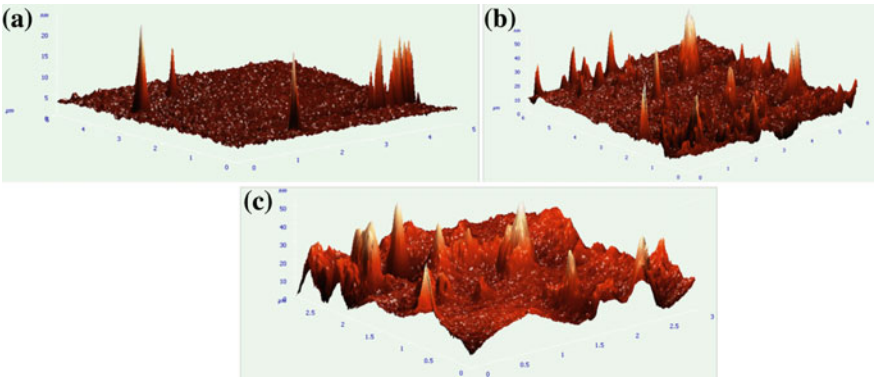

Fig. 4.2 AFM 3D images of **a** PS/SiO_2 (1%), **b** PS/SiO_2 (5%) and **c** PS/SiO_2 (7%) coatings

4.4 Conclusions

The method of spin coating and chemical etching was successfully utilized to create a superhydrophobic coating on the aluminium substrate. The surface modification did not require any special method or chemicals which indicates its ease of development. A facile, eco-friendly and low cost sol-gel method was used to produce superhydrophobic coating on aluminium metal substrates to avoid corrosion. The reported method can be tried out for other metallic substrates along with the selection of a suitable etchant to avoid a potential threat of corrosion.

Acknowledgements The authors acknowledge Inter-university Accelerator Centre (IUAC), New Delhi [Sanction Order No.: UFR-51307, dated: 04.01.2012] for the financial support.

References

1. F.G. Thierry Darmanin, Superhydrophobic and superoleophobic properties in nature. Mater. Today, 273–285 (2015)
2. C.W. Wu, X.L. Wang, X.J. Liu, F. Zhou, Spray-coated fluorine-free superhydrophobic coatings with easy repairability and applicability. ACS Appl. Mater. Interfac. **1**, 1656–1661 (2009)
3. X. Zhang, Y.G. Guo, P.Y. Zhang, Z.J. Zhang, Z.S. Wu, Superhydrophobic superoleophilic nanoparticle film: synthesis and reversible wettability switching behavior. ACS Appl. Mater. Interfac. **4**, 1742–1746 (2012)
4. W.C. Wu, X.L. Wang, D.A. Wang, M. Chen, F. Zhou, W.M. Liu, Q.J. Xue, Alumina nanowire forests via unconventional anodization and super-repellency plus low adhesion to diverse liquids. Chem. Commun. 1043–1045 (2009)
5. X.D. Wu, L.J. Zheng, D. Wu, Fabrication of superhydrophobic surfaces from microstructured ZnO-based surfaces via a wet-chemical route. Langmuir **21**, 2665–2667 (2005)

6. B.T. Qian, Z.Q. She, Fabrication of superhydrophobic surfaces by dislocation selective chemical etching on aluminum, copper and zinc substrates. Langmuir **21**, 9007–9009 (2005)
7. A. Hooda, M.S. Goyat, R. Gupta, M. Prateek, M. Agrawal, A. Biswas, Synthesis of nano-textured polystyrene/ZnO coatings with excellent transparency and superhydrophobicity. Mater. Chem. Phys. **193**, 447–452 (2017)

Chapter 5
Electrochemical Materials from the Fungal Mineralization of Manganese

Amneesh Singla, S. Krishna Moorthi and Adil Rahiman

Abstract Rechargeable Lithium Ion Batteries (LiB) with graphite as the anode has been in use for some time now in mobile phones, electric vehicles etc. But graphite largely limits the performance of this battery. Thus, efforts are being made to improve its performance using alternative electrode materials. In this experiment, we attempt to create an efficient electrode material that can be used as anode in LiBs by the bio-mineralization of manganese chloride. For this purpose, we have cultured two different fungi, Rhizopus stolonifer and Neurospora crassa in media of MnCl2, separately. After they are cultured and the manganese is deposited in the fungi sufficiently, the biomineralized complex is subjected to intense heat treatment to produce the electrode material. The material is then tested for its electrical properties such as standard potential and reactivity with an electrolytic cell by which its reactivity with other elements such as lithium is predicted.

Keywords Lithium ion battery · Rechargeable battery · Neurospora crassa · Rhizopus stolonifer · Manganese chloride · Electrode material · Electrode potential

5.1 Introduction

Sustainable energy storage systems which do not waste much energy and have a high efficiency are required everywhere for various human purposes; both domestic and industrial. Rechargeable Lithium Ion Batteries (LiB) have shown great promise as such a sustainable energy storage system. LiBs have high specific energy density (energy stored per unit mass) and act as slow, steady suppliers for large energy demands. In fact, LiBs with graphite as the anodic material has been in use for some time now in mobile batteries, electric vehicle batteries and other such power sources. But, when using graphite as the anodic material, the performance of the battery is limited by high electrolyte sensitivity and low charge capacity.

A. Singla (✉) · S. Krishna Moorthi · A. Rahiman
University of Petroleum and Energy Studies, Dehradun, India
e-mail: amneesh82@gmail.com

G. Anand et al. (eds.), *Nanotechnology for Energy and Water*,
Springer Proceedings in Energy, https://doi.org/10.1007/978-3-319-63085-4_5

Thus, efforts have been made to improve the LiB performance using carbon nanotubes or manganese oxides (MnxOy) as the alternative electrode materials. But, carbon nanotubes are hard and costly to synthesize and the current levels of research have not produced carbon nanotubes of very high efficiency to replace graphite as the electrode material. Manganese oxides produced in various ways have also not been extremely efficient or effective enough to replace the graphite in Lithium Ion Batteries Hence; research has been going on, throughout the world for the last couple of years to create an anode material that can successfully replace graphite in LiBs. Fungal biomineralization of materials is a topic that has not been studied much, and hence, properties of such bio mineralized complexes are still unknown to a large extent.

Researchers at University of Dundee in Scotland have long studied the ability of fungi to transform metals and minerals in useful ways. For example, in previous studies, the researchers showed that fungi could stabilize toxic lead and uranium. That led them to study whether the fungi could offer a useful alternative strategy for the preparation of novel electrochemical materials too, particularly for being used as electrode materials in rechargeable batteries. Thus, they created the world's first electrochemical material made from fungal mineralization of manganese, which, when tested with super-capacitors and LiBs displayed excellent electrochemical properties. In fact, when compared to other reported manganese oxides in LiBs, this newly synthesized bio-mineralized complex showed an excellent cycling stability and retained more than 90% capacity even after 200 cycles. This is excellent for the future of LiBs and other such renewable energy sources, as, the newly synthesized electrochemical material has displayed qualities, which, on further exploration, may lead to the replacement of graphite as the anode material in LiBs. This also opens the avenue for a large field of research in fungal biomineralization of materials.

The researchers at University of Dundee made this material by biomineralization of manganese chloride with the fungi Neurospora crassa, commonly called red bread mold, which is a very common fungus that is found in stale food in temperate regions, including in northern Europe. In tropical regions, such as in India, the major fungi found in stale food and bread is Rhizopus stolonifer, also called black bread mold. This project aims at testing that, if N. Crassa could create such a promising electrochemical material, could the same be achieved using its tropical 'relative', R. Stolonifer. For this purpose, in this study, R. Stolonifer has been cultured in a media of urea, agar and manganese chloride and, at the event of sufficient mineralization being observed, has been subjected to heat treatment to obtain a complex of charred carbon remains and manganese. The same has been repeated using N. Crassa as a reference study, as, it has already been proved by now that it gives an electrochemical material when subjected to the same process. This project has been undertaken by the authors due to the desire to understand these properties of these fungi, as there has been very few studies done in the field of biomineralization of materials by fungi and almost none in those by R. Stolonifer and the authors wish to see these materials studied and understood [1–3].

5.2 Experimental Studies and Methodology

The idea of this project was to develop the electrode material and make an anode, and, if possible, to test the anode and to study how to reduce the cost of a Lithium Ion rechargeable battery.

5.2.1 The Culturing of the Two Fungal Strains Neurospora Crassa and Rhizopus Stolonifer

1. The strain of fungi Neurospora crassa (Accession No: 1875) was ordered from Microbial Type Culture Collection and Gene Bank (MTCC)
2. The fungi Rhizopus stolonifer was grown in a carefully controlled atmosphere in moist bread kept in a dark, damp and warm environment.
3. After sufficient growth of R.stolonifer was observed, it was transferred from the bread to a medium of 40 g manganese chloride, 30 g urea and 10 g agar in 500 ml water carefully.
4. N. crassa was transferred to an identical medium in another container to avoid mixing between the two different fungal strains
5. Both the media were observed frequently
6. After sufficient growth was observed (8 days for R. stolonifer and 13 days for N. crassa), the solid solutes in the media were collected by evaporating the water with the help of heating mantle
7. The resultant solid was heated at 90 °C for 2 h in an oven to obtain a uniform solid manganese-carbon complex.
8. The obtained solid from the oven was cooled and collected. This is the anode material.
9. Its colour, odour, texture and solubility are all noted.

5.2.2 The Making of Anode, Cathode and Packaging Material

1. A standard copper electrode sheet was taken.
2. To create the electrode, the bio-mineralized anode material, which is in solid form, should be made into a homogenous form and should be coated on the copper electrode. So, an adhesive which is chemically inert and has a favorable piezoelectric co-efficient was to be used to stick the conventional material (carbon) to copper electrode. Usually, PVDF (Polyvinyldiene fluoride) is used for this purpose because of its excellent above-mentioned properties and high

thermal resistance. As PVDF costs around INR 7,735 per 100gms packing (from Sigma Aldrich), the study has used a cheaper epoxy binder because of its good adhesion to non-ferrous materials and chemical inertness.
3. In this study, 50 g of epoxy binder and the anode material (bio-mineralized) were treated in a Ultrasonic Homogenizer with pulse of 20:40 (ON:OFF) for 90 min at 50 °C and then coated on the copper electrode.

The initial plan in this project was to procure Lithium Manganese Nickel Oxide or Lithium Cobalt Oxide electrode from chemical manufacturers, but, as the cost of such an electrode is around 350 USD, the study uses an alternative. So, the authors took an aluminium electrode sheet and coated it slightly with MnCl2 using cyanoacrylate.

Conventionally, Aluminium Laminated pouches are used as packaging materials in batteries due to safety reasons, such as their chemical inertness towards aluminium. This study uses plastic beaker/polymer bag as the packaging material alternative.

5.2.3 Development of Separator Membrane

The separator is a separating space between anode and cathode which prevents direct contact between them, thus preventing short circuit. This membrane should allow the flow of electrons through them without any deformities or forming dendrites in case of polymers. Also, they should not react with electrolyte and the electrode materials. Industrially, ceramic and polythene materials are used as separators. Since our objective was to test the anode material, a separator material having the above properties along with a thermal resistance of up to 200 °C was preferred. In this study, the authors have taken modified synthetic rubber adhesive as the separator material as it can withstand a temperature up to 180 °C. A very small quantity of this synthetic rubber is taken and a very thin sheet of the separator membrane with thickness less than 1 mm was made.

5.2.4 Assembling

In industries, as a standard practice, a metal strip is put along with the electrode for connecting the terminals or wires with it. In this experiment, the authors have taken the electrode sheet, pierced a hole at one end and inserted a nut and bolt screw in it to connect the electrode to other components and obtain the output. As the authors were not able to procure Lithium electrolyte, the Li-ion battery couldn't be completed. Upon the instruction of a professor in the University, aqueous solution of hydrochloric acid (1% in water) as the electrolyte has been used in its stead to test the battery.

5.3 Results and Discussions

The culturing of fungi in the desired medium went very well. After transferring Rhizopus stolonifer and Neurospora crassa into the required medium, their growth was increasingly visible each day due to the increase in the greenish and reddish colours respectively in the solutions [4]. After sufficient growth (8 days for R. stolonifer and 13 days for N. crassa), their heat treatment was done to obtain the bio-mineralized material. The resultant material, which is a carbon-manganese complex, was a black semi-solid substance with a strong, pungent smell and had to be kept in airtight bags for storage (Fig. 5.1). The substance is not soluble with water but completely dissolves with large quantities of hydrochloric acid. After coating the material on the copper by the means of a thin brush with the help of a binder (Fig. 5.2), minor irregularities were found on the surface of the electrode due to lack of a good surface finishing prior to the coating and uneven spreading of the coated material on copper due to lack of proper equipment's. The cathode material, manganese chloride coated aluminium electrode, was perfectly made with the help of cyanoacrylate and used in the experiment. The separator membrane made was a light yellow, translucent material with a thickness of less than 1 mm. The obtained separator was tested in the oven for its temperature resistance and was found to melt at 180 °C, handling all temperatures lesser than that with very slight or no deformations. After piercing the electrode and tightening the nut and bolt screws in it, both the electrodes (the bio-mineralized manganese anode and the aluminium cathode) were dipped in a 1% aqueous solution of hydrochloric acid in water. After 45 cm^2 of each electrode is dipped in the solution, the output is taken through a

Fig. 5.1 Bio-mineralized carbon-manganese complex

Fig. 5.2 Electrode after coating the complex on copper

multimeter by connecting the positive of the multimeter to the anode (carbon-manganese complex) and negative to the cathode (aluminium)

The output of the battery was initially obtained as 0.612 V, which is found to be decreasing with time, reaching a value of 0.59 V after an interval of 2 h. Also, black spots were observed on the outer surface of the aluminium cathode after that interval. Both of the anode materials, the one from N. crassa and the one from R. stolonifer were found to give identical output values in the cell. The output was found to increase when the distance between the electrodes in the electrolyte is decreased. As the standard electrode potential of aluminium is −1.66 V, this makes the standard electrode potential of the bio-mineralized complex of manganese chloride as −1.05 V.

5.4 Conclusions

In this study, new materials were created by the fungal bio-mineralization of manganese by the fungi Neurospora crassa (red bread mold) and Rhizopus stolonifer (black bread mold) and their electrochemical properties, particularly their electrode potential and behaviour as part of a cell, were studied. Materials created from both the fungi showed identical texture, colour, odour and electrochemical properties, leading us to believe they react in the same manner when bio-mineralizing manganese and henceforth in this study, shall be mentioned

collectively as the material. This is explained by the fact that both fungi are closely related and are members of the division Ascomycota.

The synthesized material, a carbon-manganese complex is a black semi-solid substance with a watery outer layer and a very strong and pungent smell. It does not dissolve in water but steadily dissolves in large quantities of strong mineral acids such as hydrochloric acid. It was coated onto a copper electrode to give the required anode material. The anode material thus formed was found to be reactive with cathode material, aluminium, in a cell and give an output.

The combined cell gave an output of 0.612 V, indicating that the synthesized material has a standard potential of −1.05 V, making it a donator of electrons. This potential is close to that of Manganese (II) which has a potential of −1.18 V, but not identical, indicating that, while the manganese is still the major component in this material, the fungal mineralization has left some effect in it to alter its properties slightly. While the obtained output of 0.61 V is not spectacular, it indicates that, when Lithium (electrode potential of −3.04 V) is used as the cathode material, it will create a cell that can produce an output of about 2 V. Also, as can be predicted with its reaction with the currently used aluminium cathode, the newly synthesized material reacts very well electrochemically with metals that have a higher negative standard electrode potential, such as lithium and aluminium. This shows that the fungal bio-mineralization of manganese, especially with N. crassa and R. stolonifer produces materials with excellent electrochemical properties, thus opening avenue for promising research into this topic in the future.

Bio-mineralization of materials with the help of fungi is a rarely researched topic, and, as seen from this experiment, holds the potential for creating materials that can satisfy various needs of the mankind; particularly in the field of energy and energy storage where the need is paramount and higher than ever before [5].

Acknowledgements We would like to thank UPES RISE 2016, for funding this project.

References

1. Qianwei Li, Daoqing Liu, Zheng Jia, Laszlo Csetenyi, Geoffrey Michael Gadd, Fungal biomineralization of manganese as a novel source of electrochemical materials. Curr. Biol. **26** (7), 950–955 (2016)
2. W. Howard, C. Schmidt, E. Scott, Lithium Ion Battery. US Patent 7563541 B2
3. Stephen Mann, *Biomineralization: principles and concepts in bioinorganic materials chemistry* (Oxford Chemistry Masters Publishers, Bristol, United Kingdom, 2001)
4. James Galgan et al., The genome sequence of the filamentous fungus Neurospora crassa. Nature **422**, 859–868 (2003)
5. R. Isles, Could Bread Mold Build a Better Rechargeable Battery (2016), http://www.dundee.ac.uk/news/2016/could-bread-mold-build-a-better-rechargeable-battery.php. Accessed 17 Mar 2016

Chapter 6
Experimental Analysis of 3D Printed Microfluidic Device for Detection of Adulteration in Fluids

Ravi Kumar Patel and Mukesh Kumar Awasthi

Abstract In the field of analytical chemistry and bio-engineering, various technologies have been developed for a variety of applications and microfluidics is one of the promising technologies. Microfluidics can be combined with 3D printing mode so as to solve various types of problems. The usage of fluid is increasing gradually both in the household as well as in industrial applications. Due to increasing demands of fluid, the adulteration of fluids is also increasing gradually so as to meet the demand. Due to the addition of adulterants the properties of conventional fuel and biofuel are highly affected. In the case of a household, milk adulteration is one of the major issues which are affecting the individual's health. This paper deals with different designs of 3D printed optical microfluidic device which has the capability to measure the presence of adulterant based on the variation of viscosity in blending of biofuel and adulterants present in milk.

Keywords Microfluidic device · 3D printer · Adulteration

6.1 Introduction

The fluid term indicates the matter of state which can be divided into two parts: gas and solid [1]. Applications of these fluids are ranging for a wide range, industrial and day to day activities. Fluids for industries ranging from lubricants, fuel, engine oils, biofuels, machinery oils and drilling fluids whereas in day-to-day household actives the major fluids used include water, milk, honey, brewed liquids, etc. [2–4]. These fluids undertake or perform an act with respect to their usage. In order to check the accuracy of fluids, it has to endure several tests and measurements. Test performed for accuracy testing depend on the physical and chemical properties [5, 6].

R.K. Patel (✉) · M.K. Awasthi
University of Petroleum and Energy Studies, Dehradun 248007, India
e-mail: ravikumarpatel28@gmail.com

M.K. Awasthi
e-mail: mukeshiitr.kumar@gmail.com

G. Anand et al. (eds.), *Nanotechnology for Energy and Water*,
Springer Proceedings in Energy, https://doi.org/10.1007/978-3-319-63085-4_6

Among available devices to perform accuracy test depending on the physical property of fluids, the main issues came across are precision, price, reliability, durability, and dimension of the testing device [7, 8]. The available devices to test adulteration in these fluids cannot be operated by a common man. The testing of fluid mainly depends on the viscous property of the taken fluid. Viscosity is a property that represents the resistance of a fluid to flow. Viscosity can also be defined as the thickness or internal resistance present between the layers of flowing fluid. The importance of measuring viscosity is for both application industrial and research [9–14].

Microfluidics has emerged as a technology that is an applicable wide range of applications like analytical chemistry, bioengineering, and electro-analytical chemistry [15]. The purity of milk, biofuel blending and to check fuel adulteration, microfluidics devices can be used when integrated with a proper measurement and analysis platform.

In this paper, we report a 3D printed lab-on-a-chip microfluidic device [16] for detecting the biofuel blending and milk adulteration by real-time monitoring of the variations in their viscosity [17]. The device is very easy to operate and determines the interface shifting of the sample fluid which is immiscible with the reference fluid in a common channel. This micro-viscometer is printed by using acrylate ink [18] and it has many advantages like low cost, high accuracy, and robustness. The simple and versatile design makes it compatible for the use in applications wherein fluid viscosity plays a vital role [19]. The blending of diesel with bio-diesel and the adulteration of milk with commonly used adulterants was tested using this device for various ratios and the device was found to be highly accurate in its output.

6.2 Materials and Method

6.2.1 Hagen Poiseuille Flow Equation

Hagen Poiseuille flow equation given in Eq. (6.1) which supports in finding out the viscosity of the unknown fluid depending on reference fluid which is flowing inside the common channel. The variables like pressure differential, fluid velocity and length of the channel to be constant, the width occupied by the unknown fluid would vary based on the reference fluid flowing inside the channel [19, 20].

According to Hagen-Poiseuille's law for laminar flow in a rectangular channel:

$$Q = \frac{\Delta P b h^3}{12 L \mu} \tag{6.1}$$

Here, 'ΔP' is the difference in pressure between the inlet and outlet in Pascals, 'b' is the width of the channel in meters, 'h' is the height of channel in mm, 'L' is the length of the channel in mm, 'μ' is the fluid velocity inside the channel in ml/min.

6.2.2 Design and 3D Printing of the Microviscometer

Microviscometer was designed using computer aided design (CAD) software Rhinoceros 5.0. The 3D geometry of the device is designed by using CAD software as shown in Fig. 6.1. The channel width is kept at 1 mm in X, Y and Z planes. The X-Y geometry of microviscometer is represented in Fig. 6.2. The dimension of the device is defined in mm scale.

Here for experimental analysis three factors of dimension are being varied like 'b' is the width of the channel, 'h' is the height of channel and 'L' is the length of the channel. The values of these factors are optimized by using Taguchi analysis method. The 3D printed microviscometer device used in this experiment is shown in Fig. 6.3 and printed by using MiiCraft 3D printer. So, using this Miicraft 3D printer around 20 devices of varying dimensions like width, height and length were printed to perform the adulteration test analysis outcome.

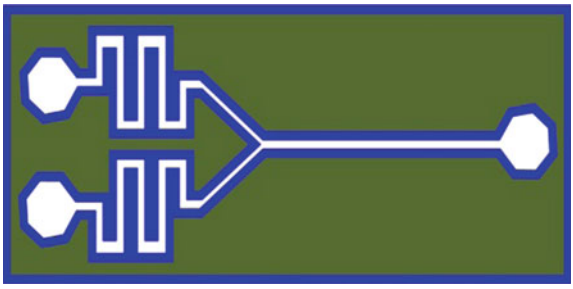

Fig. 6.1 3D geometry of microviscometer using rhinoceros ver. 5.0

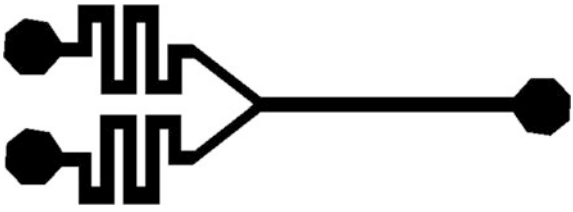

Fig. 6.2 X-Y geometry of the microviscometer (in mm)

Fig. 6.3 3D printed output of the microviscometer

6.2.3 Taguchi Method

Taguchi method is applicable to signal-to-noise (SN)-ratio for testing quality characteristics by approaching the ideal value. Taguchi's SN-Ratio is defined in basically on three conditions which are as follows (i) Taguchi's SN-Ratio for smaller-the-better where quality characteristics is usually an undesired output. (ii) Taguchi's SN-Ratio for larger-the-better where quality characteristics is usually a desired output. (iii) Taguchi's SN-Ratio for nominal-the-best where quality characteristics is usually a nominal output. Out of these three conditions, SN-Ratio for smaller-the-better and SN-Ratio for larger-the-better are opted to perform the optimization process. And finally, the one which is selected is based on Analysis of variance (ANOVA) which is giving less ANOVA error. So, using Taguchi method 3 parameters are being varied and the device is tested so as to perform in an optimized way when used for its real-time application.

6.2.4 Taguchi Experiment

For Taguchi experiment here three dimensions and three different values are taken which is shown in Table 6.1 and dimension defined are in millimeter (mm).

Here, Q is constant which is equal to 4.5 µl/min, and ΔP is equal to 1 atm (1 atm = 101325 Pa). As three parameters are defined for analysis along with three levels of values so for optimization process L9 Orthogonal Array will be created. Below Fig. 6.4 shows the Minitab screen for the starting step of Taguchi analysis and Create Taguchi Design tab is selected.

L9 Orthogonal Array (3**3) is created which is shown in Fig. 6.5 where Factors are 3 and these 3 factors are performed 9 times (Runs: 9) for analysis. Here in Taguchi design, 'C1' is a column for Length, 'C2' is a column for Height, 'C3' is a column for Width, and 'C4' is a column for Viscosity which is 'Response Column'.

Now, Taguchi's SN-Ratio for smaller-the-better where quality characteristics is usually an undesired output is performed by using SN- Ratio Eq. (6.2).

$$\eta = -10\, Log_{10} \frac{1}{n} \in \frac{1}{Y^2} \tag{6.2}$$

Taguchi analysis is done in respect of viscosity versus Length, Height, Width. Here Fig. 6.6 illustrates the main effects plot for SN- ratio. From this plot, optimal results for the defined factors can be determined. The factor values obtained from graph defines the dimension of the device to test the adulterant precisely.

Table 6.1 Factors and levels defined throughout design of experiments

S.No.	Factors (mm)	A	B	C
1	Height	1	2	3
2	Length	25	30	35
3	Channel width	0.3	0.6	0.9

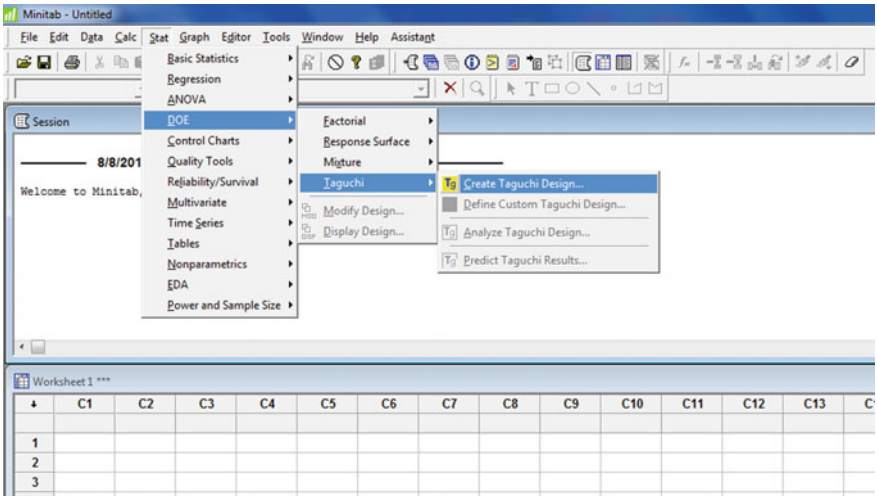

Fig. 6.4 Minitab screen representing initial step of taguchi method

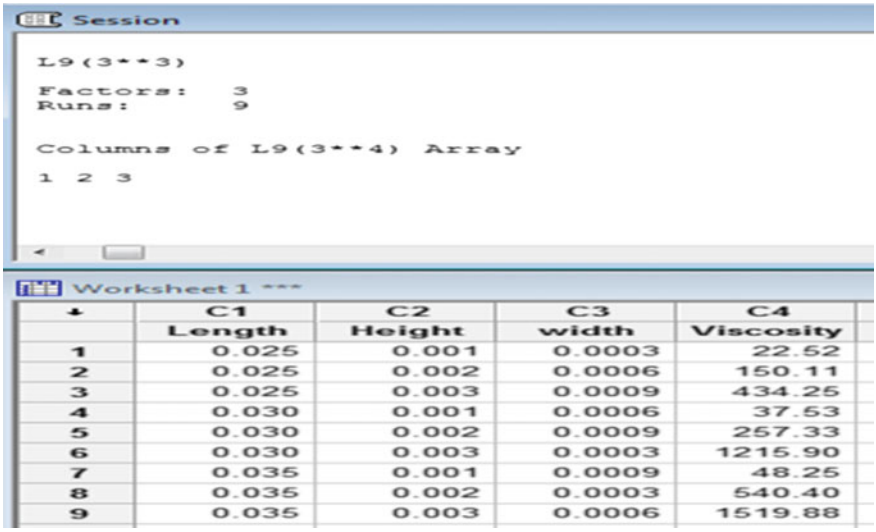

	C1	C2	C3	C4
	Length	Height	width	Viscosity
1	0.025	0.001	0.0003	22.52
2	0.025	0.002	0.0006	150.11
3	0.025	0.003	0.0009	434.25
4	0.030	0.001	0.0006	37.53
5	0.030	0.002	0.0009	257.33
6	0.030	0.003	0.0003	1215.90
7	0.035	0.001	0.0009	48.25
8	0.035	0.002	0.0003	540.40
9	0.035	0.003	0.0006	1519.88

Fig. 6.5 Minitab screen representing L9 orthogonal array taguchi design

For the validation of Taguchi method opted ANOVA test is performed so as to check the ANOVA error.

ANOVA is an analysis of variance and it is an algebraic method which controls factors that are defined. ANOVA is used to conclude the percentage of contribution of each control factors to disclose their effect on the quality characteristics (Table 6.2).

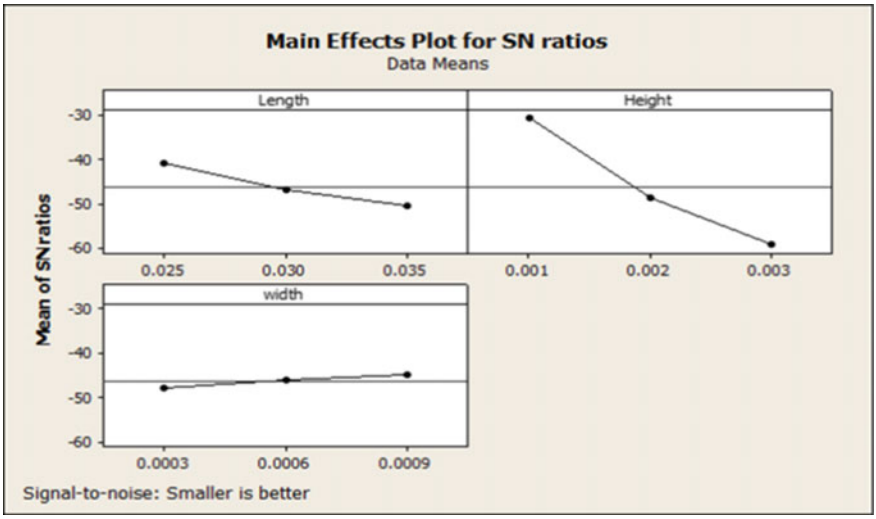

Fig. 6.6 Main Effects Plot for SN

Table 6.2 Response table for signal to noise ratios using smaller is better

Level	Length	Height	Width
1	−41.11	−30.74	−47.80
2	−47.13	−48.80	−46.22
3	−50.65	−59.36	−44.88
Delta	9.54	28.63	2.92
Rank	2	1	3

The increase in SN-ratio determines the increase in control factor. It can be used to investigate the different factors along with the degree of freedom (DF), the Sequential sum of square (Seq SS), Adjusted Sum of the square (Adj SS), Sequential mean square (Seq MS) and last column indicates the P-value for each control parameters. The row ensuring least P value was added more to the response involved and the control factor having high value than F value is insignificant.

During ANOVA test a general linear model has plotted Viscosity versus Length, Height, Width. Figure 6.7 shows normal probability graphs of residuals and figures attained shows that nearly all the normal probability graph follows a straight line outline. Table 6.3 shows detailed values of 3 parameters during ANOVA analysis (Table 6.4).

Linear regression calculation was used to compare the control factors (Length, Height, Width) and output response is viscosity.

$$R - Sq = 95.65\% \quad R - Sq(adj) = 82.61\%$$

R-Sq is the percentage of the response variable variation that is explained by a linear model.

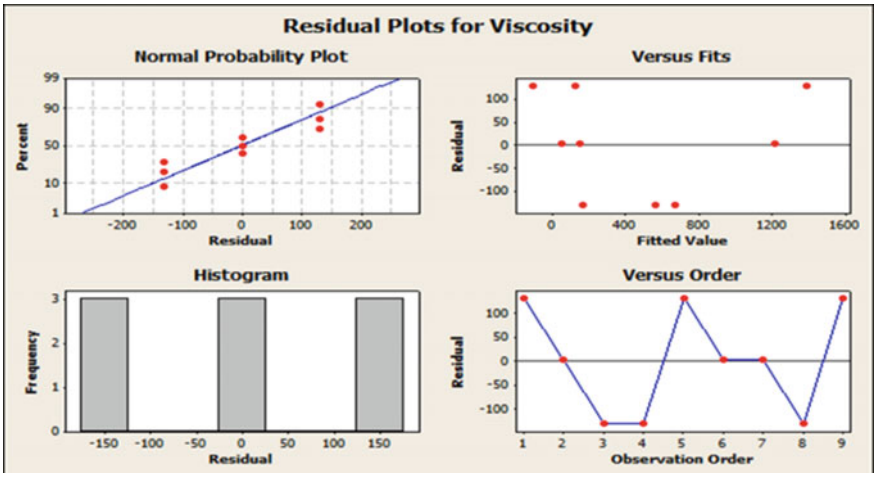

Fig. 6.7 Residual plots for viscosity

Table 6.3 ANOVA values for three parameters

Factor	Type	Levels	Values
Length	Fixed	3	0.025, 0.030, 0.035
Height	Fixed	3	0.001, 0.002, 0.003
Width	Fixed	3	0.0003, 0.0006, 0.0009

Table 6.4 Analysis of variance for viscosity which is generated using adjusted SS for tests

Source	DF	Seq SS	Adj SS	Adj MS	F	P
Length	2	381030	381030	190515	3.69	0.213
Height	2	1668569	1668569	834285	16.14	0.058
Width	2	224553	224553	112276	2.17	0.315
Error	2	103387	103387	51694		
Total	8	2377540				

6.3 Conclusion

The device designed with a varying parameter can be used for detection of adulteration of fluid in real time application with high accuracy. As Taguchi method, SN-Ratio for smaller-the-better is tested and it defines that it always predicts values which we are tending to see in the worst aspect of things or we believe that the worst will happen. Validation of Taguchi method is done by using ANOVA analysis with less error. Here, linear regression calculation finally defines that the values considered satisfying the test analysis.

References

1. W.S. Fyfe, N.J. Price, A.B. Thompson, *Fluids in the Earth's Crust*, vol. 383. (Elsevier, Amsterdam, 1978)
2. K.H. Hentschel, The influence of molecular structure on the frictional behaviour of lubricating fluids. J. Synth. Lubr. **2**, 143–165 (1985)
3. E.W. Lemmon, R. Span, Short fundamental equations of state for 20 industrial fluids. J. Chem. Eng. Data **51**, 785–850 (2006)
4. S.Z. Erhan, J.M. Perez, *Biobased Industrial Fluids And Lubricants* (AOCS Press, 2002)
5. S.L. Outcalt, M.O. McLinden, Automated densimeter for the rapid characterization of industrial fluids. Ind. Eng. Chem. Res. **46**, 8264–8269 (2007)
6. O. Ashour, C.A. Rogers, W. Kordonsky, Magnetorheological fluids: materials, characterization, and devices. J. Intell. Mater. Syst. Struct. 123–130 (1996)
7. A. Agoston, C. Ötsch, B. Jakoby, Viscosity sensors for engine oil condition monitoring—Application and interpretation of results. Sens. Actuators A **121**, 327–332 (2005)
8. G.E. Totten, *Handbook of Hydraulic Fluid Technology* (CRC Press, 2011)
9. G.S. Bisht, S. Holmberg, L. Kulinsky, M. Madou, *Diffusion Free Mediator Based Miniature Biofuel Cell Anode Fabricated on a Carbon-MEMS Electrode*, vol. 28, (Langmuir, 2012), pp. 14055–14064
10. L. Capretto, W. Cheng, M. Hill, X. Zhang, Micromixing within microfluidic devices, in *Microfluidics* (Springer, 2011), pp. 27–68
11. C.-C. Chang, R.-J. Yang, Electrokinetic mixing in microfluidic systems. Microfluid. Nanofluid. **3**, 501–525 (2007)
12. J. Chevalier, F. Ayela, Microfluidic on chip viscometers. Rev. Sci. Instrum. **79** (2008)
13. D. Ciceri, M.P. Jilska, G.W. Stevens, A study of molecular diffusion across a water/oil interface in a Y–Y shaped microfluidic device, in *Microfluidics and Nanofluidics*, vol. 11 (2011), pp. 593–600
14. J.A. Kinast, Production of biodiesels from multiple feedstocks and properties of biodiesels and biodiesel/diesel blends (National Renewable Energy Laboratory, Colorado) Report NREL/SR-510-31460, 2003/03 2003
15. S.R. Yadav, V.K. Murthy, D. Mishra, B. Baral, Estimation of petrol and diesel adulteration with kerosene and assessment of usefulness of selected automobile fuel quality test parameters. Int. J. Environ. Sci. Technol. **1**, 253–255 (2005)
16. O. Skurtys, J.M. Aguilera, Applications of microfluidic devices in food engineering. Food Biophys. **3**, 1–15 (2008)
17. M.S. El-Genk, I.H. Yang, Numerical analysis of laminar flow in micro-tubes with a slip boundary. Energy Convers. Manag. **50**, 1481–1490 (2009)
18. M. Gorji, M. Alipanah, M. Shateri, E. Farnad, Analytical solution for laminar flow through leaky tube. Appl. Math. Mech. **32**, 69–74 (2011)
19. M. Martínez, Hagen-Poiseuille flow solutions in grad-type equations. J. Stat. Phys. **142**, 710–725 (2011)
20. P.S. Venkateswaran et al., Rapid and automated measurement of milk adulteration using a 3D printed optofluidic microviscometer (OMV). IEEE Sens. J. **16**(9), 3000–3007 (2016)

Chapter 7
Exploitation and Utilization of Oilfield Geothermal Resources in INDIA

Manan Shah, Dwijen Vaidya, Shubhra Dhale, Anirbid Sircar, Shreya Sahajpal and Kriti Yadav

Abstract There are plenty of geothermal resources available in existing oil and gas sedimentary basins in India. In recent time oil and gas companies have put their efforts for exploiting and utilizing geothermal resources using various advanced technologies. The paper describes the study of geothermal energy potential in oilfields in India. Considering the existing low and medium temperature geothermal resources, researchers have discussed the possibility of various direct and indirect applications of geothermal energy. The paper also describes the Organic Rankine Cycle (ORC) technique used to generate power from low enthalpy geothermal resources. From the above studies researchers have found that sustainable and economic development of existing oil and gas fields with efficient utilization of geothermal energy sources can reduce the dependency on fossil fuel. It can be done based on the existing infrastructure, technology experience and reservoir information.

Keywords Geothermal energy · Exploitation · Oil and gas · Renewable energy · Sustainable energy

7.1 Introduction

There are numerous Oil and Gas reservoirs in India which can be good potential for geothermal resources. The abandoned Oil and Gas fields, which have high amount of heat content (higher reservoir temperatures) can be utilized for producing geothermal energy [2]. The produced geothermal energy can be utilized for different purposes such as power generation, space heating and cooling, water flooding and various direct

M. Shah · A. Sircar
School of Petroleum Technology, Pandit Deendayal Petroleum University, Gandhinagar, Gujarat, India

D. Vaidya (✉) · S. Dhale · S. Sahajpal · K. Yadav
Centre of Excellence for Geothermal Energy, Pandit Deendayal Petroleum University, Gandhinagar, Gujarat, India
e-mail: dwijen.vaidya@spt.pdpu.ac.in

G. Anand et al. (eds.), *Nanotechnology for Energy and Water*,
Springer Proceedings in Energy, https://doi.org/10.1007/978-3-319-63085-4_7

applications [16]. Water cut in many mature oil and gas fields is very high, up to almost 98% [14]. The produced water is usually considered a nuisance to oil and gas producers because it is required to be disposed or re-injected through another injection well to reservoirs. The management of water from oil and gas production is a direct cost to well-field operators and costs more than all other well services combined [3]. Some well fields produce enough water at high-enough temperatures to produce electricity with an Organic Rankine cycle (ORC) or Binary power plant [17].

7.2 Coexistence of Hydrocarbon and Geothermal Reservoir

Hydrocarbon and geothermal reservoirs coexist in sedimentary basins with abundant geothermal energy in their deepest regions [17]. In hydrocarbon basins, the reservoir conditions are similar to geothermal reservoir conditions. Hydrocarbon is generated under a specific temperature and pressure conditions in the source rock, and groundwater is always involved both in the primary migration of oil from the source rock and in the secondary migration of oil and gas to the reservoir [18].

Oil and Gas reservoirs in petroliferous basins act as geothermal reservoirs. Reservoirs with consecutive or interbedded layers of oil and gas indicate a coexisting geothermal hydrocarbon field, where the produced water is actually a geothermal resource [18]. In this scenario, generally, the geothermal reservoir volume and total resources are much larger than that of the hydrocarbon reservoir volume, which means the total amount of geothermal resources is higher than the total amount of hydrocarbon resources in oilfields [15]. However, the energy density of the geothermal resources is much lower than that of the hydrocarbon resources [12].

7.3 Geothermal Potential in Oilfields in India

India has considerable potential for geothermal energy where the surface temperature varies from 30 to 100 °C [11]. Western coast continental margin and its adjacent region and parts of Gondwana garben are the oilfield region having reasonable amount of geothermal energy. Western coast of India is covered by Cambay Graben, the Bombay offshore and the Konkan coast [11–13]. Cambay region is major oil producing area with world's largest flooding volcanic eruption.

Nearly, 30 hot spring localities in southern zone of India. But very little is reported about them except from the springs in the Godavari valley, Agnigundam and Irade [13]. Godavari spring encountered surface temperature of 62 °C; whereas the reservoir temperature is indicated to be more than 120 °C with artesian flow. Irade field have similar reservoir temperature [4]. The Godavari Graben is tectonically active zone with hydrocarbon bearing and coal bearing Gondwana formations [11]. Various hot springs with low to moderate temperatures ranging from 30 to 62 °C occur

here. Temperature gradients are also higher at 45 °C/km in certain segments of the graben [4–11].

Based on the above research, there are various oilfields which have same surface and reservoir conditions that are similar to geothermal reservoirs. These geothermal oilfields can further be exploited or utilized for power generation or direction applications.

7.4 Exploitation and Utilization of Geothermal Oilfields

7.4.1 Power Generation Using Geothermal Oilfields

The geothermal energy produced from the oil well can be utilized for indirect applications such as geothermal power generation. The oilfield geothermal resources are mainly moderate to low temperature geothermal energy [6]. There are three common types of technologies used to generate electricity are Flash steam, Dry steam and binary cycle. Binary Cycle is the most common used technology for low temperature geothermal resources [7].

Power generation in geothermal oilfield are performed during testing stage with low efficiency, which was demonstrated in Huabei Oilfield, China using helical screw expanding power generator [15]. The most promising mode is the "one-well and one-station" scattered power generation, which can be taken to provide electricity for oil production in geothermal fields with relatively high geothermal resource potential [8].

During electricity generation in oil wells at a low-temperature, the geothermal water is not fed directly into turbine/generator units. It exchanges heat with organic fluid or working fluid (which has lower boiling point than water) through a heat exchanger [5]. The exchanged heat causes the working fluid to change its phase to vapor, and then drives the turbines or generators subsequently to convert thermal energy into electrical energy [7]. This whole cycle is known as Organic Rankine Cycle (ORC), used directly on the well head for power generation [10–15]. Figure 7.1 describes two wells (production well and injection well). The water or steam produced from the well is directly injected on the evaporator side of ORC and the water or steam that exchange heat with working fluid is injected back from the injection well. Figure 7.2 describes the process flow diagram of the ORC.

7.4.2 Direct Applications of Geothermal Energy in Oilfield

Depending on the enthalpy available geothermal fluid can be utilized for electricity as mentioned above and may also be used for direct application. In oilfield geothermal reservoirs, it can be used for heat tracing gathering and transportation.

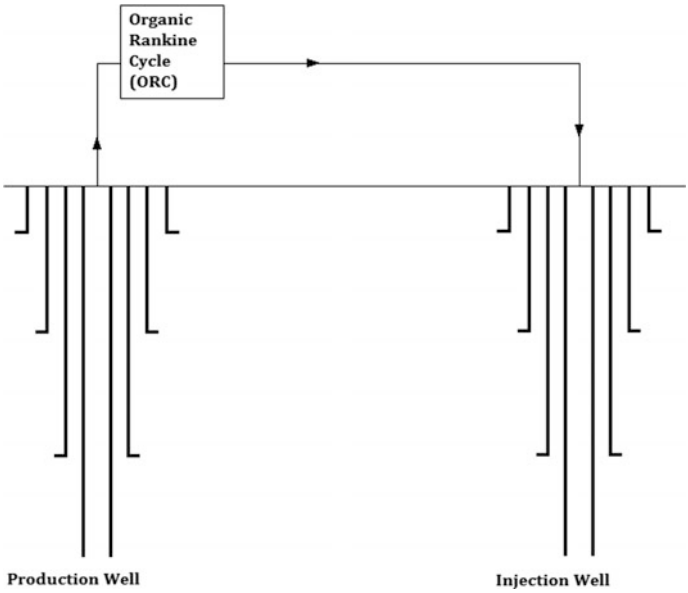

Fig. 7.1 Conceptual model for power generation from oil and gas wells

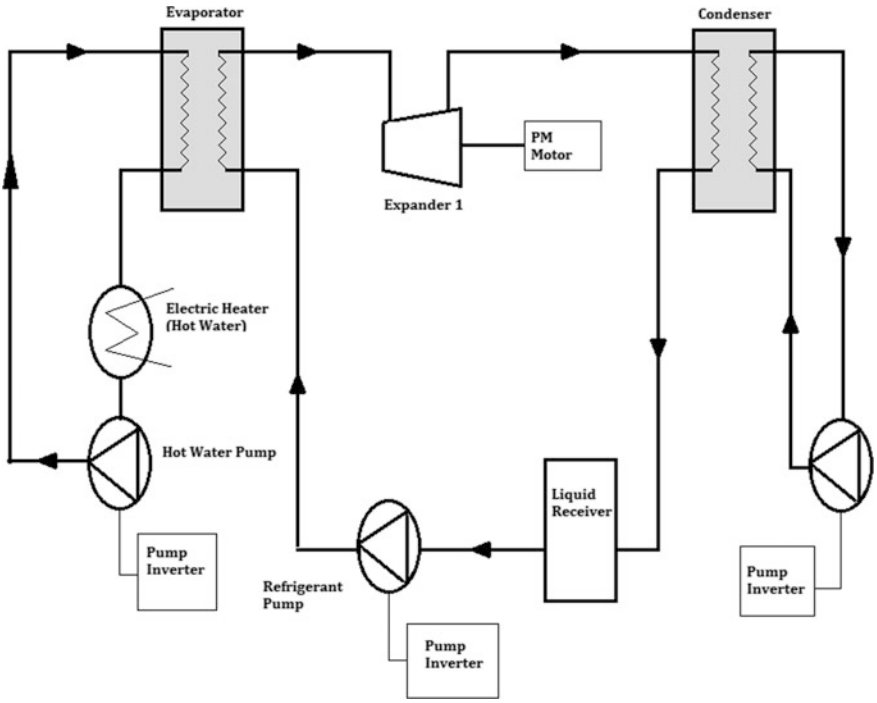

Fig. 7.2 A schematic of organic rankine cycle [1]

Oil or gas is commonly used to heat water in oilfield heat-tracing gathering and transportation systems, which results in huge consumption of oil and gas [15]. During production phase, when it enters into high water cut stage, large amount of geothermal water is produced along with oil. This geothermal water can be used to heat water for oil gathering heat tracing system [7–15].

Space or district heating is one more direct application of geothermal oilfield where the surface temperature of geothermal fluid is low or moderate. In this application, geothermal energy is used for space conditioning in cold climate as well in hot climate [9].

Also, geothermal hot water coming out of the oilfield can be utilized various other purposes such as agriculture, aquaculture, swimming, bathing, animal husbandry, milk pasteurization and balneology.

7.5 Conclusion

Majority of conventional geothermal resources in India are of low enthalpy in nature. However, if unconventional geothermal resources may be explored which includes geothermal resources in oil and gas fields as well as in coal mines, these unconventional geothermal resources can be utilized for producing higher amount of energy than that of conventional geothermal fields. In hydrocarbon fields, where drilling activities have already taken place and if the fields are abandoned, the existing infrastructure can be utilized for producing geothermal water. This may lead to reduction in huge amount expenditure for production. Moreover, the preliminary surface facilities such as storage and primary separation may also be utilized for geothermal water. The possible existence of a geothermal reservoir in any respective hydrocarbon field may also be well predicted during the exploration phase itself. If different energy sectors such as conventional hydrocarbon sector and geothermal energy are properly channelized in India, a lot of dependency on other countries for fossil fuels can be reduced.

References

1. S. Baral, D. Kim, E. Yun, K.C. Kim, Energy, exergy and performance analysis of small-scale organic rankine cycle systems for electrical power generation applicable in rural areas of developing countries. Energies **8**(684), 684–713 (2015)
2. D. Chandrasekharam, V. Chandrasekhar, Geothermal energy resources, India: country update, in *Proceedings World Geothermal Congress 2015, Melbourne*, Australia, 19–25 Apr 2015, pp. 1–6
3. R.J. Crutice, E.D. Dalrymple, Just the cost of doing business? World Oil **225**(10), 77–78 (2004)
4. G.S.I., *Geothermal Atlas of India*, vol. 19 (Geological Survey of India, Special Publication, 1991), pp. 1–143

5. W. Gosnold, The UND-CLR geothermal power plant, in *Proceedings of the 8th International Conference, Power Plays: Geothermal Energy in Oil and Gas Fields, Dallas*, TX, USA, 25–26 Apr 2016
6. L.A. Johnson, E.D. Walker, Oil production waste stream, a source of electrical power, in *Proceeding of Thity-fifth Workshop on Geothermal Reservoir Engineering*, Stanford University, Stanford, California, 1–3 Feb 2010
7. L. Junrong, L. Rongqiang, S. Zhixue, Exploitation and utilization technology of geothermal resources in oil fields, in *Proceedings World Geothermal Congress 2015*, Melbourne, Australia, 19–25 Apr 2015
8. B. Karl, I. Hebert, W. Jesse, Electric power generation using geothermal fluid coproduced from oil and/or gas wells. Geotherm. Resour. Counc. Trans. **33**, 671–672 (2009)
9. J.W. Lund, D.H. Freeston, T.L. Boyd, Direct utilization of geothermal energy 2010 worldwide review, in *Proceedings World Geothermal Congress 2015*, Melbourne, Australia, 19–25 Apr 2015
10. J.W. Lund, K. Gawell, T.L. Boyd, The United States of America country update 2010. Geo-Heat Cent. Q. Bull. **29**(1), 2–11 (2010)
11. O.P. Pandey, J.G. Negi, Geothermal field of India: a latest update, in *Proceeding World Geothermal Congress,* Florence, Italy, vol. 1 (1995), pp. 163–171
12. E. Soldo, C. Alimonti, From an oilfield to a geothermal one: use of a selection matrix to choose between two extraction technologies, in *Proceedings World Geothermal Congress 2015,* Melbourne, Australia, 19–25 Apr 2015
13. D. Vaidya, M. Shah, A. Sircar, S. Sahajpal, A. Choudhary, S. Dhale, Geothermal energy: exploration efforts in India. Int. J. Latest Res. Sci. Technol. **4**(4), 61–69 (2015)
14. M. Vajpayee, R.S. Martolia, K. Chanchlani, M. Mehta, A. Chauhan, A. Sodani, Generating electricity using co-produced brine from oil and gas wells: evaluating prospect in mehsana asset north Cambay basin Gujarat, in *International Petroleum Technology Conference,* Bangkok, Thailand, 14–16 Nov 2016, pp 1–14
15. S. Wang, J. Yan, F. Li, J. Hu, K. Li, Exploitation and utilization of oilfield geothermal resources in China. Energies **9**(798), 1–13 (2016)
16. World Energy Resources: Geothermal World Energy Council 2013, Chapter 9: Geothermal, pp. 9.1–9.62
17. L. Zhang, M. Lui, K. Li, Estimation of geothermal reserves in oil and gas reservoir, in *Society of Petroleum Engineering (SPE) 120031, 2009 SPE Western Regional Meeting,* San Jose, USA, 24–26 Mar 2009
18. L. Zhang, J. Yuan, H. Liang, W. Li, Energy from abandoned oil and gas reservoirs, in *Proceedings of the 2008 SPE Asia Pacific Oil & Gas Conference and Exhibition,* Perth, Australia, 20–22 Oct 2008

Chapter 8
Graphene-TiO_2 Photocatalyst for Efficient Sunlight-Driven Degradation of Methyl Orange

K. Alamelu and B.M. Jaffar Ali

Abstract In this study, graphene-TiO_2 nanocomposites at varying composition of graphene oxide were prepared following hydrothermal method. In order to optimize the composition and time of degradation, photocatalytic efficiency was studied for the composition range 1–10 wt% of graphene oxide. The nanocomposites exhibited good visible light photocatalytic activity for the degradation of Methyl Orange in all the composition range studied. The 10 wt% graphene-TiO_2 found to exhibit photocatalytic degradation of 98% Methyl Orange in 75 min which was 2.5 fold higher than pristine TiO_2 nanoparticles. The band gap of the composites were found to decrease continuously from 3.0 to 2.5 eV, indicating marked red-shift in absorbance spectrum with increased graphene oxide. The enhanced photocatalytic efficiency of composite in comparison to pristine TiO_2 demonstrates corresponding visible light active nature of photocatalysis. We attribute this to the synergetic effect of reduced the electron-hole pairs recombination enabled by graphene oxide intercalation, increased surface area, and creation of more reaction active sites.

Keywords Graphene oxide · TiO_2 · Methyl orange · Hydrothermal synthesis · Photocatalytic activity

8.1 Introduction

TiO_2 is one of the most studied semiconducting materials, that exhibit excellent photocatalytic activity and is used in wide range of application [1]. However, the photocatalytic efficiency of the TiO_2 is limited due to the larger band gap ($\sim$3.2 eV) of the material, faster electron-hole recombination and its absorption only in the UV range. Many methods were investigated to increase the performance of TiO_2 using metal, non-metal doping and carbon based composites materials [2].

K. Alamelu · B.M. Jaffar Ali (✉)
Centre for Green Energy Technology,
Pondicherry University, RV Nagar, Kalapet 605014, Pondicherry, India
e-mail: jaffarali.bm@gmail.com

G. Anand et al. (eds.), *Nanotechnology for Energy and Water*,
Springer Proceedings in Energy, https://doi.org/10.1007/978-3-319-63085-4_8

Graphene, an inexpensive, two dimensional sp2-hybridized novel carbonaceous material, has attracted much attention because of its unique properties such as high surface area (~2600 m^2/g), electron mobility (~15,000 m^2/V.s) of charge carriers, chemical stability, optical transparency and mechanical strength [3]. In Graphene based composites, graphene acts as an ideal electron acceptor and good electron transporting bridge due to its high electron mobility and conjugation structure [4]. Carbon materials have astonishing adsorption properties therefore mainly used in various environmental applications.

8.2 Experimental Section

8.2.1 Reagents and Material

Graphite flakes, n-propanol, titanium tetraisopropoxide, Sodium nitrate, potassium permanganate purchased from Spectrochem. Hydrogen peroxide (30%), sulphuric acid, nitric acid, hydrochloric acid, ethanol and Methyl Orange from Merck were used as received.

8.2.2 Synthesis of TiO_2

TiO_2 nanoparticles were synthesized by hydrothermal method. Titanium tetra iso-propoxide was dissolved in n- propanol to form solution. The diluted nitric acid (0.65 M) was added to the above solution magnetic stirred for 1 h to form clear solution. The transparent solution was transferred into a Teflon lined stainless steel autoclave and heated to 175 °C and maintained for 12 h. After cooling into room temperature the formed precipitates were separated by centrifugation, washed twice with distilled water and then dried at 80 °C for 24 h. The dried powder was calcinated at 400 °C for 3 h.

8.2.3 Synthesis of Graphene-TiO_2 Nanocomposites

Graphene oxide was synthesized by the modified Hummer's method. Different weight percentages (1, 3, 5, 7 and 10 wt%) of grapheneoxide-TiO_2 composites was prepared following hydrothermal method. Graphene Oxide was dissolved in mixture of water and ethanol ultrasonic treatment for 1 h. Prepared TiO_2 was added to the obtained GO solution and stirred for 2 h, to get a homogeneous suspension. The suspension was placed in a 200 mL Teflon lined stainless steel autoclave and heated to 120 °C for 24 h, to achieve reduction of GO to graphene sheets and the deposition of TiO_2 over the graphene sheets. The resulting composite was recovered by centrifugation and washed copiously with DI water, and dried at 70 °C for 12 h.

8.2.4 Characterization

The crystal structure and phase composition of the synthesized photocatalysts was examined by X- ray diffractometer (XRD, Rigaku, Ultima IV, Tokyo, Japan) operated in the reflection mode with Cu Kα radiation (λ = 1.5406 Å). UV-vis diffuse reflectance spectra (UV-DRS) were measured using UV-vis spectrophotometer (Lambda 650 Perkin Elmer Spectrometer) equipped with an integrating sphere attachment. The spectra were collected with $BaSO_4$ as a reference. A confocal micro-Raman spectrometer with a laser beam of 514 nm (Renishaw, Model: RM 2000) was used to identify the properties of carbonaceous materials. Photoluminescence spectra (PL) were recorded using Spectrofluorometer with the 325 nm excitation (Jobin Yvon, Model: Fluorolog-FL3-11. Dye degradation profile has been studied using custom configured Ocean Optics spectrophotometer with LS1 light source, USB 2000 detector and Spectrasuite data acquisition system.

8.2.5 Photocatalytic Experiment

The photocatalytic activities were determined based upon the removal of Methyl Orange in aqueous solutions. For photocatlytic reaction, 0.5 mg/mL photocatalyst was suspended in the aqueous solution of the Methyl Orange (0.02 mM), magnetically stirred in dark condition for 45 min to attain adsorption desorption equilibrium. For the photocatalytic degradation experiment the photocatalytic reaction was initiated by exposure of direct sunlight and then 2 mL of sample was drawn at 15 min interval. The suspended photocatlyst was removed by centrifugation, and the resulting solution analysed with the UV-Visible spectrometer by recording the absorption band maximum of Methyl Orange.

8.3 Results and Discussion

The crystallographic structures and phase composition of the materials were characterized by X-ray diffraction. Figure 8.1 shows the XRD pattern of TiO_2 and different weight percentage of graphene-TiO_2 composites. The XRD pattern of GO exhibits major peakat 11.12 corresponds to (002) plane with d-spacing value of 0.795 nm, which is much higher than d-spacing value of graphite,which indicates the oxidation of graphite to graphene oxide (GO) [5]. Diffraction pattern of TiO_2 shows the major peaks around the 2θ values 25.3 and 27.5 corresponding to anatase (101) and rutile (110) phases respectively which confirms the biphasic nature of the synthesized materials.

As TiO_2 nanoparticles have great absorption in the ultraviolet region, we find that introduction of graphene sheets shifts absorption edge of the nanocomposites

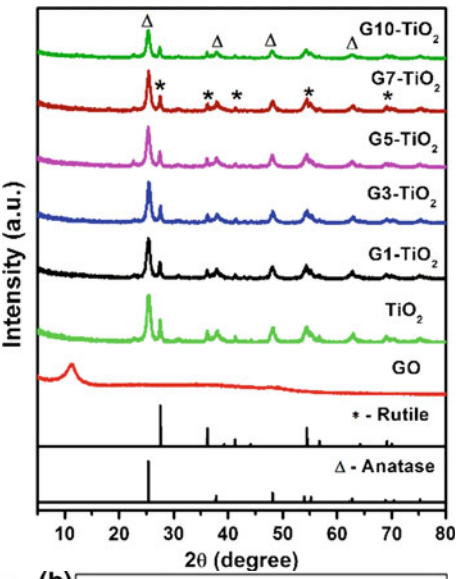

Fig. 8.1 X-ray diffraction pattern of GO, TiO_2 and (1–10 wt%) G-TiO_2 composites

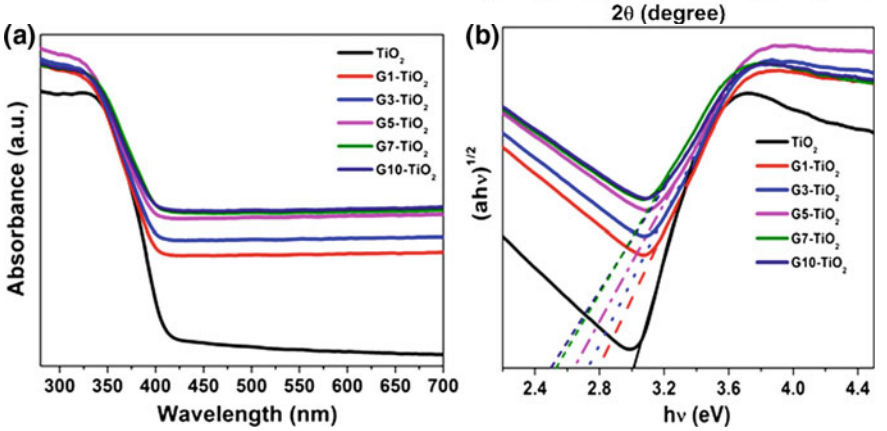

Fig. 8.2 **a** UV-DRS spectra of TiO_2 and (1–10 wt%) G-TiO_2 composites, **b** Tauc plot of TiO_2 and (1–10 wt%) G-TiO_2 composites

towards the visible region. Inorder to estimate the bandgap of the materials, a tauc plot is generated from transformed Kubelka-Munk function as a function of energy of light shown in Fig. 8.2b and bandgap values deduced. Table 8.1 gives the bandgap of graphene-TiO_2 composites for varying composition (1–10 wt%) of graphene. It is observed that increasing weight percentage of graphene resulted in decreasing bandgap (Fig. 8.3).

The Raman spectrum of GO shows D- and G- bandsat $\sim$1354 and $\sim$1617 cm^{-1}, respectively. The peak intensity ratio I_D/I_G for GO was found to be 0.91. The Raman spectrum of the TiO_2 and (1–10 wt%) G-TiO_2 exhibit peaks at 147.3, 401, 520.5 and 638 cm^{-1}, which were assigned to Eg, B1 g, A1 g + B1gand

Table 8.1 Bandgap values of TiO_2 and (1–10 wt%) G-TiO_2 composites

S. no	Samples	Bandgap (eV)
1	TiO_2	3.00
2	G1-TiO_2	2.81
3	G3-TiO_2	2.73
4	G5-TiO_2	2.64
5	G7-TiO_2	2.53
6	G10-TiO_2	2.50

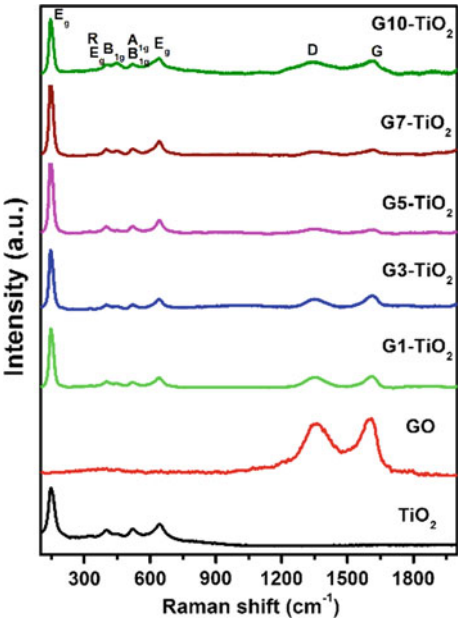

Fig. 8.3 Raman spectra of TiO_2 and (1–10 wt%) G-TiO_2 compsites

Eg of anatase phase titania. The peaks at 248 cm^{-1} were attributed to the second order effective (Eg) of rutile titania.

The PL emission spectra have been used to investigate the efficiency of the charge carrier transfer and the life time of the photogenerated electron-hole in the semiconductor. Figure 8.4 shows the PL emission spectra of TiO_2, Graphene-TiO_2 nanocomposites. Among all the samples pristine TiO_2 shows higher intensity. It is observed that introduction of graphene sheets quenches the intensity of the composite material, indicating reduced recombination rate of charge carrier.

Photocatalytic activity of TiO_2 and (1–10 wt%) G-TiO_2 nanocomposites
Photocatalytic activity of the samples was monitored by discoloration of Methyl Orange dye under direct sunlight irradiation. The percentage of dye degradation in terms of C/C_0 was reported where, C_0 is the initial concentration of the dye and C is the temporal concentration at time. Figure 8.5 plots the normalized concentration of

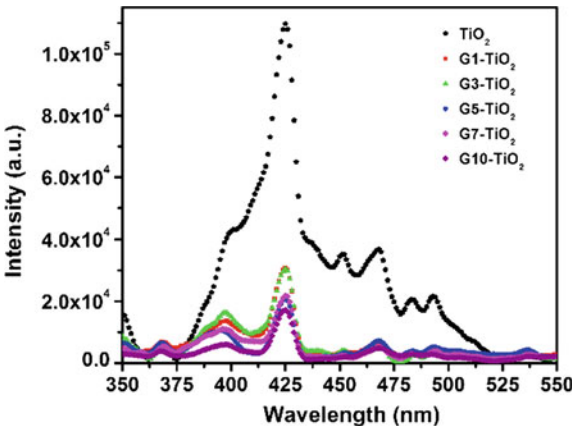

Fig. 8.4 PL emission spectra of TiO_2 and (1–10 wt%) G-TiO_2 composites

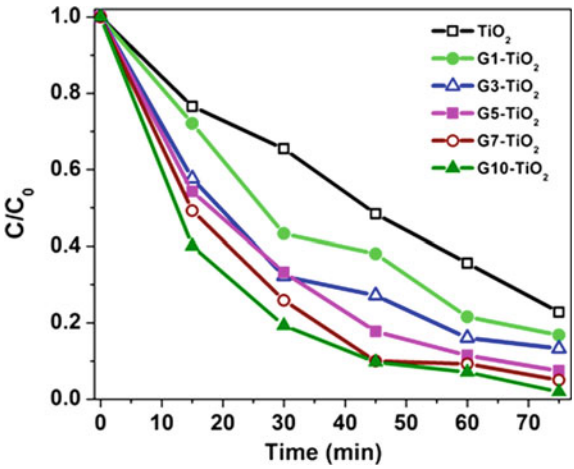

Fig. 8.5 Change in concentration of MO on TiO_2, (1–10 wt%) Graphene-TiO_2 nanocomposites under direct sunlight irradiation

Methyl Orange as a function of time period of photodegradation. Titania nanoparticles degrade about 77% of the dye; with increasing weight percentage of graphene oxide dye degradation percentage increased to 98% within 75 min. Graphene-TiO_2 composite shows excellent photocatalytic activity compare to Pure TiO_2.

The photocatalytic degradation of the dye was followed pseudo first order kinetics reaction method [6, 7].

$$-\ln\left(\frac{C}{C_o}\right) = kt$$

Where, C_0 is the initial concentration of the dye and C is the temporal concentration at time, k is the rate constant of the reaction, and was determined from a linear fit to the data as shown in Fig. 8.6. The rate constant of the photocatalyst are 0.0190, 0.02413, 0.0268, 0.0348, 0.0398 and 0.0487 min^{-1} for TiO_2, G1-TiO_2,

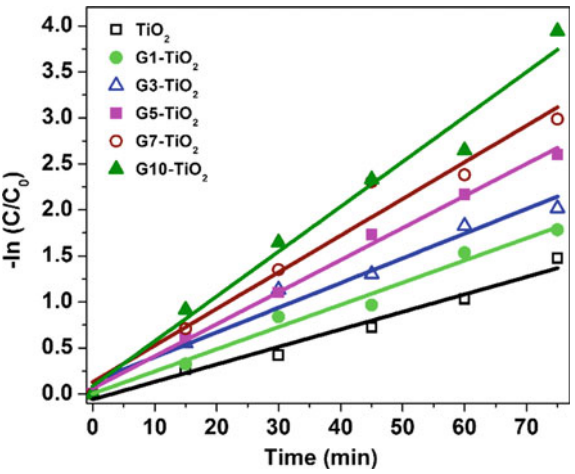

Fig. 8.6 Pseudo-first order kinetics on MO over TiO_2, (1–10 wt%) Graphene-TiO_2 nanocomposites under direct sunlight irradiation

G3-TiO_2, G5-TiO_2, G7-TiO_2 and G10-TiO_2, respectively. G10-TiO_2 exhibit 2.5 fold higher rate of degradation compare to pristine TiO_2 nanoparticles.

8.4 Conclusion

In summary, graphene-TiO_2 composite were prepared by hydrothermal method for varying concentration of graphene oxide. We found that more than 98% of dye solution could be effectively degraded in 75 min by 10 wt% graphene oxide in TiO_2. The enhanced photocatalytic property is attributed to increased surface area of the composite system due to grapheneoxide-TiO_2 intercalation, the inherent high surface area of graphene oxide sheets that enable higher adsorption of dye, suppressed electron-hole pair recombination and improved charge carrier transport. We found that 10 wt% of Graphene Oxide composite with TiO_2 is therefore optimally suited for removal of organic dye by direct sunlight.

Acknowledgements The authors gratefully acknowledge Central Instrumentation Facility (CIF) of Pondicherry University for the instrumentation facilities availed. The author K.A acknowledges the MNRE-National Renewable Energy Fellowship, for their financial support.

References

1. M.R. Hoffmann, S.T. Martin, W.Y. Choi, D.W. Bahnemann, Environmental applications of semiconductor photocatalysis. Chem. Rev. **95**, 69–96 (1995). doi:10.1021/cr00033a004
2. V. Raja, L. Shiamala, K. Alamelu, B.M.J. Ali, A study on the free radical generation and photocatalytic yield in extended surfaces of visible light active TiO_2 compounds. Sol. Energy Mater. Sol. Cells **152**, 125–132 (2016). doi:10.1016/j.solmat.2016.03.008

3. Q.J. Xiang, J.G. Yu, M. Jaroniec, Graphene-based semiconductor photocatalysts. Chem. Soc. Rev. **41**, 782–796 (2012). doi:10.1039/C1CS15172J
4. S. Bai, X.P. Shen, Graphene–inorganic nanocomposites. RSC Adv. **2**, 64–98 (2012). doi:10.1039/C1RA00260K
5. N.I. Kovtyukhova, P.J. Ollivier, B.R. Martin, T.E. Mallouk, S.A. Chizhik, E.V. Buzaneva, A. D. Gorchinskiy, Layer-by-layer assembly of ultrathin composite films from micron-sized graphite oxide sheets and polycations. Chem. Mater. **11**, 771–778 (1999). doi:10.1021/cm981085u
6. L. Sun, Z.L. Zhao, Y.C. Zhou, L. Liu, Anatase TiO2 nanocrystals with exposed 001 facets on graphene sheets via molecular grafting for enhanced photocatalytic activity. Nanoscale **4**, 613–620 (2012). doi:10.1039/c1nr11411e
7. N. Yang, *The Preparation of Nano Composites and Their Applications in Solar Energy Conversion* (Nature springer, 2017)

Chapter 9
Influence of Nanoparticle Type, Size and Concentration on Performance and Safety of Epoxy Composite Adhesively Bonded Metal Joints: A Critical Review

Guillaume Louchaert, Rajnish Garg, Amneesh Singla, Rajeev Gupta and M.S. Goyat

Abstract Epoxy composite adhesively bonded metal joints are extensively used in various industries including automobile, aerospace, oil and gas, etc. Despite their several structural advantages, the adhesively bonded composite structures suffer from peel stress concentrations due to load path eccentricity that usually act as a stimulator for cohesive and interfacial failures. Most of the adhesive and composite adhesively bonded metal joints reveal adhesive, cohesive and mixed-mode failure at the interface of adhesive and adherend interface, respectively. These failures immensely affect the whole integrity of the structure. A substantial amount of research conducted to overcome these stress concentrations by incorporating nanoparticles in epoxy adhesive for toughening of epoxy composite and achieving better wettability of adherend's surface. In the present study, a critical review has been performed to study the influence of nanoparticle type, size and concentration on performance and safety of epoxy composite adhesively bonded various metals based joints.

Keywords Epoxy · Metal-adhesive-metal joint · Nanoparticle · Nanocomposite

G. Louchaert
ENSMM Besancon, 26 Rue de L'epitaphe, 25030 Besançon, France

R. Garg · A. Singla
Department of Mechanical Engineering, University of Petroleum & Energy Studies, Dehradun 248007, Uttarakhand, India

R. Gupta · M.S. Goyat (✉)
Department of Physics, University of Petroleum & Energy Studies, Dehradun 248007, Uttarakhand, India
e-mail: msgoyat@ddn.upes.ac.in

G. Anand et al. (eds.), *Nanotechnology for Energy and Water*,
Springer Proceedings in Energy, https://doi.org/10.1007/978-3-319-63085-4_9

9.1 Introduction

The main interest of polymer nanocomposites is their improved mechanical properties. A very small amount of filler mixed with a polymer can induce significant improvement in elastic modulus, strength as well as some extra characteristics such as flame retardancy and resistance to moisture. Because of these remarkable improvements in material properties in comparison with neat polymer or other composites, industries and academicians are highly interested in this field of research. One of the main polymers used for this purpose is epoxy resin. The diversity of its fields of applications (aircraft and automobile parts, electronic packages, coatings in pipes, etc.) is one of the principal qualities of epoxy resin. Moreover, epoxy resins are versatile with excellent chemical and heat resistance, good impact resistance, and high electrical insulation [1]. However, the utilization of this polymer is limited in various situations because of its low toughness and its average strength [2]. And this is exactly why nano-fillers are so interesting in this case. A good choice of filler could allow the resin to keep its functionalities, which include low weight and easy formability, and to combine it with the unique features of nanoparticles thereby increasing its mechanical properties [3]. In this context, a lot of parameters have to be taken into account. Obviously the type of nanoparticle has a huge impact on the resulting properties of the nanocomposite. Oxide nanoparticles [2, 4] Carbon nanotubes [5], rubber particles [3] and have also shown great improvement on lap shear strength of epoxy composite adhesive based metal-metal joints in previous studies. Nanocomposites represent a new class of materials that exhibit improved performance when compared with their micro-particle counterparts which is relevant to the fact that size of a particle is also a key parameter. And finally, the concentration of fillers determines whether the characteristics of the nanocomposite will increase or decrease [6].

This review paper is focused on the influence of nanoparticle type, size and concentration on performance and safety of epoxy composite adhesively bonded various metals based joints. A brief summary of influence of some selected parameters on lap shear strength of epoxy composite adhesive based metal-metal joints are summarized in Table 9.1.

9.2 Modes of Failure of Neat Epoxy and Nano-Filler Reinforced Epoxy Adhesive Joints

Jojibabu et al., [7] studied the modes of failures for neat epoxy and carbon nano-filler reinforced epoxy adhesive joints. Figure 9.1 shows the modes of failures of the 0.0, 0.5 and 2 wt% carbon nano-filler reinforced epoxy adhesive joints. They observed that the mode of failure in case of the neat epoxy adhesive joints was almost 100% cohesive in nature. However, the reinforced epoxy adhesive joints especially at lower filler content reveal the mode of failure was adhesive as well as

Table 9.1 Summary of influence of some selected parameters on lap shear strength of epoxy composite adhesive based metal-metal joints

Processing technique	Nanoparticle			Adherend	Lap shear strength		Variation (%)	References
	Type	Size (nm)	Content (wt%)		Neat epoxy (MPa)	Nanocomposite adhesive (MPa)		
Mechanical mixing	Calcinated ZrO_2	15	1	6082 aluminium alloy	7.7	12.3	+60	[1]
Mechanical mixing	TiO_2	20	3	Glass/epoxy composite	22.6	33.2	+47	[2]
Mechanical mixing	Rubber particles	55	5	Aluminium 6060	10.2	20	+96	[3]
Mechanical mixing	SiO_2	20	20	Stainless steel plates	17.83	21.52	+21	[4]
Ultrasonic mixing	CNF	9	0.71	CF/epoxy	11.9	12.8	+8	[5]
Ultrasonic mixing	MWCNT-COOH	13-18	0.5	2024 aluminium alloy	4	8	+100	[6]
High speed mixing	MWCNT	10-20	1	AA6061 substrates	14	21.4	+53	[7]

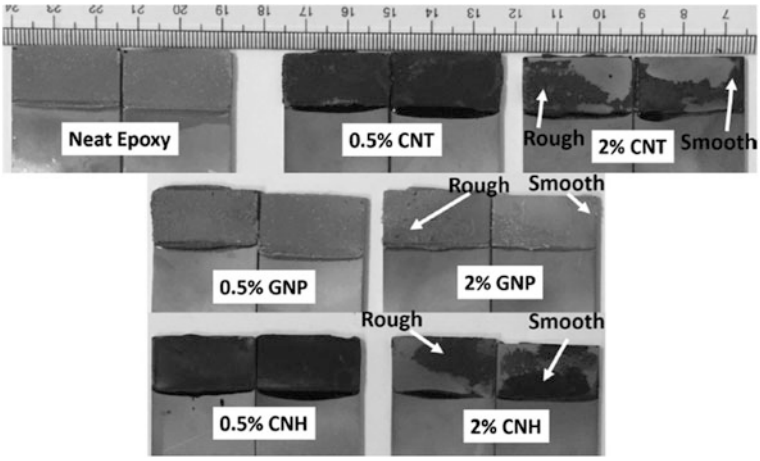

Fig. 9.1 Mode of failure of neat epoxy and nano-filler reinforced epoxy adhesive joints. Jojibabu et al., 2016 [7]

cohesive in nature. They also revealed that for the increase in nanofiller content the mode of failure evolved from cohesive to adhesive type that is from "within the adhesive" to "at the interface between the adhesive and adherend". Their claim was also supported by the fracture sample pictures of nano-filler reinforced joints. For the 0.5 wt% nano-filler reinforced joints, the cohesive failure was realized from the fracture surface. For the 2 wt% nano-filler reinforced epoxy adhesive joints, a mixed mode failure of adhesive and cohesive nature was observed. The zones corresponding to cohesive failure were quite rough while the zones corresponding to adhesive failure were quite smooth.

9.3 Dispersion of Nano-Fillers in the Epoxy Matrix and Fracture Surface Characteristics

The main problem in epoxy nanocomposites is to obtain improved properties by having an homogeneous material with nanoparticles uniformly dispersed into the epoxy matrix. Advanced tools such as electron microscopes help researchers to investigate the dispersion of nanoparticles into a polymer matrix. Jojibabu et al., [7] studied the homogeneity of the carbon nano-fillers dispersion in the epoxy adhesive joints. They investigated the fractured surfaces by scanning electron microscopy (SEM). Figure 9.2 shows the fracture surfaces of (Epoxy-carbon nano tubes) EP–CNT joints. The SEM results revealed the CNTs were dispersed homogeneously in the epoxy matrix at low content (up to 1 wt%) while at higher nano-filler content, agglomerates appeared.

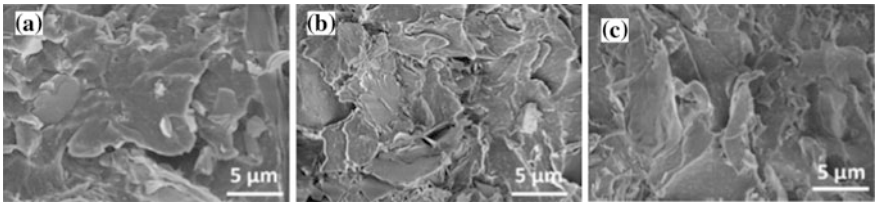

Fig. 9.2 SEM image of the fracture surfaces of **a** 0.2 EP–CNT, **b** 0.5 EP–CNT and **c** 1 EP–CNT. Jojibabu et al., 2016 [7]

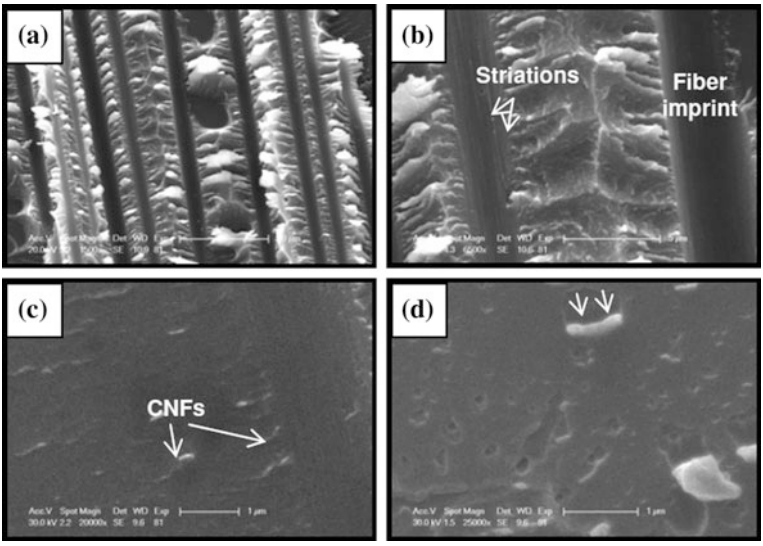

Fig. 9.3 SEM images of the fracture surface of tested joints whose adherend was treated by plasma and whose adhesive consisting 0.5 wt% CNFs. Prolongo et al., 2009 [5]

Prolongo et al. [5] studied the fracture surfaces of epoxy nanocomposite adhesive based metal-metal joints. They showed SEM micrographs of fracture surfaces of the epoxy adhesive consisting 0.5 wt% carbon nano fibers (CNFs) joints, whose adherend was treated by plasma (Fig. 9.3). Figure 9.3a and b correspond to the cohesive failure zones while Fig. 9.3c and d correspond to the adhesive failure zones. The cohesive failure zone shows the presence of fiber imprints consisting striations in form of bright bands. These striations, running along the fiber axis, provide an indication of the adhesive shear failure at the interface of matrix and fiber. In adhesive failure zones, SEM micrographs show the influence of CNFs in crack propagation and the formation of shear cusps.

9.4 Conclusions

A significant improvement in lap shear strength of epoxy based metal joints can be achieved by introducing specific type, size and amount of nanoparticles in epoxy matrix. Nanofibers or carbon nanotubes reinforced epoxy composites based joints have higher safety than the spherical nanoparticles reinforced epoxy composite based metal-epoxy-metal joints. Low weight fractions of nano-fillers can be dispersed uniformly in the epoxy matrix without any agglomerates and results in cohesive failures. For higher fractions of nano-fillers a mixed mode (cohesive and adhesive) failure was observed which can reduce the lap shear strength of the epoxy joints.

References

1. A. Dorigato, A. Pegoretti, F. Bondioli, M. Messori, Improving epoxy adhesives with zirconia nanoparticles. Compos. Interfaces **17**, 873–892 (2010)
2. A. Tutunchi, R. Kamali, A. Kianvash, Steel-epoxy composite joints bonded with Nano-Tio_2 reinforced structural acrylic adhesive. J. Adhes. **91**, 663–676 (2015)
3. Q. Meng, S. Araby, N. Saber, H.-C. Kuan, J. Dai, L. Luong et al., Toughening polymer adhesives using nanosized elastomeric particles. J. Mater. Res. **29**, 665–674 (2014)
4. H. Zhou, H.-Y. Liu, H. Zhou, Y. Zhang, X. Gao, Y.-W. Mai, On adhesive properties of nano-silica/epoxy bonded single-lap joints. Mater. Des. **95**, 212–218 (2016)
5. S.G. Prolongo, M.R. Gude, A. Ureña, Synthesis and characterisation of epoxy resins reinforced with carbon nanotubes and nanofibers. J. Nanosci. Nanotechnol. **9**, 6181–6187 (2009)
6. A.S. Subramanian, J.N. Tey, L. Zhang, B.H. Ng, S. Roy, J. Wei et al., Synergistic bond strengthening in epoxy adhesives using polydopamine/MWCNT hybrids. Polymer **82**, 285–294 (2016)
7. P. Jojibabu, M. Jagannatham, P. Haridoss, G.D. Janaki Ram, A.P. Deshpande, S.R. Bakshi, Effect of different carbon nano-fillers on rheological properties and lap shear strength of epoxy adhesive joints. Compos. Part A Appl. Sci. Manuf. **82**, 53–64 (2016)

Chapter 10
Nano Based Synthesis of PV Panels for Minimizing E-Waste

Meenal Arora, Madhu Sharma and Praveen K. Ghodke

Abstract The globally growing solar panel deployment will result into huge solar panel waste in the coming years. The solar panels will form the major portion of E-silicon waste in the future. The efficiency of the panels can be increased and waste can be minimized by utilizing the materials such as nanowires, nanoparticles, nanotubes and other similar electrically and photonically active Nano template. PV manufacturing companies are researching on quantum based and Dye sensitized solar cells to replace silicon solar cells. The waste produced during manufacturing is less and can also be recovered after end of life of the cell. This process will not only help in reducing the installation, manufacturing costs but will also lead to E-silicon waste reduction. It will also reduce the expensive electronic and electric equipment's used to produce the conventional silicon panels. If the nanosolar technology for PV panels is encouraged it will restrict the practice of exporting silicon waste to developing countries for landfill. The paper analyzes the amount of waste generated when nanotechnology is combined with solar panel technology.

Keywords Silicon solar cells · Nano-particles · Dye sensitized solar cells · Nanotechnology-waste · Recycling

10.1 Introduction

The majority of the conventional solar panels being deployed are conventional solar panels made from the silicon as silicon is easily available in nature and in abundance but the problem is high cost of manufacturing [1]. Hence there is a gradual shift towards generating solar energy from nanomaterials such as nanofiber, nanowires, nanoparticles and other various active nanotemplates [2] which will not only help in increasing the efficiency but will also reduce the manufacturing cost.

M. Arora (✉) · M. Sharma · P.K. Ghodke
Department of Electrical Power and Energy, University of Petroleum & Energy Studies, Dehradun, Uttarakhand, India
e-mail: maror@ddn.upes.ac.in

G. Anand et al. (eds.), *Nanotechnology for Energy and Water*,
Springer Proceedings in Energy, https://doi.org/10.1007/978-3-319-63085-4_10

When the conventional panels will reach their end use there will be great inflow of silicon waste but this waste will get reduced by using nano solar panels [3]. For protection of the environment, recycling of solar panels can be done but the limitation is that when these panels are recycled, it utilizes much more amount of energy as compared to recycling of nano solar panels. According to the researcher's the amount of E-silicon that can be recovered from used solar panels is 90% but the equipment's used for manufacturing as well as recycling the panels also contribute to E-waste [4]. The paper presents a comparison between the recycling of silicon solar panels and nanomaterial (perovskite) based solar panels and analyzes amount of waste generated.

10.2 Conventional Solar Cells

10.2.1 Manufacturing of the Silicon Solar Panels

Elements used in making the solar includes silicon, carbon, boron, alluminium, zinc, pottasium, silver etc. with average silicon cell diameter ranging from 6 to 15 cm and thickness of 200–250 μm. An average module contains around 36 numbers of cells [5].

The composition and thickness of the cell varies according to the type of cell. The technology requires a number of thermal or chemical processing steps such as diffusion, doping, drying, firing, annealing, deposition, and coating of the solar cell [6] and hence the required machinery. This green technology is being manufactured in developing countries like China [7] and India but they not have proper provision of protecting the environment as well the workers employed. Once the panels will complete their life cycle, if not properly disposed, will add to the silicon waste.

The below table compares the physical parameters for Single Silicon and Cadmium Telluride solar cells based on three scenarios [8]

- Business as usual (BAU)
- Realistic improvement (REAL)
- Optimistic improvement (OPT)

It is estimated that the cumulative global deployment of solar panels will reach approximately 1,632 GW in 2030 and about 4,512 GW in 2050 [9]. Depending upon the increase in number of panels deployed for generation of electricity there will be subsequent rise in the amount of materials like silicon, silver, cadmium, telluride, glass etc. required for manufacturing (Table 10.1).

Table 10.1 Physical parameters of Single Si and CdTe solar cell based upon business as usual, optimistic and realistic improvement [12]

Parameters	Single -Si				CdTe			
	TODAY	BAU	REAL	OPT	TODAY	BAU	REAL	OPT
Wafer thickness/layer thickness	190 µm	150 µm	120 µm	100 µm	4.0 µm	2.0 µm	1.0 µm	0.1 µm
Silver per cell	9.6 g/m^2	9.6 g/m^2	5.0 g/m^2	2.0 g/m^2				
Glass thickness	4.0 mm	4.0 mm	3.0 mm	2.0 mm	3.5 mm	3.5 mm	3.0 mm	2.0 mm
Operational lifetime	30 years	30 years	35 years	40 years	30 years	30 years	35 years	40 years

10.2.2 Recycling of Solar Panels

The panels contain hazardous as well as valuable materials. The process of recycling is necessary for recovering, reusing materials in order to reduce the cost of per peak of new panels as well as the dependence on the natural resources. Process of recycling requires the process of recycling requires the panel to be dismantled after which the methods such as mechanical separation, chemical dissolution and electrodeposition are used to recover the metal [10]. After layer by layer stripping the elements can be recovered parts per billion during recycling [11]. Hence, after an operational life time of 25–40 years based on early and regular loss scenario the panel waste is estimated to be 60–78 million tons globally respectively [9]. Depending upon the waste generated the great amount of elements like silver, glass and silicon recovered can be used again reducing the cost of new panels without compromising the efficiency [12].

10.2.3 Synthesizing Nano Based Solar Panels

Nano material is the future technology in solar energy. Synthesis of nanosolar panels or dye synthesized solar panels can be done using materials like ZnO, perovskite, graphene, carbon nanotubes/rods, Copper-Indium-Diselenide semiconductor ink, Silicon nanocrystalline ink, "Nano-cables" which are grown on a thin film material [13]. Recently nano cells made from lead Iodide have emerged as strong competitor to the conventional solar cells [14]. Efficiency of perovskite based solar cells is 20% more than the power conversion efficiency of the commercially available solar panels [15].

10.2.4 Recycling of Nano Based Solar Panels

The recycling of nano cells have been performed at laboratory level till date, hence it challenging to estimate the cost as well the difficulties in recycling at industrial level. The elements of the Perovskite based solar cells which contain Methylammonium lead iodide (MAPbI3), the conductive glass, gold electrodes [4] all layers when stripped which includes toxic lead as well as Fluorine doped tin oxide glass which forms the most expensive part of the cell can be reused without effecting the performance of the device as such devices gives the performance efficiency of 13.5% [16]. Recycling process of nanosolar includes technology which requires low temperature solution. Devices used for recycling at laboratory level are chemicals like dimethylformamide, chlorobenzene, ethyl acetate etc. which are easily available [4].

10.3 Limitations

Research is being done to overcome the following limitations.

- The operational lifetime for silicon solar panels is almost two decades hence more focus is on installation and generation of electricity rather than
- The manufacturing and use of nanosolar panels is still at research and laboratory stage
- There is no sufficient data available on amount of each metal recovered from nanosolar panels.
- Polysilicon is being used with ethanol instead of chlorine-based chemicals, in order to avoid the creation of silicon tetrachloride.

10.4 Conclusion

Attempt is being made to bring change in technology for recycling of solar panels. It is also observed that though there is limited data available, the recycling of 3rd generation solar cells is simpler as compared to the energy intensive equipment's required for conventional solar panels. The manufacturing cost is reduced as well as the rate of conversion of solar energy to electricity is high. The dyes used can be manufactured locally and easily. Use of nanomaterials if recycled and disposed in environmental friendly manner will not only protect the environment but also help us sustain the goal of establishing green energy.

References

1. E. Boysen, Nanotechnology in Solar Cells, UnderstandingNano.com. http://www.understandingnano.com/solarcells.html
2. D. Mulvaney, Solar energy isn't always as green as you think. IEEE Spectr. (2014)
3. N. P. a. M. S. Ali. http://www.cstep.in/uploads/default/files/publications/stuff/CSTEP_Solar_PV_Working_Series_2015.pdf
4. A. Binek, M.L. Petrus, N. Huber, H. Bristow, Y. Hu, T. Bein, P. Docampo, Recycling perovskite solar cells to avoid lead waste
5. S. P. Sukhatme, *Solar Energy: Principles of Thermal Collection and Storage* (1984)
6. A. Verma, P. Bhatt, Design and cost analysis of PV system using nano solar cells. Int. J. Sci. Res. Publ. (2014)
7. D.W. Zeng, M. Born, K. Wambach, Pyrolysis of EVA and its application in recycling of photovoltaic modules. J. Environ. Sci. **16**(6), 889–893 (2004)
8. A. Wade, Evolution of First Solar's Module Recyling Technology, First Solar Inc (2013)
9. S. Wecken(IRENA), G. H.-P. Andreas Wade, End of life management (Solar photovoltaics Panels), International Renewable Energy Agency (IRENA) and the International Energy Agency Photovoltaic Power Systems (IEA-PVPS) (2016)

10. B.J. Kim, D.H. Kim, S.L. Kwon, S.Y. Park, Z. Li, K. Zhu, H.S. Jung, Selective dissolution of halide perovskites as a step towards recycling solar cells. Nat. Commun. (2016)
11. Exploring new ways to reuse your silicon. http://poseidonsolar.com/
12. R. I. F. W. Rolf Frischknecht, Life Cycle Assessment of Future Photovoltaic Electricity Production from Residential-scale Systems Operated in Europe, IEA-PVPS Task 12 (2014)
13. I. R. E. A. (. a. t. I. E. A. P. P. S. (IEA-PVPS). http://www.irena.org/DocumentDownloads/Publications/IRENA_IEAPVPS_End-of-Life_Solar_PV_Panels_2016.pdf
14. Solar Cell Manufacturing Equipment, An AMTECH Company. http://www.btu.com/products/solar-cell-manufacturing-equipment/
15. J. Shin, J. Park, N. Park, A method to recycle silicon wafer from end-of-life photovoltaic module and solar panels by using recycled silicon wafers. Sol. Energy Mater. Sol. Cells, 1–6 (2017)
16. T.K. Kim, B.V. Saders, J. Moon, T. Kim, C.H. Liu, J. Khamwannah, D. Chun, D. Choi, A. Kargar, R. Chen, Z. Liu, S. Jin Tandem structured spectrally selective coating layer of copper oxide nanowires combined with cobalt oxide nanoparticles. Nano Energy

Chapter 11
Nano Particle Based Polymer Flooding for Enhanced Oil Recovery: A Review

Ch M. Sukesh and Barasha Deka

Abstract Polymer flooding is a conventional EOR process. Application of nanoparticle to polymer is the current research area. These paper is aimed at studying the ability of different type's polyacrylamide Nanoparticle to EOR. Some of the nanoparticles used are Magnesium oxide, Aluminium oxide, Zinc oxide etc. and are treated with silane for solving reservoir problem. Amongst them aluminium oxide, nickel oxide, hydrophobic silicon oxide and silicon oxide treated with silane are good agents for EOR by Ogolo et al. (SPE Saudi Arabia Section Technical Symposium and Exhibition 1–5, 2012) [1]. Ethanol is used as dispersing media for these nanoparticles for solving recovery problem by reducing Interfacial tension between oil and water. By using Aluminium oxide NP we can reduce oil viscosity while silicon oxide NP changes rock wettability. These results indicate that some of these nanoparticles are very effective [2] while used with polymer flooding and can be used to maximize recovery level and boost hydrocarbon production.

Keywords Polymer flooding · Wettability · Mobility control · Capillary number

Nomenclature

EOR	Enhanced Oil Recovery
NP	Nano Particle
PF	Polymer Flooding
Al	Aluminium
Si	Silica
Mg	Magnesium
Fe	Iron
Ni	Nickle

C.M. Sukesh (✉) · B. Deka
School of Petroleum Technology, Pandit Deendayal Petroleum University, Gandhinagar, Gujarat, India
e-mail: mallikarjuna.smtpe15@spt.pdpu.ac.in

B. Deka
e-mail: dekabarasha12@gmail.com

G. Anand et al. (eds.), *Nanotechnology for Energy and Water*,
Springer Proceedings in Energy, https://doi.org/10.1007/978-3-319-63085-4_11

Zn Zinc
K Permeability
IFT Interfacial Tension

11.1 Introduction

Enhanced oil recovery is come under third phase of useful oil production and therefore called as tertiary recovery of oil production. The primary phase of oil production begins with the exploration of an oil field using the natural stored energy to move the oil too well by expansion of volatile components and pumping of individuals wells to assists the natural drive. After some period of time, production get declines and secondary recovery of oil production is get launched only when supplement energy is added to the reservoir by injection of the water. As water to oil production ratio of the field approaches an economic limit of operation, when the net profit diminishes because the difference between the values of the produced oil and the cost of water treatment and injection becomes too narrow, right now tertiary recovery begins [3].

EOR procedure involves the injection of chemical compounds dissolved in the injection water, miscible gas injection alternating with water injection, the injection of micro-emulsion (composed of surfactants, alcohols and crude oil), and the injection of steam and in situ combustion as shown in Fig. 11.1.

Matured oilfields have undergone extensive drilling and production which have undergone years or decades of water flood operations (secondary recovery). Therefore, these fields are still having a rich oil source which are producing at low oil rates. The adequate well-designed and successful EOR programs can contribute

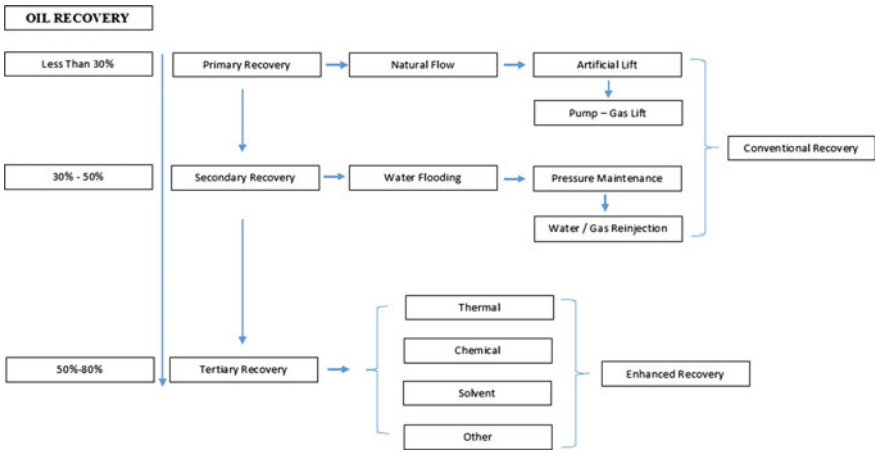

Fig. 11.1 Enhanced oil recovery stages

significantly to recover left over crude oil. There many oilfields at a matured water flood stage that can promote from different EOR process applications [3].

The initial oil production depends on the inherent energy of reservoir being spelled in terms of formation pressures to help the production and reservoir engineers for assessing the economic life of the field. This comes under the primary recovery of the field which contributes from 5 to 50% of OIIP still leaving behind the significant amount of oil which we call it EOR target oil [3].

EOR Improves recovery by changing fluid properties, fluid-fluid interactions and fluid-rock interaction. The various techniques of oil recovery basically acts in two ways [3]:

1. By altering the relative flow rates by which the oil will flow at a faster rate as compare to water through the porous media.
2. By changing the phase composition and other physico-chemical processes that takes part in the process as

Process responsible for changing the fractional flow:

- Reduction in IFT
- Alteration of Wet ability
- Viscosity alteration
- Pore plugging.

Process responsible for phase behavior change:

- Miscibility
- Swelling
- Solubilization
- Oil-Water Emulsification and Water-Oil Emulsification.

11.2 Nano Particle

Nanoparticles are the materials that are having the range in between 1 to 100 nm [4]. The term ‘nanoparticle’ is refers to inorganic materials. Nanoclusters have at least one dimension between 1 and 10 nm and a narrow size distribution. Nano powders are agglomerates of ultrafine particles, nanoparticles, nanometer-sized single crystals and ultrafine particles [1]. Different type of nanoparticles are shown in below Table 11.1.

Table 11.1 List of nanoparticles properties [1]

S.No	Nanoparticles	Particle size (nm)	Surface area (m^2/g)
1	Aluminium oxide	40	60
2	Magnesium oxide	20	50
3	Iron oxide	22–41	40–60
4	Nickel oxide	100	6
5	Tin oxide	51–72	10–30
6	Zinc oxide	12–29	90
7	Zirconium oxide	22–31	35
8	Silane treated silicon oxide	11–27	>400
9	Hydrophobic silicon oxide	11–19	100–140

11.3 EOR Using Nanoparticle

NP are spectacular for good recovery agent which are having reservoir fatigue problems. They are different types of nanoparticles, among them aluminium (Al) and Silica (Si) NP oxide are recovery agents for EOR [1].

11.3.1 Aluminium Oxide (Al) Nanoparticle

These Aluminium Oxide (Al) reduces crude oil viscosity and good for left over crude recovery only when it is used with distillation water and brine as dispersing agent [5].

11.3.2 Silica Oxide (Si) Nanoparticle

These Silica Oxide (Si) reduces IFT between oil and water caused by using ethanol as dispersing agent and also changes rock wettability of reservoir [4, 5].

11.3.3 Magnesium Oxide (Mg) and Iron Oxide (Fe) Nanoparticles

These Magnesium Oxide and Iron Oxide NP reduces crude oil viscosity only when NP are used along with distillation water because brine agent can cause permeability problem of reservoir. Therefore, remaining NP like Tin oxide are also used along with distillation water [5].

11.3.4 Nickel Oxide (Ni) Nanoparticle

These NP reduces crude oil viscosity only when NP are used along with diesel for improving oil recovery.

For nickel oxide (Fe) NP, diesel is best dispersing agent for left over crude oil recovery [5].

11.3.5 Dispersion Agent

In these review paper, we are discussing about distillation water, Brine, Diesel and Ethanol.

Distillation Water: Distillation Water gives less recovery as compared with presence of NP mixture gives high recovery. AL, Mg, Tin and Zn oxide are favorable with distilled water.

Brine agent: Brine may causes permeability problems in reservoir and it is favorable for Al, Ni and silica oxide NP.

Diesel Agent: By using diesel as dispersing agent for NP can improve oil recovery factor and therefore diesel and crude oil are miscible in nature. Al and Ni oxide NP are favorable with Diesel Dispersing Agent.

Ethanol Agent: Ethanol is retrieves better recovery than brine dispersing agent. Al and Si oxides are favorable with Ethanol media.

11.3.6 Mobility Control Chemical [3]

- Polyacrylamide
- Polysaccharide Fig. 11.2.

11.4 Effect on Wettability

Wettability is effective factor which affects the recovery efficiency [6].

$$\textit{Sweep Efficiency} \propto \textit{Mobility Ratio}$$

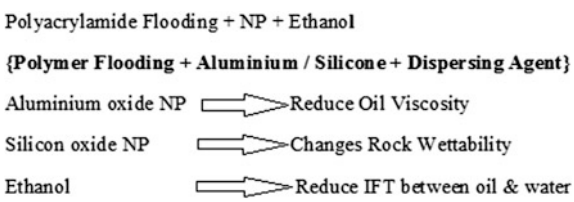

Fig. 11.2 Polyacrylamide flooding with Nanoparticle + Ethanol [1, 10, 7]

Surface Coated Poly-Silica NP—Used to stabilize both water in oil and oil in water emulsion [7].

LowPermeableReservoir

Polyacrylamide-Silica NP can changes the rock wettability which could be used to improve 50% of production recovery. Because of ion-dipole interaction between cations and silica oxide NP, viscosity of nano-suspension increases with increasing Silica oxide NP concentration. It also prevents degradation [7].

11.5 Discussion

By studying Nanoparticles reacting with different various dispersion media have different challenges takes place in reservoir properties.

- Increasing Viscosity = Increasing Oil Recovery ∼ Wettability alteration [8].
- Sweep Efficiency ∼ Mobility Ratio {Mobility of capillary trapped oil} [9].
- Advance Drag Reduction [9] Table 11.2.

Polyacrylamide + Silica NP {PSNP} used to:

Because of Ion-Dipole interaction between cation and silica NP, Viscosity of nano-suspension increases by increasing Silica NP concentration [10].

Therefore,

- Hydrophilic PSNP is used to produce **Water Wet Formation** [8].
- Neutrally wet PSNP is used for **Reduction in IFT between oil and water** [8].

11.6 Conclusion

- Oil Recovery with Silica NP produces 10% Higher than Normal Polymer Flooding [10]
- Prevent Degradation and Increase Viscosity which resembles crude Oil Recovery [10]
- Hydrophilic and Neutrally wet PSNP carries good amount trapped residual oil along with production flow [7]
- Silicon Group are stable oil in water emulsion [7].

Table 11.2 Effect of nanoparticles in sandstone and carbonate reservoir [7]

Sandstone	Carbonate
• Improves $K_{Effective}$ of water • Decrease $K_{absolute}$ • Stabilize emulsion droplet •To passage through pore throats of • reservoir rock	• Convert strongly oil wet to strongly water wet • Water W increases—increasing concentration silica

References

1. N.A. Ogolo, O.A. Olafuyi, M.O. Onyekonwu, Enhanced oil recovery using nanoparticles, in *SPE Saudi Arabia Section Technical Symposium and Exhibition held in Al-Khobar, Saudi Arabia, 8–11 April 2012, Paper No. SPE 160847* (2012), pp. 1–5
2. A.J.P. Fletcher, J.P. Davis, How EOR can be transformed by nanotechnology, in *2010 SPE Improved Oil Recovery Symposium held in Tulsa, Oklahoma, USA, 24–28 April 2010, Paper No. SPE 129531* (2010), p. 1
3. Erle C. Donaldson, G.V. Chilingarian, Enhanced Oil Recovery, I Fundamentals and Analyses (University of Southern California, Los Angeles, California, U.S.A, Elsevier Science publishers, B, V., Chap. 1–5, 1985)
4. S. Ayatollahi, M.M. Zerafat, Nanotechnology-assisted EOR techniques: new solutions to old challenges, in *SPE International Oilfield Nanotechnology Conference held in Noordwijk, The Netherlands, 12–14 June 2012, Paper No. SPE 157094* (2012), pp. 1–8
5. C. Negin, A. Saeedi, Application of Nanotechnology for Enhancing Oil Recovery a Review, Petroleum (2016), pp. 1–10, doi:10.1016/j.petlm.2016.10.002
6. M.O. Onyekonwu, N.A. Ogolo, Investigating the use of nanoparticles in enhancing oil recovery, in *34th Annual SPE International Conference and Exhibition Held in Tinapa—Calabar, Nigeria, 31 July–7 August 2010, Paper No. SPE 140744* (2010), p. 4
7. G. Cheraghian, Young, Researchers, Elite Club, Effects of nanoparticles on wettability: a review on applications of nanotechnology in the enhanced oil recovery. Int. J. Nano Dimens. **6**(5), 443–452 (2015). (Special Issue for NCNC, Dec. 2014, IRAN) (2015), pp. 1–6, doi:10.7508/ijnd.2015.05.001
8. B.A. Suleimanov, F.S. Ismailov, E.F. Veliyev, Nanofluid for enhanced oil recovery **78**(2), 431–437 (2011), doi:10.1016/j.petrol.2011.06.014
9. E. Rodriguez, M.R. Roberts, H. Yu., C. Huh, S.L. Bryant, Enhanced migration of surface-treated nanoparticles in sedimentary rocks, in *2009 SPE Annual Technical Conference and Exhibition held in New Orleans, Louisiana, USA, 4–7 October 2009, Paper No. SPE 124418* (2009), pp. 1–3
10. A. Maghzi, R. Kharrat, A. Mohebbi, M.H. Ghazanfari, The impact of silica nanoparticles on the performance of polymer solution in presence of salts in polymer flooding for heavy oil recovery, in *The Science and Technology of Fuel and Energy Accepted 6 January 2014* (2014), pp. 1–10, doi:10.1016/j.fuel.2014.01.017

Chapter 12
One Pot Synthesis of Cu_2O-RGO Composite Using Mango Bark Extract for Supercapacitor Application

J. Sharath Kumar, Milan Jana, Pranab Samanta, Naresh Chandra Murmu and Tapas Kuila

Abstract A facile and green approach is demonstrated for the simultaneous reduction of graphene oxide (GO) and copper acetate to prepare Cu_2O-reduced graphene oxide (Cu_2O-RGO) composite using mango bark extract. Reduction of GO and formation of Cu_2O-RGO has been confirmed by FT-IR spectroscopy. The morphology of Cu_2O is found to be spherical ($\sim$10 nm) shape from TEM and FE-SEM image studies. The CV profile of Cu_2O-RGO composite exhibits a working potential of −0.1 to 0.7 V with a pair of anodic and cathodic peaks at $\sim$0.15 and 0.38 V, respectively at a scan rate of $\sim$10 mV s^{-1}. The high electrochemical performance is attributed to the synergistic contribution of redox like Cu_2O and electrochemical double layer capacitance of RGO. The specific capacitance is found to be $\sim$470 F g^{-1} at a current density of 2 A g^{-1}.

Keywords Graphene · Green synthesis · Supercapacitor

12.1 Introduction

Supercapacitor, also well-known as ultracapacitor attains high power density with faster charge-discharge rates and improved number of charge-discharge cycles [1]. It stores energy via electrical double layer capacitance (EDLC) along with an electrostatic charge storage mechanism on the surface of carbonaceous materials which are conducting [2]. In converse, inorganic nanomaterials and conducting polymers hoard the electronic charges through redox-reactions which bestow towards psedocapacitance to obtain high specific capacitance (SC). In order to

J.S. Kumar · M. Jana · P. Samanta · N.C. Murmu · T. Kuila (✉)
Surface Engineering and Tribolgy, Council of Scientific and Industrial Research-Central Mechanical Engineering Research Institute, Durgapur 713209, India
e-mail: tkuila@gmail.com

J.S. Kumar · M. Jana · P. Samanta · N.C. Murmu · T. Kuila
Academy of Scientific and Innovative Research (AcSIR), CSIR-CMERI Campus, Durgapur 713209, India

G. Anand et al. (eds.), *Nanotechnology for Energy and Water*,
Springer Proceedings in Energy, https://doi.org/10.1007/978-3-319-63085-4_12

attain higher working potential along with higher SC and enduring stability the carbonaceous materials are hybridized with inorganic nanomaterials where ELDC gets hybridized with psedocapacitance nature [3].

Among a variety of inorganic materials available, Cu_2O is most usually studied for the reason that it is cost effective, environmental stable and has higher pseudocapacitance [4]. Graphene, an atomically thick with honeycomb lattice of compactly arranged sp^2 hybridized carbon atoms has grabbed massive attention in scientific and technological communities attributable to its unique properties such as large surface area, high conductivity and long term electrochemical stability [4].

The escalating requirement of high power density with the deteriorating non renewable sources of energy has trigged immense research attempts in the search of alternative sources of energy production and storage. Hereby, an effort has been put in designing a supercapacitor with the hybridization of Cu_2O NPs with graphene through eco-friendly route of synthesis using naturally abundant mango bark.

12.2 Experimental

12.2.1 Reagents and Chemicals

Graphite and copper acetate were obtained from Sigma-Aldrich. Polyvinylidenefluoride (PVDF) and conducting carbon black were obtained from MTI Corporation, USA. Mango bark was collected from the campus of CSIR-CMERI, Durgapur, which were washed and dried properly. The chemicals obtained were of analytical grade so were used as obtained without further purification. Throughout the experiment DI water was used as solvent unless it is mentioned.

12.2.2 Preparation

Graphene oxide (GO) was prepared as in available reports by modified Hummer's process [5]. In one-pot synthesis method, simultaneously Cu_2O was prepared along with reduction of GO to obtain Cu_2O decorated reduced graphene oxide (RGO). Homogenous solution of 50 mL of 0.1 M $Cu(CH_3COOH)_2$ was prepared by ultrasonication. The prepared $Cu(CH_3COOH)_2$ solution was added to the GO suspension (2 mg mL^{-1}) and stirred for $\sim$3 h to obtain a homogenous solution. To this solution, mange bark extract (which was obtained by mixing $\sim$1 g of mango bark to 30 mL DI and stirring it over-night and filtered) was added and refluxed overnight at 85 °C. The obtained product was allowed to cool to room temperature then it was filtered and dried. The schematic of the preparation technique is shown in the Fig. 12.1.

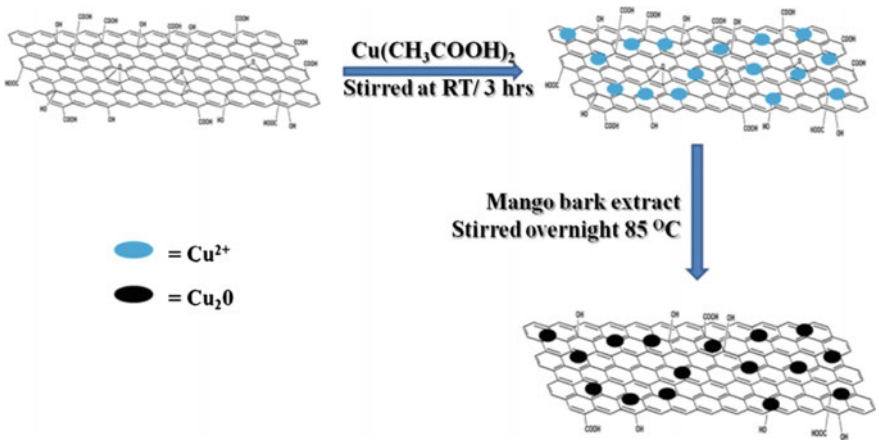

Fig. 12.1 Scheme for the synthesis of CRGO composite

12.2.3 Characterization

Transmission electron microscopy (TEM) was performed using JOEL-JEM 2200 FS instrument (Japan) at 200 kV. Field emission scanning electron microscopy (FE-SEM) was performed using Σigma HD, Carl Ziess (Germany). Fourier transform infrared (FT-IR) spectroscopy was done in JASCO FT/IR-6600 (USA). All electrochemical experiments were carried out using PARSTAT-4000 using Pt-wire as counter electrode, Ag/AgCl as reference electrode and modified glassy carbon as working electrode. The samples for electrochemical measurements were prepared by dispersing RGO/Cu_2O composite in ethanol with concentration of $\sim$2 mg ml^{-1} with 10 wt% carbon black and 5 wt% PVDF through ultrasonication. The obtained homogeneous solution was casted on to the tip of the glassy carbon electrode and dried at RT. Thus prepared electrode was used for all the electrochemical measurements.

12.3 Results and Discussion

12.3.1 Characterization of the Composites

FT-IR spectra of CRGO and GO are depicted in Fig. 12.2. The FT-IR spectrum of GO has broad peak corresponding –OH stretching vibration at $\sim$3415 cm^{-1}. The –OH bending and deformation peak of the water which has been trapped in the inter-layers can be seen at $\sim$1395 cm^{-1}. The peak corresponding to –C=O vibration of –COOH groups on edges of the graphene layer can be seen at $\sim$1715 cm^{-1}. The peak at $\sim$1625 cm^{-1} can be because of the skeletal

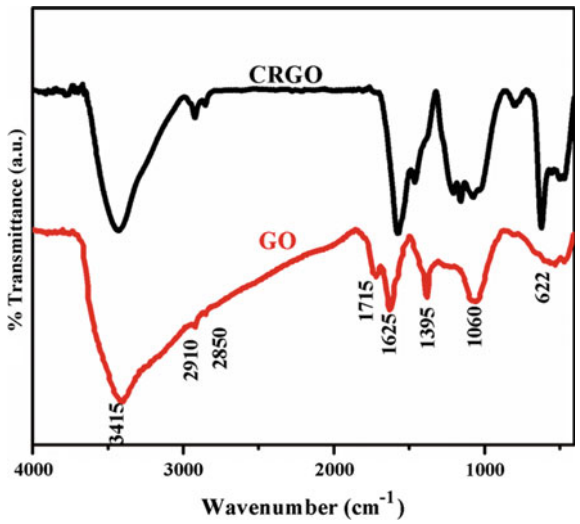

Fig. 12.2 FTIR spectra of GO and CRGO composite

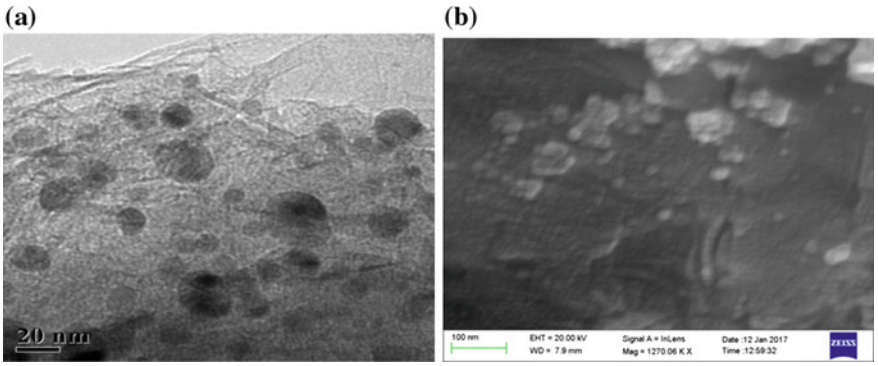

Fig. 12.3 **a** TEM and **b** FESEM image of CRGO composite

vibrations of unoxidized graphitic leftovers. The presence of alkoxy (C–O–C) groups in the graphene layer can be confirmed by the peak at $\sim$1060 cm^{-1} which is outcome of its stretching vibration. The peak at $\sim$622 cm^{-1} is contributed by the various modes of vibrations of Cu_2O.

The morphology (size and shape) of the CRGO composite were analyzed by TEM and FE-SEM analysis. For TEM, sample was prepared by dispersing the composite in ethanol solution (0.1 mg mL^{-1}) by ultra-sonicating for $\sim$20 min and then drop casting onto the fresh lacey carbon copper grid. Figure 12.3a presents the TEM image of CRGO composite. Scrupulous analysis shows that the RGO has wrinkled and crumbled morphology which is as a result of the loosening of interlayer's due to separation during oxidation. Over that wrinkled surface it has numerous small nearly ball shaped spherical structures throughout the surface of RGO. The size of the spherical structured Cu_2O was $\sim$5–10 nm. Few larger particles are also be seen

which might be due to the agglomeration of the smaller particles which results due to the small size and high surface area of the Cu_2O NPs. Figure 12.3b presents the FE-SEM image of the CRGO composite. The image shows small Cu_2O NPs of nearly spherical ball like structures anchored on to the crumbled and furrowed paper like RGO structure. Thus, from TEM and FE-SEM analysis it is evident that the Cu_2O NPs are decorated onto the surface of RGO layers.

Three dimensional microscopic images solve only one-half of the problems because the area where composition is homogenous can be selectively shown; hence it is very necessary to identify different elements present in the composite with respect to their position and distribution. To solve this problem scanning electron microscopy-energy dispersive studies (SEM-EDS) studies were done. Figure 12.4

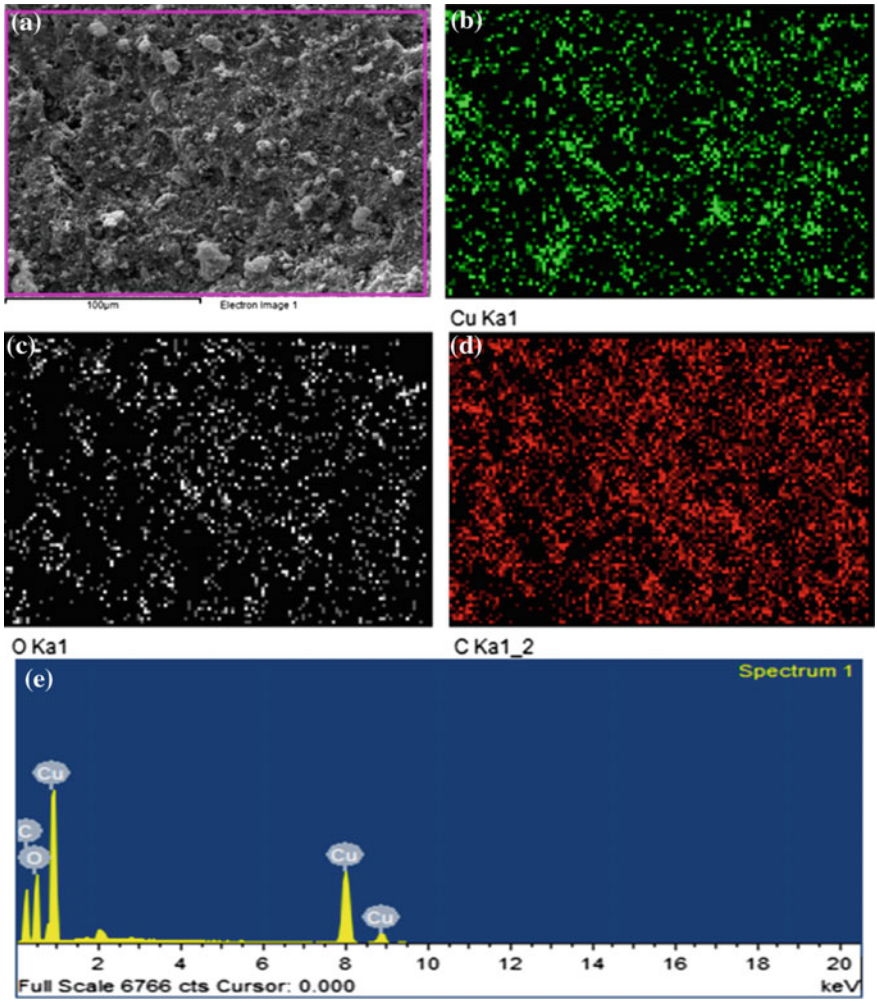

Fig. 12.4 **a** SEM image **b–d** corresponding mapping images for Cu, O, C and **e** EDS spectra

represents the FE-SEM image along with the elemental composition. Figure 12.4b–d shows the elemental mapping of different elements (Cu, O and C respectively) present. It is very apparent from the mapping studies that all the elements are evenly and well distributed throughout the area under observation. Thorough analysis of EDS spectra has been done to study the elemental composition of CRGO as presented in the Fig. 12.4e. The atomic percentages of Cu, O and C were found to be 15.27%, 28.52% and 56.21% respectively.

The electrical conductivity measurement is one of the largely reliant technique in understanding the effectiveness of reduction in GO and its derivatives. Less conductive nature of the GO is attributable to the presences of various oxygen moieties present on its surface [6]. Metal oxides are also known to be poor conductors of electricity [7]. The electrical conductivities of GO, Cu_2O and CRGO were found to be 9.3×10^{-2}, 2.01×10^{-1} and 19.6 S m^{-1} respectively. The enhancement in the conductivity of CRGO compared to GO affirms the removal of various oxygen moieties on the RGO surface suggesting successful reduction.

Raman spectroscopy is one of the well recognized techniques employed in studying the orderness and disorderness in the crystal structures of carbonaceous materials attributable to its non-destructive nature. Figure 12.5 presents the Raman spectra of CRGO and GO. The Raman spectra show two very intense peaks at $\sim$1346 and $\sim$1590 cm^{-1} which are credited to D and G band respectively. The D band is ascribed to the disorderness and defects present in the lattice and G band is ascribed to the proper arrangement of sp^2 carbon atoms of graphene lattice. Vigilant examination of spectra reveals that the D peak of GO is larger in intensity than G peak, which tends to decrease and turn into less intense than the G peak in the CRGO composite. The higher intense D peak is caused by the presence of various oxygen functionalities present on the graphene surface which results in the sp^3 hybridization of the carbon atom. The diminishing in the intensity of the D peak compared to G peak in the CRGO

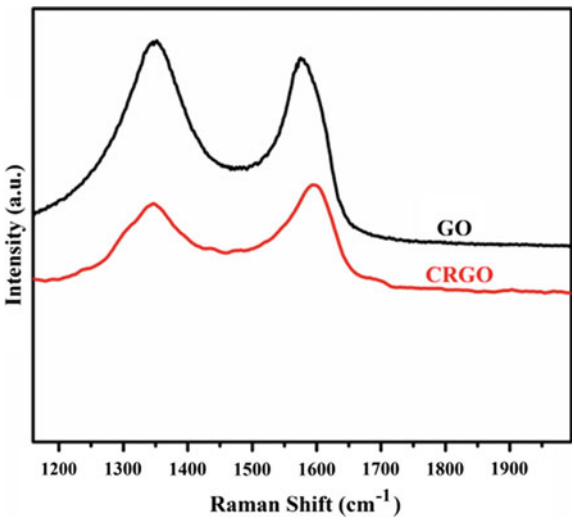

Fig. 12.5 Raman spectra of GO and CRGO composite

composite reveals that the sp^3 carbon atoms have are partially reduced and transformed back to sp^2 hybridization as in graphite. The peak intensity ratio (I_D/I_G) > 1 indicates the disorderness present in the sp^2 network of the graphene and its derivatives. The I_D/I_G ratio of the GO and CRGO were calculated to be 1.2 and 0.89 respectively signifying the restoration of the π-conjugated (sp^2) network of the graphene. This states that the mango bark has successful in reduction GO in CRGO composite which is in accordance with the other results.

12.3.2 Electrochemical Characterization

The electrochemical analysis was carried out in 3 electrode organization in 6 M NaOH solution. Figure 12.6a presents the cyclic voltammetry (CV) curve of the CRGO composite with the potential window of −0.1 to 0.7 V (vs. Ag/AgCl) at different scan rates of 10, 30, 50, 100 and150 mVs^{-1}. Each voltammogram showed a pair of well defined redox peaks demonstrating that the capacitance characteristics are ruled by Faradic reactions in the place of EDLC. The anodic and cathodic peaks can be seen at ∼0.15 mV and ∼0.38 mV, respectively.

The galvanometric charge-discharge was performed within the potential window of −0.1 to 0.7 V as shown in the Fig. 12.6b. The specific capacitance (SC) was calculated using the following formula.

$$SC = i\Delta t/m\Delta v$$

Where i, Δt, m and Δv represents the discharging current, time taken for discharging, mass of the composite deposited and voltage window selected, respectively. The SC for the CRGO composite were found to be ∼470, 356, 305, 275, 240, 230, 222, 213, 212 and F g^{-1}, respectively at a current density of 2, 3, 4, 5, 6, 7, 8, 9 and 10 A g^{-1}, respectively. The decline in the SC with mounting current density can be attributed to the rapid electronic movement to that of ion transportation.

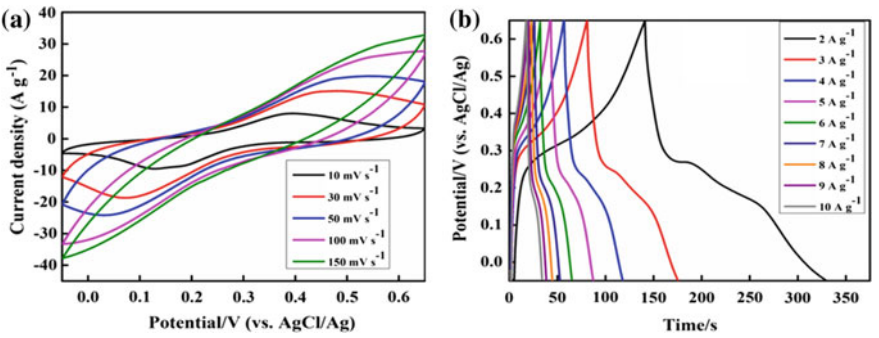

Fig. 12.6 **a** CV at different scan rates and **b** charge-discharge cycles at different current densities

12.4 Conclusions

Herein, it is in detail explained how CRGO composite was synthesised by simple one-pot solution mixing method and usefulness of bio-compounds in the mango bark extract for simultaneous reduction of GO as well as in the formation of Cu_2O NPS. The morphology of the CRGO composite is well described using TEM and FE-SEM analysis. FTIR and Raman studies shows the successful reduction of GO and formation of Cu_2O NPs. SEM-EDS studies shown the distribution of Cu_2O NPs over graphene sheet and atomic percentages of constituting elements. Voltammetry studies have shown the usefulness of the CRGO as the supercapacitor electrode material with a SC of 470 F g^{-1} at a current density of 2 A g^{-1}. The preparation technique publicized here is easy, eco-friendly and cost-effective in comparison to other available techniques which use hazardous, toxic and expensive chemicals which are harmful for our environment.

Acknowledgements The authors would like to thank the Director of CSIR-CMERI. Authors are also thankful to Council of Scientific and Industrial Research for the financial support through Fast Track Translational project (MLP210812) and Department of Science and Technology, New Delhi, India for the financial support vide DST-INSPIRE Faculty Scheme. Authors are also thankful to the CRF (CSIR-CMERI) for their assistance in the structural study analysis.

References

1. G. Wang, L. Zhang, J. Zhang, A review of electrode materials for electrochemical supercapacitors. Chem. Soc. Rev. **41**, 797–828 (2012). doi:10.1039/c1cs15060j
2. X. Cao, Z. Yin, H. Zhang, Three-dimensional graphene materials: preparation, structures and application in supercapacitors. Energy Environ. Sci. **7**, 1850–1865 (2014). doi:10.1039/C4EE00050A
3. M. Jana, J.S. Kumar, P. Khanra, P. Samanta, H. Koo, N.C. Murmu, T. Kuila, Superior performance of asymmetric supercapacitor based on reduced graphene oxide-manganese carbonate as positive and sono-chemically reduced graphene oxide as negative electrode materials. J. Power Sources **303**, 222–233 (2016). doi:10.1016/j.jpowsour.2015.10.107
4. J.S. Kumar, M. Jana, P. Khanra, P. Samanta, H. Koo, N.C. Murmu, T. Kuila, One pot synthesis of Cu_2O/RGO composite using mango bark extract and exploration of its electrochemical properties. Electochim. Acta. **193**, 104–115 (2016). doi:10.1016/j.electacta.2016.02.069
5. M. Jana, S. Saha, P. Khanra, C.N. Murmu, K.S. Srivastava, T. Kuila, H.J. Lee, Bio-reduction of graphene oxide using drained water from soaked Mung Beans (Phaseolus Aureus L.) and its application as energy storage electrode material. Mater. Sci. Eng., B **186**, 33–40 (2014). doi:10.1016/j.mseb.2014.03.004
6. M. Jana, S. Saha, P. Samanta, N.C. Murmu, J.H. Lee, T. Kuila, Investigation of the capacitive performance of tobacco solution reduced graphene oxide. Mat. Chem. Phys. **151**, 72–80 (2015). doi:10.1016/j.matchemphys.2014.11.037
7. S. Saha, M. Jana, P. Samanta, N.C. Murmu, N.H. Kim, T. Kuila, J.H. Lee, Hydrothermal synthesis of Fe_3O_4/rGO composites and investigation of electrochemical performances for energy storage application. RSC Adv. **4**, 44777–44785 (2014). doi:10.1039/C4RA07388F

Chapter 13
Performance Analysis of a Geothermal Air Conditioner Using Nanofluid

Suvanjan Bhattacharyya, Plaban Das, Ayan Haldar and Aritra Rakshit

Abstract Energy Saving is a serious challenge faced by mankind due to rapid increase in energy depletion. Geothermal energy along with nanotechnology is used in the proposed air conditioning model. This paper reports the design and experimental investigation of a vertical closed loop geothermal air conditioner. The system operates under different ground water condition at different mass flow rate. Nanofluid Al2O3R134a has been used as a working fluid. The result reports that the geothermal air conditioning system using refrigerant R134a is better than the conventional air conditioning system both in terms of performance and power saving. Although the best output characteristics are achieved by using geothermal air conditioner by means of nanofluid. The COP is showing some promising results and shows outgrowth of nanotechnology in renewable energy system.

Keywords Ground water · Geo-thermal · Experimental study · Nanofluid · Air conditioner · COP

13.1 Introduction

Now a day energy requirement is increasing rapidly due to the high population rate all over the world. As the energy consumption is growing fast, energy crisis is one of the major topics of concern in the society. Energy resources can be divided into three categories including fossil fuels, renewable energy and nuclear energy. Fossil fuel causes a tremendous amount of air pollution whereas Nuclear energy can cause serious problems for the environment and human health. But in other hand Renewable energy sources, which are sustainable and environmental friendly, are hence under emerging exploitation. Geothermal energy, has profuse quantity of

S. Bhattacharyya (✉) · P. Das · A. Haldar · A. Rakshit
Mechanical Engineering Department, MCKV Institute of Engineering,
Howrah 711204, West Bengal, India
e-mail: suvanjanr@gmail.com

G. Anand et al. (eds.), *Nanotechnology for Energy and Water*,
Springer Proceedings in Energy, https://doi.org/10.1007/978-3-319-63085-4_13

storage as well as significant base-load potential, expected to make an increasing contribution for energy supply in a near future.

Large amount of electric power is consumed by thermal systems like air conditioner and refrigerators. Heat exchanger is an important member in this group. Modification of heat exchanger design can improve the efficiency of the system and enhance heat transfer [1–6]. Heat exchanger is an integrated component of condenser. As a result, many researchers investigate to reduce the power consumption using alternative ways. Misra et al. [7] prepared an experiment of EAHE system in hybrid with air conditioner (AC) at Ajmer in India. From the experiment it was concluded that suitable combination of EAHE system with conventional AC in mode-III could preserve substantial amount of energy. Said et al. [8] experimented feasibility of air-conditioning systems by using ground fixed condensers. When compared to original air cooled condenser it was found that there is an increment in COP and reduced electrical power consumption. Wang et al. [9] experienced performance of a DX-GCHP system in heating mode. The values of COP of the heat pump and the whole system are found to be 3.55, 3.28 and 0.599, 0.553 respectively. Coumaressin and Palaniradja [10] use CuO-R134a in the vapour compression system and found that evaporator heat transfer coefficient increases due to the use of nanoCuO. Shafahi et al. [11] by utilizing nanofluids study the thermal performance of a cylindrical heat pipe and establish that particles that are smaller in size have a more prominent outcome on the temperature gradient along the heat pipe.

So as to have effective refrigeration and air conditioning nanofluids are used along with conventional refrigerant. Nanofluids are a new class of fluid that are prepared by suspending nano size particles in base fluid having a good increment in the heat transfer rate. R134a is widely used refrigerant for cooling purpose. Nanoparticles of Al_2O_3 having 0.2% concentration is mixed with the base fluid, refrigerant R134a. This nanofluid is used as a refrigerant in the geothermal air conditioner in order to have a renewable system with an enhancement of coefficient of performance (COP) of the air conditioner and promising decrement in power consumption. This experiment is a step towards sustainable development and a cleaner environment.

13.2 Experimental Setup and Procedure

Figure 13.1 shows the experimental set-up which consists of mainly 5 components —Compressor (1.5 ton capacity), extended surface heat exchanger, water maintained condenser (Capacity—80 L), expansion valve and an evaporator unit. The electrical circuit contains ammeter, voltmeter, energy meter and automated cut-off control. For precious measurement of temperature and pressure of various sections in that setup 4 thermocouples and 4 pressure sensors are used.

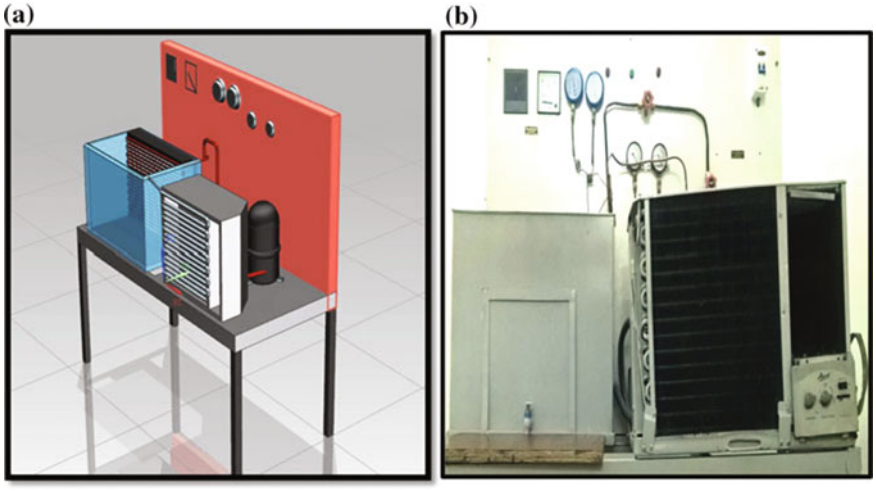

Fig. 13.1 **a** and **b** Experimental set-up of the geo thermal air-conditioning setup

Figure 13.2 shows the schematic diagram of the experimental test rig in which it is clearly seen that the condenser is dipped in water having constant temperature which acts as geothermal sink for the rejection of heat.

The underground water act as a fixed temperature infinite source or fixed temperature sink. In conventional air refrigeration heat rejection is performed incorporating forced convectional heat transfer, which can be at high temperature at some instant. But in this case underground water at constant temperature is used as sink to reject the heat in the water maintained condenser. So the heat transfer in the condenser will be enhanced by increased temperature difference and therefore the load on the compressor as well as the blower power consumption in case of

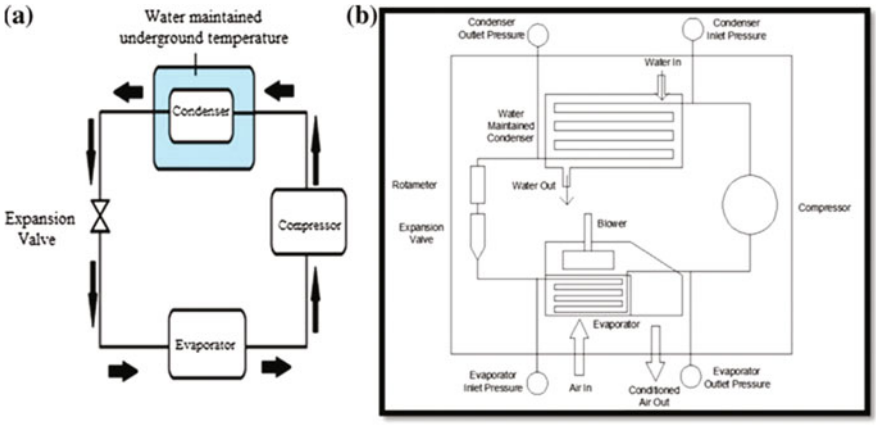

Fig. 13.2 **a** and **b** The schematic diagram of the experimental test rig

conventional AC will be decreased. A comparative study with conventional air conditioning, which uses blower forced convection heat transfer mechanism is also carried out.

Water in condenser is maintained at constant temperature and varied in between 15°–20°C, simulating the constant temperature sink, (which is the groundwater in actual scenario). The condenser coils will run through this water reservoir for rejecting heat. The water in the reservoir will be recirculated through the cooling chamber in order to be cooled for maintaining the temperature close to mean groundwater temperature.

13.3 Data Reduction

Refrigerating Effect,

$$R_E = h_1 - h_4 \tag{13.1}$$

Compressor Work,

$$W_C = h_2 - h_1 \tag{13.2}$$

Theoretical COP,

$$COP_{theoritical} = \frac{R_E}{W_C} = \frac{h_1 - h_4}{h_2 - h_1} \tag{13.3}$$

The density of conditioned air,

$$\rho_a = \frac{1.293 \times 273}{273 + DBT_c} \tag{13.4}$$

Mass flow rate of air,

$$m_a = \rho_a \times V_a \times A \tag{13.5}$$

Actual Ref. Effect,

$$R_{E_{act}} = m_a \times C_p \times (T_a - DBT_c) \tag{13.6}$$

Actual Compressor Work,

$$W_{C_{act}} = \frac{3600 \times n}{t_c \times EMC_c} \tag{13.7}$$

Actual COP,

$$\mathrm{COP}_{\mathrm{actual}} = \frac{\mathrm{R}_{\mathrm{E}_{\mathrm{act}}}}{\mathrm{W}_{\mathrm{C}_{\mathrm{act}}}} \tag{13.8}$$

Heat rejected by the condenser to the water due to convection,

$$\mathrm{Q}_{\mathrm{conv}} = \mathrm{hA}_{\mathrm{s}}(\mathrm{T}_{\mathrm{s}} - \mathrm{T}_{\infty}) \tag{13.9}$$

Density of nanofluid,

$$\rho_{\mathrm{nf}} = (1 - \varphi)\rho_{\mathrm{bf}} + \varphi\rho_{\mathrm{p}} \tag{13.10}$$

Specific heat of nanofluids,

$$\mathrm{C}_{\mathrm{p,nf}} = \left[(1 - \varphi)\rho_{\mathrm{bf}}\mathrm{C}_{\mathrm{p,bf}} + \varphi\rho_{\mathrm{p}}\mathrm{C}_{\mathrm{p.p}}\right]/\rho_{\mathrm{nf}} \tag{13.11}$$

13.4 Results and Discussion

From the Fig. 13.3, one can easily say that the geothermal copper tube is more efficient at any flow rate of refrigerant through the cycle. COP is higher in water maintained condenser in any flow rate than that of the conventional blower forced convectional air conditioning setup. Though using more amount of refrigerant in

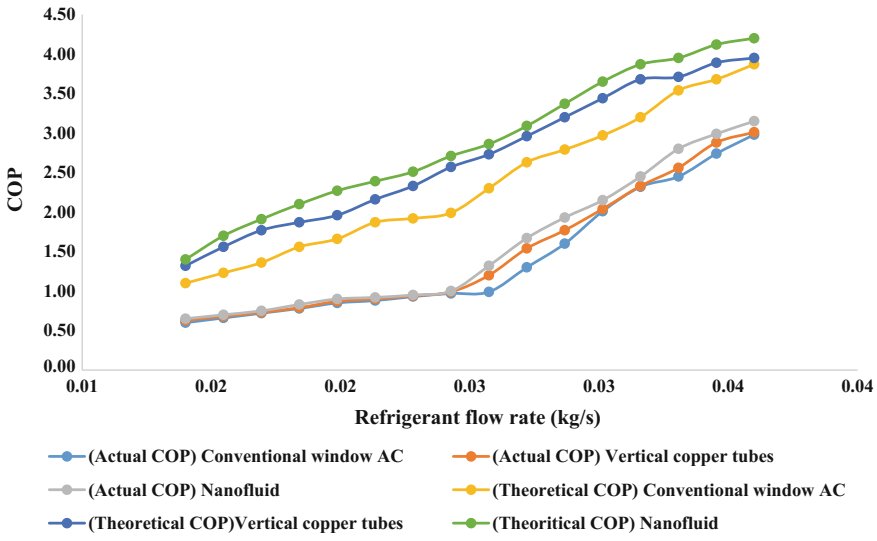

Fig. 13.3 Variation of theoretical and actual COP at different mass flow rate of the refrigerant

the test set-up do not increase the COP at the same rate after a certain amount. But when R134a is substituted by using nanofluid Al_2O_3R134a theoretical COP shows a significant growth in COP. The nature of the curve of actual COP curve is almost similar like the theoretical COP curve. From the figure one can see that mass flow rate up to 0.03 there is not much variations between geo-thermal COP and the conventional one, this is because at lower mass flow rate geo-thermal air conditioner machine is not that much promising as compared to conventional air conditioning machine. But, at higher mass flow rate COP is higher in water maintained condenser than that of the conventional blower forced convectional air conditioning setup. While using nanofluid Al_2O_3R134a as a refrigerant the actual COP though decreases due to some losses through pipes, ducts, etc. but still its value is more as compared toR134a refrigerant based geothermal one. It can be seen that for all the cases COP increase with the increase of mass flow rate.

Electrical energy consumption (kW) for different ground water temperatures (20^o, 18^o, 16^o and 13^o) in summer season is presented in Fig. 13.4. It is observed from Fig. 13.4 that power consumption is higher for 20 °C ground water temperature as compared to other tested ground water temperature. It is also observed as per percentage change in electrical energy consumption w.r.t. all the tested ground water temperature, ground water temperature at 13 °C provides better results.

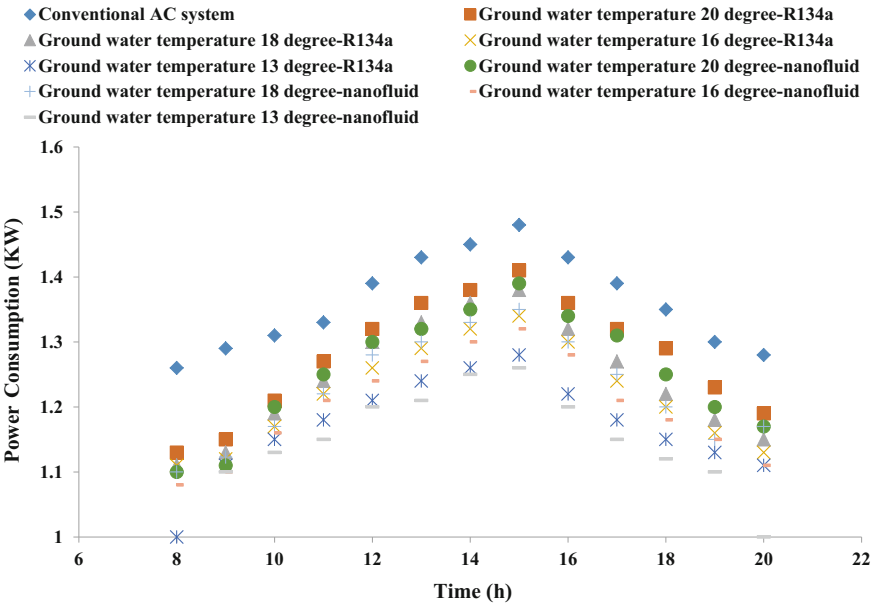

Fig. 13.4 Electricity power consumption (kW) at different ground water temperatures in tested time duration

13.5 Conclusion

In present era growth in construction sector is remarkable, which impacts on increase in energy demand mainly due to space heating and cooling. For space heating and cooling Geo-thermal air-conditioner system is the proficient and energy efficient equipment. Incorporation of nanofluid Al_2O_3R134a as a refrigerant along with the geothermal system shows some significant result. The most interesting ones are:

- saving energy and reduce the problem regarding heat rejected to surrounding air;
- reducing the noise of condensing fan;
- reducing electrical energy by reducing compressor's load of 1.5 TR window AC. Electrical energy consumption as compared to conventional 1.5 TR window AC is reduced by 9.77% during summer season in vertical configuration with nanofluid Al_2O_3R134a as a refrigerant.

References

1. S. Bhattacharyya, H. Chattopadhyay, Computational of studies of heat transfer enhancement in turbulent channel flow with twisted strip inserts, in *Proceedings of CHT-15, ICHMT International Symposium on Advances in Computational Heat Transfer, Rutgers University, Piscataway, USA* (2015)
2. S. Bhattacharyya, A. Roy, A. Bhattacharyya, K. Dey, D. Seth, Computational heat transfer analysis of a counter-flow heat exchanger with fins, in *Proceedings of Recent Developments in Mechanical Engineering, Pune* (2015)
3. S. Bhattacharyya, H. Chattopadhyay, S.K. Saha, Numerical study on heat transfer enhancement of laminar flow through a circular tube with artificial rib roughness. J. Refrig. Air Cond. Heat Vent. **1**(3), 14– 19 (2014)
4. S. Bhattacharyya, A. Roy, H. Chattopadhyay, A. Rakshit, A numerical investigation based on heat transfer and fluid flow characteristics of air in a circular tube heat exchanger with inclined ribs, in *Proceedings of ICACE 2015, Recent Advances in Chemical Engineering* (2016), pp. 11–20
5. S. Bhattacharyya, H. Chattopadhyay, S. Bandyopadhyay, Numerical study on heat transfer enhancement through a circular duct fitted with centretrimmed twisted tape. Int. J. Heat Technol. **34**(3), 401–406 (2016)
6. S. Bhattacharyya, H. Chattopadhyay, A. Roy, A.A. Rakshit, I.R. Chowdhury, Thermohydraulic transport characteristics of micro mixer in micro channel, in *Proceedings of ICACE 2015, Recent Advances in Chemical Engineering* (2016), pp. 29–39
7. R. Misra, V. Bansal, G.D. Agarwal, J. Mathur, T. Aseri, Thermal performance investigation of hybrid earth air tunnel heat exchanger. Energy Build. **49**, 531–535 (2012)
8. S. Said, M. Habib, E. Mokheimer, M. El-Sharqawi, Feasibility of using groundcoupled condensers in A/C systems. Geothermics **39**(2), 201–204 (2010)
9. X. Wang, C. Ma, Y. Lu, An experimental study of a direct expansion ground-coupled heat pump system in heating mode. Int. J. Energy Res. **33**, 1367–1383 (2009)
10. T. Coumaressin, K. Palaniradja, Performance analysis of a refrigeration system using nano fluid. Int. J. Adv. Mech. Eng. **4**(4), 459–470 (2014). ISSN 2250-3234
11. M. Shafahi, V. Bianco, K. Vafai, O. Manca, An investigation of the thermal performance of cylindrical heat pipes using nanofluids. Int. J. Heat Mass Transf. **53**, 376–383 (2010)

Chapter 14
Performance Improvement of a Novel Flat Plate Photovoltaic Thermal (PV/T) System Using Copper Oxide Nanoparticle—Water as Coolant

Dudul Das and Pankaj Kalita

Abstract Accelerated fossil fuel depletion and growing climate change concern placed solar energy into focal point of global solar energy scenario. Solar Photovoltaic (PV) unit is growing in demand as source of electric power due greenhouse gas (GHG) emission from conventional coal based power generation and rapid depletion of fossil fuel reserves but it suffers from lower efficiency as temperature increases (>25 ^{o}C). In this investigation an attempt has been made to develop a solar hybrid PV-thermal system having modified rear panel assembly and copper based Nano fluid as heat transfer medium. This system effectively cools the PV module and delivers waste heat generated for low temperature applications. It is observed that Nano fluid shows better heat removal properties than contemporary heat transfer fluids. In the present investigation copper oxide based Nano fluid is used because it's high thermal conductivity and to enhance the performance of the PV/T system by providing effective cooling, which is installed at Guwahati (26.14° N, 91.73° E).

Keywords Hybrid PV-thermal system · Rear panel assembly · Nano fluid · Exergy efficiency

Nomenclature

$\eta_{electrical}$	Electrical efficiency of PV
$\eta_{overall}$	Overall efficiency of PV/T
η_I	First law efficiency
η_{II}	Second law efficiency
ρ	Density of the fluid
$\dot{Q}_{th}$	Thermal energy recovered from the PV/T
$\dot{m}$	Mass flow rate in kg/s
c_p	Specific heat capacity of the fluid in J/kg-K

D. Das · P. Kalita (✉)
Centre for Energy, Indian Institute of Technology Guwahati, Guwahati 781039, Assam, India
e-mail: pankajk@iitg.ernet.in

G. Anand et al. (eds.), *Nanotechnology for Energy and Water*,
Springer Proceedings in Energy, https://doi.org/10.1007/978-3-319-63085-4_14

T_{in}	Inlet temperature of heat transfer fluid, in K
T_{out}	Inlet temperature of heat transfer fluid in K
$\dot{T}_a$	Ambient temperature in K
$\dot{T}sun$	Sun temperature (6000 K)
I	Incident solar radiation on the system in W/m^2
A	Area of the panel in m^2
$\dot{E}_{electrical}$	Useful electrical energy
$\dot{X}_{water,in}$	Exergy of inlet water
$\dot{X}_{water,out}$	Exergy of outlet water
$\dot{X}_{useful}$	Useful exergy gain
$\dot{X}_{solar}$	Solar radiant exergy
IR	Exergy loss in the process

14.1 Introduction

The oil crisis in the early 1970s and the global climatic change concerns are pushing for the need of renewable and clean energy sources. Renewable energy sources are becoming important as these are significantly helpful in protecting environment and are in abundance. Solar energy is the most prominent renewable source due to its availability around the globe. The most important component in solar energy system is the solar collector. Two prominent solar energy collection systems commonly used are the flat plate collectors and photovoltaic cells. Usually, these two collection systems are used separately. But if looked from energy efficiency point of view present trends of research use two systems together in a hybrid photovoltaic thermal (PV/T) energy system. This is also a key area of research for scientists and researchers to enhance the electrical efficiency of PV cells. The electrical efficiency of PV module is not only strongly depended on solar radiation, but also depends on the operating temperature of PV panels [1, 2, 4, 5]. Various researchers tried different fluids as heat carrying medium in solar applications. Nano fluid is one of the most sought after heat transfer fluid owing to its superior thermo-physical properties compared to other fluids. Nano fluid is homogeneous solution of particles of size 1 to 100 nm in base fluid such as water or other chemicals [2]. A number of works has been carried out to analyze the thermal properties for solar nano-fluid.

Liu et al. (2006) concluded from their experiment that thermal conductivity increase with increase in concentration and decrease in particle size [3]. Shamani et al. (2016) reported that PV/T having rectangular tube absorber gives highest overall efficiency of 81.73% and electrical efficiency of 13.52% with Silicon carbide nano particle [4]. Hasan et al. (2017) reported that with the use of SiC nanofluid improved the power output of the PV/T module by 62.5% as compared to PV module without cooling [5]. Copper oxide—water Nano fluid increased overall

efficiency with glazing by 19.25% compared to water as heat transfer fluid as reported by Michael and Iniyan (2015) [6]. Liu et al. (2011) also studied CuO nano fluid and reported that there is 30% increase in heat transfer coefficient compared to water [7]. Xuan and Li (2003) reported that heat transfer coefficient increases with increase in weight% and flow velocity in turbulent regime [8]. In this work an attempt was made to design a collector which helps to efficiently cool the PV panel for optimum efficiency with copper oxide-water as cooling medium.

14.2 Methodology

14.2.1 Experimental Setup Description

In order to get maximum PV panel electrical efficiency a provision for cooling of PV panel has been made. A polycrystalline PV panel of rated power 12 Wp (Make: Maharishi Solar Technology, Model: MUM DG 12) was purchased and modified the module for providing cooling effect. The module is modified in such a way that optimal operating temperature of PV module be maintained. The modified absorber shown in the Fig. 14.1 has 15 transverse rectangular fins of dimension 10 cm × 0.5 cm × 0.5 cm has been fabricated and attached with the PV module. Two inlet ports and one outlet port of diameter 12 mm are provided in order to have effective fluid circulation in the channel. An experimental facility was developed for measurement of various operating parameters to calculate electrical efficiency, heat removal rate and exergy efficiency. The schematic of the experimental facility is shown in the Fig. 14.2. The arrangement consists of a modified PV panel, a rheostat, a pump (Make: Bosch, 0.25 hp), a water tank, two multi-meter (Metravi-XB-33F), an infrared thermometer (Testo 835-T2) and thermocouple sensors (T-type). A heat recovery system is also integrated with the system.

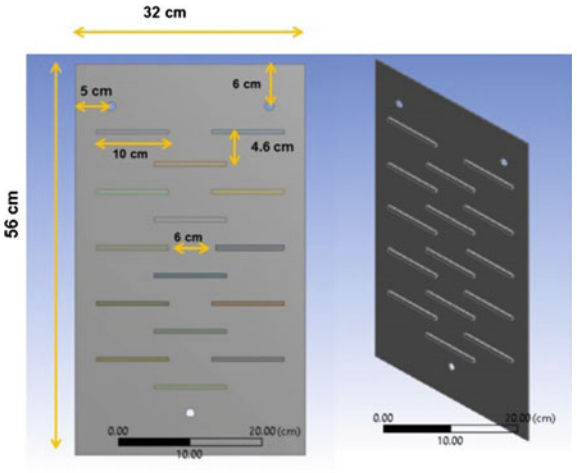

Fig. 14.1 Absorber plate integrated on the rear side of PV panel

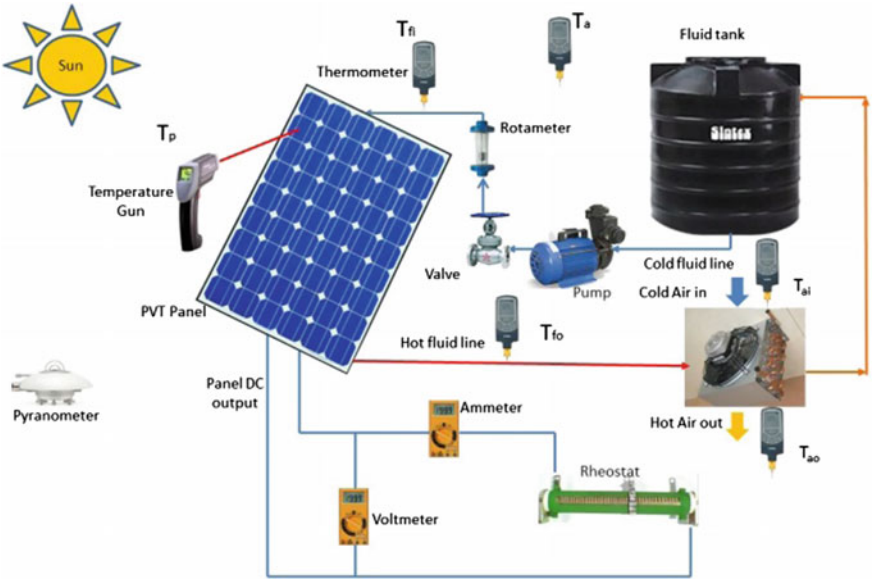

Fig. 14.2 Experimental setup

14.2.2 Experimental Procedure

A series of experiments were performed to investigate the electrical efficiency, heat removal rate and exergy efficiency by using two different fluids viz. water and copper oxide-water solution and compared the results. The experiment was carried out from 11 am to 1 pm in the day and data was collected at an interval of 15 min. Ambient temperature, solar insolation, inlet fluid temperature, outlet fluid temperature, outlet temperature of the air from the cooling chamber and temperature of PV panel at four different points across its surface was measured. Before turning on the pump PV/T panel was filled with fluid. The flow rate was maintained at 60 litre per hour. A 0.25 hp pump attached with the PV/T system for circulation of cooling fluid. A ball valve was used in the cold fluid to regulate the fluid flow, this is shown in the Fig. 14.2. For measuring the temperature inlet and outlet fluid, T-type thermocouples were located appropriately. The temperature of PV panel surface is measured by an infrared temperature gun. Pyranometer was used to measure the incident solar radiation per unit area.

Experiment was carried out at three different stages during the month of January 2017, when ambient temperature reported to be 27 °C. In the first stage surface temperature was measured and electrical efficiency of the PV panel without cooling was calculated. In the second stage water was used as cooling fluid and in the third stage water with copper oxide nano particle was used. The cooling fluid passes through channel between the PV panel and absorber plate attached on its rear side.

In the second and third stage along with PV panel surface temperature and electrical efficiency of the panel, exergy efficiency was calculated.

14.2.3 Formulation

Electrical efficiency

$$\eta_{electrical} = \frac{V_m I_m}{IA} \tag{14.1}$$

The exergy balance equation for the system

$$\dot{X}_{water,in} + \dot{X}_{solar} = \dot{X}_{water,out} + \dot{X}_{electrical} + IR \tag{14.2}$$

The useful exergy gain provided by the system

$$\dot{X}_{useful} = \dot{m}c_p \left[T_{out} - T_n - T_a \ln\left(\frac{T_{out}}{T_{in}}\right) \right] + V_m I_m \tag{14.3}$$

Solar radiant exergy as presented by Petela [9]

$$\dot{X}_{solar} = IA \left[1 - \left(\frac{4T_a}{3T_{sun}}\right) + \frac{1}{3}\left(\frac{T_a}{T_{sun}}\right)^4 \right] \tag{14.4}$$

The second law efficiency

$$\eta_{II} = \frac{\dot{X}_{useful}}{\dot{X}_{solar}} \tag{14.5}$$

14.3 Results and Discussion

14.3.1 I-V Characteristics and Variation of PV Panel Surface Temperature

A sample I-V characteristic curve at 12 noon on 18-01-2017 is shown in the Fig. 14.3. In the same figure maximum voltage (V_m) and maximum current (I_m) are also shown.

PV panel temperature strongly depends on wind velocity, ambient temperature, and solar radiation. It is important to measure the PV panel temperature, because it is detrimental to the performance of the panel. When cooling fluid is circulated in the PV/T panel, it is observed that the temperature falls. Figure 14.3 shows the

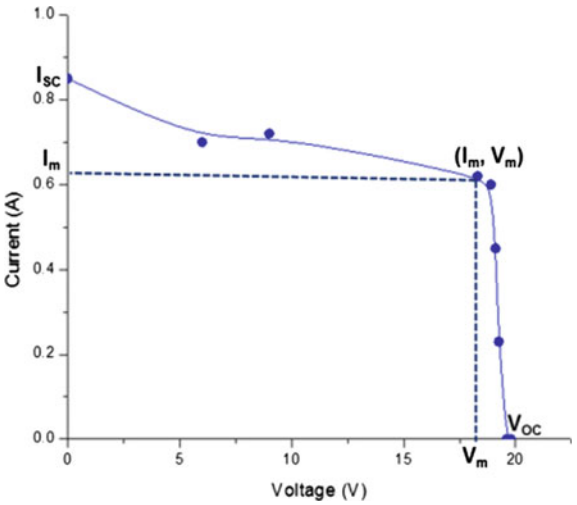

Fig. 14.3 I-V characteristic at 12 noon on 18-01-2017

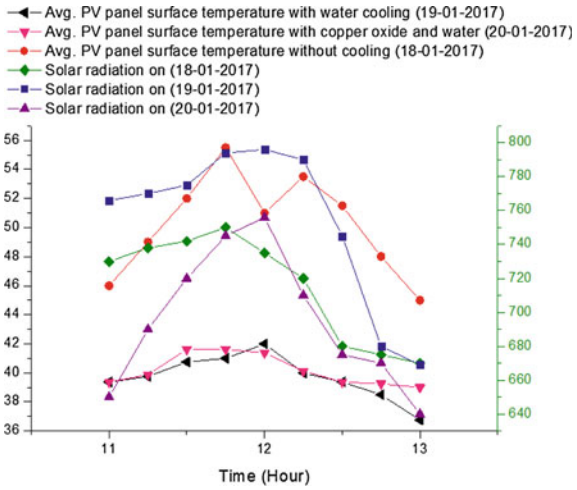

Fig. 14.4 Variation of PV panel surface temperature

variation of average PV panel surface temperature with time. It is observed that the PV panel temperatures increases and become the maximum at 11.45 am before it decreases to a minimum value at 1 pm. The increase in PV temperature is due to high absorptivity of the solar cells.

14.3.2 Variation in Electrical Efficiency and Exergy Efficiency

The variation of electrical efficiency with respect to time of the day is shown in the Fig. 14.4. As observed the electrical efficiency is found to be more with Copper

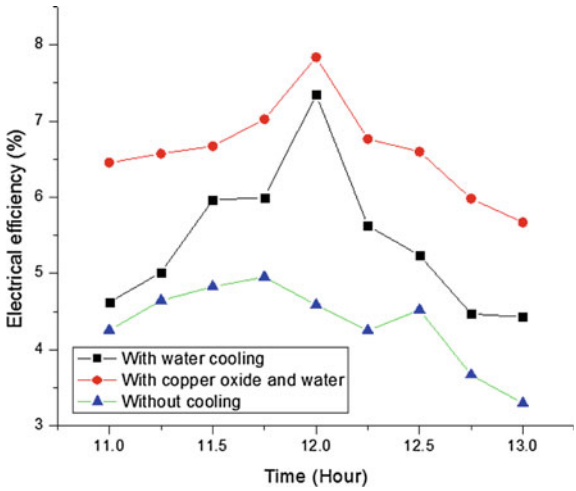

Fig. 14.5 Variation of electrical efficiency

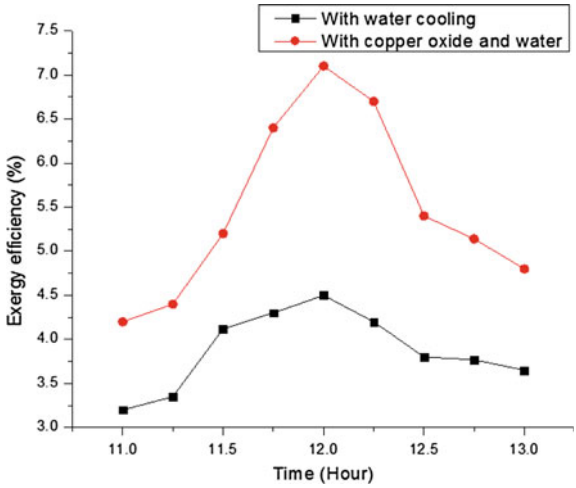

Fig. 14.6 Variation of exergy efficiency

oxide-water solution in comparison to pure water. A maximum electrical efficiency of 7.8% has been found at 12 noon. This is due to the higher heat removal capacity of copper oxide-water solution Fig. 14.5.

Exergy efficiency gives actual measure of useful energy. It takes into consideration of different irreversibilities associated in the process. The trend of exergy variation along the length of the day is shown in Fig. 14.6. The exergy efficiency is higher when copper oxide-water solution is used as cooling medium as that of pure water. This is due to higher thermal conductivity of copper oxide-water solution.

14.4 Conclusions

This investigation put forward different important findings. Some of the major findings of the experiment are as follows:

1. The panel temperature without cooling reaches a maximum value of 55.5 °C whereas with copper oxide water solution the panel temperature reduced to 41 °C.
2. The highest electrical efficiency of 7.8% is reported with Copper oxide-water as cooling medium in comparison to 7.3% in the case of pure water
3. The exergy efficiency is found to be 57.78% more with copper oxide-water solution as compared to water.

References

1. S. Chokmaviroj, R. Wattanapong, Y. Suchart, Performance of a 500 kWp grid connected photovoltaic system at Mae Hong Son Province, Thailand. Renew. Energy **31**(1), 19–28 (2006)
2. A.S. Mujumdar, X.-Q. Wang, Heat transfer characteristics of nanofluids. Int. J. Therm. Sci., 1–19 (2007)
3. M.S. Liu, M.C.C. Lin, I.T. Huang, C.C. Wang, Enhancement of thermal conductivity with CuO for nanofluids. Chem. Eng. Technol. **29**, 72–77 (2006)
4. A.N. Al-Shamani, K. Sopian, S. Mat, H.A. Hasan, A.M. Abed, M.H. Ruslan, Experimental studies of rectangular tube absorber photovoltaic thermal collector with various types of nanofluids under the tropical climate conditions. Energy Convers. Manag. **124**, 528–542 (2016)
5. H.A. Hasan, K. Sopian, A.H. Jaaz, A.N. Al-Shamani, Experimental investigation of jet array nanofluids impingement in photovoltaic/thermal collector. Sol. Energy **144**, 321–334 (2017)
6. J.J. Michael, S. Iniyan, Performance analysis of a copper sheet laminated photovoltaic thermal collector using copper oxide—water nanofluid. Sol. Energy **119**, 439–451 (2015)
7. L. Lu, Z.-H. Liu, H.-S. Xiao, Thermal performance of an open thermosyphon using nanofluids for high-temperature evacuated tubular solar collectors. Sol. Energy **85**, 379–387 (2011)
8. Y. Xuan, Q. Li, Investigation on convective heat transfer and flow features of nanofluids. J. Heat Transf. **125**, 151–155 (2003)
9. R. Petela, Exergy of undiluted thermal radiation. Sol. Energy **74**, 469–488 (2003)

Chapter 15
Production of Biofuel from Animal Fat Using Nano-catalyst via Single Step Transesterification Process

Booramurthy Vijaya Kumar, Kasimani Ramesh and Pandian Sivakumar

Abstract The present investigation is carried out for the production of biofuel (biodiesel) from animal fat with an active and promising nano-catalyst ($Cs/Al/Fe_3O_4$) via transesterification process. The catalyst was prepared by chemical precipitation and impregnation method through which nano size was controlled. Characterization was done by using SEM, XRD, TGA and BET to identify morphology, chemical composition, thermal stability and surface area respectively. The conversion of animal fat to fatty acid methyl ester was influenced by reaction conditions such as molar ratio of methanol to oil, catalyst concentration, reaction time and temperature. The optimum results were obtained at 60 min reaction time at 60 °C for 3 wt% nano-catalyst and 12:1 methanol to oil molar ratio to achieve a maximum yield of 97 wt%. The processed biodiesel was characterized as per ASTM methods and compare with ASTM standards.

Keywords Animal fat · Nano-catalyst · Transesterification · Biodiesel

15.1 Introduction

The dependence on fossil fuel resources has been waning due to the concern about the environment and decrease in petroleum reserve [1]. Therefore, researches have been focused on finding an alternative source for the growth of mankind. Biodiesel

B. Vijaya Kumar
Department of Petrochemical Engineering, RVS College of Engineering and Technology, Coimbatore 641402, India

K. Ramesh
Department of Mechanical Engineering, Government College of Technology, Coimbatore 641013, India

P. Sivakumar (✉)
School of Petroleum Technology, Pandit Deendayal Petroleum University, Gandhinagar 382007, India
e-mail: sivakumar.p@spt.pdpu.ac.in

G. Anand et al. (eds.), *Nanotechnology for Energy and Water*,
Springer Proceedings in Energy, https://doi.org/10.1007/978-3-319-63085-4_15

(Fatty acid methyl ester) will be the best option to replace petro diesel. Use of biodiesel comparatively reduces the unburned hydrocarbon, carbon monoxide and particulate matter. They are biodegradable, non toxic and renewable being derived from organic materials such as animal fats, edible and non edible oils. It is produced through transesterification reaction using homogeneous and heterogeneous catalyst with methanol. The use of conventional catalyst has more problems in purification process, and recycling and hence economically undesirable [2]. Implementation of nano catalysts can reduce the time for purification and recycling process and also their high catalytic surface increases biodiesel conversion. This catalyst will eliminate the problems related to conventional catalysts. Recent study on nano form of catalyst showed high activity, less reaction time, better catalytic activity and stability for the biodiesel production. Beef tallow is one of the cheap raw materials used for the production of biodiesel. In all the developing as well as the under developing countries, huge amount of animal fat is thrown out as waste. Only partial amount of animal fat is utilized by the soap manufacturing industries. Beef tallow contains lesser free fatty acid when compared to other edible and non edible oils due to which the acid value range lies between 2–10 mg $KOHg^{-1}$ of oil. Therefore, in order to reduce the production cost of biodiesel combination of waste beef tallow with nano based catalyst was identified.

The nano catalyst ($CS/Al/Fe_3O_4$) was prepared from CS, Al and Fe_3O_4 via impregnation method. The physical appearance, thermal properties, shape and structure were characterized using scanning electron microscopy (SEM), Thermo-gravimetric analyzer (TGA) and X-ray diffractometer (XRD) respectively. The optimum condition for transesterification and the various parameters that affects biodiesel production were investigated using nano catalyst.

15.2 Experimental Materials and Methods

15.2.1 Preparation of ($CS/Al/Fe_3O_4$) Nano-catalyst

The catalyst $Cs/Al/Fe_3O_4$ was prepared by impregnation method. Three moles of NaOH were added to 1 L of deionized water and dissolved. Sodium metaaluminate solution was produced by the addition of aluminum sheet into it. Then, a 2 M of $CsNO_3$ aqueous solution was mixed with sodium metaaluminate solution and this mixture was taken in a round bottomed flask fitted with a condenser heating around 60 °C. The mixture was kept under rigorous stirring at 60 °C to obtain pH to 12. The obtained precipitate was then dried in the oven at 120 °C for 12 h to produce the catalyst precursor [3]. Then the precursor was thermally treated at 650 °C for 6 h to give CsO. The magnetic property of the catalyst was identified via co precipitation method while adding Fe_3O_4 nanoparticles into the mixed solution of

NaOH, Al and CsOH under vigorous stirring at 70 °C for 6 h and the wet powder was dried under vacuum for 10 h. In order to achieve the magnetic composite solid catalyst the dried powder was calcined at 700 °C for 6 h.

15.2.2 Catalyst Characterization

The morphology of the nano-catalyst was identified using SEM (Hitachi S 4300). TGA for the catalyst was done to find the thermal degradation at a higher temperature using TA Instrument, TGA Q50. The powder form of catalyst was analyzed using XRD to determine the specific structure in TF-XRD, Rint-2500 diffractometer [4].

15.2.3 Feedstock

Waste beef tallow was collected from the slaughter house at Coimbatore, India. It was melted at 80 °C and filtered to remove the suspended particles and residue. The melted tallow was further centrifuged and decanted to make the oil clean for the next step. The chemicals required for the experiments were purchased from Merk, Mumbai, India.

15.2.4 Transesterification

The experiments were carried out in a 250 mL three-neck flat bottom round flask equipped with a reflux condenser to condense the methanol vapor. The reactants were mixed thoroughly by using a magnetic stirrer at 500 rpm. The whole setup was placed in a heating oil bath to maintain desirable reaction temperature. The mixture of methanol with catalyst was prepared separately and charged into the reactor containing 50 g tallow. Then it was heated up to a desired temperature. The process parameters like methanol to oil molar ratio, catalyst quantity, reaction temperature and reaction time were varied from 3:1 to 15:1, 1 to 6 wt%, 30 to 65 °C and 10 to 70 min respectively. When the reaction was completed, the sample was poured into a separating funnel kept without any disturbance. Due to gravity two layers were formed, the upper layer containing biodiesel and the lower layer containing glycerol [5]. The biodiesel yield was determined gravimetrically after removing methanol.

15.2.5 Characterization of Biodiesel

The physical and chemical properties of biodiesel were identified as per ASTM test methods to determine their qualities. The tests were repeated three times to determine its repeatability. The results obtained were compared with ASTM D 6751 standard for biodiesel.

15.3 Result and Discussion

15.3.1 Characterization of Catalyst

The SEM results show that the catalyst have large pores and eventually distributed granules provide very less dense particles. TGA thermogram indicates that a weight loss of 1.1 wt% takes place between 220–420 °C due to the removal of bounded moisture. The weight remains constant even with a further increase in temperature up to 800 °C. This reveals that catalyst is stable even at higher temperature. The powder XRD identifies that the $Cs/Al/Fe_3O_4$ forms a specific structure which has been clearly specified in the peaks.

15.3.2 Effect of Methanol to Oil Molar Ratio

The yield of biodiesel increases with increase in methanol to oil ratio from 3:1 to 15:1. The addition of excess methanol will shift the equilibrium to right and brings better transesterification process yield. Optimum ratio was identified at 12:1 by consuming 3 wt% catalyst around 50 °C with the reaction being carried out for 50 min giving a conversion of 93 wt% of yield as shown in Fig. 15.1.

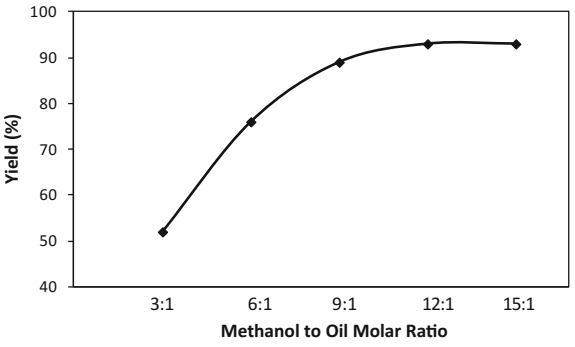

Fig. 15.1 Effect of methanol/oil molar ratio

15.3.3 Effect of Catalyst Loading on Yield

Biodiesel yield was investigated for different catalyst quantity from 1 to 4 wt%. The maximum yield obtained was 93 wt% at 3 wt% where the reaction took place at 50 °C for 50 min and 12:1 methanol to oil molar ratio. Further increase in the amount of catalyst (4 wt%) resulted in no change in the yield as shown in Fig. 15.2.

15.3.4 Effect of Reaction Temperature

Figure 15.3, shows yield of biodiesel on varying the reaction temperature from 30 to 65 °C (approx. boiling point of methanol) with 3 wt% catalyst loading, 12:1 methanol to oil ratio and reaction time of 50 min. The yield increases with increase in temperature up to 60 °C. Thereafter, it remains constant at 96 wt%. Therefore, the optimum temperature for the biodiesel was at 60 °C.

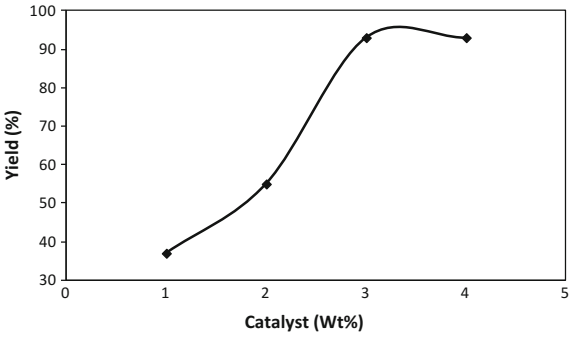

Fig. 15.2 Effect of catalyst loading

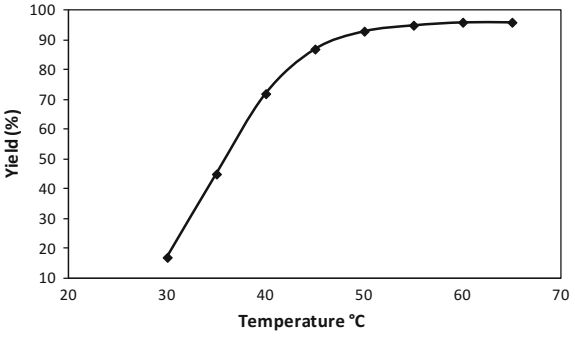

Fig. 15.3 Effect of reaction temperature

15.3.5 Effect of Reaction Time

The variation of reaction time is also a parameter of conversion. Figure 15.4, shows that the conversion increases with the reaction time from 10–70 min. The reaction reaches the equilibrium at 60 min after which the yield of biodiesel remains constant. Therefore, 60 min reaction time is identified as an optimum for maximum yield of 97 wt% of biodiesel.

15.4 Characterization of Biodiesel

Table 15.1, shows the physical and chemical properties of the produced biodiesel. The fuel properties obtained were more compatible with the engines and in accordance with ASTM D 6751 standard.

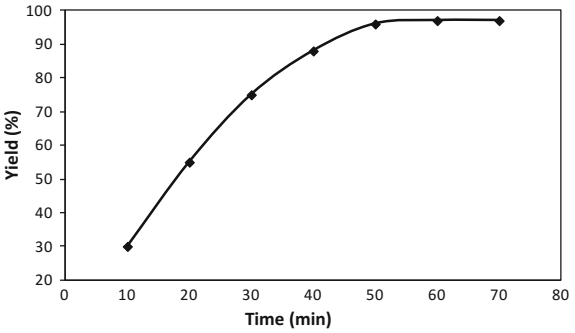

Fig. 15.4 Effect of reaction time

Table 15.1 Characterisation of beef tallow biodiesel

Property	Unit	ASTM method	ASTM D 6751 standard	Beef tallow biodiesel
Viscosity at 40 °C	$mm^2\ s^{-1}$	D 445	1.9–6.0	4.39
Density	$Kg\ m^{-3}$	D 1298	0.86–0.89	889
Flash point	°C	D 93	34 min	61
Cloud point	°C	D 2600	–	5
Bottom water and sediment	% vol	D 1796	0.05 max	Trace
Centane number	–	D 975	47 min	46
Water by distillation	% vol	D 95	–	Trace

15.5 Conclusion

The use of nano catalyst ($Cs/Al/Fe_3O_4$) took 60 min for the complete transesterification of tallow oil at 12:1 methanol to oil molar ratio, 3 wt% of catalyst at 60 °C thereby better result for synthesis of biodiesel. The catalyst confirms that it is effective in converting beef tallow into biodiesel. At optimum reaction condition the maximum yield of biodiesel was 97 wt%. The produced biodiesel was analyzed as per ASTM test methods and compared with ASTM D6751 standards. The results showed that they are in line with the standards and hence can be used in internal combustion engine without any modification.

References

1. J.W. Guo, T.S. Zhao, J. Prabhuram, R. Chen, C.W. Wong, Preparation and characterization of a PtRu/C nanocatalyst for direct methanol fuel cells. Electrochimi. Acta **51**, 754–763 (2005)
2. M. Feyzi, A. Hassankhani, H.R. Rafiee, Preparation and characterization of $Cs/Al/Fe_3O_4$ Nano catalysts for biodiesel production. Energy Conv. Manag. **71**, 62–68 (2013)
3. M. Kaur, A. Ali, Lithium ion impregated calcium oxide as nano catalyst for the biodiese production from karanja and jatropha ois. Renew. Energy **36**, 2866–2871 (2011)
4. R. Madhuvilakku, S. Piraman, Biodiesel synthesis by TiO_2-ZnO mixed oxide nano catalyst catayzed palm oil transesterification process. Bioresour. Technol. **150**, 55–59 (2013)
5. F. Qiu, Y. Li, D. Yang, X. Li, P. Sun, Heterogeneous solid base nano catalyst: preparation, characterization and application in biodiesel production. Bioresour. Technol. **102**, 4150–4156 (2011)

Chapter 16
Production of Biofuel from *Shorea Robusta* Seed Oil Using Nano MgO Catalyst

Arumugamurthi Sakthi Saravanan, Siva Periyasamy and Pandian SivaKumar

Abstract In this study, MgO nano-catalyst was used to produce biofuel (biodiesel) from *Shorea robusta* seed oil. The catalyst was synthesized and its physiochemical properties were characterized by XRD, SEM and EDX analyses. An optimum weight of 2.5% of MgO nano-catalyst was used to obtain a maximum conversion (98.5%) of triglycerides. The optimum parameters that influence the process were 9:1 molar ratio of methanol to oil, reaction temperature of 60 °C, 60 min and agitation speed of 500 rpm. Fuel properties were compared with ASTM standards. From the obtained results, it is evident that *Shorea robusta* seed oil is a viable feedstock for biofuel production.

Keywords *Shorea robusta* · Transesterification · Biodiesel · MgO nano-particles

16.1 Introduction

The increase in environmental pollution, depletion of reserves and increasing demand for energy have forced many researchers to identify new alternative fuels [1]. Among the various alternate fuels, biodiesel is the only fuel that can be used directly in the existing engine with minor or no modification. It is composed of mono alkyl esters of long chain fatty acids produced by the transesterification of lipid sources obtained from vegetable oils, animal fats etc. [2]. This reaction can be

A.S. Saravanan
Department of Petrochemical Engineering, RVS College of Engineering and Technology, Coimbatore 641402, India

S. Periyasamy
Department of Mechanical Engineering, Government College of Technology, Coimbatore 641013, India

P. SivaKumar (✉)
DSchool of Petroleum Technology, Pandit Deendayal Petroleum University, Gandhinagar 382007, India
e-mail: sivakumar.p@spt.pdpu.ac.in

G. Anand et al. (eds.), *Nanotechnology for Energy and Water*,
Springer Proceedings in Energy, https://doi.org/10.1007/978-3-319-63085-4_16

performed with the help of homogeneous and heterogeneous catalyst in the presence of alcohol as a reactant. The main drawback of biodiesel production is its high feedstock and process cost. From the literature study it was evident that the cost can be reduced by using non-edible oil, waste cooking oil and waste animal fats as feedstocks whereas the process cost can be reduced by using recyclable heterogeneous catalyst. Currently, heterogeneous catalysts are costly and the yield of biodiesel is low which can be eliminated by using nano based catalyst. Nano catalysis has the advantage of high catalytic activity and can be easily recovered like heterogeneous catalyst [3, 4]. There are many numbers of non edible oil such as neem, jatroph, karanja, cotton, palm, flax etc. Among these *Shorea robusta* (sal) seed oil is one the underutilized in the sub continent [5].

This study focuses on the use of inadequately explored *Shorea robusta* oil as a low cost feedstock and nano MgO as a catalyst to reduce the process cost of biodiesel production. The produced biodiesel physiochemical properties were analysed as per ASTM method and compared with ASTM D 6751 standard.

16.2 Materials and Experimental Methods

16.2.1 Feedstock

Shorea robusta seeds were collected from IIT Madras campus, Chennai, India. The seeds were cleaned manually and dried in sunlight. The kernels were separated manually, ground to fine powder and stored in airtight containers. The total oil content was determined by Soxhlet apparatus using n-hexane as solvent. The physiochemical analysis of the extracted oil was determined by following standard methods.

Chemicals like magnesium nitrate, oxalic acid, dehydrated methanol, etc., were purchased from S.D Fine Chemicals, Chennai, India. Deionised water was used in all experiments.

16.2.2 Synthesis of Nano MgO Catalyst

The nano MgO catalyst was synthesized by following the described method. Initially, 100 mL $Mg(NO_3)_2.6H_2O$ solution (1 M) was mixed slowly drop wise into 100 mL $(COOH)_2.2H_2O$ solution (1 M) which was kept vigorously stirred for 12 h. Then the solution was dried into powder at 100 for 24 h. The reaction scheme of the precursor mixture is expressed in Eq. (16.1). The dried powder was ground and sieved through a 270 mesh screen. This was followed by oxidization process at 650 °C in a muffle furnace for 2 h in the presence of oxygen and cooled at a rate of 10 °C min^{-1}. The oxidization reaction is given in Eq. (16.2).

$$Mg(NO_3)_2 \cdot 6H_2O + (COOH)_2 \cdot 2H_2O \rightarrow MgC_2O_4 \cdot 2H_2O + 2HNO_3 + 6H_2O \quad (16.1)$$

$$MgC_2O_4 \cdot 2H_2O + 0.5O_2 \rightarrow MgO + 2CO_2 + 2H_2O \quad (16.2)$$

16.2.3 Catalyst Characterization

The synthesized nano catalyst was characterized by XRD, SEM and EDX analysis. Crystal structure and size of the nano catalyst were characterized using Empyrean, PANalytical X-ray diffractometer (Netherlands) with 2θ ranging from 10 to 80°, using Cu Ka (λ = 0.15141 nm) radiation operated at 45 kV and 30 mA. The morphology and the structure of obtained powder were determined by S-3400 N SEM (HITACHI, Japan). The elemental composition of the prepared samples was investigated by EDX (Thermo Electron Corporation, Japan).

16.2.4 Transesterification

The transesterification reaction was carried out in a 250 mL three-necked round-bottom flask equipped with a mechanical stirrer and a water-cooled condenser. The flask was loaded with 30 g oil and, heated to the desired temperature. The catalyst was mixed with methanol without preheating and added to the reactor to start the transesterification reaction. The stirring rate and reaction time were varied to get optimum yield. After the completion of the reaction the catalyst was recovered by centrifugation at 6000 rpm for 15 min and excess methanol by distillation [6].

16.3 Result and Discussion

16.3.1 Characterization of Oil

The physiochemical properties of the extracted oil were presented in Table 16.1. The moisture content of *Shorea robusta* seed was 0.05 wt%. This is a good sign for a longer shelf life of the oil and a better choice for transesterification reaction where low moisture content is desirable. Acid value of the oil was 2.10 mg KOH g^{-1} which was enabled by the use of alkali catalyst (MgO). Lower iodine number signifies lower degree of unsaturated fatty acid. The saponification value was196.2 mg KOH g^{-1}, which is used to find the average molecular weight of oil.

Table 16.1 Physiochemical properties of *Shorea robusta* seed oil

Properties	Value
Moisture	0.05 wt%
Acid value	2.10 mg KOH g^{-1}
Iodine number	49
Saponification value	196.2 mg KOH g^{-1}
Specific gravity	0.895
Viscosity @ 40 °C	36 m^2 s^{-1}

16.3.2 Characterization of Catalyst

The X-Ray diffraction patterns were similar to the peaks of standard MgO. This confirms that synthesized MgO was of high purity. This result also shows that the crystals match with the lattice parameters of nano MgO where the reflections are sharp with a slight broadening phase. The average crystal size of the catalysts determined by Scherrer equation was 58 nm. EDX spectra shows that the nano MgO particles were composed of magnesium and oxygen element. The molar ratio of Mg:O and stoichiometric data of Mg:O were close to each other. Except magnesium and oxygen no other peak was found in the spectrum, which conforms that the developed nano particles are pure MgO. The SEM microgram confirms the crystal shape of MgO nano particles.

16.3.3 Effect of Methanol to Oil Molar Ratio

The formation of fatty acid methyl ester was increased with the increase in methanol to oil ratio from 3:1 to 12:1. The addition of excess methanol will shift the equilibrium and bring in better transesterification process. Optimum ratio was identified in 9:1 while consuming 2 wt% catalyst around 60°C with the reaction being carried out for 45 min giving an optimum yield of 93 wt%.

16.3.4 Effect of Catalyst Loading

Biodiesel conversion was investigated by the effect of catalyst loading with respect to its varying concentration from 1 to 3 wt%. The maximum yield of 95.2 wt% was attained at 2.5 wt% where the reaction took place at 60 °C for 45 min and 9:1 methanol to oil molar ratio. A further increase in the catalyst amount (3 wt%), resulted in no increase in yield.

16.3.5 Effect of Reaction Temperature

The reaction temperature was varied from 30 to 70 °C with 2.5 wt% catalyst loading, 9:1 methanol to oil molar ratio and reaction time of 45 min. The yield increases with the increase in temperature up to 60 °C. Thereafter, a slight decrease in yield was observed when the temperature increased beyond the boiling point of methanol. Therefore, the optimum temperature for the biodiesel yield of 97 wt% was 60°C.

16.3.6 Effect of Reaction Time

Reaction time is also an important parameter for maximum yield. The variation in yield was studied for the reaction time up to 90 min. The yield increased with the reaction time from 30 to 60 min. When the equilibrium reached 60 min, the yield of biodiesel remained constant. Therefore, 60 min reaction is identified as an optimum for the yield of 97.6 wt% biodiesel.

16.3.7 Effect of Stirring Rate

The stirring rate of the reaction was varied from 200 to 600 rpm. The reaction was incomplete at the lower speed of 200 to 400 rpm where the rate of mixing was insufficient for transesterification reaction. The yield of biodiesel at 500 rpm remained constant for a further increase in the stirring rate. Therefore, the optimum yield of biodiesel at the optimised condition was 98.5 wt%.

16.3.8 Characterization of Biodiesel

Physicochemical properties of *Shorea robusta* seed biodiesel are within the ASTM D6751 standards as shown in Table 16.2. Viscosity of 4.85 $mm^2\ s^{-1}$ at 40 °C is the most important factor, which affects the fluidity of biodiesel. The flash point is

Table 16.2 Physicochemical properties of *Shorea robusta* seed biodiesel

Properties	ASTM Testing procedure	Shorea robusta biodiesel	ASTM standard
Specific gravity	D4052	0.856	–
Viscosity @ 40 °C	D445	4.85	1.9–6.0
Flash point	D93	153°C	130 minimum
Cetane number	D613	57	47 minimum
Cloud point	D2500	6	−3 to 12

153 °C, which makes storage and transport issues less important. Specific gravity is 0.856 which is a lower value than *Shorea robusta* seed oil. This indicates the completion of reaction and the effective removal of glycerin.

16.4 Conclusions

Shorea robusta seed biodiesel was prepared successfully by using nano MgO. A higher yield of 98.5 wt% biodiesel was obtained which can be compared with the homogeneous catalyst, thus making the former catalyst superior. The optimized reaction conditions for the maximum yield of biodiesel were 2.5 wt% catalysts, 9:1 methanol to oil molar ratio, reaction time 60 min, reaction temperature of 60 °C and stirring rate at 500 rpm. The production of catalyst is quiet simple and the yield is higher when compared to other MgO catalyst reported in the literature. In this regard the attempts to recover and reuse the catalyst use of these catalysts for continuous production of biodiesel at the industrial level can be the subject for further investigation.

References

1. A.F. Lee, J.A. Bennett, J.C. Manayil, K. Wilson, Heterogeneous catalysis for sustainable biodiesel production via esterification and transesterification. Chem. Soc. Rev. **43**, 7887–7916 (2014). doi:10.1039/C4CS00189C
2. J. Qian, H. Shi, Z. Yun, Preparation of biodiesel from Jatropha curcas L. oil produced by two-phase solvent extraction. Bioresour. Technol. **101**, 7025–7031 (2010). doi:10.1016/j.biortech.2010.04.018
3. M.B. Gawande, P.S. Brancoa, R.S. Varma, Nano-magnetite (Fe_3O_4) as a support for recyclable catalysts in the development of sustainable methodologies. Chem. Soc. Rev. **42**, 3371–3393 (2013). doi:10.1039/C3CS35480F
4. J.W. Guo, T.S. Zhao, J. Prabhuram, R. Chen, C.W. Wong, Preparation and characterization of a PtRu/C nanocatalyst for direct methanol fuel cells. Electrochim Acta **51**, 754–763. doi:10.1016/j.electacta.2005.05.056
5. N. Vedaraman, Sukumar Puhan, G. Nagarajan, B.V. Ramabrahmam, K.C. Velappan, Methyl ester of Sal oil (*Shorea robusta*) as a substitute to diesel fuel-A study on its preparation, performance and emissions in direct injection diesel engine. Indcrop **36**, 282–288 (2012). doi:10.1016/j.indcrop.2011.09.003
6. F. Qiu, Y. Li, D. Yang, X. Li, P. Sun, Heterogeneous solid base nanocatalyst: preparation, characterization and application in biodiesel production. Bioresour. Technol. **102**, 4150–4156 (2011). doi:10.1016/j.biortech.2010.12.071

Chapter 17
Productivity Comparison of Solar Still with Nano Fluid and Phase Changing Material with Same Depth of Water

Amrit Kumar Thakur, Prashant Khandelwal and Bhushan Sharma

Abstract Quality and quantity of water is reducing day by day and it is very important to find a way for availability of pure water. Sun base still is a creative implement that uses sunlight based vitality to deliver distilled water from saline water but limitation is productivity of solar still. Warm vitality gathered by sun based authorities should be efficiently put away. Sun based vitality is accessible just amid the day and its application requires proficient TES constituents. In this way, the abundance warm vitality gathered amid the day time could be put away for later use amid the night. In this work method of enhancing productivity of solar still has been studied in month of June 2016 in Jaipur, India. Comparison of productivity of simple solar still having water depth of 0.01 m has been done with solar still having Nano fluid Al_2O_3 used in water basin and Phase changing material in water basin for same depth. It was observed that productivity of solar still reaches maximum when nano fluid Al_2O_3 is used in water basin as compare to both cases. Due to heat storage capacity of nano fluid, convective rate of heat transfer improves and finally productivity increases.

Keywords Nano fluid · Solar still · Passive heating · Phase changing material · Convection heat transfer

Nomenclature

$h_a=(h_{ew} + h_{cw} + h_{rw})$	Total heat transfer coefficient from water surface to glass cover ($W/m^2\ ^\circ C$)
h_{cw}	Convective heat loss coefficient in solar still ($W/m^2\ ^\circ C$)
h_{ew}	Evaporative heat loss coefficient in solar still ($W/m^2\ ^\circ C$)
h_{rw}	Radiative heat loss coefficient of still ($W/m^2\ ^\circ C$)
A_a	Aperture area of concentrator (m^2)
h_a	Heat transfer coefficient from lower glass cover to flowing water ($W/m^2\ ^\circ C$)

A.K. Thakur (✉) · P. Khandelwal · B. Sharma
Arya College of Engineering and IT, Jaipur, Rajasthan, India
e-mail: amritt1@gmail.com

G. Anand et al. (eds.), *Nanotechnology for Energy and Water*,
Springer Proceedings in Energy, https://doi.org/10.1007/978-3-319-63085-4_17

17.1 Introduction

Approximately 70% of the ecosphere populace is expected to stand challenged by freshwater scarcity through 2025. A current report demonstrations that underground water levels and rainwater stay in debility [1, 2]. In the imminent, through populace and per capita ingesting development, the condition drive grow into even further challenging. In villages, underground water is the main source of drinking need. Groundwater is the foremost basis of water in the dry and semi dry atmosphere which satisfies the necessity of unlike useful usages viz., consumption, local, and/or irrigation mostly for the rural populace. With faster and unrestrained growth schemes such as stock agri-business, irrigation, suburbanization, and industrial development, a huge amount of leftover goods are actuality produced and cleared which eventually pollute both underground water and surface water. The inordinate and improper utilization of substance composts, creature excrements, bug sprays, and pesticides, disgracefully manufactured or inadequately found as well as kept up septic frameworks for family unit wastewater, releasing or surrendered underground stockpiling tanks and funneling, dishonorable transfer or capacity of squanders and compound spills at neighborhood mechanical locales, over abuse and indiscreet utilization of groundwater have exhausted groundwater accessibility, as well as made its quality inferior and rare. It has been harmed by different poisons like nitrate, arsenic, fluoride etc. Renewable energy can be used for purifying and filter the water such as wind, solar. Other method of purifying water is also available such as RO, UV but they all need electricity to run which itself is a very big issue in small town and villages of India. Among the several clean energy assets, solar energy potential the highest in the country. The comparable vitality prospective is about 6000 million GWh of vitality per year. India lies in the sunshiny areas of the ecosphere. Maximum portions of countries collect 4–7 kWh of solar energy/m^2/day with 250–300 bright days in a year [3]. The solar still (SS) is a modest and ecological water fabrication technique which is in process for several years but its main limitation is comparatively low production of distilled water as compared to other distillation approaches. This trial is attention of rigorous investigation with the objective of increasing improved SS with advanced yields. For the most part, water is being utilized as warm storing component in sun powered water warming frameworks for family unit applications. In any case, the primary disadvantages of utilizing water are low working temperature, little term of thermal energy storage and low thermal conductivity. Look into has been completed to improve thermal conductivity of water by doping of nano materials to use in sun based authorities [4]. Ionic fluids have points of interest over ordinary liquids of high working temperature range, thermal conductivity and specific heat capacity. Amid the previous four decades phase change materials (PCM) are increasing more consideration as heat transfer fluid. PCMs are for the most part delegated natural, (for example unsaturated fats, ketones, paraffin wax) and inorganic materials, (for example, hydroxides, carbonates and nitrates). To expand the sun powered thermal energy storage, PCM fills in as a superior decision. Moreover, propels in nanotechnology prompted the blend of novel nanoparticle which enhances warm

execution of base liquids, paraffin's and liquid salts [5]. The imperative elements/parameters for thermal energy storage materials are (i) High thermal conductivity, (ii) Eco-accommodating (iii) High warm storing limit and (iv) Low cost and low warm vitality adversity [6]. Warm vitality gathered by sun powered authorities should be effectively put away. Sun based vitality is accessible just amid the day and its application requires effective thermal energy storage materials. In this manner, the abundance warm vitality gathered amid the day time could be put away for later use amid the night [7]. A few examinations have been accounted for to upgrade thermal conductivity of base liquids, paraffin's and liquid salts through doping on nano materials [8, 9]. Utilizations of nano liquid for flat plate collector was tentatively researched by Yousefi et al. [10] utilizing Al_2O_3 nano particle. By scattering 0.2 wt% of Al_2O_3 nano particle in water, thermal energy expanded by 28.3%. In another trial, expansion of 0.021 wt% triton X-100 surfactant to the blend of 0.4 wt% of Al_2O_3 nano particle in water brought about upgraded thermal energy by 15.63%. Low nano particle fixation and nearness of surfactant in base liquid contributes towards higher reliability and subsequently higher thermal conductivity improvement. Absorber plate material selection is very important. At 2 cm of water level, Al plate which is black painted improved the effectiveness by 28% [11]. H. N. Panchal et al. [12] studied that distilled water output of passive solar still fitted with aluminum plate in water basin was maximum as compared to solar still having galvanized iron plate as well as conventional solar still. T. Elango et al. [13] studied single basin and double basin slope glass stills. In this, still were concentrated under insulated and un-insulated conditions for their generation at different water depth of 1, 2, 3, 4 and 5 cm. The yield was high at the lower water depth of 1 cm for both single and double basin still.

17.2 Methodology

In this work, a passive type single basin solar still has been used. Testing for the present study was carried out for Jaipur, Rajasthan, India climatic conditions month of June, 2016. In this work, water basin of solar still was black painted to absorb maximum radiation from sun. Aluminum plate has been used as an absorber plate inside the water basin to absorb maximum solar radiation. Nano fluid Al_2O_3 is used inside the water basin to increase the heat storage capacity of sink. Phase changing material such as wax is also used in water basin to increase the heat storing capacity of sink.

17.3 Description of Experimental Set Up and Observations

The experimental image of simple solar still is shown in Figs. 17.1 and 17.2. The experimental set up are installed in Jaipur, India (26.9124° N latitude, 75.7873°E longitude). Solar stills is south facing to receive the maximum solar radiation.

Fig. 17.1 Solar still with thermocouple display

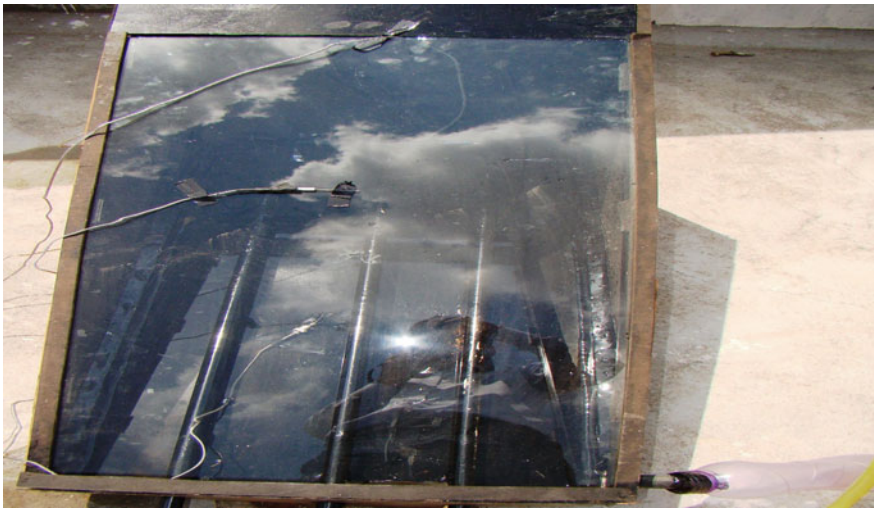

Fig. 17.2 Solar still with water output

Table 17.1 Description of instrument

Instrument	Accuracy	Range	% Error
Digital thermometer	±1 C	0–100 C	1
Pyranometer	±25 W/m^2	0–1800 W/m^2	3
Thermocouple	±1 C	0–100 C	1

The SS having sink area of 1 m^2 is made-up by using an absorber plate of aluminum sheet 1.5 mm thickness. All the sides of the still unit are insulated by a 2 cm thick plywood and thermocol to protect side heat loss to the ambient. Glass area of solar still made up of simple window glass is 1.45 m^2 with single glass mounted on still. The glass cover of the still is of 4 mm thick and inclined at the angle 26° as from past work angle should be equal to latitude of experimental site to achieve maximum productivity of still. The experiments are carried out in time duration of 7:00 AM–7:00 PM on typical days in June, 2016. The temperatures are recorded by using four K-type thermocouple and Multi point data recorder (thermocouples reader). The ambient temperature is recorded by using temperature meter (K-type). A pyranometer is used to screen the solar radiation. The comparative performance simple solar stills, solar still having nano fluid used in water basin and solar still having wax used in water basin are analyzed at the water depths of 0.01 m. Accuracies and error for various measuring instruments are given below in Table 17.1.

17.4 Mechanism

The solar radiation is transmitted through the single slope solar still cover and temperatures of water in basin of still increase. Part of the energy absorbed by the basin is transferred by convection to the water. Black paint done inside water basin of solar still increases its absorptivity and rate of convection increases. When solar radiation decreases approx. after 4 pm in evening, the still components start to cool down and productivity of solar still starts falling down. PCM such as wax and Nano fluid both absorbs excess energy when solar radiation has high value and release it when the radiation starts decreases and due to this temperature still attain a significant value to produce a better yield as compare to simple solar still.

17.5 Thermal Modeling

Position of various thermocouple position placed at different position of SS has been shown in Table 17.2

Table 17.2 Position of various thermo couple

Thermo couple	Position
T_1	Upper glass surface
T_2	Glass lower side temperature
T_3	Ambient air temperature
T_4	Absorber plate temperature

The energy balance equations for the glass cover of SS is as follows:
Solar still:

[1] Glass cover

$$h_a(T_4 - T_1) = h_{a'}(T_1 - T_4) \tag{17.1}$$

[2] Thermal Efficiency

The overall thermal efficiency of the system under the active mode of operation can be calculated as,

$$\eta = \frac{Me.l \times 3600}{(Aa).I(t)} \tag{17.2}$$

l latent heat of vaporization	2270000.00 J/kg,
M_e	Full day yield
I (t)	Solar radiation on glass cover of SS

17.6 Results

Figures 17.3, 17.4 and 17.5 shows the temperature distribution of solar still at various location which is measured by thermocouple. From Fig. 17.3 graph it was observed that for depth of 0.01 m absorber plate has highest temperature of 96 °C at 1 pm and ambient temperature is lowest. For Fig. 17.4, highest temperature has attained by absorber plate which is 92 °C at 2 pm and for Fig. 17.5, highest temperature was achieved by glass lower surface which is 81 °C at 1 pm.wind velocity has very important influence on productivity.

Figures 17.6, 17.7 and 17.8 shows the global radiation and production of distilled water. Wind velocity play a very important role in productivity of SS. For Fig. 17.6 with water depth of 0.01 m radiation reaches a value of 4.10 MJ/m^2 at 1 pm to give yield of 0.79 L. For Fig. 17.7, radiation attain a value of 4.02 MJ/m^2 at 1 pm to give yield of 0.70 L. For 6.6, radiation has maximum value of 3.46 MJ/m^2 at 2 pm and production is highest at 12 noon of 0.65 L.

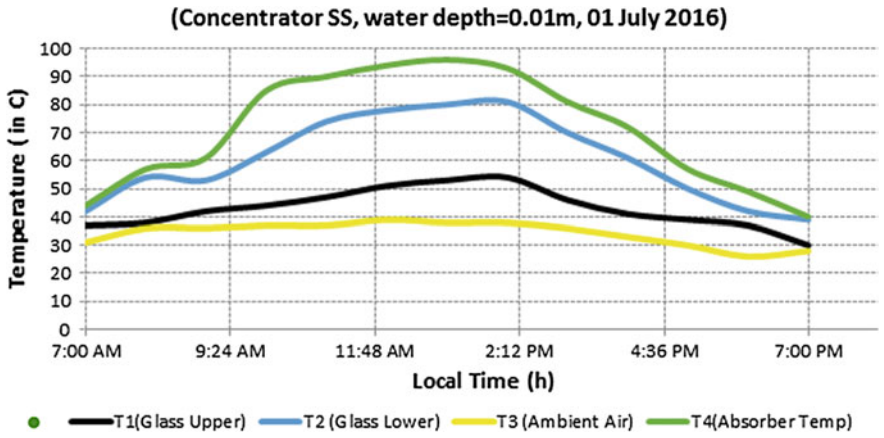

Fig. 17.3 Temperature measurement of Nano fluid used in sink of SS for 0.01 m depth

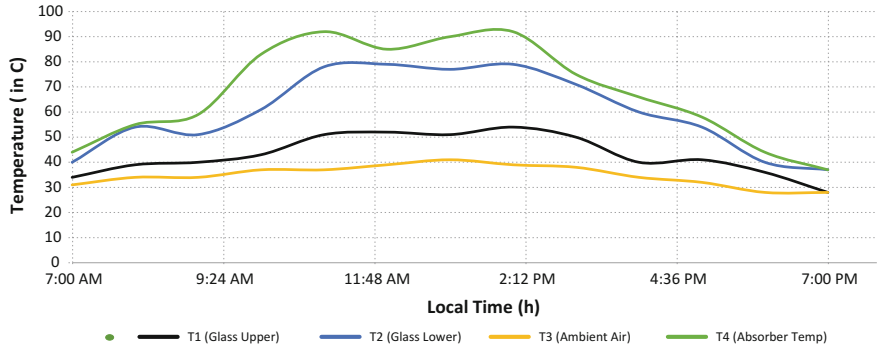

Fig. 17.4 Temperature measurement of PCM (Wax) used in sink of SS for 0.01 m depth

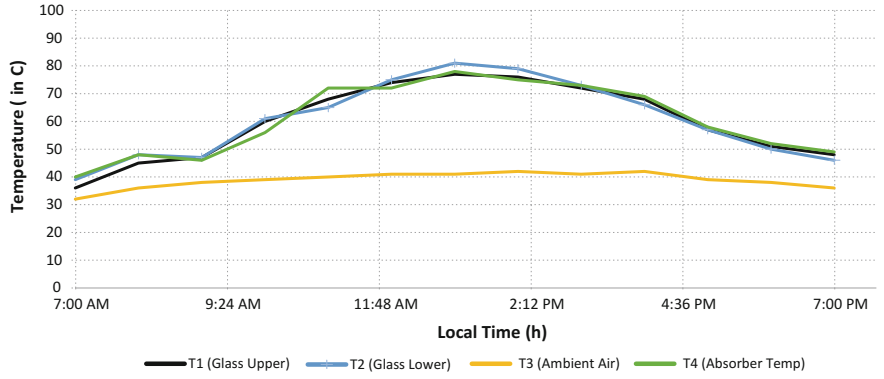

Fig. 17.5 Temperature measurement of simple SS for 0.01 m depth

Full day production at 0.01 water depth (Liter)		Thermal efficiency (%)
Nano fluid is used in sink of SS	5.47	44.47
PCM(Wax) is used in sink of SS	5.1	41.46
Simple solar still	4.66	39.18

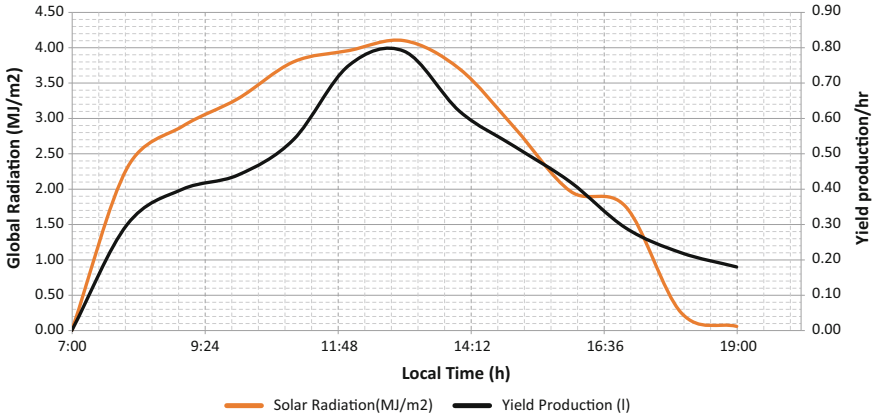

Fig. 17.6 Solar radiation and yield production when Nano fluid is used in sink of SS

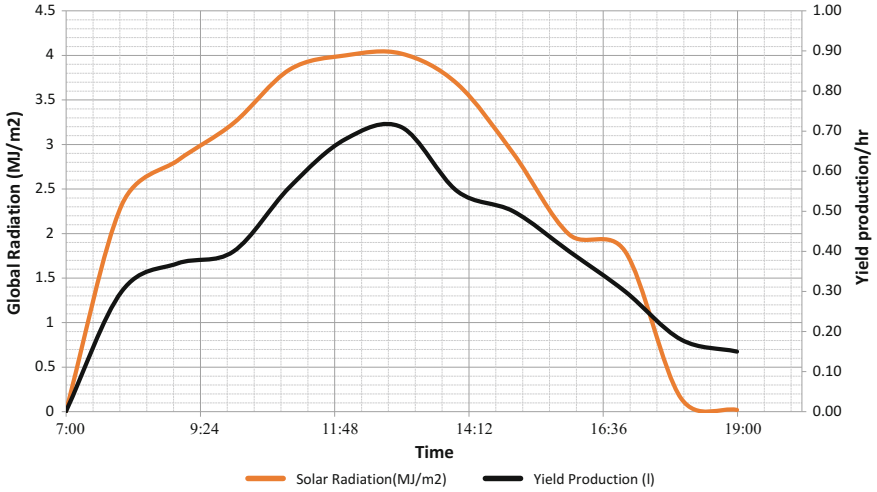

Fig. 17.7 Solar radiation and yield production when wax is used in sink of SS

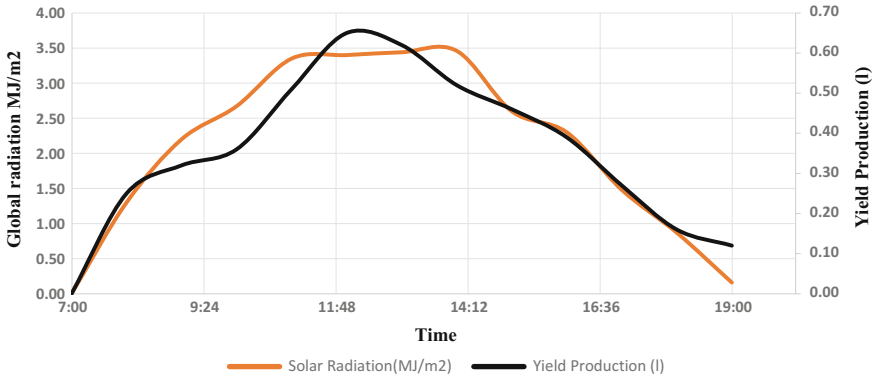

Fig. 17.8 Solar radiation and yield production for simple solar still

17.7 Discussion

Evaporative heat transference from sink water to glass shield be subject to the absorber plate area and the modification amongst partial pressure of sink water temperature and partial pressures of glass shield temperature. Rate of evaporation of SS is mainly depends on sink water, glass shield and ambient temperature change. Rate of evaporation of basin water is maintained at good level when solar radiation value decreases because of nano fluid Al_2O_3 and phase changing material, due to their thermal energy storage behavior at the time when maximum amount of solar radiation is available they store the excessive energy and release it when needed. Rate of evaporation of SS plays a significant role in production. Rate of evaporation mostly be subject to on solar radiation convenience which is shown by formula given by Malik et al. [14] and Dunkle [15]. The driving force of the solar distillation technique is the difference between temperature of water in the basin and the cover [16–18]. Angle of glass of SS is vital as it direct and deflect the amount of radiation when its value is equal to latitude of site and hence help in absorbing maximum value of solar radiation.

17.8 Conclusion

A single slope SS is fabricated and its performance has been compared with various energy storing material. In this research, same water depth with simple solar still, SS with Al_2o_3 in water basin and SS with PCM (Wax) in water basin has been studied. Energy storing material help in increasing productivity of solar still even when solar radiation value got reduced.

The following conclusions are drawn from the experimental results:

- Nano fluid and PCM both helped in increasing yield of solar still especially after 3 PM when solar radiation value has reduced but as they releases the excessive stored energy into the water basin and productivity reached a specifically good value as compare to simple solar still.
- Nano particle used in nano fluid increases its thermal conductivity and due to this overall productivity of nano fluid based solar still was better as compare to PCM based solar still.
- Selection of material for absorber plate is very important for achieving increased value of yield for SS.
- Inclination angle of glass cover is equal to the latitude angle of experimental site for achieving better results.

17.9 Future Recommendations

- Forced convection can used to increase the productivity of SS.
- V-Shape concentrator can be combined with parabolic SS, Triangular SS and other good yield designed still for achieving better results.
- Wick material and dyes, sponge ball can be used to increase the rate of evaporation.

References

1. NASA. http://www.nasa.gov/topics/earth/features/wetter-wet.html
2. NASA. http://www.nasa.gov/topics/earth/features/india_water.html
3. M. Alam, S.K. Yasin Mohammad, M. Gain, S. Mondal. Renewable energy sources (res): an overview with Indian context. Int. J Eng. Computer Sci. **3**(10), 8871–8878 (2014). ISSN:2319- 7242
4. T.C. Paul, A.M. Morshed, J.A. Khan, Nanoparticle enhanced ionic liquids (NEILS) as working fluid for the next generation solar collector. Procedia Engg. **56**, 631–636 (2013)
5. S.U. Choi, Nano fluids: from vision to reality through research. J. Heat Trans. **131**, 033106 (2009)
6. S. Kuravi, J. Trahan, D.Y. Goswami, M.M. Rahman, E.K. Stefanakos, Thermal energy storage technologies and systems for concentrating solar power plants. Prog. Energy Combust. Sci. **39**, 285–319 (2013)
7. Y. Hou, R. Vidu, P. Stroeve, Solar energy storage methods. Ind. Engg. Chem. Res **50**, 8954–8964 (2011)
8. O. Mahian, A. Kianifar, S.A. Kalogirou, I. Pop, S. Wongwises, A review of the applications of nano fluids in solar energy. Int. J. Heat Mass Transf. **57**, 582–594 (2013)
9. l.-W. Fan, X. Fang, X. Wang, Y. Zeng, Y.-Q. Xiao, Z.-T. Yu et al., Effects of various carbon nano fillers on the thermal conductivity and energy storage properties of paraffin-based nano composite phase change materials. Appl. Energ. **110**, 163–72 (2013)

10. T. Yousefi, F. Veysi, E. Shojaeizadeh, S. Zinadini, An experimental investigation on the effect of Al_2O_3–H_2O nano fluid on the efficiency of flat-plate solar collectors. Renew Energ. **39**, 293–298 (2012)
11. N.H.A. Rahim, Utilization of new technique to improve the efficiency of horizontal solar desalination still. Desalination **138**, 121–128 (2001)
12. H.N. Panchal, P.K. Shah, Char performance analysis of different energy absorbing plates on solar stills. Iran. J. Energ. Environ. **2**, 297–301 (2011)
13. T. Elango, K. Kalidasa Murugavel, The effect of the water depth on the productivity for single and double basin double slope glass solar stills. Desalination **359**, 82–91 (2015)
14. M.A.S. Malik, G.N. Tiwari, A. Kumar, M.S. Sodha, *Solar distillation* (Pergamon Press, UK, 1982)
15. R.V. Dunkle solar water distillation; the roof type still and a multiple effect diffusion still. In: International Developments in Heat Transfer, ASME proceedings of international heat transfer, Part V. University of Colorado (1961)
16. S.O. Onyegegbu, Nocturnal distillation in basin-type solar stills. Appl. Energ. **24**, 29–42 (1986)
17. Tanaka Hiroshi, Solar thermal collector augmented by flat plate booster reflector: optimum inclination of collector and reflector. Appl. Energ. **88**, 1395–1404 (2011)
18. P.T. Tsilingiris, The glazing temperature measurement in solar stills—errors and implications on performance evaluation. Appl. Energ. **88**, 4396–4944 (2011)

Chapter 18
Qualitative and Quantitative Analysis of Lipid Derived via Cell Disruption Techniques from *Chlorella vulgaris* for Biodiesel Production

N. Nirmala, S.S. Dawn and S. Shiyam Rengith

Abstract The fast growing microalgae *Chlorella vulgaris* were isolated from fresh water bodies Pallikaranai at Chennai, Tamil Nadu, India and the species were focused for high lipid extraction for biodiesel production. The Optical Microscope and Field Emission Scanning Electron Microscope studies were performed to examine the morphology of *Chlorella vulgaris*. The Quantitative analysis of Intracellular components of *Chlorella vulgaris* were also examined by performing Nile red staining and observed under Epifluorescence Microscope. Various methods including Bligh and Dyer, Modified Bligh and Dyer method, Ultrasonication, Bead Vortexing, Shake Mill, Water Bath and Osmotic Shock methods were experimented to identify the effective cell disruption of *Chlorella vulgaris* for high yield of lipid content. Among which the Osmotic shock method was found to be an effective method for the cell disruption of *Chlorella vulgaris* which gives a yield of 26.1%. Therefore the extracted lipids were subjected to GC—MS for the analysis of fatty acid composition which is responsible for biodiesel production. Fatty acid methyl esters like C14:0, C16:0, C17:0, C18:1 are found to be present in the lipid content of *Chlorella vulgaris* which ensures its capabilities for biodiesel production.

18.1 Introduction

Biodiesel production uses in engines have gained significant legislation and fossil fuel demand. Biofuel research is now exploring third generation. The first and second generation fuels seem to be more cost competitive when compared to the

N. Nirmala (✉) · S.S. Dawn
Centre for Waste Management, Sathyabama University, Chennai 600119, India
e-mail: nirmala.amutha@gmail.com

S.S. Rengith
Department of Chemical Engineering, Sathyabama University, Chennai 600119, India

G. Anand et al. (eds.), *Nanotechnology for Energy and Water*,
Springer Proceedings in Energy, https://doi.org/10.1007/978-3-319-63085-4_18

existing fossil fuel. The third generation biofuel by targeting the oil sources present in the algal biomass [1]. The advantages of third generation fuel is that which the biomass can be grown using land and water which are unsuitable for food production, algae are the potential source to produce more energy than the conventional crops. The fourth generation bio-fuels are identified to not only to produce sufficient energy but also to pave a way of capturing and storing the carbon dioxide.

Due to its renewable nature and adaptability to any climatic conditions microalgae are considered as an efficient renewable fuel to replace the existing fossil fuels strongly. Microalgae are capable to grow in various environments like fresh, brackish or salt water, possess higher growth rate and high lipid productivity of about 20–50% by dry weight basis. As these microalgae species are fast growing and have good photosynthetic efficiency, considerable biomass productivity, efficient fatty acid profile, easy and inexpensive they are strongly recommended for biodiesel production [2]. Cultivation, cell harvest, lipid extraction and transesterification of lipids are the four major stages involved in the production of Biodiesel from Microalgae. The efficiency of lipid extraction depends on the polarity and combination of polar and non-polar solvent mixtures. Some lipid extraction techniques extract more lipids from microalgae based on the solvents that are used for the extraction purpose and its mechanical properties [3]. The aim of the present study is to improve the lipid content of the microalgae and to compare the methods for effective lipid extraction and to analyze qualitatively and quantitatively the Intracellular lipid in microalgae for the bio-diesel production.

18.2 Materials and Methods

The water samples from Pallikaranai were collected aseptically for the isolation of microalgae from fresh water bodies. The collected 10 ml of water samples were inoculated with 200 ml of sterilized BG- 11 Medium in 500 ml Erlenmeyer conical flask and incubated at 27 ± 2 °C under 1500 µmol-1m2 s-1 intensity with 12:12 h's photoperiod. The incubated flasks were continuously examined for the growth of microalgae using optical microscope. Subcultures were made onto sterilized BG- 11 agar plate and observed for the growth of individual colonies [4].

18.2.1 Optical Microscopy and Scanning Electron Microscopy

The pure cultures of *Chlorella vulgaris* were obtained from subcultures and the flask by placing a drop of aliquots of the sample in a glass slide and covered with a cover slip and observed under the optical microscope (BX51 OLYMPUS, Japan). The Field emission Scanning Electron microscope (FESEM—SUPRA 55)—CARL ZEISS, GERMANY, was used to analyze the three dimensional image of the

surface of the fast growing microalgae. The dried microalgae fragments were deposited on an adhesive carbon tape mounted on a metal stub and coated with Gold/Palladium using a sputter Coater (DC Magnetron Sputtering—Hind High Vacuum, Bangalore) to allow a better conduction of the sample. The gold plated Microalgae sample was then loaded into the Field emission Scanning Electron Microscope for the topography analysis.

18.2.2 Quantitative Analysis of Intracellular Lipid by Nile Red Staining

0.5 ml of algae was subjected to centrifugation at 1500 rpm for 10 min and the supernatant were discarded. The centrifuged algal cells were washed with 0.5 ml of physiological saline for several times in order to remove the debris. 0.5 ml of diluted Nile red (9-(Diethyl amino) -5H benzo [α] phenoxazin-5-one) stain were then added to the microalgae cells and suspension was kept for incubation at room temperature for 10 min [5]. The stained microalgae cells were washed with 0.5 ml of physiological saline to remove the excess stain by centrifugation at 1500 rpm for 10 min. Stained Microalgae cells and intracellular lipids were observed under Epifluorescence Microscope (ECLIPSE 80i, Nikon, Japan).

18.2.3 Comparison of Cell Disruption Methods for Higher Lipid Extraction

18.2.3.1 Bligh and Dyer Method

500 mg of dried biomass was mixed with 4 ml of Chloroform, 8 ml of Methanol and 3.2 ml of distilled water and incubated in dark at room temperature for 24 h. The mixture was centrifuged at 5000 rpm for 5 min and the supernatant was collected into preweighted glass tube (M_1g). 4 ml of methanol, 2 ml of chloroform was added to the supernatant and incubated again in dark for 24 h at room temperature. The mixture was then centrifuged again at 5000 rpm for 5 min and 6 ml of chloroform and 7.6 ml of distilled water was added to the supernatant for the phase separation. The top whitish layer was removed and the bottom layer was dried (M_2g).

$$M_1g - M_2g = \text{Total lipid content of the biomass}$$

18.2.3.2 Modified Bligh and Dyer Method

500 mg of dried algal biomass was homogenized using mortar and pestle by adding 2:1 ratio of chloroform and methanol along with a pinch of silica glass powder.

The homogenized mixture was then centrifuged at 5000 rpm for 10 min and the crude supernatant was transferred to the separating funnel and equal volume of water was added to it and shake vigorously and allowed to settle for phase separation. The bottom lipid layer was then drained and hot air dried at 60 °C until it reaches the constant weight to calculate the percentage of the total lipid content [6].

18.2.3.3 Ultrasonication

500 mg of biomass was mixed with 3.25 ml of methanol and sonicated for 3 min. 6.25 ml of Dichloromethane was added to the mixture and sonicated again for 27 min and the mixture was centrifuged to remove the crude lipid supernatant at 5000 rpm for 10 min. To the supernatant 4.68 ml of KCl (0.88 w/v) was added and allowed to settle in a pear shaped separating funnel at room temperature for 24 h. The bottom lipid layer was hot air dried till it reaches the constant weight to measure the total lipid content [7].

18.2.3.4 Water Bath

20 ml of sample containing biomass was subjected to thermolysis by placing it in a preheated water bath. The biomass was heated at 90 °C for 30 min to induce the breakdown of cell wall of *Chlorella vulgaris*. The heated biomass was then allowed to cool and centrifuged at 5000 rpm for 10 min and the crude supernatant was dried and weighed for its lipid content [8].

18.2.3.5 Osmotic Shock

500 mg of dried biomass was suspended with 30 ml of 10% NaCl solution and vortexed for 2 min and the mixture was incubated at room temperature for 48 h. After the incubation period the mixture was then centrifuged at 5000 rpm for 10 min and supernatant was subjected to solvent extraction procedure using 2:1 ratio of Chloroform and Methanol and the total lipid content was measured [7].

18.2.3.6 Bead Vortexing

500 mg of biomass was suspended with 30 ml of solvents and zirconia beads size ranging from 0.4–0.6 mm and the mixture were vortexed for 30 min. The mixture was subjected to centrifuge at 5000 rpm for 10 min. The obtained supernatant was then subjected to lipid extraction procedure using organic solvents [9].

18.2.3.7 Shake Mill

The 3:1 ratio of biomass and bead concentration was taken for the shake mill experimental procedure and exposed to maximum speed for 15 min. The mixture was then centrifuged at 5000 rpm for 10 min and subjected to solvent extraction procedure.

18.2.4 Qualitative Analysis of Fatty Acid Methyl Ester by Gas Chromatography

The Total lipids were extracted from the exponential phase of Microalgae by performing modified Bligh and Dyer method. The extracted oily lipid sample was subjected to Fatty acid composition analysis using Gas Chromatography—Mass Spectrometric (JOEL GC MATE II) analysis equipped with a HP5 Capillary column. 0.2 µl of sample were injected into column head pressure of the carrier gas (High pure Helium) was 3 kPa at a flow rate of 1 ml/min with the oven temperature programmed from 50 to 250 °C at the rate of 10 °/min. The mass spectrometer was operated in Electron Ionization mode at 70 eV and the interface temperature was about 250 °C.

18.3 Results and Discussion

The characteristics and morphological features of algal cells observed under the optical microscope (BX51 OLYMPUS, Japan) were found to be *Chlorella vulgaris*. The algal cells are green colored, unicellular, spherical in shape about 2–10 µm in size surrounded by a cell wall consists of an out thin layer and inner bulky microfibrillar layer Shows in Fig. 18.1. Scanning Electron microscopy images clearly shows the spherical cell shape of *Chlorella vulgaris* at the magnification of 8.23KX with a width of 8.5 mm and extra high tension voltage (EHT) of 20.00 kV using conventional secondary electron detector shows in Fig. 18.2.

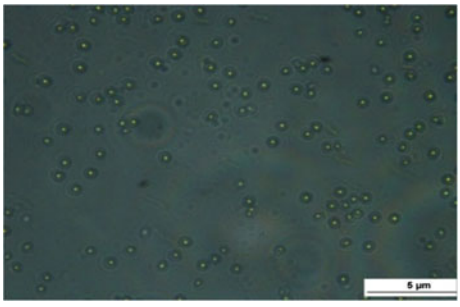

Fig. 18.1 Optical microscopic observation of *Chlorella vulgaris*

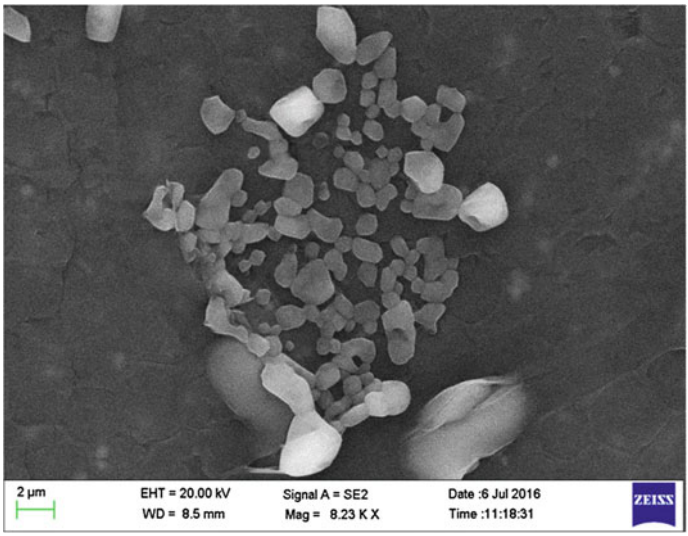

Fig. 18.2 Field emission scanning electron microscopic observation of *Chlorella vulgaris*

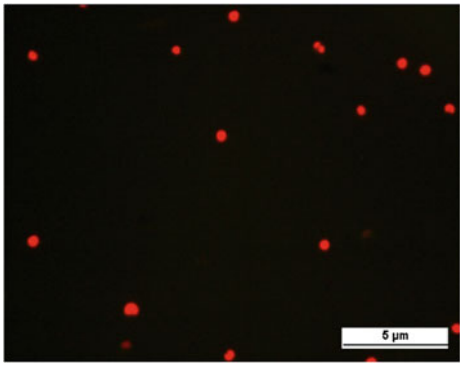

Fig. 18.3 Intracellular lipid analysis of *Chlorella vulgaris* by nile red staining

The accumulation of lipid bodies were examined in Nile red fluorescence dye stained *Chlorella vulgaris* cells under Epifluorescence Microscope. The preliminary observation of stained microalgal cells under the microscope indicates the interaction between the intracellular lipid globules and the Nile red dye. Thus resulted in fluorescence of red colour as seen in microscopic images indicates the presence of lipid globules in the cells of *Chlorella vulgaris* when observed under the Epifluroscence Microscope with excitation at 450–490 nm and emission at 515 nm Fig. 18.3.

Various cell disruption techniques were experimented to obtain a maximum amount of Intracellular components from *Chlorella vulgaris*. This cell disruption technique helps to break the cell and helps in releasing the intracellular materials for extraction purpose. The plot between treatment methods and lipid yield of

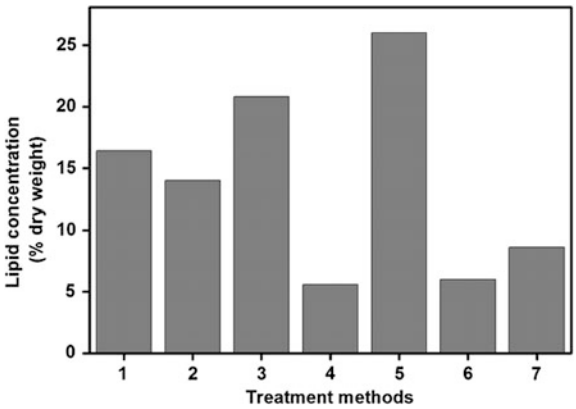

Fig. 18.4 Effect of cell disruption techniques of *Chlorella vulgaris* 1. Bligh and Dyer, 2. Modified Bligh and Dyer, 3. Ultrasonication, 4. Bead Vortexing, 5. Osmotic Shock, 6. Shake Mill, 7. Water Bath

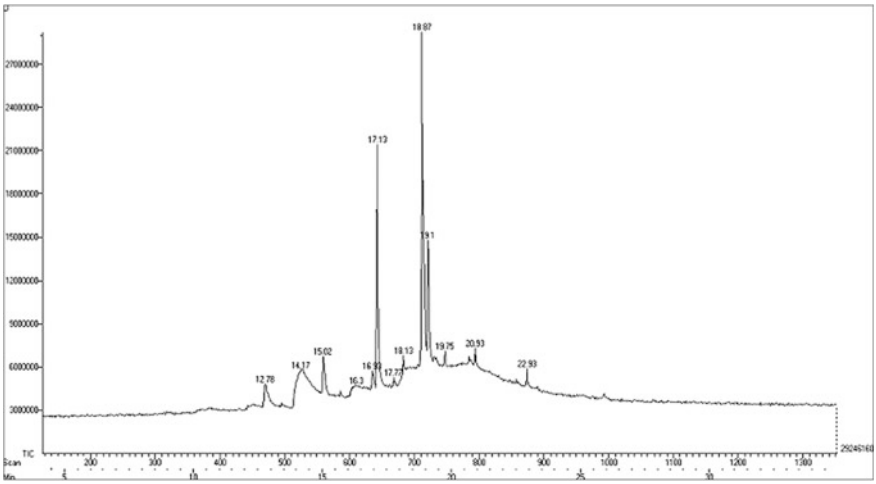

Fig. 18.5 Gas chromatography analysis of fatty acid methylesters

Chlorella vulgaris is shown in Fig. 18.4 and it shows highest lipid concentration of 26.1% was achieved by osmotic shock method whereas the lowest lipid concentration of 5.6% was obtained by bead mill method.

The fatty acid profile by GC-MS of lipid extracted from *Chlorella vulgaris* is shown in Fig. 18.5 and the composition, retention time and common name is tabulated in Table 18.1 The fatty acid is present in both saturated and polyunsaturated form while saturated form is dominating. Margaric acid (C17:0), palmitic acid (C16:1), and stearic acid (C18:1) acid are present in the highest for the fatty acids composition of *Chlorella vulgaris* as reported in [10]. The most significant fatty acid used for biodiesel production include saturated fatty acid and

Table 18.1 Fatty acid composition of *Chlorella vulgaris*

Retention time	Fame	Common name	Fame %
19.1	Heptadecanoic acid (C17:0)	Margaric acid	30.7
18.87	Octadecenoic acid (C18:1)	Stearic acid	24.45
17.77	Hexadecanoic acid (C16:0)	Palmitic acid	0.41
16.93	Trans-2- Hexadecanoic acid (C16:1)	Palmitic acid	2.45
16.3	n-Hexadecanoic acid (C16:0)	Palmitic acid	1.93
22.93	Docosanoic acid (C22:0)	Behenic acid	1.2
20.93	Nonadecanoic acid (C19:0)	–	12
19.75	9,15 Octadecadienoic acid (C18:2)	Stearic acid	1
12.78	Undecanoic acid (C11:0)	–	2.754
18.13	Hexadecanoic acid (C16:0)	Palmitic acid	1.07
14.17	Dodecanoic acid (C12:0)	Lauric acid	4.26
15.02	Methyl tetradecanoate (C14:0)	Myristic acid	3.21
17.13	Hexadecanoic acid (C16:0)	Palmitic acid	14.49

polyunsaturated fatty acid such as C14:0, C16:0, C17:0 and C18:1. The fatty acid such as C14:0, C16:0 and C18:0 are ideal for biodiesel production because this fatty acid has high Cetane number and good combustion property [11].

Acknowledgements The authors wish to acknowledge the Management of Sathyabama University- Dean (Research and Development), and The Ministry of Human Resource and Development (Sanctioned no: 5-5/2014-TS. VII 4th September 2014), Government of India for their consistent encouragement and financial support for the Research activities.

References

1. A. Josephine, C. Niveditha, A. Radhika, A. Brindha Shali, T.S. Kumar, G. Dharani, R. Kirubagaran, Analytical evalulation of different carbon sources and growth stimulators on the biomass and lipid production of Chlorela vulgaris—Implications for biofuels. Biomass Bioenerg. **75**, 170–179 (2015)
2. I. Ponnuswamy, S. Madhavan, S. Shabudeen, Isolation and characterization of green microalgae for carbon sequestration, waste water treatment and bio-fuel production. Int. J. Bio Sci. Bio Technol. **5**(2) (2013)
3. A.R. Byreddy, A. Gupta, C.J. Barrow, M. Puri, Comparison of cell disruption methods for improving lipid extraction from thraustochytrid strains. Marine Drugs **13**(11), 5111–5127 (2015)
4. N. Nirmala, S.S. Dawn, Environmental stress control to enhance lipid content in oleginous microalgae for biodiesel production. Int. J. Chem. Tech. Res. **9**(02), 237–241
5. R. Abou-shanab, I.A. Matter, S.N. Kim, Y.K. Oh, J. Choi, B.H. Jeon, Characterization and identification of lipid-producing microalgae species isolated from a freshwater lake. Biomass Bioenerg. **35**, 3079–3085 (2011)
6. R. Ranjith Kumar, P. Hanumantha Rao, M. Arumugam, Lipid extraction methods from microalgae: a comprehensive review. Front. Energ. Res. (2015)

7. H. Zheng, J. Yin, Z. Gao, H. Huang, X. Ji, C. Dou, Disruption of chlorella vulgaris cells for the release of biodiesel- producing lipids: a comparison of grinding, ultrasonication, bead milling, enzymatic lysis and microwaves. Appl. Biochem. Biotechnol. **164**, 1215–1224 (2011)
8. M. Onay, C. Sonmez, H. Oktem, M. Yucel, Evaluation of various extraction techniques for efficient lipid recovery from thermo-resistant microalgae, hindakia, scenedesmus and mixractinium species. Am. J. Anal. Chem. **7**, 141–150 (2016)
9. P. Prabakaran, A.D. Ravindaran, A study on effective lipid extraction methods from certain fresh water microalgae. Elixir Int. J. **39**, 4589–4591 (2011)
10. T. Mathimani, L. Uma, D. Prabaharan, Homogeneous acid catalysed transesterification of marine microalga Chlorella sp.BDUG 91771 lipid—an efficient biodiesel yield and its characterization. Renew. Energ. **81**, 523–533 (2015)
11. S.A. Adhoni, C.T. Shivasharana, B. Kaliwal, Identification and characterisation of chlorella vulgaris for biodiesel production. Int. J. Scient. Res. Eng. Stud. **3**(1) (2016)

Chapter 19
Simulation of Three Phase Voltage Source Inverter Based on SVPWM Technique

Shivani Sachan, Shivam Saway and Ankit Singhal

Abstract This paper presents simulation of two level voltage source inverter based on SVPWM (space vector pulse width modulation) technique. The concept of two level inverter is used to reduce the harmonic distortion in output voltage waveform without decreasing the inverter output power. Simulation results are presented to realize the validity of SVPWM technique.

Keywords Voltage source inverter · PWM · SVPWM · LCL filter with series damping resistor

19.1 Introduction

The inverter is used to convert the DC voltage into AC voltage with controlled voltage and frequency. The waveform of the output voltage depends on the switching states of six switches. However there are three major limitations regarding this [1, 2]. The first limitation is the harmonic content in the output of the inverter, second is the switching frequency of the switches and the last one is utilization of the dc link voltage. In general drive system with low harmonic content are better than that with high harmonic content. High switching frequency usually improves the motor current and technique. SVPWM technique leads to recent utilization of parallel three phase consequently the whole performance of the drive system. However, high switching frequency leads to more switching losses in the inverter switches. The best utilization of the DC link voltage depends on the applied switching inverters [3, 4]. The LCL filter with series damping is to limit the harmonics content [5].

S. Sachan (✉) · S. Saway · A. Singhal
Krishna Institute of Engineering and Technology, Ghaziabad, India
e-mail: shivani.1421152@kiet.edu

G. Anand et al. (eds.), *Nanotechnology for Energy and Water*,
Springer Proceedings in Energy, https://doi.org/10.1007/978-3-319-63085-4_19

19.2 Space Vector Pulse Width Modulation

Space vector modulation is an algorithm for the control of pulse width modulation. It is used for creating the alternating current waveform most commonly used to drive three phase AC powered motors at varying speed. Space vector pulse width modulation is provided a constant switching frequency. Therefore the switching frequency can be adjusted easily. Consider the six switches configuration shown in Figs. 19.1 and 19.2. If top switch is on we will use 1 and if bottom switch is on then we will use 0. Therefore we get eight possible switching sequence which are 111, 100, 110, 010, 011, 001, 101, 000 where 111 and 000 are the zero state vectors [6]. The remaining six switching sequence are called active state vectors (the output voltage will not be zero). These switching sequences can be represented in vector form as shown in Fig. 19.2

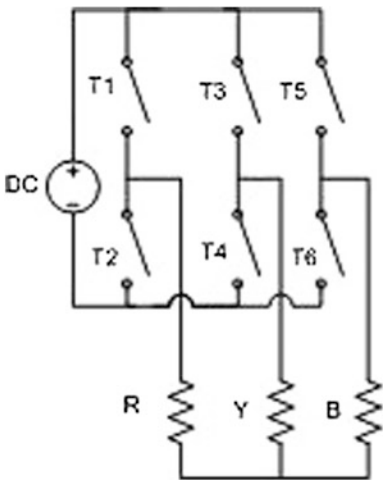

Fig. 19.1 Six switches configuration of two level inverter

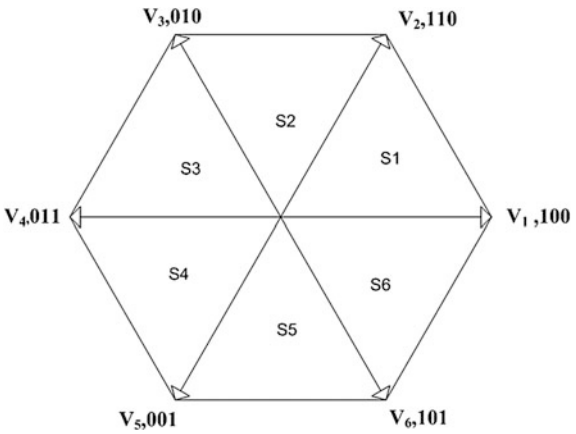

Fig. 19.2 Voltage space vector diagram

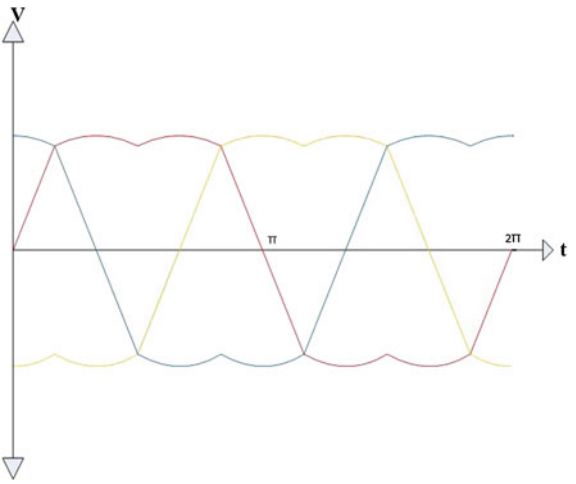

Fig. 19.3 Average voltage variation over whole cycle

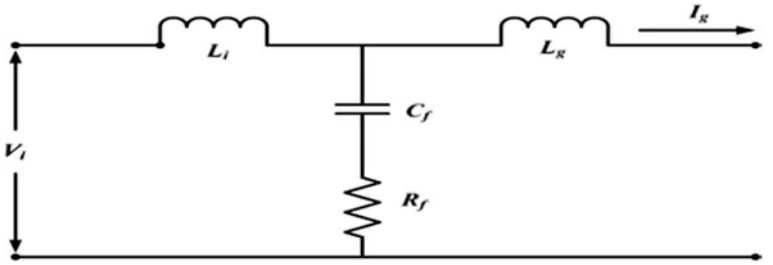

Fig. 19.4 LCL filter with series damping resistance

We get average pole voltage variation in a sector [6]. The average voltage variation shows in Fig. 19.3

19.2.1 LCL Filter with Series Damping Resistance

An *L* filter with high value can be used in order to reduce the current harmonics around the switching frequency.In the case of high voltage applications the dynamic response of *L* filter is poor. Then, *LCL* filter is utilized considering the limit regarding sizing of the components and the losses in the filter. When the impedance of the inductances becomes equal to the impedance of the capacitor appears a resonance frequency. In order to avoid the resonance effects, the increase of the harmonic current and to improve the stability of the voltage/current control a passive damping will be introduced in the filter [7]. This method is done by adding a resistance either in series or parallel to the inductance or capacitance of the *LCL* filter (Fig. 19.4).

When a LCL filter has to be design, some constraints may be considered:

- Capacitor value is limited by tolerable decrease of power factor at rated power, usually is less than 5%.
- The total value of inductance should not more than 10% to limit the AC voltage drop during normal operation.
- The resonance frequency should be in the range between ten times the line frequency and one half of switching frequency to avoid the resonance problems in lower and higher harmonic spectrum.
- Passive damping cannot be too low to avoid oscillations.
- Loses may not be too high to not reduce efficiency (Table 19.1).

19.2.2 Simulation Model

The simulation circuit diagram is presented in this section. The simulation is done using matlab Simulink. The simulation circuit diagram consist of six subsystem, three phase two level inverter with V_{DC} = 725 v, LCL filter with series damping and a star connected load. The Fig. 19.5 shows the simulation circuit diagram.

19.2.2.1 Simulation Results

Simulation results are also presented in this section. Without filter, the total harmonic distortion in the output current of the inverter is 1.79%. After filtration, the total harmonic distortion is 0.36% in the output current and voltage (Figs. 19.6, 19.7 and 19.8).

Table 19.1 Values of parameter for LCL filter

Input side inductance (L_i)	11 Mh
Load side inductance(L_a)	0.26 Mh
Filter capacitance(C_f)	5 μF
Damping resistance(R_f)	2.5 Ω

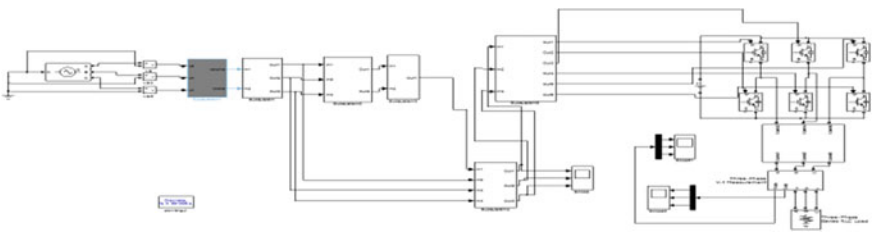

Fig. 19.5 Block diagram of simulation of two level voltage source inverter based on SVPWM technique

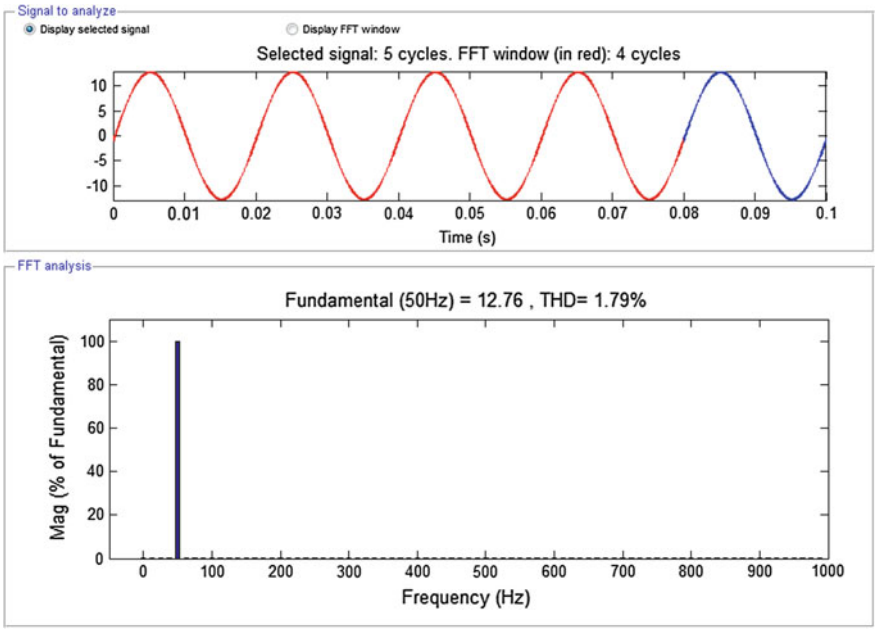

Fig. 19.6 FFT analysis of inverter output current

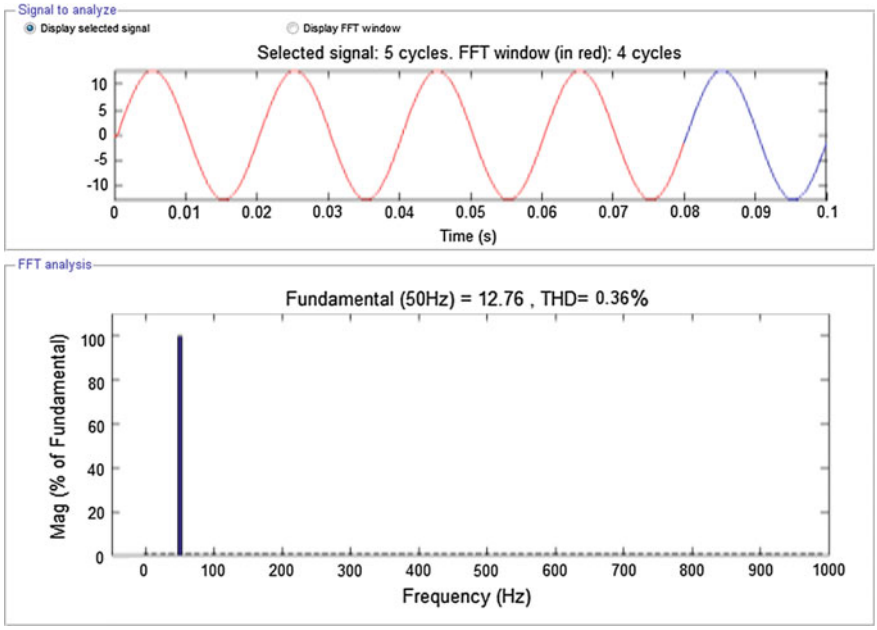

Fig. 19.7 FFT analysis of filter output current

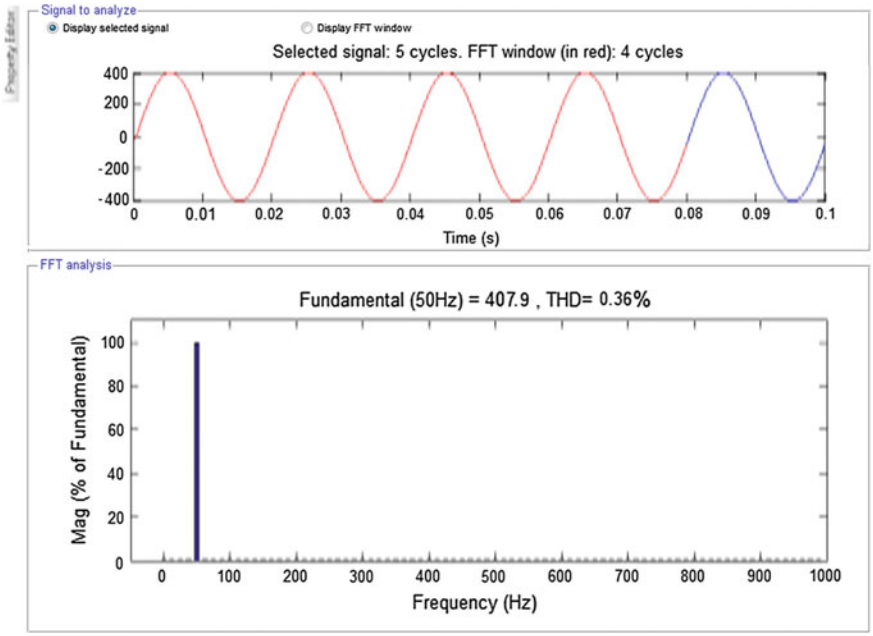

Fig. 19.8 FFT analysis of filter output phase to ground voltage after filter

19.3 Conclusions

Analysis of space vector pulse width modulation and simulation of two level three phase inverter is presented. Experimental results and their FFT analysis are done and attached. Total harmonic distortion is less than 5% as per IEEE standard.

References

1. P. Vas, *Electrical Machines and Drives a Space-Vector Theory Approach* (Oxford University Press, 1992)
2. E. Hendawi, F. Khater, A. Shaltout, Analysis, simulation and implementation of space vector pulse width modulation inverter, in *9th WSEAS International Conference on Application of Electrical Engineering*, pp. 124–131
3. H.R. Pouya, H. Mokhtari, Control of parallel three phase inverter using optimal and SVPWM technique, in *IEEE International conference on industrial Electronics ISIE, Seoul* (2009)
4. B. Hua, Z. Zhengming, M. Shuo, L. Jianzeng, S. Xiaoying, Comparison of three PWM strategies SPWM, SVPWM and one cycle control, in *The Fifth International Conference On Power Electronics and Drive System PEDS*, vol. 2, pp. 1313–1316 (2003)
5. A. Reznik, M.G, LCL filter design and performance analysis for grid interconnected system
6. P. Gopakumar, in http://nptel.ac.in. Accessed Dec 2009. http://nptel.ac.in/courses/108108077/
7. M. Liserre, F. Blaabjerg, R. Toedorescu, Grid impedence estimation via excitation of LCL filter resonance. IEEE Trans. Ind. Appl. 1401–1407 (2007)

Chapter 20
Structural and Optical Properties of $Zn_{1-X}Co_xS$ Nanoparticles Prepared by Solvothermal Technique

Sudesh Sharma, Sanjay Kumar, M.S. Goyat, Charu Pant and P. Mandal

Abstract Structural and Optical properties of wide bandgap $Zn_{1-x}Co_xS$ (x = 0.00, 0.05, 0.10 and 0.15) nanoparticles are reported here. The nanopowders are prepared by simple solvothermal route. The structural and optical properties are studied using X-ray diffraction and UV-Vis absorption spectra measurements. The X-ray diffraction pattern reveals that as-prepared $Zn_{1-x}Co_xS$ nanoparticles are crystallized in predominant cubic zinc blende phase with three prominent diffraction peaks corresponding to (111), (220) and (311) lattice planes. A weak hexagonal wurtzite phase of ZnS is also visible. Optical absorption spectra of ZnS and Co doped ZnS show a slight blue shift in the band gap due to quantum size effect.

Keywords Zinc sulphide · X-ray diffraction · UV-VIs · Co doped nanopowders

20.1 Introduction

In last few years, nanocrystalline ZnS has drawn remarkable attention from research community to explore its potential for optical coatings, optical sensors, photo catalysts, solar cell, light emitting diodes and other optoelectronic devices [1, 2]. ZnS mainly crystallizes in cubic sphalerite structure and hexagonal wurtzite structure. While the

S. Sharma (✉) · M.S. Goyat · P. Mandal (✉)
Department of Physics, University of Petroleum and Energy Studies,
248007 Dehradun, India
e-mail: sudesh@ddn.upes.ac.in

P. Mandal
e-mail: pmandal@ddn.upes.ac.in

S. Kumar
Department of Chemistry, University of Petroleum and Energy Studies,
248007 Dehradun, India

C. Pant
Nanotechnology Lab, University of Petroleum and Energy Studies,
248007 Dehradun, India

G. Anand et al. (eds.), *Nanotechnology for Energy and Water*,
Springer Proceedings in Energy, https://doi.org/10.1007/978-3-319-63085-4_20

cubic phase is stable at low temperature, the wurtzite phase remains metastable below 1020 °C in its bulk form [3]. The bulk band gap of ZnS is reported to be 3.68 eV for cubic structure, and 3.77 eV for hexagonal structure. Room temperature preparation of nanocrystalline ZnS is promising due to attractive structural and optical manipulation. It is also challenging to prepare high optical quality ZnS and transition metal ion doped ZnS nanoparticles through simple solvothermal route [4, 5]. In this work, pure ZnS nanoparticles and transition metal ion (Co) doped ZnS nanoparticles are synthesized using simple solvothermal route below 100 °C.

20.2 Experimental Details

Nanocrystalline powder samples of $Zn_{1-x}Co_xS$ (x = 0.00, 0.05, 0.10 and 0.15) were prepared by solvothermal technique and the details are described below. To prepare undoped ZnS powder, we first dissolved requisite amount of $ZnNO_36H_2O$ in DI water with simultaneous rigorous stirring. Thereafter, Na_2S solution prepared in water was added drop by drop (solution temperature was maintained at 60 °C). The obtained precipitate was then filtered and washed with water. The collected powder was dried at 80 °C for 12 h in an oven. Finally, the dried nanocrystalline ZnS powder was grounded for 20 min in a mortar and pestle. Through similar approach, nanocrystalline Co doped ZnS powder was also prepared by dissolving precalculated amount of $CoNo_3.6H_2O$ in addition to $ZnNO_3.6H_2O$ in DI water (in different proportion of salts to vary x). Phase analysis of the prepared nanopowders were carried out by X-ray diffractometer using Cu K_α radiation (λ = 0.15406 nm). A double beam UV-Vis spectrophotometer was employed to determine the normal absorbance (A) of the nanopowders with in range of wavelength change from 200 to 1200 nm. For absorbance measurements the samples were dispersed in DI water.

20.3 Results and Discussion

Figure 20.1a shows X-ray diffraction patterns of the prepared nanopowder of different compositions. Analysing the diffraction patterns we identified the peaks for ZnS and doped ZnS. The nanocrystalline doped and undoped ZnS crystallized predominantly in cubic zinc blende structure with three main diffraction peaks corresponding to (111), (220) and (311) lattice planes. However, weak signature of hexagonal wurtzite phase is also observed. Presence of hexagonal wurtzite phase at much lower temperature is understandable in terms of nucleation and growth of nano grains in hydrothermal conditions. Formation of stable wurtzite phase along with cubic phase in low temperature atmosphere at nanoscale has been reported previously. [6]. Figure 20.1b shows the photographs of as-prepared nanopowders of $Zn_{1-x}Co_xS$ with varying compositions ranging from x = 0.00–0.15. The variation in colour contrast of the prepared samples suggests the successful incorporation of

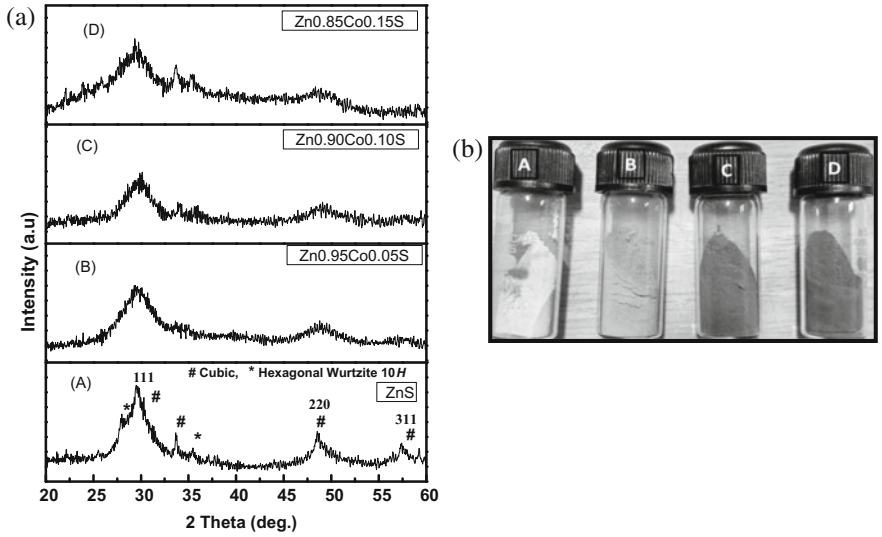

Fig. 20.1 **a** X-ray diffraction spectra of $Zn_{1-x}Co_xS$ nanopowder with varying compositions, x = 0.00 (A), 0.05 (B), 0.10 (C) and 0.15 (D). The corresponding powder samples are as labelled in (**b**)

Co in ZnS matrix. Widely used Scherrer's formula (see Eq. 20.1) was employed to determine the crystallite size of the naopowders, where θ_{hkl} is the Bragg angle that corresponds to the (hkl) reflections and λ is the wavelength of the x-ray. The

$$t = \frac{0.9\lambda}{\mathrm{FWHM}_{hkl} \quad \cos\theta_{hkl}} \tag{20.1}$$

$$\delta = \frac{1}{t^2} \tag{20.2}$$

$FWHM_{hkl}$ is the full width at half maximum of (hkl) plane of nanopowders. In the present case, peak position and broadening of (111) plane of cubic zinc blende was used to estimate the size of nanopowders. The calculated crystallite size was found to be in the range of 2.7–4 nm (Fig. 20.2). As the Co content in ZnS increases from x = 0.00 to 0.15 the peak broadening occurs. The larger $FWHM_{hkl}$ reflects the smaller crystallite size in the sample. Dislocation density (δ), present in nanopowders, was also calculated by using the formula given in Eq. 20.2 [7], where 't' is the crystallite size of the samples. It is found that values of dislocation density increases with increasing Co concentration. The calculated values of crystallite size for different samples are mentioned in Table 20.1 along with the dislocation density.

UV-Vis absorbance spectra were determined for pure and Co doped ZnS nanopowders and shown in Fig. 20.3. Calculation of optical bandgap (E_g) was carried out using equation, $E = hc/\lambda$, where 'c' indicates the velocity of light, 'h'

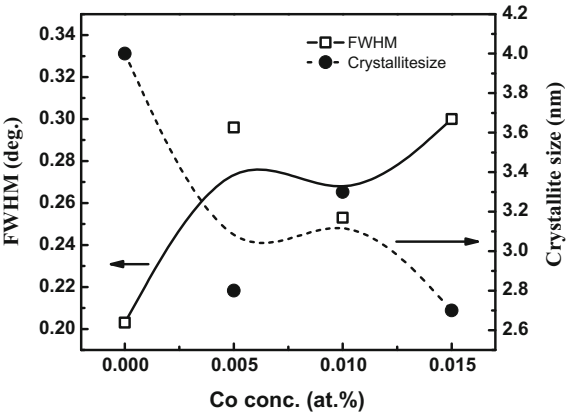

Fig. 20.2 Estimated FWHM and Crystallite size with varying Co concentrations

Table 20.1 variation in FWHM, crystallite size 't' and imperfection density '**δ**' with increasing Co content 'x'

Co conc. 'x'	FWHM (deg.)	Crystallite size 't' (nm)	Imperfection density 'δ' (10^{-2} nm^{-2})
0.00	2.03	4.0	6.25
0.05	2.96	2.8	12.76
0.10	2.53	3.3	9.18
0.15	3.00	2.7	13.72

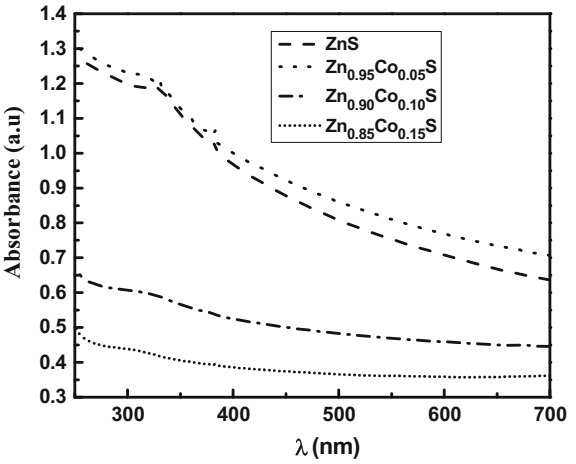

Fig. 20.3 Absorbance spectra of $Zn_{1-x}Co_xS$ with varying compositions, x = 0.00–0.15

refers to Planck constant absorption wavelength is indicated by 'λ'. From the spectra it is observed that as the concentration changes from x = 0.00 to 0.15 the corresponding optical bandgap blue shifts from 3.75 to 4.01 eV. This can be noted that the bulk band gap of ZnS is 3.66 eV which is less compared to band gap values

observed in nanopowders. This increased band gap in the pristine and Co incorporated ZnS can be attributed to the quantum size effect [8–10] for small crystallite size. The reduction in crystallite size as observed in UV-Vis further supports our X-ray diffraction results.

20.4 Conclusions

Nanocrystalline powder samples of $Zn_{1-x}Co_xS$ (x = 0.00–0.15) are prepared via simple solvothermal route to investigate their structural and optical properties. Structural measurement reveals that Co is successfully incorporated in ZnS with predominant cubic zinc blende phase. UV-Vis absorbance spectra show blue shift in band gap due to quantum size effect due to the presence of Co ions in ZnS.

References

1. M. Wang, L. Sun, X. Fu, C. Liao, C. Yan, Synthesis and optical properties ofZnS:Cu(II) nanoparticles. Solid State Commun. **45**, 493–496 (2000)
2. P. Yang, M.D. Lu, D. Yuan Xu, G. Zhou, Photoluminescence properties of ZnS nanoparticles codoped with Pb2+ and Cu2+. Chem. Phys. Lett. **336**(1–2), 76–80 (2001)
3. S.B. Qadri, E.F. Skelton, D. Hsu, A.D. Dinsmore, J. Yang, H.F. Gray, R. Ratna, Size-induced transition-temperature reduction in nanoparticles of ZnS. Phys. Rev. B. **60**, 9191–9193 (1999)
4. X. Fang, T. Zhai, U.K. Gautam, L. Li, L. Wua, Y. Bando, D. Golberg, ZnS nanostructures: from synthesis to applications. Prog. Mater. Sci. **56**, 175–287 (2011)
5. C.S. Tiwary, P. Kumbhakar, A.K. Mondal, A.K. Mitra, Synthesis and enhanced green photoluminescence emission from BCT ZnS nanocrystals. Phys. Status Solidi A **207**, 1874–1879 (2010)
6. F. Huang, J.F. Banfiled, Size-Dependent Phase Transformation Kinetics in Nanocrystalline ZnS. J. Am. Chem. Soc. **127**, 4523–4529 (2005)
7. C.K. De, N.K. Mishra, Indian J. Phys. **71A**, 535 (1997)
8. D. Denzier, M. Olschewski, K. Sattler, Luminescencestudies of localized gap states in colloidal ZnS nanocrystal. J. App. Phys. **84**, 2841–2845 (1998)
9. K. Jayanthi, S. Chawla, H. Chanda, D. Haranath, Structural optical and photoluminescence properties of ZnS: Cu nanoparticles thin films as a function of dopant concentration and quantum confinement effect. Cryst. Res. Technol. **42**, 976–982 (2007)
10. A. Alvaro, A.D. Quiroz, M. Martins, A.W. Demetrio, E.J.F. Soares, Modeling of ZnS quantum dotssynthesis by DFT techniques. J. Mol. Struct. **873**, 121–129 (2008)

Chapter 21
Sustainable Energy Harvesting Using Efficient α-Fe_2O_3 Photoanode Through Photocatalytic Water Splitting Using Facile Chemical Route

Avinash Rokade, Vidhika Sharma, Mohit Prasad and Sandesh Jadkar

Abstract Here, a simple, controlled and cost effective electrodeposition technique was used to synthesize α-Fe_2O_3 hematite photo-electrode for solar water splitting. We have synthesized thin films of α-Fe_2O_3 by varying electrodeposition potential from −0.2 to 0 V at optimum conditions of cycles by using potentiostat. The obtained ferrihydrite thin films were transformed into α-Fe_2O_3 thin films by annealing them at 600 °C for 1 h. Films were investigated by XRD, SEM, UV-Visible and Raman spectroscopy for their structural, optical and morphological properties. Further suitability of α-Fe_2O_3 thin films as a photo-electrode has been evaluated by photoelectrochemical (PEC) measurements which exhibited photocurrent density of 65 μA/cm^2 at 0.5 V versus SCE under AM 1.5 100 mW/cm^2 illumination. The effective enhancement in photocurrent conversion efficiency with optimum film thickness has been observed upon light irradiation. The absorption spectrum of the α-Fe_2O_3 shows significant absorption in the visible region. However, photo-conversion efficiency is quite low. The obtained results suggest that the well controlled thick α-Fe_2O_3 material can be utilized as a shell layer with wide band gap nano-structured semiconductor like ZnO, TiO_2 to form hetero-structure for solar water splitting application.

Keywords α-Fe_2O_3 · Photoelectrochemical · XRD · SEM · UV-Visible spectroscopy · Raman spectroscopy

A. Rokade
School of Energy Studies, Savitribai Phule Pune University, Pune 411 007, India

V. Sharma · M. Prasad · S. Jadkar (✉)
Department of Physics, Savitribai Phule Pune University, Pune 411 007, India
e-mail: sandesh@physics.unipune.ac.in

G. Anand et al. (eds.), *Nanotechnology for Energy and Water*,
Springer Proceedings in Energy, https://doi.org/10.1007/978-3-319-63085-4_21

21.1 Introduction

Semiconductor photocatalyst is one of the most promising technologies for conversion of solar energy into hydrogen via water-splitting process for the future fuel is a viable alternative to fossil fuels because large quantity of hydrogen can potentially be generated in a clean and sustainable manner [1]. Fujishima and Honda in 1972 demonstrated the phenomenon of photocatalysis using single crystal TiO_2 as a working electrode [2]. Iron oxide (α-Fe_2O_3) is an important semiconductor which has recently attracted the attention for production of hydrogen via water splitting. It has the ability to absorb a large part of solar spectrum due to its favorable band gap (2.0–2.2 eV) [3, 4]. It is also inexpensive, plentiful, readily available, non toxic, chemically stable in aqueous environment and has good environmental acceptability [5, 6] which favors the fundamental and practical research for its applications in many fields such as Li-ion batteries [7, 8], supercapacitors [9], peroxide sensor [10], solar energy conversion via water splitting [11], dye degradation [12], water purification and treatment [13, 14]. Thus, study of α-Fe_2O_3 thin films for photocatalytic water splitting is a important topic of research in production of hydrogen fuel. The maximum theoretical solar-to-hydrogen (STH) conversion efficiency at standard solar illumination conditions for α-Fe_2O_3 was found $\sim$15% [15, 16].

The α-Fe_2O_3 thin films can be prepared by various methods such as chemical vapor deposition [17], sol-gel process [18], pulsed laser evaporation [19], reactive sputtering [20], hydrothermal technique [15, 21], spray pyrolysis [22, 23] etc. However, for preparation of hematite α-Fe_2O_3 thin films there are certain challenges which need to be overcome such as non-optimal conduction band edge alignment for hydrogen evolution potential and indirect band gap causing low absorption of light. Also it possesses short carrier diffusion length in the range of 2–4 nm [24], 20 nm [25] giving low transport and low conductivity of photo generated carriers [11, 26]. The short diffusion length of holes can be overcome by synthesis of extremely thin films of hematite α-Fe_2O_3 material by controlled deposition technique. With this motivation an attempt has been made to prepare α-Fe_2O_3 thin films of well-defined thickness by simple electrochemical deposition technique. This technique consists of three electrode system with FTO coated glass working substrate, platinum counter electrode and SCE as the reference electrode. In this study we have tried to use thin films of α-Fe_2O_3 as working electrode by controlling thickness of deposition layers using cyclic voltammetry.

21.2 Experimental

The potentiostatic electrochemical deposition were performed by an Metrohm Autolab potentiostat PGSTAT302 N model in three-electrode cell configuration system controlled by a personal computer (PC), working electrode (FTO glass

substrate), reference electrode (SCE) and counter electrode (Pt). The FTO coated glass substrate were ultrasonically cleaned before starting the deposition using acetone, ethanol and distilled water for 5 min each. The chemical solution were prepared using aqueous electrolyte of 0.05 M Ferric Chloride ($FeCl_3$), 0.05 M Potassium Fluoride (KF), 0.1 M Potassium Chloride (KCl) and 1 M Hydrogen Peroxide (H_2O_2). The films of Fe_2O_3 are electrochemically synthesized by 30 deposition cycles from −0.2 to 0 V (scan rate 20 mV/S) at room temperature. The obtained ferrihydrite thin films were transformed into α-Fe_2O_3 thin films by annealing at 600 °C in ambient atmosphere for 1 h. The surface morphology of the films was analysed using a JEOL JSM-6360A scanning electron microscope (SEM) with operating voltage 20 kV. The optical band gap of the films was calculated from absorption spectra and was measured in the range of 200–800 nm using a JASCO, V-670 UV-Visible spectrophotometer. Rein-shaw Raman spectrometer was used to record raman spectra in the range of 100–800 cm^{-1}. Raman spectrum was detected using the spectrometer having backscattering geometry with the resolution of 1 cm^{-1}. The He–Ne laser of 632.8 nm line was used as the excitation source at room temperature. To avoid laser induced crystallization the power of the Raman laser was kept less than 5 mW. X-ray diffractometer (Bruker D8 Advance, Germany) using CuKα line (λ = 1.54 Å) was used to obtain the x-ray diffraction patterns. The photoelectrochemical measurements with a potentiostat (AUTOLAB N302) were carried out in a three electrode configuration by employing a platinum foil as the counter, SCE as the reference and α-Fe_2O_3 as working electrode. The 1 M NaOH was used as an aqueous electrolyte. The Electrochemical Impedance Spectra (EIS) measurement was recorded under illumination and darkness.

21.3 Results and Discussion

21.3.1 Structural and Phase Analysis

The structure and phase of the films was analyzed using x-ray diffraction (XRD) and Raman spectroscopy. Figure 21.1a shows the XRD pattern of the α-Fe_2O_3 thin film. The presence of multiple numbers of peaks in XRD pattern suggests the polycrystalline nature of α-Fe_2O_3 film. As seen from the figure main diffraction peaks were observed at $2\theta \sim 24.2^o$, 33.2^o, 35.5^o, 54.5^o, 61.5^o and 64.1^o corresponding to (012), (104), (110), (116), (213) and (300) crystal orientations respectively [27, 28]. These peaks are in agreement with JCPDS data file # 33-0664 of α-Fe_2O_3 with hexagonal crystal structure. The * indicates the diffraction peaks obtained from FTO glass substrate. The lattice parameters are calculated from peaks a = 5.03 Å and c = 13.7 Å, which are in agreement with standard reported values

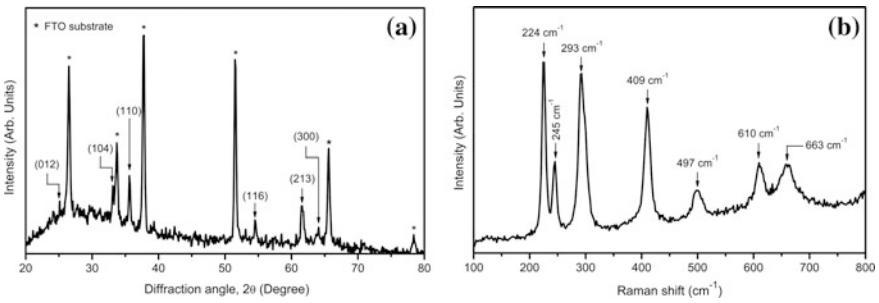

Fig. 21.1 **a** XRD pattern and **b** Raman spectra of α-Fe_2O_3 thin films electrodeposited on FTO substrate

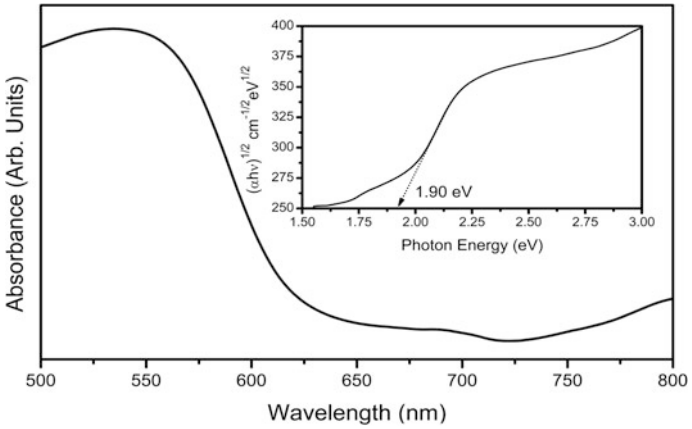

Fig. 21.2 UV-Visible absorbance spectra of α-Fe_2O_3 thin film. Inset shows Tauc's plot of α-Fe_2O_3 thin film used for estimation of band gap of α-Fe_2O_3 thin film

for α-Fe_2O_3 crystal structure. The crystallite domain size calculation was performed for the major diffraction peak (200) using the Scherrer's formula,

$$d_{x-ray} = \frac{0.9\,\lambda}{\beta \cos\theta_\beta} \tag{21.1}$$

where λ is the wavelength of the x-ray used, β is full-width at half-maximum (FWHM) and θ_β is the Bragg diffraction angle. The estimated average grain size using Scherrer's formula was found to be ~29 nm (Fig. 21.1a).

Raman spectroscopy is a powerful characterization tool to investigate molecular, vibration and chemical structure by interacting laser light with the sample. It is a non-destructive technique that offers a fast and simple way to determine the phase of the film. Figure 21.1b shows the Raman spectra of α-Fe_2O_3 thin film in the range 100–800 cm^{-1} deposited for 30 electrochemical cycles. As shown in figure major

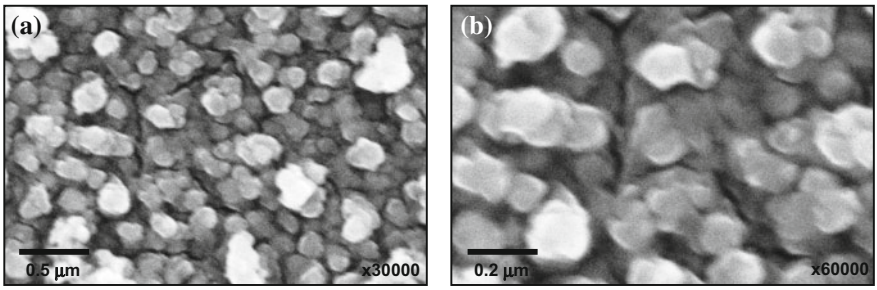

Fig. 21.3 Scanning electron microscopy images of electrodeposited α-Fe_2O_3 on FTO substrate at two different magnifications **a** At 30,000 and **b** At 60,000

Raman peaks were observed at ~224, 245, 293, 409, 497, 610 and 663 cm^{-1}. The Raman peaks located at ~224 and ~497 cm^{-1} corresponds to the A_1g mode whereas other peaks located at ~245, ~293, ~410, ~610 and 663 cm^{-1} corresponds to Eg mode of α-Fe_2O_3 [27, 28]. No other peaks were observed in the Raman spectra suggesting the formation of pure phase of α-Fe_2O_3.

21.3.2 Optical Analysis

In order to reveal the optical properties of the α-Fe_2O_3 thin films, UV-Visible spectroscopy has been used. Figure 21.2 shows the UV-Visible absorption spectra of α-Fe_2O_3 synthesized by electrodeposition. As seen the α-Fe_2O_3 exhibits a strong excitonic absorption around ~620 nm. Tauc relation was used to calculate the optical band gap (E_{opt}) of the electrodeposited α-Fe_2O_3 film [29],

$$(\alpha E)^{1/2} = B^{1/2}(E - E_{opt}) \tag{21.2}$$

where α is the absorption coefficient, B is the optical density of state and E is the photon energy. The optical band can be then calculated from a linear fit of the $(h\nu)^{1/2}$ versus hν plot (Tauc plot) [29]. Inset of Fig. 21.2 shows typical Tauc plot for the α-Fe_2O_3 thin film. The estimated value of optical band gap was found to be ~1.9 eV.

21.3.3 Surface Morphological Analysis

Scanning electron microscopy (SEM) was used to investigate the surface morphology of α-Fe_2O_3 thin film. Figure 21.3a, b show typical SEM micrographs of α-Fe_2O_3 thin film taken at two different magnifications. The surface of the films

shows granular morphology with uniform and dense growth of α-Fe_2O_3 on the FTO surface without having defects such as cracks, pinholes, and protrusion. The compositional analysis of the α-Fe_2O_3 thin film was carried out using energy dispersive x-ray analysis (EDAX) technique and found that Fe and O are approximately in the ratio of 2:3.

21.3.4 Photoelectrochemical (PEC) Measurements

The grown α-Fe_2O_3 thin films were used as working electrode (WE) in PEC cell. Electrochemical cell was used to conduct PEC performance, which was fitted with a water jacket around it, to prevent heating. Placed inside the cell were three electrodes; α-Fe_2O_3 thin film working electrode (WE), platinum foil counter electrode (CE), and saturated calomel reference electrode (SCE). 1 M NaOH was used as an aqueous electrolyte. Metrohm Autolab Potentiostat (PGSTAT302 N) and 150 W Xenon Lamp (PEC-L01) with 100 mW/cm^2 (AM 1.5) illumination intensity were used to record J-V characteristics, both under darkness and illumination.

To study the PEC performance of the synthesized α-Fe_2O_3 photoelectrodes we have performed electrochemical impedance spectroscopy (EIS) in a frequency range varying from 0.1 Hz to 100 kHz at a bias of 0 V versus SCE under UV-Visible light irradiation. The Nyquist diagram of EIS data is an effectual way to measure the electron transfer resistance. The arc radius in the Nyquist plot is directly related to electron transfer resistance reflecting energy barrier of the electrode reaction [30]. Figure 21.4a shows the EIS measurements using the Nyquist plot. The minimum of arc radius (∼25 Ω) shown in Fig. 21.4a reveals that there is large reduction in interfacial resistance between semiconductor and electrolyte due to the absorption of light and separation of electron-hole pairs away from interface. The photoelectrochemical (PEC) performance shown in Fig. 21.4b also supports this. The incident photon creates electron-hole pair when absorbed within photo electrode due to ejection of an electron from the valence band into the conduction

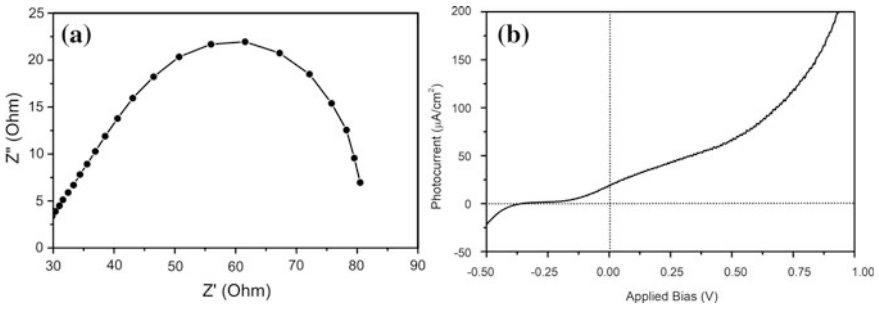

Fig. 21.4 **a** EIS Nyquist plot and **b** Photoelectrochemical (PEC) performance of α-Fe_2O_3 thin films electrodeposited on FTO substrate

band, leaving behind a hole in the valence band. The electron reduces the absorbed H^+ to produce H_2 and the hole oxidizes the OH^- ions to form stable OH [31]. In α-Fe_2O_3 it is difficult to separate photogenerated carriers due to the recombination loss and low diffusion length of charge carriers. However, in the present study an attempt has been made to obtain high photocurrent density with optimum film thickness. An excellent PEC performance for water splitting with higher photocurrent density ∼65 μA/cm^2 at 0.5 V versus SCE under 100 mW/cm^2 illumination has been obtained.

21.4 Conclusions

In summary, hematite (α-Fe_2O_3) thin films photo-electrode were synthesized using a simple, controlled and cost effective electrodeposition technique for solar water splitting. Films were investigated using XRD, SEM, UV-Visible and Raman spectroscopy for their structural, optical and morphological properties. Further suitability of α-Fe_2O_3 thin films as a photo-electrode has been evaluated by photoelectrochemical (PEC) measurements with photocurrent density of 65 μA/cm^2 at 0.5 V versus SCE under AM 1.5 100 mW/cm^2 illumination. The absorption spectrum of α-Fe_2O_3 shows significant absorption in the visible region. However, photo-conversion efficiency is quite low. The obtained results suggest that a well controlled thick α-Fe_2O_3 material can be use as a shell layer with wide band gap nano-structured semiconductor like ZnO, TiO_2 to form hetero-structure for solar water splitting application. The effective enhancement in photocurrent conversion efficiency with optimum film thickness has been observed upon light irradiation.

References

1. J. Nowotny, C. Sorrell, L. Sheppard, T. Bak, Solar-hydrogen: environmentally safe fuel for the future. Int. J. Hydrogen Energy **30**(5), 521–544 (2005), doi:10.1016/j.ijhydene.2004.06.012
2. A. Fujishima, Electrochemical photolysis of water at a semiconductor electrode. Nature **238**, 37–38 (1972). doi:10.1038/238037a0
3. A. Kay, I. Cesar, M. Gratzel, New benchmark for water photooxidation by nanostructured -Fe2O3 films. J. Am. Chem. Soc. **128**(49), 15714–15721 (2006). doi:10.1021/ja064380l
4. F.L. Souza, K.P. Lopes, E. Longo, E.R. Leite, The influence of the film thickness of nanostructured -Fe2O3 on water photooxidation. Phys. Chem. Chem. Phys. **11**(8), 1215–1219 (2009). doi:10.1039/B811946E
5. J.H. Park, S. Kim, A.J. Bard, Novel carbon-doped TiO_2 nanotube arrays with high aspect ratios for efficient solar water splitting. Nano Lett. **6**(1), 24–28 (2006). doi:10.1021/nl051807y
6. D.K. Zhong, M. Cornuz, K. Sivula, M. Gratzel, D.R. Gamelin, Photo-assisted electrodeposition of cobalt- phosphate (Co-Pi) catalyst on hematite photoanodes for solar water oxidation. Energy Environ Sci **4**(5), 1759–1764 (2011), doi:10.1039/C1EE01034D

7. M. Chen, W. Li, X. Shen, G. Diao, Fabrication of core-shell α-fe_2o_3@ $Li_4Ti_5O_{12}$ composite and its application in the lithium ion batteries. ACS Appl. Mater. Interfaces. **6**(6), 4514–4523 (2014). doi:10.1021/am500294m
8. X. Zhu, Y. Zhu, S. Murali, M.D. Stoller, Nanostructured reduced graphene oxide/Fe_2O_3 composite as a high-performance anode material for lithium ion batteries. ACS Nano **5**(4), 3333–3338 (2011). doi:10.1021/nn200493r
9. Shao X. Zhao, Y. Zhang, X. Qian, Fe_2O_3/reduced graphene oxide/Fe_2O_3 composite in situ grown on Fe foil for high-performance supercapacitors. ACS Appl. Mater. Interfaces **8**(44), 30133–30142 (2016). doi:10.1021/acsami.6b09594
10. S. Jana, A. Mondal, Fabrication of SnO_2/α-Fe_2O_3, SnO_2/ α-Fe_2O_3-PB heterostructure thin films: Enhanced photodegradation and peroxide sensing. ACS Appl. Mater. Interfaces. **6**(18), 15832–15840 (2014). doi:10.1021/am5030879
11. J. Krysa, M. Zlamala, S. Kmentb, Z. Hubickab, Photo-electrochemical properties of wo3 and α-Fe2O3 thin films. Chem. Eng. Trans., 41 (2014) doi:10.3303/CET1441064
12. M. Niu, F. Huang, L. Cui, P. Huang, Y. Yu, Y. Wang, Hydrothermal synthesis, structural characteristics, and enhanced photocatalysis of sno_2/α-Fe_2O_3 semiconductor nanoheterostructures. ACS Nano **4**(2), 681–688 (2010). doi:10.1021/nn901119a
13. Z. Wei, R. Xing, X. Zhang, S. Liu, H. Yu, P. Li, Facile template-free fabrication of hollow nestlike α-Fe_2O_3 nanostructures for water treatment. ACS Appl. Mater. Interfaces. **5**(3), 598–604 (2012). doi:10.1021/am301950k
14. L.S. Zhong, J.S. Hu, H.P. Liang, W.G. Song, L.J. Wan, Self-assembled 3D flowerlike iron oxide nanostructures and their application in water treatment. Adv. Mater. **18**(18), 2426–2431 (2006). doi:10.1002/adma.200600504
15. K. Sivula, F.L. Formal, M. Gratzel, Solar water splitting: progress using hematite (α-Fe_2O_3) photoelec-trodes. Chem Sus Chem **4**(4), 432–449 (2011). doi:10.1002/cssc.201000416
16. A. Murphy, P. Barnes, L. Randeniya, I. Plumb, I. Grey, M. Horne, Efficiency of solar water splitting using semiconductor electrodes. Int. J. Hydrogen Energy **31**(14), 1999–2017 (2006). doi:10.1016/j.ijhydene.2006.01.014
17. A. Chai, J. Peng, B. Yan, Characterization of α-Fe_2O_3 thin films deposited by atmospheric pressure CVD onto alumina substrates. Sensors and Actuators B: Chemical **34**(1-3), 412–416 (1996). doi:10.1016/S0925-4005(97)80014-7
18. Y. Zhu, Y. Qian, M. Zhang, Z. Chen, D. Xu, L. Yang, Preparation and characterization of nanocrystalline powders of cuprous oxide by using ϒ-radiation. Mater. Res. Bull. **29**(4), 377–383 (1994). doi:10.1016/0025-5408(94)90070-1
19. S. Joshi, R. Nawathey, V. Koinkar, V. Godbole, S. Chaudhari, S. Ogale, S. Date, Pulsed laser deposition of iron oxide and ferrite films. J. Appl. Phys. **64**(10), 5647–5649 (1988). doi:10.1063/1.342258
20. S. Wilhelm, K. Yun, L. Ballenger, N. Hackerman, Semiconductor properties of iron oxide electrodes. J. Electrochem. Soc. **126**(3), 419–424 (1979). doi:10.1149/1.2129055
21. Q. Chen, Y. Qian, H. Qian, Z. Chen, W. Wu, Y. Zhang, Preparation and characterization of iron (iii) oxide (α-Fe_2O_3) thin films hydrothermally. Mater. Res. Bull. **30**(4), 443–446 (1995). doi:10.1016/0025-5408(95)00028-3
22. Y. Xie, W. Wang, Y. Qian, L. Yang, Z. Chen, Deposition and microstructural characterization of NiO thin films by a spray pyrolysis method. J. Cryst. Growth **167**(3-4), 656–659 (1996). doi:10.1016/0022-0248(96)00285-0
23. M. Mahadik, S. Shinde, V. Mohite, S. Kumbhar, A. Moholkar, J. Kim, C. Bhosale, Photoelectrocatalytic oxidation of rhodamine B with sprayed α-Fe_2O_3 photocatalyst. Mater. Express **3**(3), 247–255 (2013). doi:10.1166/mex.2013.1120
24. M.P. Dare-Edwards, J.B. Goodenough, A. Hamnett, P.R. Trevellick, Electrochemistry and photoelectro-chemistry of iron (III) oxide. J. Chem. Soc., Faraday Trans. 1 79/9:2027–2041 (1983) doi:10.1039/F19837902027
25. J.H. Kennedy, K.W. Frese, Photooxidation of water at α-Fe_2O_3 electrodes. J. Electrochem. Soc. **125**(5), 709–714 (1978). doi:10.1149/1.2131532

26. J. Krysa, M. Zlamal, S. Kment, M. Brunclikova, Z. Hubicka, TiO_2 and Fe_2O_3 films for photoelectrochemical water splitting. Molecules **20**(1), 1046–1058 (2015). doi:10.3390/molecules20011046
27. Q. Wei, Z. Zhang, Z. Li, Q. Zhou, Y. Zhu, Enhanced photocatalytic activity of porous α-Fe_2O_3 films prepared by rapid thermal oxidation. J. Phys. D Appl. Phys. **41**(20), 202002 (2008). doi:10.1088/0022-3727/41/20/202002
28. X. Hu, J.C. Yu, J. Gong, Fast production of self-assembled hierarchical α-Fe_2O_3 nanoarchitectures. J Phys Chem C **111**(30), 11180–11185 (2007). doi:10.1021/jp073073e
29. J. Tauc, A. Menth, States in the gap. J. Non-Cryst. Solids **8**, 569–585 (1972). doi:10.1016/0022-3093/72:90194-9
30. A. Mayabadi, A. Pawbake, S. Rondiya, A. Rokade, R. Waykar, A. Jadhavar, A. Date, V. Sharma, M. Prasad, H. Pathan, S. Jadkar, Synthesis, characterization, and photovoltaic properties of TiO_2/CdTe core-shell heterostructure for semiconductor-sensitized solar cells (SSSCs). J Solid State Electrochem, 1–12 (2016), doi:10.1007/s10008-016-3473-3
31. M.M. Ba-Abbad, M.S. Takri, A. Benamor, A.W. Mohammad, Size and shape controlled of α-Fe_2O_3 nanoparticles prepared via sol-gel technique and their photocatalytic activity. J Sol-Gel Sci. Technol **81**(3), 880–893 (2016). doi:10.1007/s10971-016-4228-4

Chapter 22
SVPWM Based Inverter Design for Synchronization of Renewable Energy with Grid

Shivam Saway, Shivani Sachan and Ankit Singhal

Abstract This paper aims to Synchronize the three phase Space vector pulse width modulated inverter with the AC grid. Phase, frequency and amplitude of the AC grid is tracked using the synchronous rotating frame phase locked loop while of inverter are controlled using PI controller. The primary application of the proposed synchronization method is for the distributive generation with renewable energy resources in which power converter plays an integral role.

Keywords SVPWM · Synchronous rotating frame phase locked loop · Proportional integral current controller · LCL filter with series damping resistance

22.1 Introduction

In the last few years renewable energy have experienced one of the largest growth areas in percentage of over 30% per year, compared with the growth of coal and lignite energy. The goal of European community is to reach 20% in 2020, but EU-27 energy is only 17% of the world energy. In fact countries like China and India requires continuously more energy (china energy share has increased 1 point every year from 2000). Even India has uplifted its goal to 175GW of energy form renewable energy resources by 2022. This paper presents a method to interconnect the renewable energy sources generation with our conventional AC grid. Synchronous rotating frame phase locked loop are used to track the phases angle of the AC grid [1, 2] and proportional integral current controller is used to and sync the renewable energy resource generation with AC Grid [3]. SVPWM is used to

S. Saway (✉) · S. Sachan · A. Singhal
Krishna Institute of Engineering and Technology, Ghaziabad, India
e-mail: Shivam.1421148@kiet.edu

G. Anand et al. (eds.), *Nanotechnology for Energy and Water*,
Springer Proceedings in Energy, https://doi.org/10.1007/978-3-319-63085-4_22

control the output voltage [4] of the inverter of renewable energy generation. A LCL filter with series damping is used to limit the harmonics content of current injected into the AC Grid [5, 6].

22.2 Two-Dimensional Model

The block diagram of the proposed model is shown in Fig. 22.1. The grid voltage angles have been tracked by using the Synchronous rotating frame Phase locked loop. The control strategy is in the Synchronous Reference Frame. The Synchronous reference control can also be called as the dq control. The three phase AC variables are converted to DC variables to work in dq Frame. This is done to achieve the control of variables easily. The active and Reactive power are obtained to set the reference for the active and reactive current controller. The current controller here used are the Proportional Intergral current controller because of its satisfactory performance while working with the DC variables. Proportional integral current controller is used for the current error compensation. Synchronous rotating frame Phase locked loop is used to Synchronize the system with the phase angle of the grid. It is also used to observe the grid conditions to comply with the grid codes.

22.2.1 Power Block

The power block in the proposed model uses the active and reactive power from the grid and generates the reference active and reactive current for obtaining the

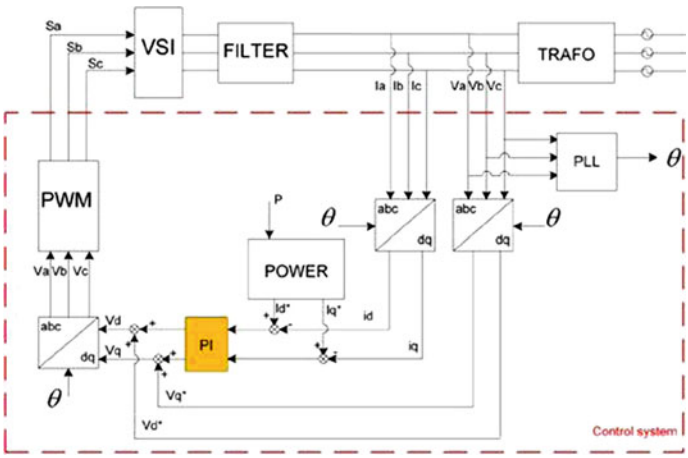

Fig. 22.1 Block diagram of proposed model

required reference signal for the Pulse Width modulation. The concept of power invariance has been employed to generate reference active and reactive current.

22.2.2 PWM Block

The PWM block uses the reference signals as the input and Generates the gate pulses for the six switches of the voltage source Inverter. The gate pulses in this model has been generated by employing the Space Vector Pulse Width Modulation Technique.

22.2.2.1 Space Vector Pulse Width Modulation

The conceptual scheme behind Space Vector Pulse Width Modulation Technique is that if the reference voltage space vector is rotated in space at a very high frequency then the periphery obtained will be close to circle. Hence, the wavefrom obtained from it will be close to sinusoidal waveform. In space vector pulse width modulation there are eight states of voltage space vector out of which six are the active states and the other two are the zero states. The vector corresponding to the active states and zero states are called active vector and zero vector respectively [4]. The voltage space vectors are shown in Fig. 22.2. The average voltage variation in the Space Vector Pulse Width Modulation Technique is shown below in Fig. 22.3.

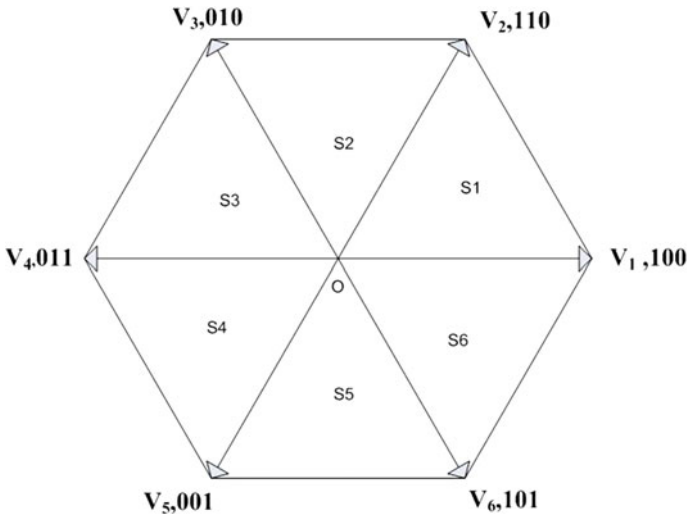

Fig. 22.2 Voltage space vector diagram

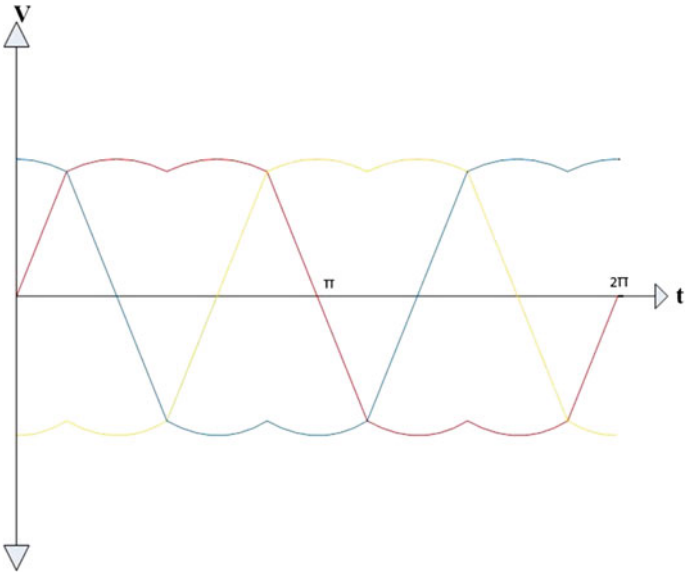

Fig. 22.3 Average voltage variation

22.2.3 Simulation

The simulation of the proposed model is done using matlab Simulink 2009b. The DC link voltage is 725 V and the load is of 5 kW with resistive nature. The grid has been represented by three phase sinosuidal voltage source at 50 Hz of frequency of amplitude of phase to phase voltage equal to 400 V.

22.2.4 Simulation Results

The simulation results are presented in this section. Figure 22.4 shows the simulink model of the proposed design and Fig. 22.5 shows the Synchronous rotating frame Phase locked loop output. Figure 22.6 shows the FFT analysis of the inverter output current with total harmonic distortion of 2.02%. Figure 22.7 FFT analysis of filter output current with total harmonic distortion of 0.87%. Figures 22.6, 22.8 and 22.9 shows the Power generated from renewable energy and sharing of Power between load and Grid respectively. The results are shown for both ideal and non ideal grid condition. To show the non ideal grid condition results the variation in grid voltage amplitude and frequency are done. Figures 22.10 and 22.11 shows the non ideal grid condition results.

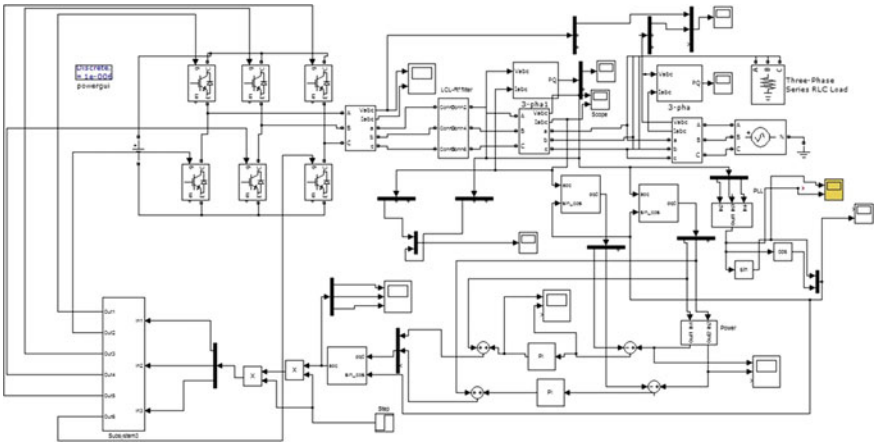

Fig. 22.4 Matlab simulink model of proposed design

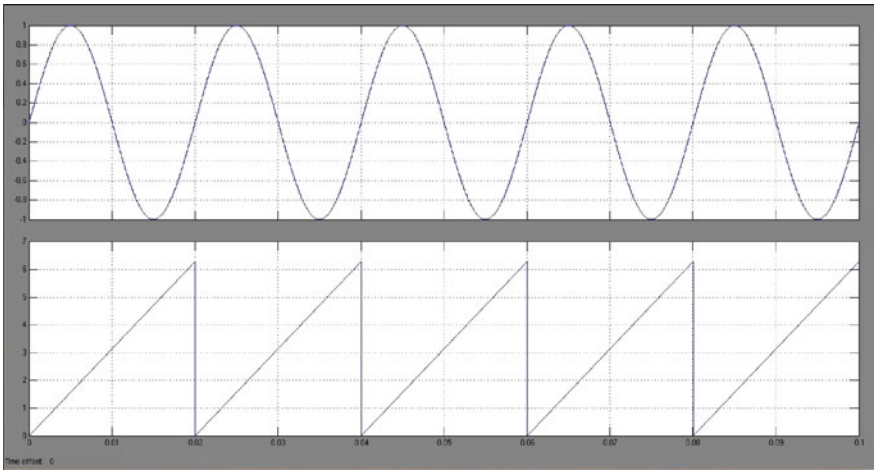

Fig. 22.5 Phase locked loop output

22.2.4.1 Simulation Results for Ideal Grid Condition

In this section the Simulation results are shown for the ideal grid condition. In ideal grid condition no variation in the grid voltage amplitude and frequency are done.

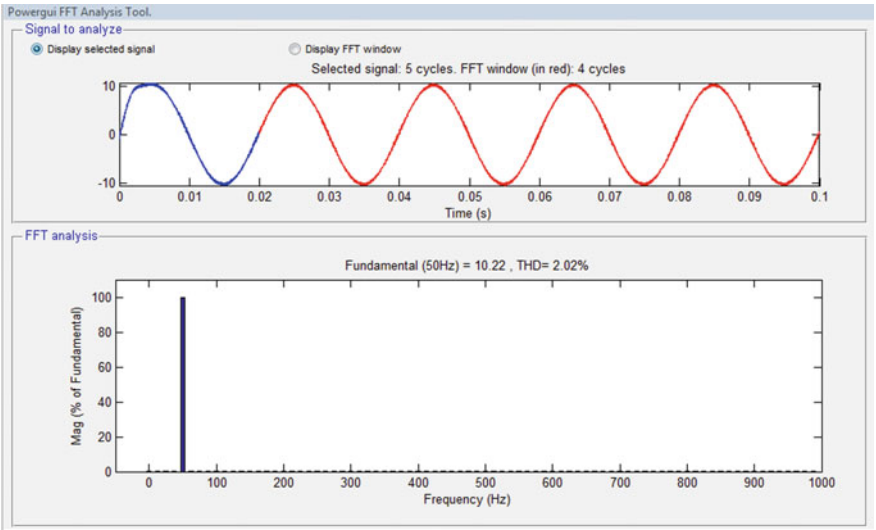

Fig. 22.6 FFT analysis of filter input current

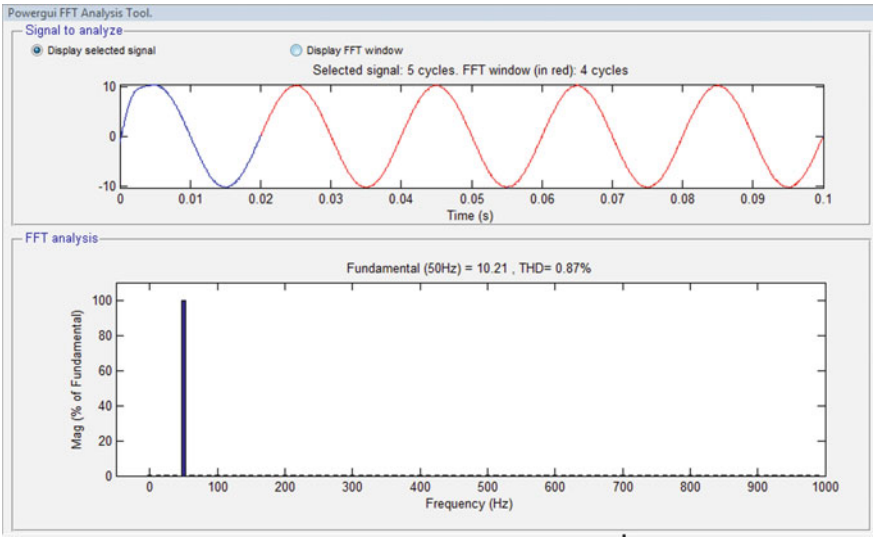

Fig. 22.7 FFT analysis of filter output current

22.2.4.2 Simulation Results for Non Ideal Grid Conditions

In this section the simulation results for non ideal grid condition are shown. 10% variation is done in the voltage amplitude and 5% variation in frequency is done.

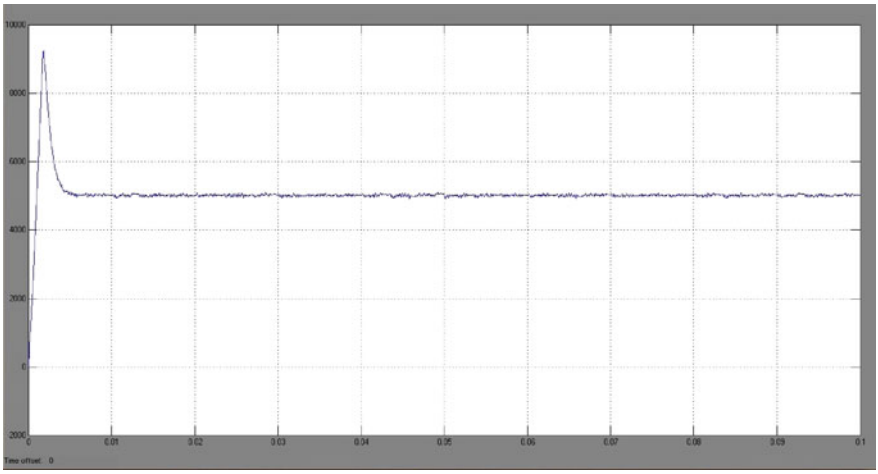

Fig. 22.8 Active power fed from inverter to the grid

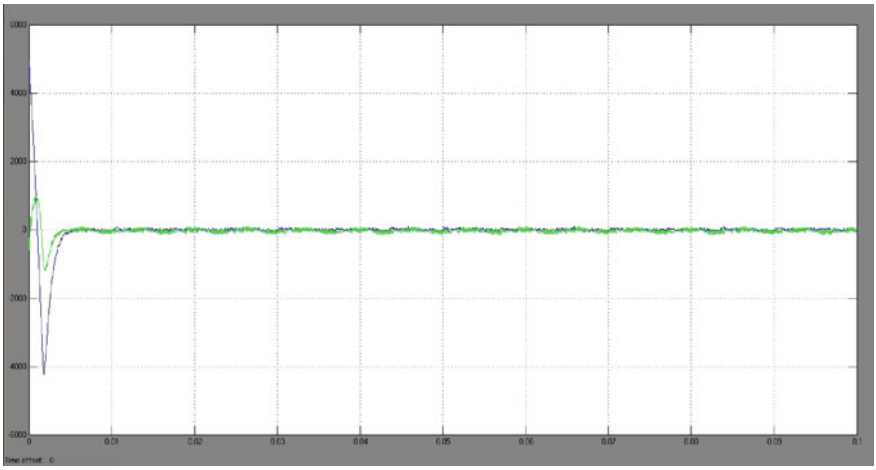

Fig. 22.9 Power sharing between load and grid

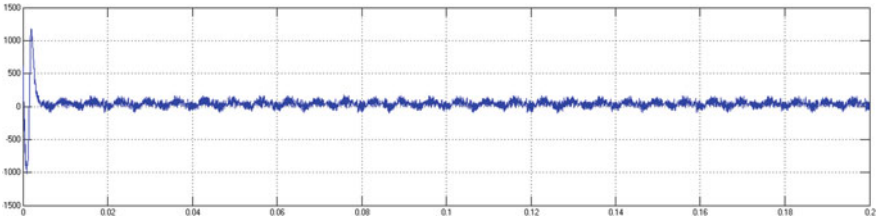

Fig. 22.10 Reactive power fed into the grid

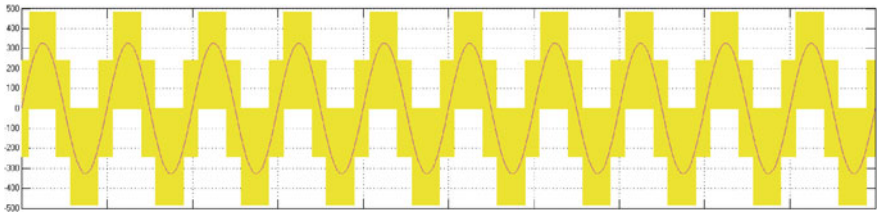

Fig. 22.11 Phase to phase inverter output voltage (*Yellow*) and grid voltage (*Red*) is synchronized

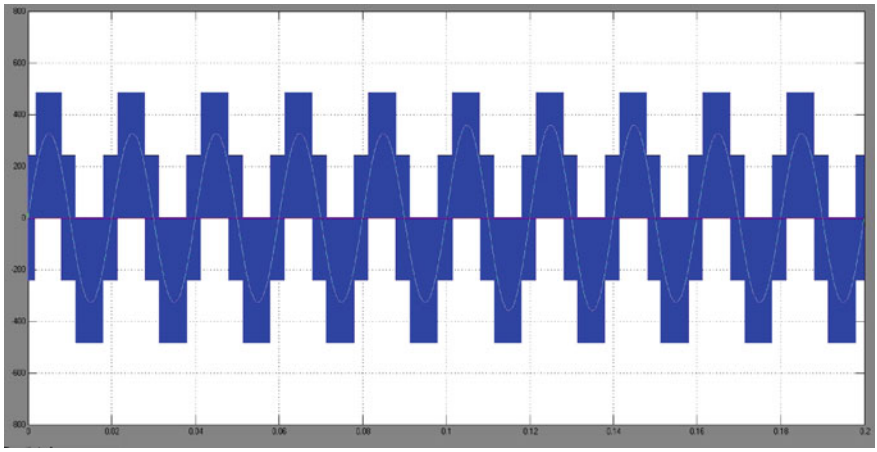

Fig. 22.12 Showing grid synchronization of inverter with 10% of voltage amplitude variation in grid

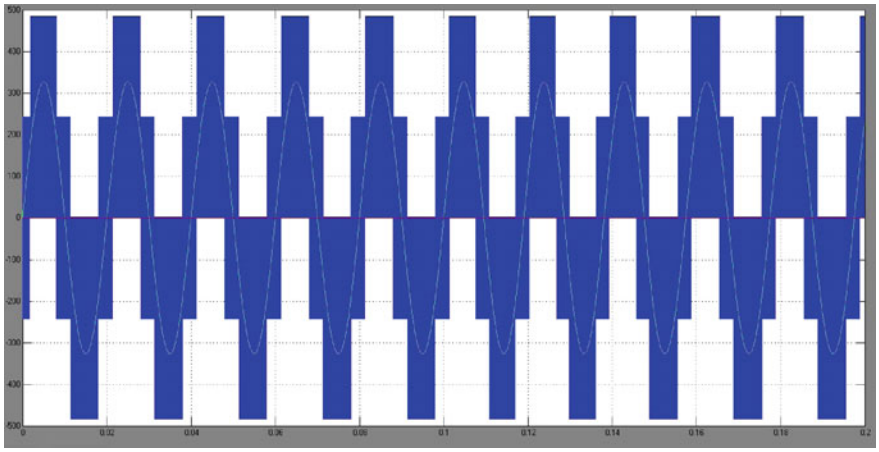

Fig. 22.13 Showing grid synchronization of inverter with 5% variation in grid frequency

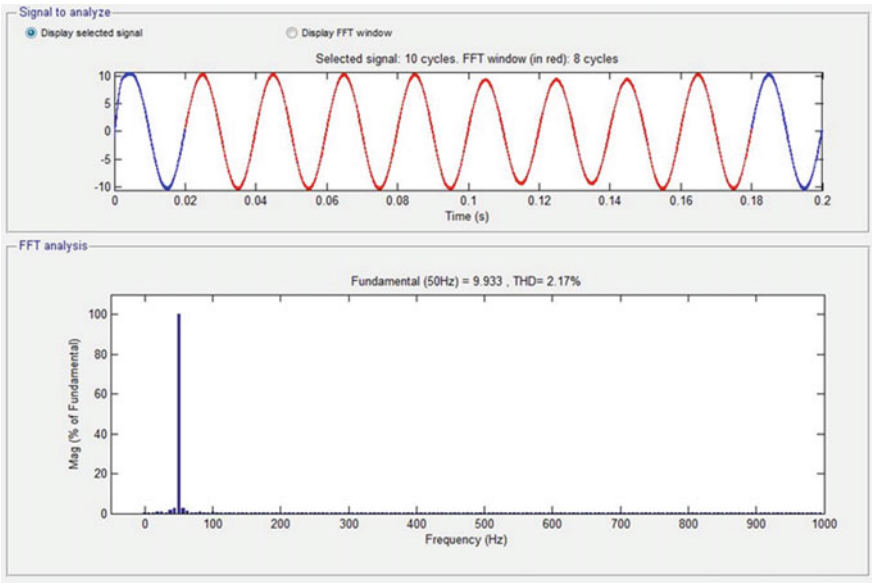

Fig. 22.14 FFT analysis of filter input current showing THD of 2.17% with 10% variation in grid voltage amplitude

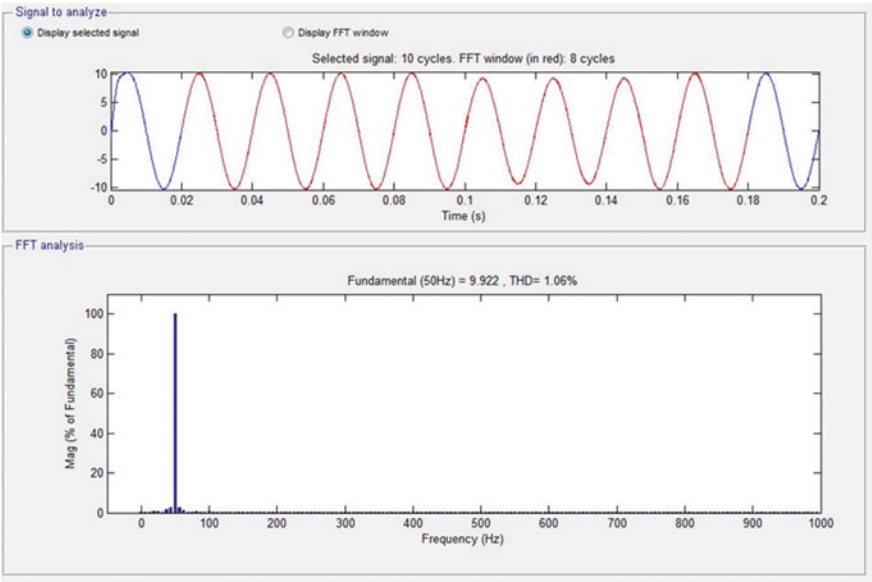

Fig. 22.15 FFT analysis of current injected into the grid showing THD of 1.06% with 10% variation in grid voltage amplitude

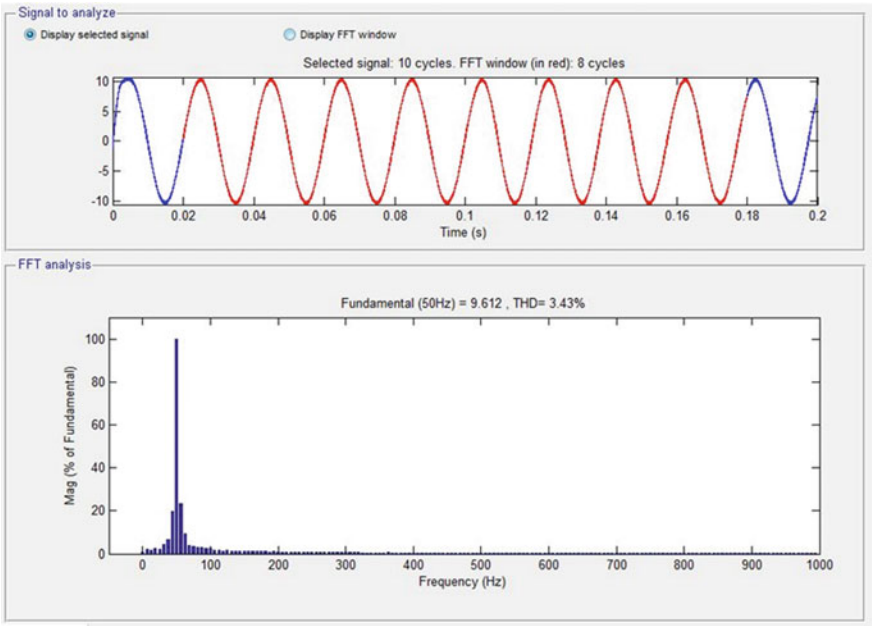

Fig. 22.16 FFT analysis of filter input current showing THD 3.43% with 5% variation in grid frequency

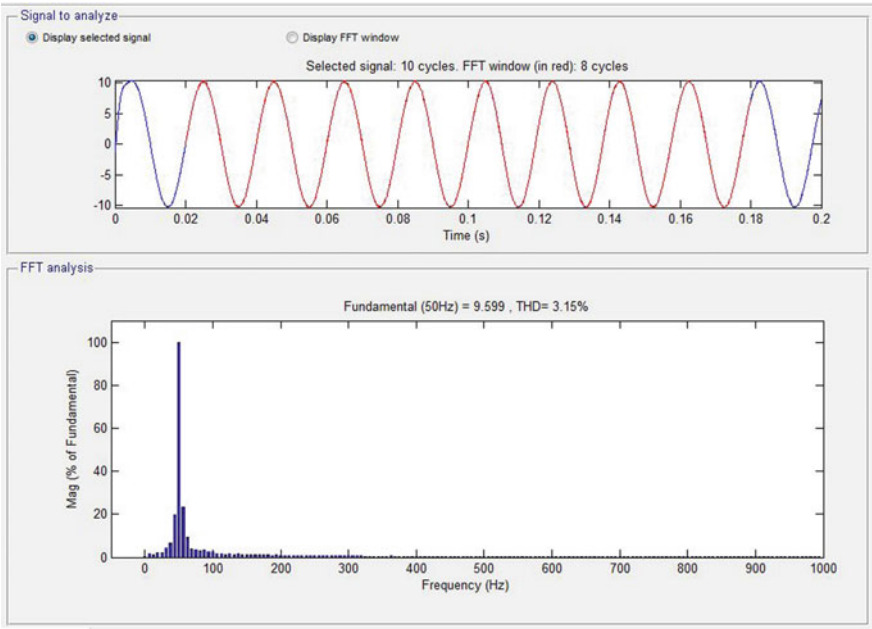

Fig. 22.17 FFT analysis of current injected into the Grid showing THD 3.15% with 5% variation in grid frequency

The variation is done for the time interval between 0.1 and 0.15 s (Figs. 22.12, 22.13, 22.14, 22.15, 22.16 and 22.17).

22.2.5 Conclusion

The Synchronization of renewable energy generation has been achieved using Synchronous rotating frame phase locked loop and Proportional integral current control method. The control over output voltage has been achieved by applying SVPWM technique. The harmonics contents are limited by using the LCL filter with series damping. The result of Simulation of proposed scheme are qualifying the standards specified by IEEE.

References

1. A. Goshal, J. Vinod, A method to improve pll performance under abnormal Grid condition, in *National Power electronics Conference*, Banglore (2007)
2. V. Kaura, V. Blasko, Operation of a phase locked loop system under distorted utility conditions. IEEE Trans. Ind. Appl. **33**(1), (1197)
3. R. Teodorescu, F. Blaabjerg, Flexible control of small wind turbine with grid failure detection operating in stand-alone and grid connected mode. IEEE Trans. Power Electron., 1323–1332 (2004)
4. P. Gopakumar, http://nptel.ac.in. Available at: http://nptel.ac.in/courses/108108077/
5. A. Reznik, M. Godoy, A. Al-urra,S.M. Muyeen, LCL filter design and performance analysis for grid interconnected system
6. M. Liserre, F. Blaabjerg, R. Toedorescu, Grid impedence estimation via excitation of LCL filter resonance. IEEE Trans. Industry Application **43**(5), 1401–1407 (2007)

Chapter 23
Synthesis and Characterization of Surface Functionalized Maghemite Nano Particle for Biofuel Applications

Ragunathan Balasubramanian, Anirbid Sircar and Pandian Sivakumar

Abstract A surface functionalized nano magnetic catalyst was prepared by loading Calcium Oxide (CaO) onto maghemite by chemical precipitation followed by impregnation method. This work focuses on the synthesis, improved size control, enhanced active sites and characterization of nano particles. The parameters like molar ratio of precursors, pH, reaction temperature and time were investigated. The surface modified magnetic catalyst was produced by imbuing of calcium hydroxide on maghemite continued by calcining process. Physicochemical analysis of synthesized catalyst was done by using TGA, SEM-EDX, XRD and BET. Furthermore, the catalytic activity was determined for biodiesel production by transesterification reaction. An effective conversion of 97.3% was achieved for this catalyst under optimum conditions. Recoverability, reusability and regenerability of the catalyst were also studied. From these results, it can be concluded that the catalyst is economically viable and eco friendly.

Keywords Biodiesel (Biofuel) · Maghemite · Transesterification · Impregnation

23.1 Introduction

In recent times biodiesel has gained wide popularity as a renewable biofuel for the simple reason that it emits less pollutant when compared to fossil fuel [1]. The most common method for biodiesel production is transesterification in which, homogeneous catalysts such as sodium or potassium methoxide, sodium or potassium hydroxide are commonly used [2]. Usage of these catalyst results in complicated post treatment process and pollution. Hence, in this scenario there is a need for finding an alternate suitable heterogeneous catalyst which is easier to separate and

R. Balasubramanian · A. Sircar · P. Sivakumar (✉)
School of Petroleum Technology, Pandit Deendayal Petroleum University, Gandhinagar 382007, India
e-mail: sivakumar.p@spt.pdpu.ac.in

G. Anand et al. (eds.), *Nanotechnology for Energy and Water*,
Springer Proceedings in Energy, https://doi.org/10.1007/978-3-319-63085-4_23

more effective [3]. Therefore, the research in this field focuses on the higher catalytic activity of heterogeneous catalyst.

In this research, the heterogeneous nano sized magnetic catalyst was synthesized and investigated for transesterification process. This catalyst behaves as a homogeneous during the reaction phase and it is easily separated as a heterogeneous catalyst by applying magnetic field. Isolated maghemite nano particles were prepared by co-precipitation method which is surface modified by imbuing of calcium oxide. It highlights that the maghemite phase of iron-oxide nano particles were present at room temperature whose magnetic response was superparamagnetic. There are many conventional methods available for the synthesis of maghemite core. In spite of considerable achievements, many efforts are still needed to be taken in relation to synthesis, structure and understanding the underlying properties of iron oxides nanoparticles in general and nano-maghemite in particular. A few significant examples are: the co-precipitation, sol-gel, micro emulsion, flow injection synthesis, hydrothermal synthesis, flame spray pyrolysis and decomposition of organic precursors at high temperature and the oxidation of magnetite nano particles methods [4].

The objective of my research is to investigate the effectiveness of particle size, magnetic properties and the total processing time of the maghemite nano particle. Physicochemical nature of synthesized catalyst was analyzed by TGA, SEM-EDX, XRD and BET. The catalytic activity was evaluated using transesterification of fish oil extracted from fish waste. The characterization and optimization of produced biodiesel were studied.

23.2 Materials and Methods

Maghemite (γ-Fe_2O_3) was prepared by soggy route of chemical reaction; it consists of two different reactions. In the first reaction 0.33 M ferrous chloride tetrahydrate ($FeCl_2$) and 0.6 M ferric chloride hexahydrate ($FeCl_3$) were mixed in 30 mL of distilled water separately. Then, both solutions were mixed together at room temperature using magnetic stirrer at 1000 rpm for about 40 min. To this mixture 1 M of sodium hydroxide was added slowly till the pH of the solution reached 11. The resulting brownish black precipitate was isolated by applying magnetic field and dried at 80 °C. The product was then ground to fine powder and annealed at 220 °C for 3 h to obtain the required nanoparticles.

Maghemite nano base catalyst was prepared by the impregnation of CaO on the surface. About 5 g of maghemite was mixed with 5 g of CaO and immersed in 15 mL of saturated solution of calcium hydroxide. The mixture was subsequently dried at 110 °C to get a solid mass. Finally, the dried material was calcinated at 550 °C in muffle furnace. The final catalyst was crushed and dispersed in methanol by ultrasonication and later the magnetized materials were separated.

The thermal stability of catalyst was examined using Netzsh TG F3 209C Tarsus (Germany) from 35 to 900 °C at a heating rate of 10 °C min. Scanning electron microscope (SEM) images were captured using SEM Hitachi S-3400 N microscope

(Japan). Powder X-ray diffraction (XRD) patterns were obtained on a Rigaku D/Max-RB diffractometer (Japan). BET surface area was measured with Autosorb-1-C-8 (Quantachrome, USA).

Fish oil was extracted from Siluriformes, obtained from fish market Gandhinagar. The average molecular weight of the extracted oil was 905 $gmol^{-1}$ and the free fatty acid composition was 0.19%. The experiments were performed in a 100 mL glass reactor equipped with a condenser and a magnetic stirrer. The reaction was performed at 500 rpm and under atmospheric pressure. In every reaction, weighted quantity of oil was added to a mixture of measured quantity nano-magnetic solid base catalyst and anhydrous methanol. The mixture was refluxed at the boiling point of methanol with mechanical stirring for a predetermined time. After the reaction was completed, the catalyst was isolated by a permanent magnet whereas biodiesel was separated by decantation. The biodiesel yield was determined by gravimetric analysis.

23.3 Result and Discussion

23.3.1 Characterization of Catalyst

TGA curve of non calcinated catalyst shows two events, one at 250–271 °C, associated with the crystal water loss, and another at 490–534 °C which is the result of the decomposition of calcium hydroxide to calcium oxide. The weight losses of these two events were 20.1 wt% and 11.4%, respectively. TGA curve of calcinated catalyst showed one weight loss peak at 530–551 °C, corresponding to sintering of the preformed compound (0.9%) respectively.

The nano-magnetic solid catalysts are further analyzed by powder XRD. The calcinated catalyst is composed of CaO (32.3º, 37.4º, 53.9º and 64.2º). The result shows that magnetic cores are well encapsulated in the catalyst, which is beneficial to separate the catalyst. Thus, the newly formed crystal phase is favorable for enhancing the catalytic activity and stability of the catalyst.

23.3.2 Effects of the Process Parameters for Transesterification Reaction

The parameters affecting the conversion of the oil to biodiesel in the presence of nano catalyst were studied. The variables that were investigated are methanol to oil molar ratio, temperature, time and catalyst concentration. The effect of the reaction time on yield was studied by collecting samples from the reactor at 10 min time interval from 10 to 60 min. The biodiesel yield increased with increase in time and the optimum was achieved at 50 min (yield 89.12 wt% at 1.5 wt% catalysts; 6:1 methanol to oil molar ratio; 50 °C)

For transesterification reaction, 3:1 stoichiometric molar ratio of alcohol to triglycerides is required 1. However, higher molar ratios are necessary for optimum conversion of the oil to biodiesel [5]. The methanol to oil molar ratio, was varied in the range of 6:1–12:1. The other parameters including reaction temperature, reaction time and catalyst concentration, were kept constant at 50 °C, 50 min and 1.5 wt% catalysts respectively. Molar ratios of 9:1 generated optimum yield of 90.3 wt% and it was observed that a further increase in the methanol ratio resulted in no considerable increase in the yield.

The dependency of the biodiesel yield on the catalyst was studied by varying the amount from 1–2.5 wt% at 50 min; 9:1 molar ratio; 50 °C. The optimum catalyst concentration was 2 wt% to achieve a yield of 95.2 wt% biodiesel. Similarly, the yield of the biodiesel at different temperatures were studied (40–60 °C). The other optimal conditions of the earlier studies were kept constant. Thus, the optimum biodiesel yield was 97.7 wt% at the optimum condition of 50 min, 9:1 methanol to oil ratio, 2 wt% of catalyst and 60 °C.

23.4 Conclusion

The study reveals the synthesis and optimization of biodiesel production using a nano-sized magnetic catalyst. The catalyst was synthesized by impregnation of base catalyst (calcium oxide) on a magnetic support. The biodiesel reaction was investigated using waste fish oil extracted from waste siluriformes. The optimum biodiesel yield of 97.7 wt% was obtained at the optimal parameters of 50 min, 9:1 methanol to oil ratio, 2 wt% of catalyst at 60 °C. The catalysts are easily separable from the reaction mixture under a magnetic field and showed high stability and no significant loss of productivity when compared to conventional catalysts.

References

1. S.K.Hoekman, C. Ribbinss, Review of the effects of biodiesel on NOx emissions. Fuel Process. Technol. **96,** 237–249 (2010), doi:10.1016/j.fuproc.2011.12.036
2. L. Wu, T. Wei, Z. Tong, Y. Zou, Z. Lin, J. Sun, Bentonite-enhanced biodiesel production by NaOH-catalyzed transesterification of soybean oil with methanol. Fuel Process. Technol. **144,** 334–340 (2016), doi:10.1016/j.fuproc.2015.12.017
3. A.F.Lee, J.A. Bennett, J.C. Manayil, K. Wilson, Heterogeneous catalysis for sustainable biodiesel production via esterification and transesterification. Chem. Soc. Rev. **43**, 788–779 (2014), doi:10.1039/C4CS00189C
4. K. Ali, A.K. Sarfraz, I.M. Mirza, A. Bahadur, A.U. Haq, Preparation of superparamagnetic maghemite (γ-Fe_2O_3) nano particles by wet chemical route and investigation of their magnetic and dielectric properties. Cure Appl Phys. **15**, 925–929 (2015), doi:10.1016/j.cap.2015.04.030
5. W. Xie, H. Li, Alumina-supported potassium iodide as a heterogeneous catalyst for biodiesel production from soybean oil. J Mol Catal A. **255**, 1–9, (2006), doi:10.1016/j.molcata.2006.03.061

Chapter 24
Synthesis and Optoelectronic Studies of Low Band Gap Polymers and Their Role in Highly Efficient Solar Cells: An Overview

Sonika Pathania and Satbir Singh

Abstract Polymer solar cells are widely used in a variety of large and small scale applications. For organic photovoltaic cells (OPV), bulk heterojunction polymers are most suitable device structures. The use of new active material results into improvement in the power conversion efficiency of (polymer solar cells) PSCs. To improve the absorption of solar irradiation or light harvesting capacity, use of side-chain conjugated polythiophenes is most preferable. As we know, photon flux of solar radiation has a peak of 680 nm. Thus various kinds of low band gap materials have been used in PSCs to increase this flux and hence results into more absorption of sunlight. In this review paper, we have studied the PSCs based on two different low band gap conjugated polymers and their role in fabricating highly efficient solar cells.

Keywords Polymer solar cell · Light harvesting · Low band gap material

24.1 Introduction

Most commonly, conversion of solar light into electricity has been achieved with the help of inorganic solar cells based on photo voltaic effect associated with p-n junctions (PVs). These devices have high power conversion efficiency (PCE) but have high manufacturing cost. Thus new kinds of solar cells are introduced that are based on organic semiconductors and has light weight, mechanically flexible, easy to process and comparably low cost. These solar cells work on the two form of active material. The first one has donor-acceptor material. Sunlight is absorbed in

S. Pathania (✉) · S. Singh
Guru Nanak Dev University Regional Campus, Gurdaspur, Punjab, India
e-mail: sonia.pathania11@gmail.com

G. Anand et al. (eds.), *Nanotechnology for Energy and Water*,
Springer Proceedings in Energy, https://doi.org/10.1007/978-3-319-63085-4_24

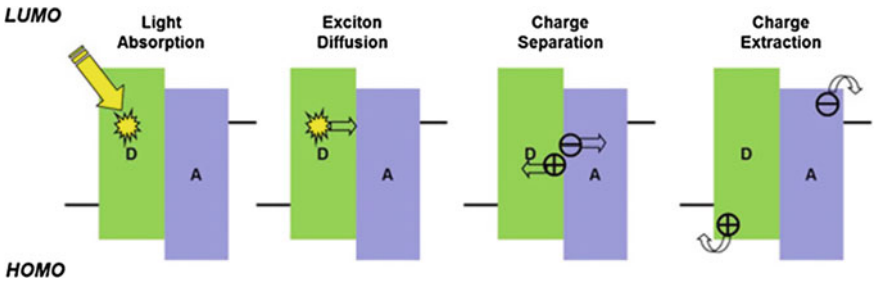

Fig. 24.1 Bilayer organic photovoltaic functional mechanism

photoactive layer composed of donor/acceptor semiconducting organic material to generate photocurrents. The donor material (D) donates electrons and mainly transports holes. The acceptor (A) material withdraws electrons and mainly transports electrons. The second is based on composite material containing both donor and acceptor molecules known as bulk heterojunction (BHJ) material which is more effective approach for organic photovoltaic (OPV) devices (Fig. 24.1).

24.1.1 What Is an OPV Solar Cell?

A study by Friend et al. suggested the solution based, bulk heterojunction (BHJ) Solar Cells. This study later followed by Heeger et al. in 1995 with polymer/fullerene composite. Device architecture of OPV cells is fabricated in sandwich geometry, which consist of substrate such as ITO which is structured by chemical etching and one interfacial layer consist of poly (ethylene dioxythiophene) doped with polystyrene-sulphonic acid (PEDOT:PSS). This interfacial layer is used to facilitate the hole injection/extraction.

Performance of polymer solar cells is evaluated by three parameters (1) Open Circuit Voltage (2) Short Circuit Voltage (3) Fill Factor (ff). Physical property of polymers and morphology of active layers can also affect the device performance.

Low Band Gap polymers are commonly used as donor materials and fullerene derivatives such as $PC_{71}BM$ have been used as the acceptor component because of their relatively high electron affinity and charge carrier mobility. Vacuum evaporation and solution processing tech are two of the most used thin film preparation methods to coat the blended active layers.

General mechanism picture of OPV consist of four steps (1) Light absorption and Exciton formation (2) Exciton migration (3) Charge separation (4) Charge transport and Charge collection.

Controlling the morphology in BHJ solar cells is important. Different studies have suggested the use of e-/hole blocking layer is useful for achieving high efficiency in solar cells (Fig. 24.2).

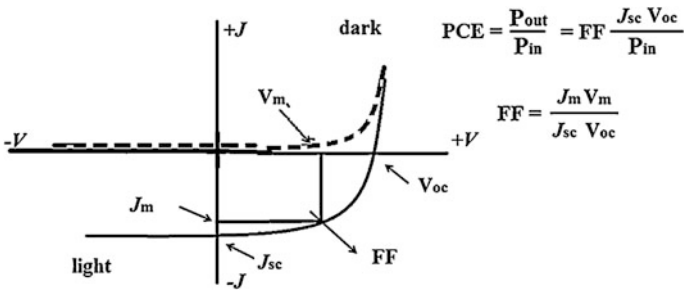

Fig. 24.2 Typical current-voltage characteristics for dark and light current

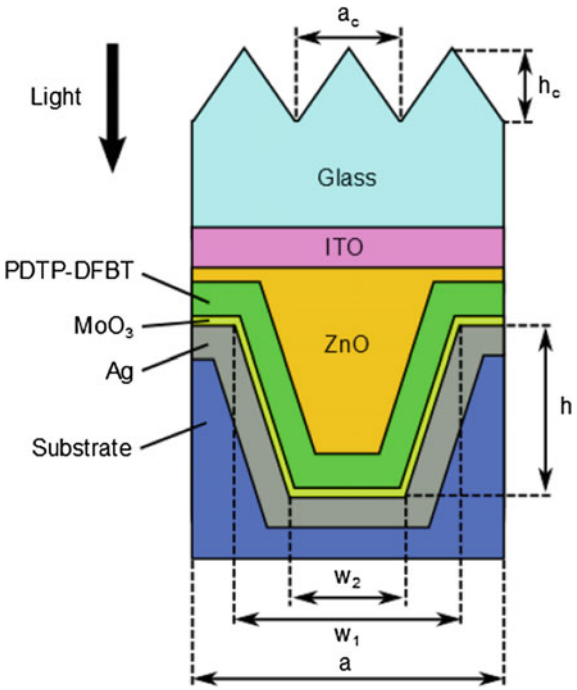

Fig. 24.3 Diagram of cell structure studied [1]

24.1.1.1 Light Trapping Design for Low Band Gap Polymer Solar Cells

A diagram of device architecture studied is shown in Fig. 24.3. Given Diagram consist of various layers. These layers are: Device substrate, Ag, MoO3, PDTP-DFBT:PC71BM, Nanocrystalline ZnO (nc-ZnO), ITO and glass. This substrate is given a periodic trapezoidal structure with Ag, MoO3, and PDTP-DFBT: PC71BM on top and nc-ZnO nanostructures filling the remaining gaps. Ag is used as substrate material. Because of the high cost of Ag (silver), for practical use, a thin layer of Ag is used and "substrate" of air beneath the cell. Thickness of MoO3,

PDTP-DFBT:PC71BM, ITO layers and the planer layer of ZnO placed above the nanostructure kept fixed at 15 nm, 100 nm, 180 nm, and 50 nm respectively. The geometry of entire structure is defined by periodicity (a), height (h), opening width (w1) and bottom width (w2). Corrugation geometry is specified by corrugation height (hc) and corrugation periodicity (ac).

Incident light is treated as a TM-polarized plane wave (magnetic transverse to plane of cell) of incidence θ [1]. If one full electric field E and incident magnetic field H0 and E0 is known, one fraction of light absorbed by any given region of cell can be found out by calculating them.

24.2 Synthetic Principles Toward High Performance Materials

Bandgap of 1.1 eV (1100 nm) is capable of harvesting 77% of solar radiations but semiconducting polymers have more bandgap up to 2 eV (620 nm) and can only absorb 30% of solar photons. For better light harvesting, conjugated polyaromatic polymers, especially with thiophene moieties have been developed to give polymers tunable bandgaps from 1.0–2.0 eV. the tuning of energy levels along with solubility is really important to have high PCE values in OPV via optimization of solar cell parameters.

Above mentioned polymers can work with two strategies: various substitutes are attached to the polymer backbones so that morphology and performance of electroactive layer can optimized which can also tune both solubility and energy levels.

For thiophene-containing polymers stille coupling polycondensation is used. These polymers can tolerate various functional groups.

24.2.1 Fused Heterocycles

These are the important class building blocks to achieve either low bandgap or high carrier mobility depending on the orientation of fused ring to polymer main chain. Polyisothianaphthlene (PITN) was the first narrow bandgap polymer that has fused ring normal to polymer backbone.

The main chain of PITN favors the quinoidal mesomeric structure to maintain benzene aromaticity, which further results in achieving the band gap of 1.0 eV. Polymers based on fused thienothiophene (TT) moiety are known as the most successful low bandgap polymers for solar cell applications.

Monomers such as benzothiadiazole and pyridalthiadiazole, when copolymerized with carbazole (PCDTBT) or cyclopentadithiophene-type units (PCPDTBT, PSBTBT and PCPDTPT) result into achieving low band gaps. Moieties called PTBs polymers achieved by alternating TT and benzodithiaophene (BDT) can achieve bandgap as low as 1.6 eV and performance of over 50%.

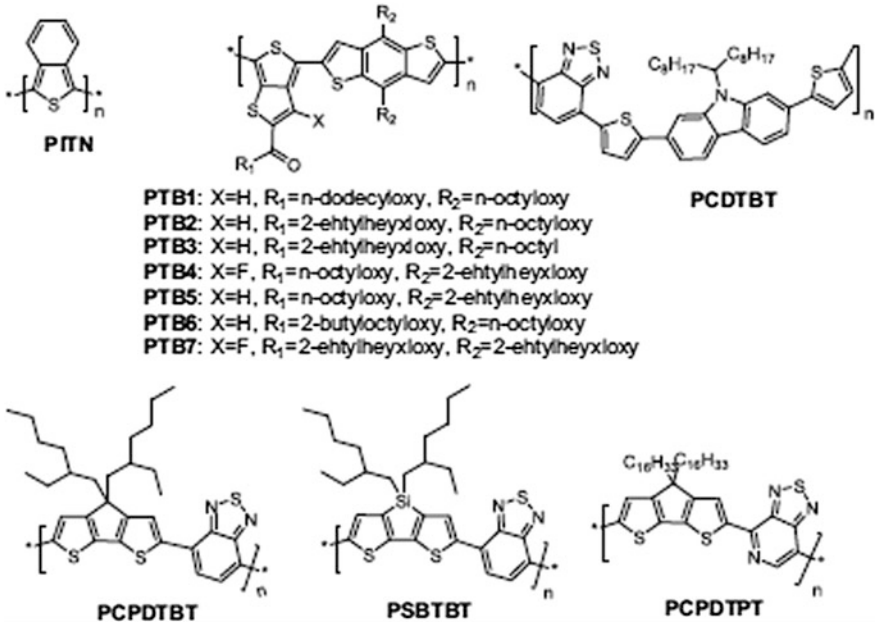

Fig. 24.4 Chemical structure of fused heterocycle based polymer

Conventional device architecture blended with PC71BM polymer can exhibit optimized solar cell efficiency of around 5–7%. When bithiophene is bridged by sp^3 carbon of the ketal group (PCPDT), resulted into achieving bandgap as low as 1.2 eV (Fig. 24.4).

24.2.2 Fluorination Effect

Fluorine is known as the most electronegative element that has the Pauling electronegativity of 4.0. Although it has the comparable size to hydrogen but fluorine tends to have completely different electronic properties. If hydrogen gets replaced by fluorine in polymeric backbone, it can tune energy levels without any steric hindrance.

Although applications of fluorination conjugated materials have been already studied in organic field effect transistors (OFET) and organic light emitting diodes (OLED) but fluorination effect on solar cell performance came into notice, recently.

TT and BDT units along with fluorine have the observation of approximately 1.1 eV lowering of HOMO energy level per fluorine on repeating unit. As the number of fluorine substitutions increase, both HOMO and LUMO energy level reduced. First polymer that broke the 7% PCE value using polymer/fluorine blends

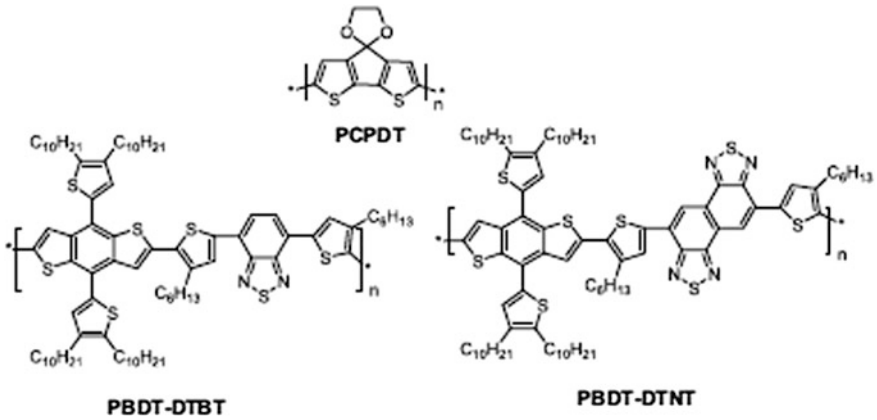

Fig. 24.5 Chemical structure of PCPDT, PBDT-DTBT and PBDT-DTNT

(Voc = 0.74 eV, Jsc = 14.50 mA/cm2, ff = 68.97%, PCE = 7.40%) was polymer PTB7.

Effect of fluorination is complicated as compared to changing the energy levels. Dipolar moment changes in polymer repeating unit between ground state and excited state is affected by the fluorination effect. It also affects the polymer/fluorine compatibility. A study of relationship between dipolar changes in polymer repeating units and solar cell performance leads to an interesting correlation between PCE and Dmge. It shows that an optimized Dmge help to achieve high PCE values.

Fluorinated benzothiadiazole and benzotriazole as building blocks (PBnDT-DTftBT and PBnDT-FTAZ) has been studied and improved solar cell parameters like Voc were observed. Both polymer systems can have efficiency more than 7% in device structure of ITO/PEDOT; PSS/polymer: PCBM/Ca/Al (Fig. 24.5).

24.2.3 Summary and Outlook

The power conversion efficiency of organic solar cells has steadily improved to 10%. Main challenge in the field of organic solar cells is to develop a predictive understanding of structure-property relationship. Characteristics like, materials with low cost and easy fabrication, higher power conversion efficiency in larger areas and longer life are the factors that make organic solar cells more commercially competitive. So far, future of these solar energy harvesting devices looks bright.

Acknowledgements This work has been supported by Guru Nanak Dev University, Regional Campus Gurdaspur (Punjab), India

References

1. K.S. Nalwa, S. Chaudhary, Design of light-trapping microscale-textured surfaces for efficient organic solar cells. Opt. Express **18**(5), 5168–5178 (2010)
2. X. Li, W.C.H. Choy, L. Huo, F. Xie, W.E.I. Sha, B. Ding, X. Guo, Y. Li, J. Hou, J. You, Y. Yang, Dual plasmonic nanostructures for high performance inverted organic solar cells. Adv. Mater. **24**(22), 3046–3052 (2012)
3. Z. He, C. Zhong, S. Su, M. Xu, H. Wu, Y. Cao, Enhanced power-conversion efficiency in polymer solar cells using an inverted device structure. Nat. Photonics **6**(9), 591–595 (2012)
4. J. You, L. Dou, K. Yoshimura, T. Kato, K. Ohya, T. Moriarty, K. Emery, C-C. Chen, J. Gao, G. Li, Y. Yang, A polymer tandem solar cell with 10.6% power conversion efficiency. Nat. Commun. **4**, 1446 (2013)
5. S. Nam, J. Han, Y. R. Do, H. Kim, S. Yim, Y. Kim, Two-dimensional photonic crystal arrays for polymer: fullerene solar cells. Nanotechnology **22**(46), 465–403 (2011)
6. A. Raman, Z. Yu, S. Fan, Dielectric nanostructures for broadband light trapping in organic solar cells. Opt. Express **19**(20), 19015–19026 (2011)
7. D.H. Wang, J. Seifter, J.H. Park, D-G. Choi, A. J. Heeger, Efficiency increase in flexible bulk heterojunction solar cells with nano-patterned indium zinc oxide anode. Adv. Energy Mater. **2** (11), 1319–1322 (2012)
8. D.-H. Ko, J.R. Tumbleston, L. Zhang, S. Williams, J. M. DeSimone, R. Lopez, E.T. Samulski, Photonic crystal geometry for organic solar cells. Nano Lett. **9**(7), 2742–2746 (2009)
9. L. Chen, W.E.I. Sha, W.C.H. Choy, Light harvesting improvement of organic solar cells with self-enhanced active layer designs. Opt. Express **20**(7), 8175–8185 (2012). http://www.opticsinfobase.org/oe/abstract.cfm?uri=oe-20-7-8175.
10. Z. He, C. Zhong, X. Huang., W.-Y.Wong., H. Wu., L. Chen., S. Su., Y. Cao, Simultaneous enhancement of open-circuit voltage, short-circuit current density, and fill dactor in polymer solar cells. Adv. Mater, **23**(40), 4636–4643 (2011)
11. J. You, X. Li, F. X. Xie, W.E.I. Sha, J.H.W. Kwong, G. Li, W.C.H. Choy, Y. Yang, Surface plasmon and scattering-enhanced low-bandgap polymer solar cell by a metal grating back electrode, Adv. Energy Mater. **2**(10), 1203–1207 (2012)
12. How to design low bang gap polymer solar cells (2013), https://www.youtube.com/NGS-2013

Chapter 25
Synthesis of Silver Nano Particles on Sol-Gel Base and Its Effect Against Water Purification

Amneesh Singla, Manjeet Singh Goyat and Suridhi Sahu

Over the past few decades, our main and big problem is how to purify saline sea water, contaminated and waste water. The most serious problems worldwide are water pollution by toxic contamination various technologies has been proposed to water purification like ion exchange, water precipitation, membrane filtration, coagulation and other electrochemical method. From past few decades, nanotechnology has drawn few attentions because Nano materials are widely used for water purification. In the present review article, Nano-material synthesis is discussed, which is used in water purification. This review article will give the synthesis of silver nanoparticles by sol gel technique with the help of Silver Nitrate ($AgNO_3$) and Tri-sodium Citrate ($C_6H_5O_7Na_3$). Silver nanoparticles are used in purification of water. This study will help researchers in giving better and economical use of silver nanoparticles in purification.

25.1 Introduction

The nanocrystal silver Nano particles have attended the attraction due to widely potential applications in many fields such as catalyst optoelectronics, surface enhanced scatterings (SERS), chemical and biological sensing and especially called as most common antibacterial material [1]. In addition to traditional methods of their production, new methods have also been developed. Among various metallic Nano particles, silver Nano particles have been widely investigated because of its unusual property exhibition raised due to their size which bring a wide range of possibilities with respect to technical applications [2]. A key issue among these techniques is the control of particle size, which is very important in various applications. Implementation of some techniques is not cost effective and therefore,

A. Singla (✉) · M.S. Goyat · S. Sahu
University of Petroleum and Energy Studies, Dehradun, Uttarakhand, India
e-mail: amneesh82@gmail.com

G. Anand et al. (eds.), *Nanotechnology for Energy and Water*,
Springer Proceedings in Energy, https://doi.org/10.1007/978-3-319-63085-4_25

most researcher focus on the chemical reduction method because of its low cost and ease of operating appratus [2, 3].

In this study, silver Nano particles are synthesized by using sol-gel technique by chemical reduction of $AgNO_3$ in the presence of Tri-sodium Citrate ($C_6H_5O_7Na_3$) as a stabilizing agent and acetone and double distilled water as a reduction agent at room temperature. The structure and nature of the resultant particles were characterized by using analytical methods [4–6].

X-ray powder diffraction (XRD), atomic force microscope (AFM), zetasizer rand UV-Vis spectroscopy.

25.2 Experiment Procedure and Characterisation

Materials to be used
Silver Nitrate ($AgNO_3$), Tri-sodium Citrate ($C_6H_5O_7Na_3$), Acetone, double distilled water.

25.2.1 Experiment Procedure

Weighing Procedure
First of all, we weighed reactants used in the method. While weighing, the technical weighing equipment is cleaned by brush, so it doesn't slow the kinetics of the reactions taking place, by not mixing the chemical of other properties in our compound [7]. While weighing, we used butter paper and that is also considered in our weighing calculation [8, 9].

Magnetic Stirring Process
In magnetic stirring process, the torque and temperature knob is operated properly. We needed temperature of 80° while dissolving both the reactants separately in a beaker with 50 ml of water which is distill [7]. After temperature reached at 80° then we have turned off the knob of temperature and only torque knob is on, which worked for 15 min for both dissolving solution, so that it mixes properly [9, 10].

Dissolving the solution
While dissolving both the solution we needed burette, which is washed with distilled water then filled with the solution of tri-sodium citrate. Slowly we mixed tri-sodium citrate with silver nitrate solution. After periods of minutes, we observed that pale yellow (golden) color solution appeared. The solution is colloidal in nature [11].

25.2.1.1 Characterisation

The prepared sample is now taken for characterization by X-ray diffraction and UV-Vis spectroscopy.

UV-VIS spectroscopy is done firstly because for this procedure we need diluted solution of sample prepared. A typical sample cell (commonly called as cuvette);

From an experimental point of view, three considerations must be made:

- A longer path length, I through the sample will cause more UV light.to be absorbed—linear effect.
- The greater the concentration of the sample, the more UV light will be absorbed —linear effect.
- Some electronic transitions are more effective at the absorption of photons than molars—molar absorptivity.

Figure 25.1 the X-axis determines wavelength and Y-axis determines absorbance angle.

X-ray powder diffraction (XRD) is a rapid analytical technique primarily used for phase identification of a crystalline material and can provide information on unit cell dimensions. The analyzed material is finely ground, homonised, and average bulk composition is determined. The atomic planes of crystals cause an incident beam of X-rays to interfere with one another as they leave the crystal. The phenomena is called X-ray diffraction.

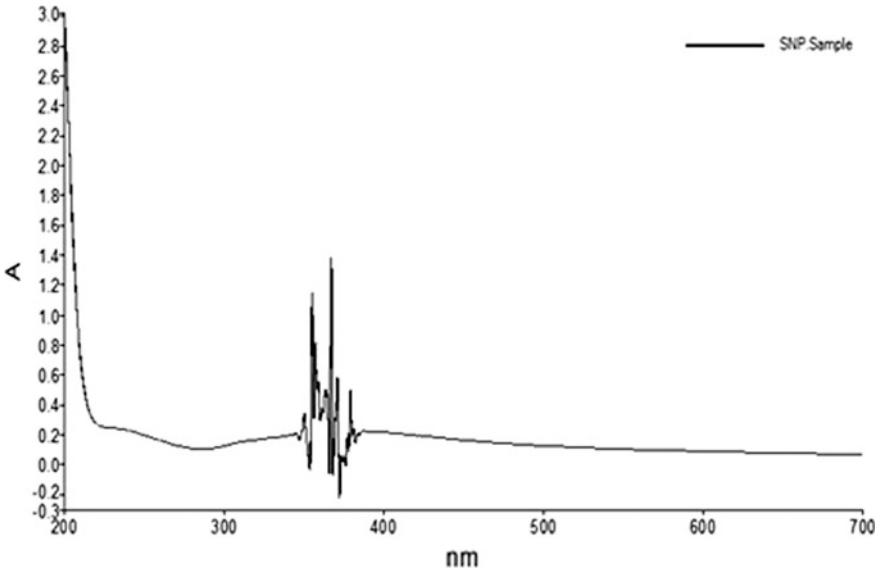

Fig. 25.1 The X-axis determines wavelength and Y-axis determines absorbance

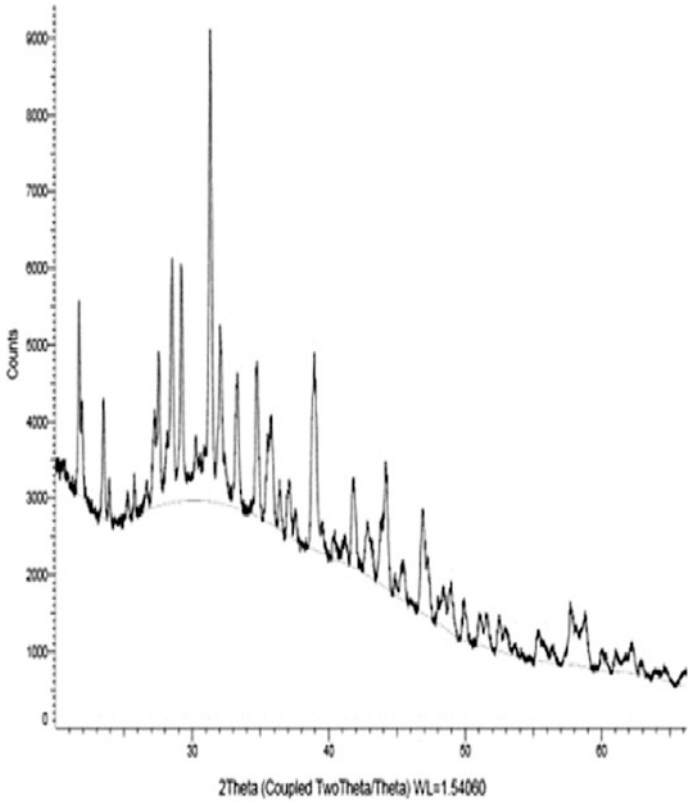

Fig. 25.2 In this X-axis determines the intensity and Y-axis the diffraction angle

Figure 25.2 in this X-axis determines the intensity and Y-axis the diffraction angle.

25.3 Conclusion

From above characterization process, we conclude that the analysed particle is finely ground, homonized and averaged bulk composition is determined. The result from XRD analysis is a diffract gram showing the intensity as a function of diffraction angle and the size determine was about 17–22 nm. In UV we determined the absorptivity of light passing through the sample and it will be determined by the detector present in instrument which will difference between transmitted light versus incident light. The absorbed wavelength was about 375–420 nm.

References

1. D. Phong Pham, K. Khanh Huynh, C. Vinh Tran, V. Quang Vu, T. Thanh, Int. J. Mater. Sci. Appl. **3**(5), 147–151 (2014), doi:10.11648/j.ijmsa.20140305. 13 **19**(2) Summer 1390/2011 pp. 47–50, Mahshid Farasat1, Seyyed Maqsood Golzan1, Ali Hassanzadeh
2. D. Yu, X. Sun, X. Bian, X. Tong, Y. Qian, Phys. E. **23**, 50 (2004)
3. H. Yin, T. Yamamoto, Y. Wada, Yanagid Sh., Mater. Chem. Phys. **83**, 66 (2004)
4. E. Elghanian, J.J. Storhoff, R.C. Mucic, R.L. Letsinger, C.A. Mirkin, Science, **277**, 1079 (1997)
5. Q.X. Lui,C.X. Wang, C.X. Yang, Eur. Phys. J. **B41**, 476 (2004)
6. M. Majur, Electrochem. Commun. **6**, 400 (2004)
7. L.K. kurihara, G.M. Chow, P.E. Scheon, Nanostruct. Mater. **5**, 607 (1995)
8. K. Esumi, T. Tano, K. Torgae, K. Meguro, Mater. Chem. Phys. **5**, 264 (1990)
9. X. Suno, X. Luo, Mater. Lett. **59**, 3847 (2005)
10. C.H. Bae, S.H. Nam, S.M. Park, Appl. Surf. Sci. **628** (2003)
11. Z. Jian, Z. Xiang, W. Yongchang, Microelectronics **77**, 58 (2005)

Chapter 26
The Role of Various Spinel Ferrites Magnetic Nanoparticles in the Improvement of Photovoltaic Performance of Organic Solar Cell: A Review

Ruchi Sharma and Satbir Singh

Abstract Bulk heterojunction (BHJ) organic solar cells (OSCs) have been experiencing larger attention because of its advantages in terms of the low-cost, light-weight, and flexibility. In BHJ organic solar cells, half of the total efficiency lost in the midst of all energy passage ways due to the photo generated charge carrier recombination within OSCs. So in order to mark this issue, we introduce spinel ferrites magnetic nanoparticles (MNPs) such as super paramagnetic and ferromagnetic MNPs. Additionally; these superparamagnetic and ferromagnetic MNPs are doped at active layer of OSCs and further improve the photovoltaic performance of the cell. However with the increase in efficiency, the enhancement in the short circuit current and reduction in the open circuit voltage of OSC has been observed in previous papers. In this paper, various essential parameters of the OSCs are explained and the role of spinel ferrites in the improvement of photovoltaic performance has been reviewed.

Keywords Bulk heterojunction · Organic solar cells · Magnetic nanoparticles · Spinel ferrites

26.1 Introduction

Ferrites are type of chemical or ceramic compounds that composed of iron oxide as a standard component. In 1930 Yogoro Kato and Takeshi Takei of the Tokyo institute of technology the first ferrite compound [1]. Ferrites are derived from iron oxides named as magnetite (Fe_3O_4) or hematite (Fe_2O_3), usually not able to

R. Sharma (✉)
Guru Nanak Dev University Regional Campus Gurdaspur, Punjab, India
e-mail: ruchisharrma285@gmail.com

S. Singh
Punjab, India

G. Anand et al. (eds.), *Nanotechnology for Energy and Water*,
Springer Proceedings in Energy, https://doi.org/10.1007/978-3-319-63085-4_26

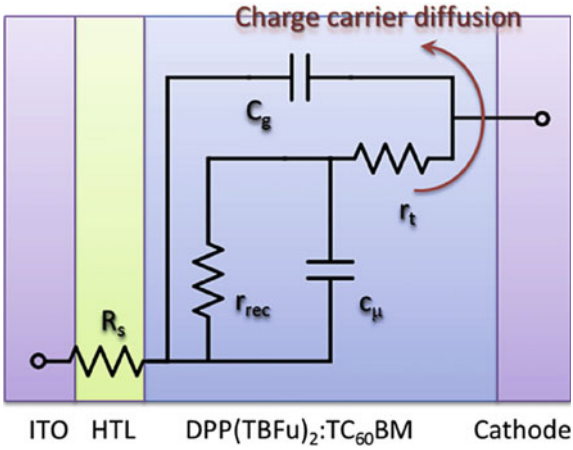

Fig. 26.1 Equivalent schematic of BHJ solar cell [3]

conduct electrically and are ferrimagnetic ceramic compounds. The terms electrically nonconductive and ferrimagnetic means they can be magnetized or attracted to a magnet. Further based on the magnetic coercivity and the resistance to get demagnetized, ferrites can be categorized into two families. One is soft ferrites that do not retain their magnetism after being magnetized for example nickel, zinc, cobalt, magnesium and manganese ferrites and other one is hard ferrites that also known as permanent magnets and can sustain their magnetism after being magnetized. Most of the ferrites are basically spinels having formula AB_2O_4, where A and B denotes various metal cations like iron [1].

A rapid increase in the power conversion efficiency (PCE) of OSC which is further depends upon short circuit current (I_{sc}) and open circuit voltage (V_{oc}), is possible due to the doping of the photo active layer with more advanced and sophiscated spinel ferrites MNPs such as ferromagnetic ($CoFe_2O_4$) and superparamagnetic (Fe_3O_4, $ZnFe_2O_4$—high magnetization and $NiFe_2O_4$—low magnetization) which are dissolved in the mixture of DPP(TBFu)$_2$:TC$_{60}$ BM [3, 4]. In this regard, the effective life time constant of OSC is enlarged adequately [3–5]. Hence, increases the efficiency of the exciton (electron-hole pair) and ultimately the effective lifetime constant is incremented. In the Fig. 26.1 a simple schematic of the bulk heterojunction OSC has shown.

26.2 Parameters Determining the Performance of the Solar Cells

26.2.1 Open Circuit Voltage

The difference between the HOMO level of the donor and the LUMO level of the acceptor can determine the open circuit voltage (V_{oc}). This parameter is generally

affected by the temperature among all parameters. According to Eq. (1) due to the temperature dependence on reverse saturation current I_o, the open-circuit voltage decreases.

$$V_{oc} = \frac{nKT}{q} \ln [I_L / I_0] \tag{1}$$

$$I_{sc} = I_L - I_0 \left[\frac{Qv}{e_{nKT}} - 1 \right] \tag{2}$$

where k is the Boltzmann constant, T is the temperature in terms of Kelvin, q is Electric charge, V is output voltage of solar cell, I_L is light generated current, and I_o is the reverse saturation current [6].

26.2.2 Short Circuit Current

Short circuit current (I_{sc}) is depend upon the multiplication of the photo induced charge carrier density and the charge carrier mobility within the photoactive material [11]. According to Eq. (2) the short circuit current increases with the increase in temperature [6].

26.2.3 Fill Factor

Fill factor is basically the measurement of the squareness of the I-V characteristics of the solar cells. It can be determined by the charge carriers that reach the electrodes of the solar cells by lowering down the field towards the open circuit voltage.

$$FF = \frac{V_{mp} I_{mp}}{V_{oc} I_{sc}} \tag{3}$$

where V_{oc} and I_{sc} are the open circuit voltage and short circuit current, I_{mp} and V_{mp} are the current and the voltage at a maximum point of power respectively [6].

26.2.4 Power Conversion Efficiency

Basically power conversion efficiency is how much portion of energy is converted into electricity in the form of sunlight. It can be calculated by taking various factors that are open circuit voltage, short circuit current, and fill factor and incident light power into account.

$$\eta = \frac{V_{oc}\, I_{sc}\, FF}{P_{in}} \tag{4}$$

where P_{in} is the incident light power [6].

26.3 Various Chemical Methods for the Synthesis of Ferrites

To control the size and surface area of the materials synthesis plays an important role. The synthesis of ferrite MNPs can be done using different chemical methods that are discussed as follows:

(A) Sol-Gel method:
In this method, a high degree of uniformity can be maintained by the formation of a gel and the reduction in the need for atomic diffusion during the solid state calcinations is obtained. In this method first of all a solution of appropriate precursors is formed and then after the hydrolysis and condensation process, conversion of solution into a homogeneous oxide gel is performed. [2].

(B) Precipitation method:
The creation of a solid from a solution is called as precipitation. When the reaction occurs in a liquid solution, the formation of solid is called the'precipitate'. The chemical that causes the liquid solution to convert into solid is called the'precipitant'. In this method under the employed conditions, the precipitation of substances normally soluble [2].

(C) Ball milling:
A ball mill is nothing but a type of grinder which is used to grind and blend materials for use in mineral dressing processes, selective laser sintering pyrotechnics, ceramics and paints. The basic principles behind the working of ball milling are impact and attrition. With the principle of impact, size reduction can be done as the balls fall from the top of the shell [2].

(D) Solid-state reaction:
This method is the widely used method for the preparation of polycrystalline solids in which mixture of solid materials are used. As we know that solids do not react mutually at room temperature over normal time scales and for the occurrence of reaction at an appreciable rate, it is mandatory to heat them at much larger temperatures, often to 1000 to 1500 °C [2].

26.4 Literature Survey

In the year 2006, Daliya S. Mathew et al. reviewed the structure and magnetism of various spinel ferrite nanoparticles like manganese-zinc ferrite, nickel-zinc ferrite cobalt ferrite and zinc ferrite, and their synthesis in microemulsions [12].

In the year 2011, W. Zhang et al. observed the enhancement in efficiency of solar cell up to approximately 50% by doping the P3HT: PCBM layer of bulk heterojunction polymer solar cells with Fe_3O_4 nanoparticles and further investigated the PCE comparison by different means of doping in P3HT: PCBM or PEDOT: PSS layer [7].

In the year 2014, Boris I. Kharisov et al. reviewed the recent applications of ferrite nanoparticles in organic processes as catalysts. The various spinel ferrites magnetic nanoparticles are:

(a) Cobalt ferrites

The synthesis of spinel $CoFe_2O_4$ MNPs average size up to 40–50 nm was achieved by the combined sono chemical and co-precipitation method in liquefied solution without any type of surfactant or any other type of natural capping agent. These uncapped MNPs made use of aldol reaction in ethanol. After the reaction completed, the magnetic nanoparticles (MNPs) were separated by using a superficial magnet [8].

(b) Nickel ferrites

The ultra small spinel oxide $NiFe_2O_4$ particles that are 3–8 nm in size were prepared by the combination of chemical precipitation and high-energy ball milling synthesis methods. The result of these procedures was the formation of ultra small crystalline nickel ferrite, where the particle size can be controlled. Their catalytic behavior was tested in methanol decomposition to Carbon monoxide and methane that show the dissimilarity in the phase composition and catalytic behavior which depend upon the preparation method [9].

(c) Zinc ferrites

Non-nano-sized zinc ferrites ($ZnFe_2O_4$) have been used in organic oxidative reactions. Thus, the investigation of the catalytic behavior for coupling of methane and oxidative conversion which is prepared by the combustion method can be done by pure and neodymium zinc ferrites [9].

In the year 2015, Kai Wang et al. investigated the effects of MNP and external magnetostatic field on the bulk heterojunction polymer solar cells and also observed enhancement in efficiency over 50% by incorporated MNPs within BHJ polymer solar cells [11].

In the year 2015, Raghvendra Singh Yadav et al. investigated the impact of Nd^{3+} by X-ray photoelectron spectroscopy on cation distribution of Co^{2+} and Fe^{3+} in spinel ferrite cobalt ferrite nanoparticles and also demonstrated structural and magnetic properties of Nd^{3+} oped cobalt ferrite nanoparticles that were synthesized by starch-assisted sol-gel auto-combustion method [10].

In the year 2016, Ayah F.S. Abu-Hani et al. fabricated H_2S gas sensors based on $ZnFe_2O_4$ and $CuFe_2O_4$ nanoparticles. These nanoparticles were synthesized by the co-precipitation method and by the solution casting method; the membranes were obtained [11].

In the year 2016, Alexander Kovalenko et al. presented the study of organic solar cells that are doped with various types of spinel ferrite magnetic nanoparticles such as ferromagnetic and superparamagnetic and with the help of impedance

Table 26.1 Table shows the photovoltaic performance of the fabricated OSCs with and without MNPs under the illumination of light [3]

Fabricated OSCs (with or without MNPs)	Short circuit current (mA/cm^2)	Open circuit voltage (mV)	Fill factor (%)	Power conversion efficiency (%)
Reference cell	8.87	906	50	4.02
Fe	9.18	902	49	4.05
F aligned	10.34	864	49	4.37
NiF	9.33	891	50	4.16
NiF-aligned	9.42	873	50	4.11
ZnF	9.06	898	52	4.23
ZnF-aligned	10.06	877	52	4.58
CoF	6.69	320	38	0.81
CoF-aligned	6.71	286	39	0.75

spectroscopy the dependence of photovoltaic performance of organic solar cells by doping it with MNPs were analyzed.

As it is clearly depicted from the Table 26.1 that first, second and third highest power conversion efficiencies are 4.58%, 4.37% and 4.23% respectively. Out of nine fabricated OSCs, the cell which is aligned with CoF has lowest power conversion efficiency that is 0.75% and it is 3.83% less than the highest one. The fabricated OSC which is aligned with ZnF has highest power conversion efficiency but the short circuit current is 10.06 mA/cm^2 which is 0.28 mA/cm^2 and it is less than the short circuit current of second highest fabricated OSC that is F aligned. An increase in short circuit current I_c that is 10.34 mA/cm^2 which is the highest current exceeds power conversion efficiency to 4.37%, decreases open circuit voltage and fill factor to 864 mV and 49% respectively. It can be summarized from the Table 26.1 that OSCs aligned with MNPs have more power conversion efficiency than OSCs without MNPs. Hence the role of various spinel ferrites MNPs in the improvement of photovoltaic performances is justified.

26.5 Conclusion

In this paper, various parameters that determine the performance of organic solar cells are presented. Also the various chemical methods for the synthesis of MNPs or ferrites are discussed. In this research paper, the role of doping of the OSC with various MNPs effects photovoltaic performance is reviewed from previous papers. Generally it is good enough to say that superparamagnetic MNPs merged with BHJ active layer can renovate performance of the solar cells concerning to their magnetic moments. Moreover, classification of MNPs with an external magnetic field at raised temperature further can maximizes photovoltaic performance of the device by the proficient charge collection at short-circuit condition, results in higher short circuit current.

Acknowledgements This research work has been supported by Guru Nanak Dev University, Regional Campus Gurdaspur (Punjab), India.

References

1. https://en.wikipedia.org/wiki/Ferrite_(magnet)
2. http://www.slideshare.net/nikita_liferocks/ferrites
3. A. Kovalenko, R. Singh Yadav, J. Pospisil, O. Zmeskal, D. Karashanova, P. Heinrichova, M. Vala, J. Havlica, M. Weiter, Towards improved efficiency of bulk-heterojunction solar cells using various spinel ferrite magnetic nanoparticles. Org. Electron. **39**, 18–126 (2016)
4. S. Günes, H. Neugebauer, N.S. Sariciftci, Conjugated polymer-based organic solar cells. Chem. Rev. **107**(4), 1324–1338 (2007)
5. H. Hoppe, N.S. Sariciftci, Organic solar cells: an overview. J. Mater. Res. **19** (07), 1924–1945 (2004)
6. D.M. Tobnaghi1, R. Madatov, D. Naderi, The effect of temperature on electrical parameters of solar cells, IJAREEIE **2**(12), 2278–8875 (2013)
7. Wenfeng Zhang, Xu Ying, Haitao Wang, Xu Chenhui, Shangfeng Yang, Fe_3O_4 nanoparticles induced magnetic field effect on efficiency enhancement of P3HT:PCBM bulk heterojunction polymer solar cells. Sol. Energy Mater. Sol. Cells **95**, 2880–2885 (2011)
8. I. Boris, H. Kharisova, V. Rasika Dias, B. Oxana, V. Kharissova, Mini-review: ferrite nanoparticles in the catalysis. Arab. J. Chem., (2014)
9. Kai Wang, Chao Yi, Chang Liu, Hu Xiaowen, Steven Chuang, Xiong Gong, Effects of magnetic nanoparticles and external magnetostatic field on the bulk heterojunction polymer solar cells. Sci. Rep. **5**, 9265 (2015). doi:10.1038/srep09265
10. R.S. Yadav, J. Havlica, J. Masilko, L. Kalina, J. Wasserbauer, M. Hajdúchová, V. Enev, I. Kuřitka, Z. Kožáková, Impact of Nd^{3+} in $CoFe_2O_4$ spinel ferrite nanoparticles on cation distribution, structural and magnetic properties. J. Magn. Magn. Mater. **399,** 109–117 (2016)
11. F.S. Ayah, S. Abu-Hania, T. Mahmoudb, F. Awwada, A.I. Ayesh, Design, fabrication, and characterization of portable gas sensors based on spinel ferrite nanoparticles embedded in organic membranes. Sens. Actuators B **241**, 1179–1187 (2017)
12. S. Daliya, Mathew, Ruey-Shin Juang, An overview of the structure and magnetism of spinel ferrite nanoparticles and their synthesis in microemulsion. Chem. Eng. J. **129** (1e3), 51e65 (2007)

Chapter 27
Tyre Pyrolysis by Using Nano-catalyst to Improve Energy Efficiency and Fuel Quality

Chandresh Gabani, Yash Ranchh, Riddhi Barodia and Pandian Sivakumar

Abstract Scrap tires are harmful waste because they are non-biodegradable, emit toxins, create disposable problems and produces dioxines when burnt. Technological conversion of scrap tires to fuel by pyrolysis exists. This study is about taking it one step further by using nano Calcium Oxide (CaO) catalyst derived from mineral industry waste. The nano-catalyst was synthesized from waste and characterized by XRD, FTIR, TGA, BET analysis. From the laboratory studies it was observed that this catalyst reduces the associated pollution problems and increases the energy economy. The fuel thus produced had reduced sulphur due to the formation of sulphated salts during pyrolysis. Further, it is intended towards optimizing the process to produce quality fuel. The fuel produced was recovered in three distinct product streams and characterized as per ASTM test methods. Thus, this advanced process gives an integrated solution which is environmentally and economically superior for conversion of waste tyres to fuel.

Keywords Nano-catalyst · Pyrolysis fuel · Characterization · Energy efficiency

27.1 Introduction

The disposal of solid waste is a major environmental pollution contributor across the globe. This waste mainly includes non-biodegradable high-density materials such as rubber and plastic waste, municipality solid waste, industrial waste, agriculture waste and their generation is increasing at higher rates day by day [1]. Waste management codification demands an economical and environmental system that can solve the waste disposal problem.

One of the major source of solid waste management problem is disposal of scrap tyres because they are non biodegradable, artificial long chain hydrocarbon con-

C. Gabani · Y. Ranchh · R. Barodia · P. Sivakumar (✉)
School of Petroleum Technology, Pandit Deendayal Petroleum University, Gandhinagar 382007, India
e-mail: sivakumar.p@spt.pdpu.ac.in

G. Anand et al. (eds.), *Nanotechnology for Energy and Water*,
Springer Proceedings in Energy, https://doi.org/10.1007/978-3-319-63085-4_27

taining polymer and can last for several decades when proper handling is not carried out. Annually, about 1.6 billion scrap tyres are generated which is attributed to the increase in global consumption of tyres for both public and commercial transportation [2, 3]. To solve this problem there are various tyre disposal options such as landfills, burning, open dumping, reclaiming, grinding, incineration, retreading etc. But these processes have their setback and serve as a potential health and environmental hazard. To curb this leading problem, it is essential to dispose it safely.

Recently, pyrolysis of waste tyres is becoming an important topic of research, because it is a technically feasible and an eco friendly way to dispose and the resultant energy recovery is an added advantage [4, 5]. Pyrolysis is a thermo chemical process in which organic materials are thermally decomposed into simpler constituent components when subjected to high heat and oxygen free atmosphere [2, 3]. The three basic products of pyrolysis are solid residue (char), liquid (crude oil) and gases. Here, the gases having a mixture of H_2, H_2S, CO, CO_2, CH_4, C_2H_4, C_3H_6 etc. have high calorific value that can be recycled in the same process. The liquid can be used as a substitute for diesel in internal combustion engine, fuel oil or petroleum refinery feedstock whereas, the solid residue can be used as a low-grade activated carbon, in cement manufacturing process and as an additive for road bitumen [6].

The main advantages of the pyrolysis process include simple equipment, ability to handle any sort of rubber material and, low pressure operation. It has negligible waste product, high energy conversion efficiency, neither toxic nor environmental hazardous [7]. However, there is an existence of some problem related to the use of liquid products due to their low quality, high sulfur content and variability of properties [8]. So, catalysts were introduced into the process to reduce sulfur content in the fuel and the extreme operating conditions. There are various catalysts used for pyrolysis process. Among them, calcium oxide is an attractive option because it produces low sulfur content liquid product when compared to other catalysts. The calcium carbonate obtained from mining industries wastes is easily available and cheaper. In this study, calcium carbonate was reduced to nano size and converted into calcium oxide nano catalyst that was investigated for catalytic pyrolysis of waste tyres.

The main objectives of this study are to solve the major environmental and economic problem related to tyre pyrolysis, and to obtain high quality and low sulfur fuel by using nano catalyst. This reduced the solid mass, sulfur content in liquid fuel and operating temperature.

27.2 Experimental Section

27.2.1 Materials Preparation

The scrap tyres used in this experiment were collected from the Chiloda waste tyre dump site, Gandhinagar district. They were cut into small pieces and the steel treads were removed manually. Further, it was washed, dried and shredded to 3–5 mm.

Calcium oxide nano catalyst was prepared by decomposing mineral rich in calcium carbonate. This waste material was obtained from mineral processing industry. Initially, it was crushed in a gyrated crusher and further it was reduced to nano size in a high rate planetary mill. These nano sized particles were calcinated at high temperature to get nano calcium oxide. The calcination temperature of the carbonate mineral was determined by TGA thermogram (TA instruments SDT Q600, German). FTIR spectrum of calcium carbonate mineral and calcium oxide were obtained from Perkin Elmer, spectrum RX I (USA) using spectroscopically pure KBr.

For the synthesis of nano calcium oxide catalyst 100 g of calcium carbonate was heated up to 800 °C and maintained for 30 min in a muffle furnace. The produced calcium oxide was cooled in desiccators and sealed in polypropylene bags to prevent from poisoning by CO_2 and H_2O.

27.2.2 Characterization

To get the desired efficiency of nano catalyst in pyrolysis process, the crystal structure, shape, size and surface area of nano catalyst are more important and must be specific. Thus nano calcium oxide catalyst was characterized by XRD, BET analysis. Crystal structure and size of the nano catalyst was characterized using Empyrean, PANalytical X-ray diffractometer. The total surface area was analyzed by HORIBA SA-9600 series surface area analyzer (Japan).

27.2.3 Pyrolysis

Pyrolysis is the chemical decomposition of organic material at an elevated temperature in the absence of oxygen. The main reaction was carried out with 100 g of shredded scrap tyre and 1 g of nano calcium oxide as catalyst in a parr reactor up to 500 °C temperature heated at the rate of 15 °C min^{-1}. The system was maintained at this temperature for 30 min to ensure the complete conversion of tyres. To validate the positive effects of nano-catalyst pyrolysis a controlled reaction was also carried out without a catalyst under the same process condition.

27.3 Results and Discussion

27.3.1 Preparation and Characterization of Catalyst

The results of TGA showed the thermal decomposition pattern for $CaCO_3$ rich mineral in three steps. The initial decrease was observed at 80–173 °C. It was 2.3 wt% which

is due to the removal of bounded and unbounded moisture. The second small decrease of 0.82 wt% at 470–546 °C was observed which is due to the removal of hydrates and the final decomposition occured at 697–792 °C this was due to the calcinations of calcium carbonate to calcium oxide. Even with a further increase in temperature, the peak remained constant indicating that the conversion was complete. According to stoichiometric proportion 56 wt% of CaO should be obtained but 61.4 wt% was obtained due to the presence of 5.4 wt% of natural impurities (Silica, Magnesium oxide etc.).

The FTIR spectrum clearly showed that the raw sample containing calcium carbonate that resembled by the peak at 721, 883, 1495, 1801, 2535, 2909 and 2995 cm^{-1}. The band at 1490 cm^{-1} is due to asymmetrical and symmetrical lengthening of the O-C-O bond whereas, inplane and outplane bending modes of carbonate anion bands were correspond to 715 and 880 cm^{-1} respectively. Absorption bands at 715, 880 and 1490 cm^{-1} were assigned to calcite phase of $CaCO_3$. After calcinations, the broad bands obtained between 250 and 600 cm^{-1} indicate calcium oxide. Peaks at 1417 and 866 cm^{-1} were ascribed to C-O bond. Thus, the FTIR spectrum conforms the formation and presence of calcium oxide.

In XRD, peaks appeared at 32.1, 37.2, 53.4, 64.8 and 67.9 associated with (111), (200), (220), (311) and (222) cubic structure of calcium oxide. The crystal sizes determined by Sherrer's equation were between 40–89 nm. Surface area was analyzed by BET. Surface area of $CaCO_3$ and CaO were 5.25 and 435.54 m^2g^{-1} respectively. The pore volume and pore diameter of CaO were 0.467 cm^3g^{-1} and 28 nm.

27.3.2 Thermal and Catalytic Pyrolysis

Pyrolysis was performed in parr reactor with 100 g of different tyre samples loaded without and with 1 wt% of nano calcium oxide catalyst. The results obtained are listed in Table 27.1. It is clear that the use of nano catalyst increased the yield of

Table 27.1 Physiochemical characterization of tyre pyrolysis product

Characteristics	Thermal pyrolysis	Catalytic pyrolysis
Weight of tyre charged	100 g	100 g
Max. temp	500 °C	500 °C
Holding time at 500 °C	30 min	30 min
95% oil recovery temp	496 °C	454 °C
Catalyst (wt%)	0%	0.5%
Liquid (wt%)	34%	46%
Residue (wt%)	38%	19%
Gas product (wt%)	28%	35%
Sulfur (Gas)	4.2%	5.1%
Sulfur (Liquid)	1.6%	0.2%
Sulfur (Solid)	1.2%	1.4%

liquid and gaseous product. The catalyst, being in nano size, it mixes thoroughly with the reactant at transition temperature of rubber to make the reaction efficient. While comparing the sulphur content, it was found that the sulfur in gaseous and solid products was high. This is due to the cracking of organic sulfur compounds into smaller non condensable gases whereas the fixing of sulfur takes place in residue to form of elemental sulfur and sulfates in solid.

27.4 Conclusion

In this study, the conversion of waste tyres into valuable liquid hydrocarbons by catalytic pyrolysis was investigated. The effects of nano catalyst on maximum recovery temperature of the product and quality of oil from catalytic pyrolysis were investigated. The main conclusions obtained by applying nano catalyst in pyrolysis are as follows:

1. The main problem preventing the use of waste tires as an alternative fuel is due to the high levels of sulfur compounds in the pyrolysis product which is solved by nano catalyst. The nano calcium oxide catalyst increases the concentration of sulfur in gaseous and solid phases to reduce the percentage of sulfur in liquid yield.
2. The process became economically viable owing to moderate temperature requirement. Reduction of above 50 °C was observed to yield maximum oil (95 wt%) was obtained in catalytic pyrolysis. The uncondensed gaseous product has high calorific value which is enough to be reused for heating purpose in the pyrolysis reaction after scrubbing.
3. Lesser amount of solid residue remained in catalytic pyrolysis than thermal pyrolysis resulting in increased quantity liquid and gas phase.

Thus, the eco-friendly technique of tyre pyrolysis was optimized and the nano catalyst solves the main problem of environment pollution by existing tyre pyrolysis plant. With further studies can result into commercially profitable business.

References

1. S.T. Kumaravel, A. Murugesan, A. Kumaravel, Tyre pyrolysis oil as an alternative fuel for diesel engines—A review. Renew Sust Energy Rev **60**, 1678–1685 (2016). doi:10.1016/j.rser.2016.03.035
2. D. Bunthid, P. Prasassarakich, N. Hinchiranan, Oxidative desulfurization of tire pyrolysis naphtha in formic acid/H_2O_2/pyrolysis char system. Fuel **89**, 2617–2622 (2010). doi:10.1016/j.fuel.2010.04.026
3. P.T. Williams, Pyrolysis of waste tyres: a review. Waste Manag. **33**, 1714–1728 (2013). doi:10.1016/j.wasman.2013.05.003

4. A. Quek, R. Balasubramanian, Liquefaction of waste tires by pyrolysis for oil and chemicals-A review. J. Anal. Appl. Pyrol. **101**, 1–16 (2013). doi:10.1016/j.jaap.2013.02.016
5. J.I. Osayi, S. Iyuke, S.E. Ogbeide, Biocrude production through pyrolysis of used tyres. J. Catal. **1**, 1–9 (2014). doi:10.1155/2014/386371
6. M.R. Islama, M.N. Islama, N.N. Mustafia, M.A. Rahima, H. Haniub, Thermal recycling of solid tire wastes for alternative liquid fuel: the first commercial step in Bangladesh. Procedia Eng **56**, 573–582 (2013). doi:10.1016/j.proeng.2013.03.162
7. K. Tudu, S. Murugan, S.K. Patel, Light oil fractions from a pyrolysis plant-an option for energy use. Energy Procedia **54**, 615–626 (2014). doi:10.1016/j.egypro.2014.07.303
8. S. Boxiong, W. Chunfei, I. Cai, G. Binbin, W. Rui, Pyrolysis of waste tyres: the influence of USY catalyst/tyre ratio on products. J. Anal. Appl. Pyrol. **78**, 243–249 (2007). doi:10.1016/j.jaap.2006.07.004

Chapter 28
Utilization of Geo-Solar Hybrid System for Efficient Power Production in India

Anirbid Sircar, Shishir Chandra and Manan Shah

Abstract Geothermal, Solar Energy combined can give a suitable working temperature for an Organic Rankine Cycle to be highly efficient. Solar energy is utilized to raise the temperature of the geothermal fluid (at 60–65 °C) up to 85 °C (minimum temperature for power generation through ORC). The paper focusses on major comparisons between combined Geothermal-solar energy source and conventional energy source. As CO_2 issues continue to degrade the environment and fossil fuels become more expensive, interest in low grade heat recovery has grown in the past few years. Hybrid Solar and Geothermal energy, as a clean, renewable, pollution-free and sustainable energy has great potential for the use of ORC systems.

28.1 Introduction

Numerous technical reasons are associated with a renewable geothermal-solar hybrid plant to make it a growing energy demand. The energy consumption in India is quite significant because of the resources consumption due to vast number of population for agriculture, residents, and industries purposes. Despite the increased power availability in India, the supply still continues to elude the demand [1].

The basis of writing this paper is the inability to produce power from the widely spread existence of low enthalpy geothermal reservoir in India. However, the utilization of low enthalpy geothermal resources in hybrid with the solar energy for electricity generation has not received sufficient attention so far [2]. Geothermal plants lose a lot of efficiency when operating in low temperatures where drilled holes yield steam at a temperature of around 100 °C [3]. Motivation to consider the hybrid power plants in geothermal power production is the decreasing production fluid temperature, flow rate, or both. Employing such carbon-free sources can help to combat climate change by lowering the extensity of fossil fuel combustion [4].

A. Sircar · S. Chandra (✉) · M. Shah
School of Petroleum Technology, Pandit Deendayal Petroleum University, Gandhinagar, Gujarat, India
e-mail: shishir.cmtpe15@spt.pdpu.ac.in

G. Anand et al. (eds.), *Nanotechnology for Energy and Water*,
Springer Proceedings in Energy, https://doi.org/10.1007/978-3-319-63085-4_28

28.2 Potential in India

Promising areas of geothermal energy are identified in Himalayan area, Puga, Manikaran, Chhumatang, Beas and Satlej field, Chamoli and Western India [5] as shown in Fig. 28.1. India has good potential for geothermal; the potential geothermal provinces can produce 10,600 MW of power [6].

Whereas, the installed capacity of solar energy projects in India is approximately 3000 MW [7] as shown in Fig. 28.2. Solar energy recently experienced a vast

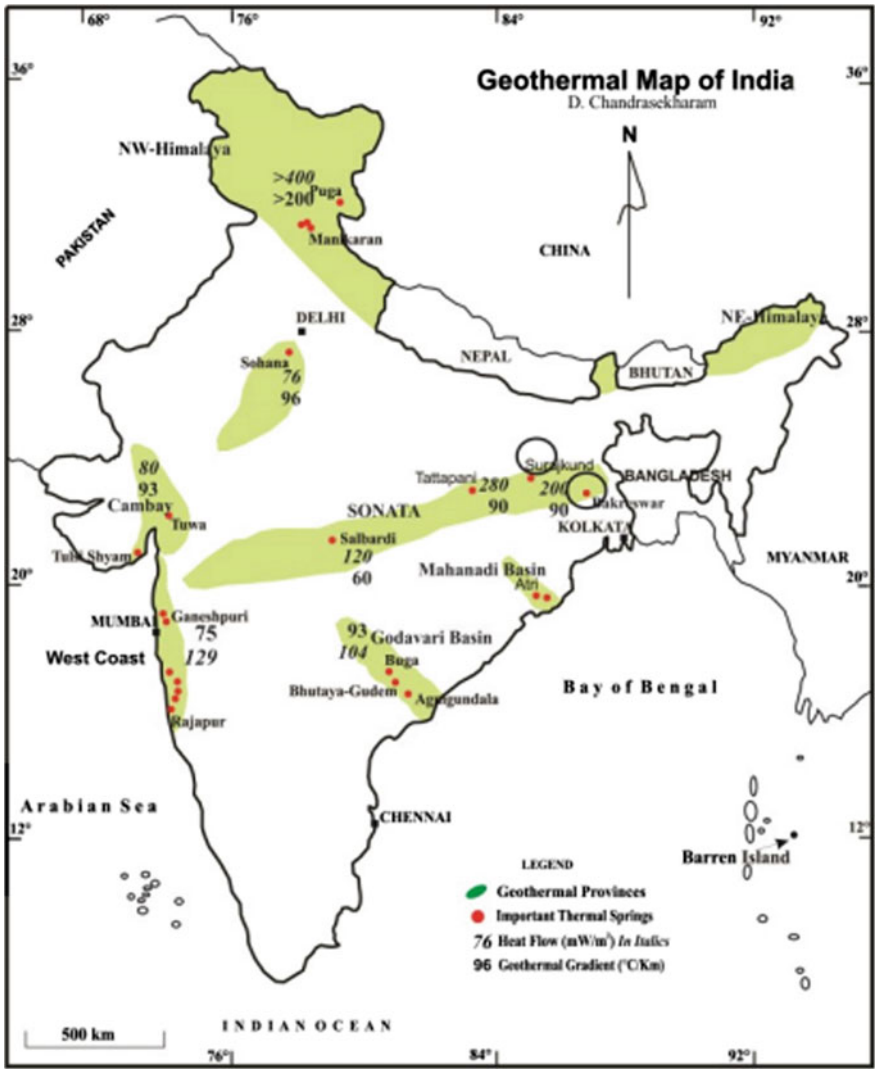

Fig. 28.1 Geothermal provinces in India (Chandrasekharam 2010)

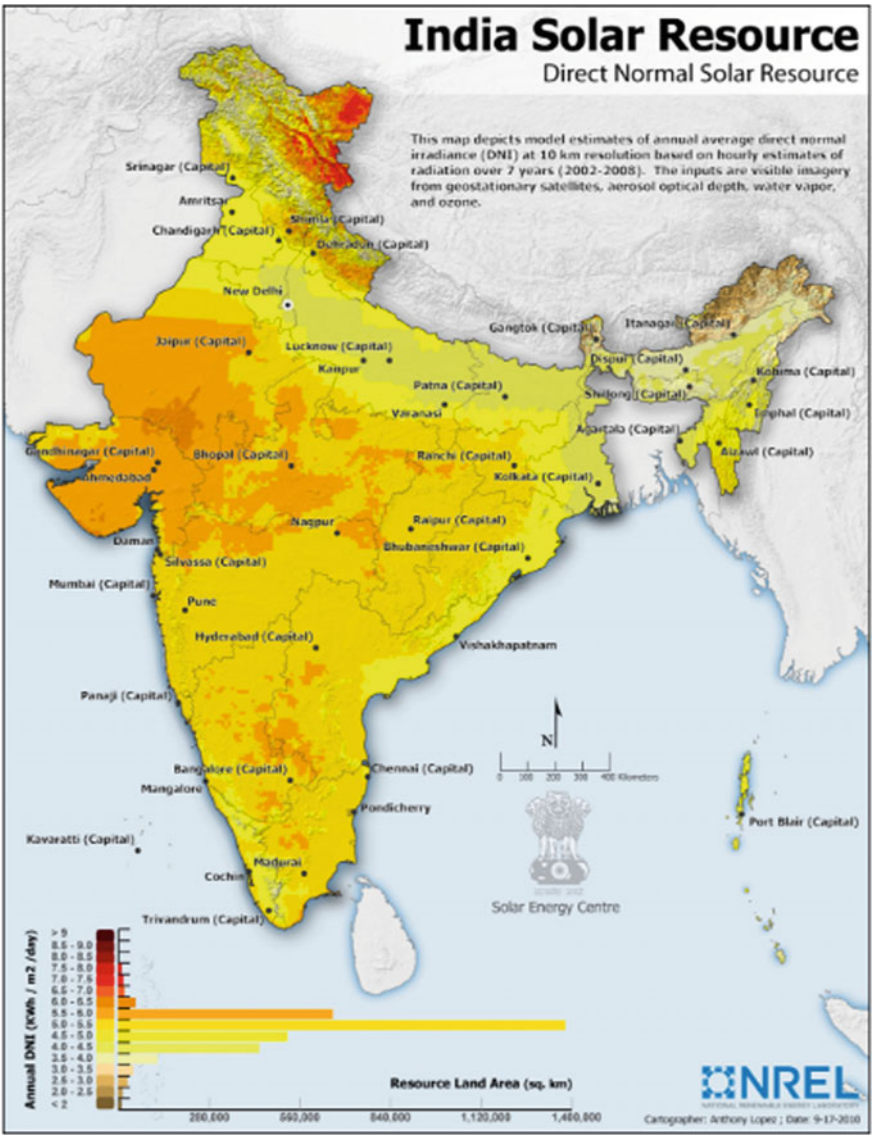

Fig. 28.2 Direct normal solar resource (National Renewable Energy Laboratory)

growth due to technological improvements resulting in cost reductions and government policies supportive of renewable energy development and utilization.

A low enthalpy geothermal resource means that the brine, or water from the Earth, comes out at a temperature between **100–150 °C**, which is considered too low for economic electricity production. By augmenting the thermodynamic quality of the brine with solar energy, higher performance should be possible. The goal is

to find cost-effective hybrid power cycles that take advantage of the potential synergies of solar thermal and geothermal resources. There are certain areas in India like Tattapani, Cambay Basin, Mahanadi Basin, and Godavari Basin that have a geothermal reservoir and also get a good amount of sunlight. These are the areas where [8].

28.3 Methodology

The most popular configurations that have been analyzed are as follows [9]:

1. **Superheating the working fluid**: In order to achieve a greater exergy from working fluid and higher power generation, the heat from the sun is used to heat up the working fluid just before it enters the turbine.
2. **Brine recirculation**: a fraction of brine, coming from the heat exchangers, is heated using solar energy and then mixed again with the feed brine. The higher power generation is achieved with the reduction fresh brine requirement.
3. **Brine preheat**: this method results in increased brine enthalpy and higher power generation. Before entering the heat exchangers, the solar heat raises the geothermal brine temperature.
4. **Brine preheat/recirculation concept**: the temperature of both the geothermal brine entering the heat exchanger and the fraction of recirculating brine is raised. Hence the fresh brine requirement is reduced, the brine enthalpy increases and henceforth the power generated is higher.
5. **Brine cascade reheat concept**: the temperature of recirculating brine is raised at the exit of the heat exchanger. The temperature is raised up to original value and this is fed into the second heat exchanger. Hence, the same field produces the higher power.

The previous studies done indicate that the above different configurations are useful to enhance various parameters of the hybrid system. It was seen that in order to achieve the lowest per unit cost of electricity, the pre-heat and the superheat configurations are the most suited. Similarly, to achieve the highest maximum solar energy utilization, the cascade and reheat configuration are suitable.

28.4 Discussion

There are many common grounds on which one can point out the similarities between the geothermal and solar thermal systems. Some parameters on the basis of which the viability of both the systems can be analyzed are as follows [10].

- **Ability to Meet Demand Better**: Geothermal power plants, commonly use air-cooled condensers and hence there is a decrease in power produced during

day. This is because of the increased ambient temperature. As a result the plant is not able to reject heat to the surroundings. The solar energy can be used to enhance the plant performance.

- **Boosting Power to Existing Plants**: solar thermal technology can take advantage of the existing infrastructure and hardware
- **Maximizing operational efficiency**: Higher renewable energy generation from the same geothermal technology.
- **Equipment Sharing**: Turbines, condenser and heat exchangers are common, hence can be jointly used
- **Financial preview**: Cost of electricity higher than geothermal plants but lower than solar thermal plants [11].
- **Incentives**: A hybrid system is qualified for more forms of economic support [11].

28.5 Conclusion

Geothermal energy is one of the emerging alternative for power generation as it can provide base load electricity [3]. Thermal efficiency of geothermal electric plants are in the range of 10–23% as heat or energy extraction limits the efficiency of the process [6]. Hybridizing a low enthalpy geothermal plant with a solar thermal energy conversion system increases the thermal efficiency; higher than the stand alone geothermal plant [12]. Thermal efficiency of the hybrid plant are always higher than the stand alone geothermal plant and less than the stand alone solar thermal plant. The cost of electricity generation from hybrid system is higher than geothermal plant but lower than the solar thermal plant [13].

References

1. F.A. Ahangar, *Feasibility Study of Developing A Binary Power Plant in the Low-Temperature Geothermal Field in Puga, Jammu and Kashmir, India*. (Geothermal Training Programme, United Nations University, Iceland, 2012)
2. D. Wendt, G. Mines, C. Turchi, G. Zhu, Geothermal risk reduction via geothermal/solar hybrid power plants. Final Report (Idaho National Laboratory, 2015)
3. M.C. Bora, Geothermal energy: Indian scenario. (2010)
4. A. Turan, Assessment of geothermal and solar hybrid power generation technologies in Turkey and its application to Menderes Graben, in *Proceedings World Geothermal Congress 2015,* Melbourne, Australia, 19–25 April 2015
5. V. Kakkar, N.K. Agarwal, N. Kumar, Geothermal energy: new prospects. Int. J. Adv.Eng. Technol., (2012)
6. D. Chandrasekharam, Geothermal energy resources of India: past and the present, *in Proceedings World geothermal congress 2005,* Antalya, Turkey, 24–29 April 2005
7. A. Upadhyay, A. Chowdhury, Solar energy fundamentals and challenges in indian restructured power sector. Int. J. Sci. Res. Publ. **4**(10), (2014)

8. D. Vaidya, M. Shah, A. Sircar, S. Sahajpal, A. Choudhary, S. Dhale, Geothermal energy: exploration efforts in India. Int. J. Latest Res. Sci. Technol. J. **4**(4), 61–69 (2015)
9. A.D. Greenhut, J.W. Tester, R. DiPippo, R. Field, C. Love, K. Nichols, C. Augustine, F. Batini, B. Price, G. Gigliucci, I. Fastelli, Solar—geothermal hybrid cycle analysis for low enthalpy solar and geothermal resources, *in Proceedings World Geothermal Congress* 2010, (Bali, Indonesia; 2010)
10. Ö. Çağlan Kuyumcu, Umut Z.D. Solaroğlu, Sertaç Akar, B.M. Onur Serin, Holdings Inc, Turkey Ankara, Hybrid geothermal and solar thermal power plant case study; Gümüsköy GEPP. Geoth. Res. Counc. Trans. **36**, 1091–1096 (2012)
11. A.D. Greenhut, *Modeling and Analysis of Hybrid Geothermal-Solar Thermal Energy Conversion Systems* (Dept. of Mechanical Engineering, Massachusetts Institute of Technology, USA, 2010)
12. C. Zhou, E. Doroodchi, B. Moghtaderi, An in-depth assessment of hybrid solar—geothermal power generation. Energy Conver. Manage. **74,** 88–101 (2013) Elsevier
13. P.N. Mathur, Assessment of solar—geothermal hybrid systems concepts (1979), p. 47

Chapter 29
Wear Properties of A356/Al2O3 Metal Matrix Composites Produced by Insitu Squeeze Casting Techniques

Amneesh Singla, Rajnish Garg and Mukesh Saxena

Abstract Tribological behaviour of vanadium pentoxide reinforced A356 composite prepared by reacting oxide particles in different weight percentage with A356. The effect of oxide powder addition on tribological properties of produced composite was investigated. Sliding velocity, sliding distance, normal load and mass fraction of V_2O_5 particles were among the factors considered in the study. The influence of these factors on the tribological behaviour of the fabricated composite was analysed experimentally and discussed with surface morphologies. A notable augmentation in terms of hardness has been recorded which in turn enhanced and improved the tribological properties of prepared composites in comparison with the base alloy i.e. A356. Refinement of in situ V_2O_5 particles can be attributed the formation of hardened precipitates which in turn resulted in increase in the hardness of the composites.

Keywords A356 alloy · V_2O_5 · Hardness · Insitu · Dry sliding wear

29.1 Introduction

Al–Si is one of the most preferred Aluminium alloy available so far, due to their excellent mechanical properties. Commercially they are accessible as hypoeutectic & hypereutectic materials. Al–Si alloys are also known as foundry alloys and contributing around 80% of aluminium casting because of their good cast ability [1]. In case of Al–Si alloy the presence of Si phase provides good wear resistance to these alloys. Aluminium alloys in itself exhibit discouraging tribological properties but the induction of ceramic or oxide particles inside the Aluminium alloys significantly helps in eradicating these drawbacks and improve mechanical and

A. Singla (✉) · R. Garg
University of Petroleum and Energy Studies, Dehradun, India
e-mail: amneesh82@gmail.com

M. Saxena
University of Technology and Management, Shilong, India

G. Anand et al. (eds.), *Nanotechnology for Energy and Water*,
Springer Proceedings in Energy, https://doi.org/10.1007/978-3-319-63085-4_29

tribological properties altogether. These particles were incorporating in the melt by the conventional stir casting route which could lead to poor bonding & segregation of reinforcement particles at the interfaces [2, 3]. In recent times, in situ techniques have been developed which prompt the better mechanical properties because of better adhesion at the interface. In situ process give points of interest for example, uniform dispersion, thermodynamically stable and clear interface of reinforcements compared to exsitu processes [4].

The intent of present work is to carry out an experimental study on A356 alloy composite prepared with the substitution of vanadium pentoxide. The metal oxides added externally which aluminium melt reduces and generate alumina particles. Vanadium pentoxide believes to form covalent bonding at the interface and possesses commendable hardness and strength compare to other reinforced particles inside the aluminium matrix. There is growing interest among the researchers these days to carry out studies on these materials. The effect of significant parameters such as sliding velocity, sliding distance, mass fraction, and normal load of V_2O_5 particles on wear rate has been study in the present investigation.

29.2 Experimental Procedure

29.2.1 Composite Development

The experimental study involved readily available A356 and V_2O_5 extra pure particles. For the casting purpose furnace having bottom pouring facility has been used. The stirrer blade used in the experiment was made up of stainless steel having three bent and is coated with fine paste of graphite in order to prevent the dissolution of steel in molten aluminium takes place. When the melt temperature reaches at 750 °C, V_2O_5 was added at a very slow rate in the presence of argon gas. The position of the stirrer was kept constant to disperse the V_2O_5 particle into the melt. The stirrer speed was kept at 700 rpm for the vortex formation. After 15 min of stirring the melt is poured in a preheated steel mould. Degassing of the melt is carried out at this stage for vacuum casting. The Stir casting furnace used for the composite development is shown in Fig. 29.1.

29.2.2 Pin on Disc Test Configuration

Pin on disc tribo meter, in compliance with standard test methods of ASTM G99-95 has been used to probe the tribological behaviors of multitude of composites. Frictional forces and wear has been estimated by the use of sensors and LDTV

Flat cylindrical pins with dimensions of 5 mm radius and 30 mm height had been utilized for test. The counter face disc of EN-31 steel hardened to 60 HRC was

Fig. 29.1 Stir casting furnace

of maximum diameter of 165 mm. thickness of disc was 8 mm; limit of disc track diameter was 145 mm. 10, 20 and 30 N were the values of applied loads with constant values of sliding distance and sliding velocity of 1000 m and 0.83 m/s. Ambient conditions were maintained during the progression of test. Grit papers of 400, 600, 800, and 1000 were utilized for the cleaning and polishing purpose of the surface.

29.3 Result and Discussion

Figure 29.2, shows the variation of pin volume loss as the function of load for 1000 m sliding distance (steady state regime).

Decrease in volume loss is observed in the cast in situ composite as compared to cast Al–Si alloy. The comparison of volume loss at 10, 20 and 30 N with sliding distance 1000 m is shown in figure. At reduction in volume loss has been observed

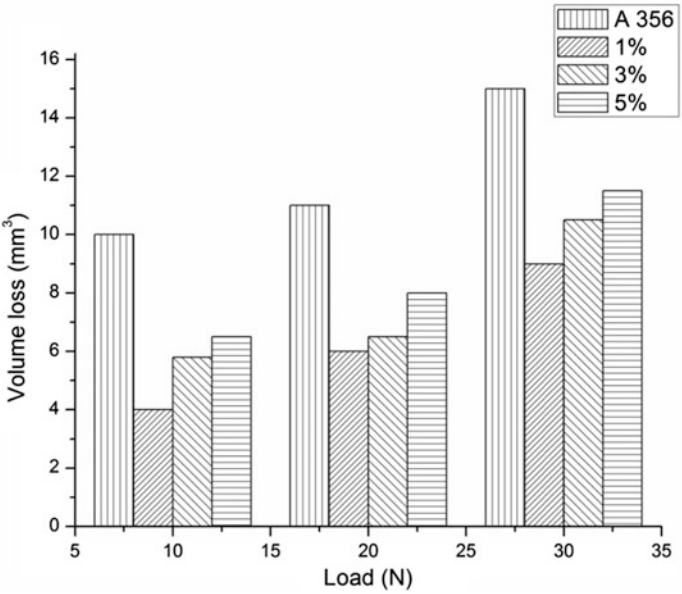

Fig. 29.2 Variation of volume loss with respect to load

in as cast insitu composite as compared to Aluminium alloy. The average reduction in volume loss was 47.3, 36.3 and 27.5% for Al-7Si-1, 3 and 5% cast samples respectively. The porosity content in cast composites is little higher than that in pure aluminium. Therefore, reduction in volume loss in insitu composite over the pure aluminium could be attributed to the effect of reinforcing particles in the aluminium matrix.

From the Fig. 29.3, it can be inferred that with higher percentage of V_2O_5 particles wear debilitates. Hardness shoots up with the progressive introduction of oxide particles. The formation of oxide debris during the dry sliding test led to locking of these debris which eventually resulted in surge in wear. However, these particles form a compressed protective layer at low loading condition. Hence, this layer corresponds to the dwindling wear rate [5]. But for 7% addition specific wear rate tends to increase. Again porosity in cast in situ composite is responsible for this increase. Hardness and tensile properties also get influenced by porosity. The real area of contact increases with higher porosity and eventually increases the wear rate.

Hence porosity not only leads to softening of material but it also encourages the delamination and subsurface cracks.

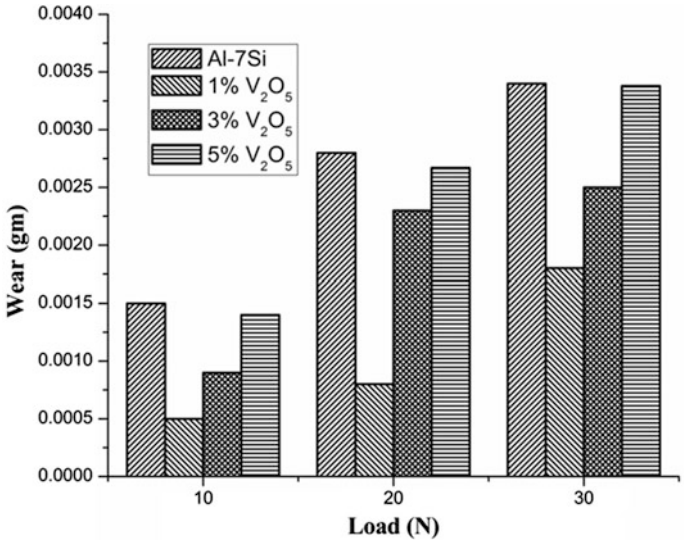

Fig. 29.3 Wear variation with different loads

29.4 Conclusions

The nonlinear downfall of wear rate has been observed with increasing mass fraction of V_2O_5 particles. This increase in hardness may be attributed to presence of hard phase of alumina. Also with high degree of dislocations around the V_2O_5 particles due to difference in thermal expansion between matrix and reinforcement led to increase on resistance to wear.

References

1. J.E. Gruzleski, B.M. Closset, *Liquid treatment to Al-Si alloys* (AFS, Illinois, 1990), pp. 1–254
2. L.N. Thanh, M. Suéry, Influence of oxide coating on chemical stability of SiC particles in liquid aluminium. Scr. Metall. Mater. **25**(12), 2781–2786 (1991)
3. B.S. Murty, S.K. Thakur, B.K. Dhindaw, On the infiltration behavior of Al, Al-Li, and Mg meltas through SiC p bed. Metall. Mater. Trans. A **31**(1), 319–325 (2000)
4. S.C. Tjong, Z.Y. Ma, Microstructural and mechanical characteristics of in situ metal matrix composites. Mater. Sci. Eng. R: Rep. **29**(3), 49–113 (2000)
5. T.P. Murali, S.V. Prasad, M.K. Surappa, P.K. Rohatgi, Friction and wear behavior of aluminum alloy coconut shell char particulate composites. Wear **80**, 149–158 (1982)

Chapter 30
Effect of Heterogeneous Catalyst on Esterification of Pyrolysis Oil

Praveen Ghodke and S. Vamsi Krishna

Abstract The bio-oil from fast pyrolysis of biomass cannot be used effectively as engine fuel because of its high corrosiveness and instability mainly due to substantial amounts of organic acids and reactive aldehydes. In this paper treatment of acids in the bio-oil was focused and esterification with different catalyst to convert the acids. Synergistic interactions among reactants and products were determined. Acid-catalyst removed water and drove the esterification reaction formation equilibria toward ester products. Effect of Amberlyst-15 on different acids present in the bio-oil was carried out and characteristics properties of bio-oil shown after treatment were improved. Catalyst characterization was carried and observed that carbon deposition on the surface of catalyst reduces the activity of the Amberlyst-15. The catalysts with high surface area, large pore size distribution, and strong acid sites may be beneficial for the esterification reaction.

Keywords Bio-oil · Esterification · Amberlyst-15 · Pyrolysis

30.1 Introduction

One of the main fields of energy consumption is the transportation sector, constituting about one fifth of the total [1]. This requirement constitutes one of the major challenges of the near future, as present fuels primarily are produced from crude oil and these reserves are depleting [2]. Substantial research is being carried out within the field of energy in order to find alternative fuels to replace fossil fuels. The optimal solution would be renewable energy resource which is sustainable and will decrease the CO_2 emission. Biomass derived fuels could be the prospective fuels of tomorrow as these can be produced within a relatively short cycle and are considered benign for the environment [3].

P. Ghodke (✉) · S.V. Krishna
University of Petroleum and Energy Studies, Dehradun, Uttarakhand, India
e-mail: gpkumar@ddn.upes.ac.in

G. Anand et al. (eds.), *Nanotechnology for Energy and Water*,
Springer Proceedings in Energy, https://doi.org/10.1007/978-3-319-63085-4_30

Fast pyrolysis can directly produce a liquid fuel from biomass which can be readily stored or transported [4–10]. A large variety of applications for bio-oil have been proposed. Examples are the use as a fuel in boiler systems, stationary diesel engines, gas turbines and sterling engines [5, 11]. However, Bio-oil has many inferior properties, such as low heating value, high oxygen content, high water content, acidity, instability, and incompatibility with standard petroleum fuels [1, 5, 12–16]. It cannot be used as high-quality fuels like gasoline and diesel without any treatments. A number of bio-oil upgrading technologies have been proposed to improve the product properties and to increase the range of possible applications. The majority of the past bio-oil upgrading efforts to date have revolved around catalytic hydrotreating [14, 17–25] and zeolite upgrading [26–31]. These methods suffer from several drawbacks such as catalyst coking and low yields to valuable products [27, 29, 32, 33]. Hence, it is imperative to develop alternative bio-oil upgrading technologies.

A number of studies have been reported dealing with esterification of crude bio-oil by reacting it with alcohol (e.g., methanol) [15, 31, 34–45]. Simultaneous hydrotreating and esterification reactions to upgrade bio-oil have also been investigated [14, 19, 46, 47]. It is anticipated that reactive molecules like organic acids and carbonyl compounds are converted by the reactions with alcohols to esters and acetals as shown in Fig. 30.1a, b, respectively.

It is possible to produce high quality bio-oils by in-line esterification of pyrolysis vapor using ethanol [48]. A reactive distillation based process that uses alcohols like butanol, ethylene glycol and 2-Ethyl hexanol in the presence of solid acid Nafion as a catalyst has been proposed [32]. The heating value and acidity are reported to be considerably improved. In another study [49], it has been revealed that one-pot hydrogenation and esterification improves the bio-oil quality significantly. Pt supported on zeolite was used as a catalyst. Amberlyst-70 is reported to have worked well to facilitate both esterification and acetalization simultaneously. Removal of water is essential to drive the equilibrium in the forward direction. For this purpose molecular sieves have also been proposed to capture the water during the reaction [50]. Though there have been successful attempts to stabilize bio-oil using these techniques on laboratory level, a substantial work still needs to be done on various fronts to scale up this technique. The systematic experimentation on the progress of reaction, effect of different parameters, catalyst reusability etc. is necessary to take this approach forward. It is with this purpose that the present work is undertaken.

In this paper, esterification of bio-oil based on reactive distillation using n-butanol as the reacting alcohol is studied in the presence of Amberlyst-15 as the solid acid catalyst is studied. The bio-oil obtained by this process is examined for the heating value (HHV), water content, viscosity, pH and the shelf life.

Fig. 30.1 Esterification of carboxylic acids

Reactive distillation combines both distillation and chemical reaction into a single unit. In this process, the water in the crude bio-oil as well as the water produced by the various chemical reactions is removed simultaneously by distillation in a single step. It drives the equilibria to completion and is expected to reduce acidity. To prevent excessive evaporation of the reacting alcohol, those alcohols with a boiling point higher than water are chosen. n-Butanol was selected as it is available from renewable resources by fermentation processes [51]. The use of a homogeneous acid catalyst such as sulfuric acid for esterification causes difficulties in recovery after the reaction and produces toxic waste water. Solid acid catalysts such as Amberlyst-15 have been studied as substitutes for sulfuric acid, and have the advantages of being easy to recover and reuse, as well as being compatible with environmental considerations [52–55].

The article is organized as follows: First we describe the experimental setup and procedure. The characterization of the product and the effect of different process parameters on the same are discussed. The catalyst was found to deactivate during the course of the reaction. The factors responsible for deactivation are identified through systematic experiments and characterization of the fresh and used catalyst.

30.2 Experimental Setup and Procedure

30.2.1 Materials

Babul wood vacuum pyrolysis is carried out in an existing pyrolysis unit at IIT-Bombay. The properties of crude bio-oil are summarized in Table 30.1. Dry Methanol (GR grade; 0.02% water max), pyridine-free Karl Fischer solution, sulfuric acid (about 98% GR) and 1-Butanol were supplied by Merck Ltd., India. The catalyst used in the experiments is a commercial strong-acid ion-exchange resin Amberlyst-15 (Dry) obtained from Rohm and Hass, India.

Table 30.1 Properties of crude bio-oil

Physical properties	Values
Moisture content (wt%)	26.36
pH	2.80
Density (kg m^{-3})	1.08
Ash (wt%)	0.03
HHV (MJ kg^{-1})	22.20
Viscosity (cP) at T = 40 °C	73.62
Elemental composition (wt%)	
Carbon	50.92
Hydrogen	8.27
Oxygen (by difference)	38.57
Nitrogen	2.23

30.2.2 Experimental Procedure

The reactive-distillation setup mainly consists of a three-neck round bottom glass flask (250 ml) equipped with stirrer and Dean-stark apparatus as shown in Fig. 30.2. The temperature in the reactor was measured using a thermometer and boil-up is maintained with the help of a heating mantle.

Typically, 50 ml of bio-oil and 50 ml of 1-butanol are mixed and mixture is filtered over a filter paper of 11 μm by applying vacuum. The filtrate thus obtained is then centrifuged for 30 min at a rate of 2420 RPM. The clear liquid is separated and charged into the reactor vessel. The reactor mixture is heated to the boiling temperature and a certain boilup is maintained. Subsequently, Amberlyst-15 (10 wt % of bio-oil) is added in the reaction mixture. The time at which the first drop of distillate appears in the condenser is considered as zero reaction time. A reaction is typically performed over a period of 120–150 min.

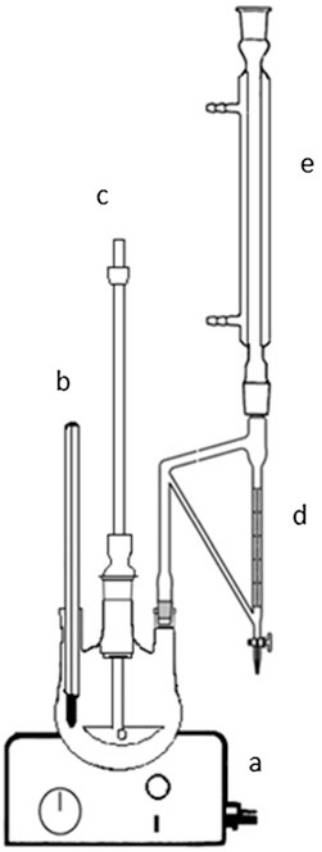

Fig. 30.2 Batch reactive distillation set-up

30.2.3 Catalyst Characterization

Thermogravimetric analysis of Amberlyst-15 is carried out over a temperature range of 120–1000 °C at rate of 2 °C/min and then kept constant for 10 min to ensure the completion of analysis and under flowing N_2 atmosphere with gas flow rate was 150 ml/min. Surface area of the catalyst is determined by a standard BET (Nitrogen adsorption at −195 °C) technique on an automated adsorption apparatus (ASAP 2020 V3.01 H, Micromeritics, USA), and surface area of fresh Amberlyst-15 was found to have 43.9 m^2/g.

30.2.4 Bio-oil Characterization

As Bio-oil is a complex matrix with more than 400 different chemical compounds present, it is difficult to evaluate the catalyst performance based on the conversions of individual components [7, 32]. However, physical properties of esterified bio-oil can be accurately quantified by various techniques. They include, moisture content by means of a Karl-Fischer titration, heating value from elemental analysis, viscosity using Cannon-Fenske viscometer tube and product identification and composition by Gas chromatography-Mass spectrometer (GC-MS).

Bio-oil distillate is analyzed qualitatively by GC-MS and quantitatively by GC-Flame ionization detector. The separation was achieved on 30 m long BP-5 column (i.d. = 0.32 mm) and film thickness of 0.25 μm. The GC oven temperature was set initially at 50 °C and then raised to 200 °C at a rate of 10 °C/min. The injector split ratio was set at 50:1, and hydrogen is used as a carrier gas with a flow rate of 0.5 ml/min. The moisture content of the crude bio-oil was determined using a Karl-Fischer titrator (VEEGO/MATIC-D). Standard method ASTM E 203 is used to measure the moisture content of crude bio-oil as well as esterified bio-oil.

30.3 Result and Discussion

30.3.1 Bio-oil Distillate

Table 30.2 Shows different components distilled out over a temperature range of 370–378 K with their weight percentages. Some of them are formed due to chemical reactions shown in Fig. 30.1. A significant amount of water is present in the bio-oil and in addition, small amount is formed in the reactions; much of it is removed using Dean-stark apparatus. This analysis shows that desired reactions proceed in forward direction and organic acids such as formic acid, acetic acid and propanoic acid which are responsible for high acidity of crude bio-oil are converted to respective 1-butyl esters. Low boiling point compounds such as methanol are

Table 30.2 Different components in distillate of Bio-oil

Sr. no	Component name	wt%
1	Methanol	0.52
2	Methyl acetate	0.26
3	1-butanol	79.83
4	1-butyl formate	7.70
5	1-butyl acetate	11.37
6	Furfural	0.19
7	di-butyl ether	0.17
8	1-butyl propionate	0.07

distilled out at this reaction temperature. di-Butyl ether is also formed in the reaction and organic layer is recycled back into the reactor vessel using Dean-stark arrangement as shown in Fig. 30.2. Small amount of furfural also appears in distillate.

30.3.2 Esterified Bio-oil

The physical properties of bio-oil such as kinematic viscosity, pH, HHV and water content are evaluated before and after the alcohol treatment. Physical appearance (e.g., color) of the products was close to that of the original bio-oil. However, the odor changed dramatically from smoky pungent to banana like. This change is due to the formation of butyl esters of organic acids having a very typical sweet, banana-like odor.

The experiments are carried out using 1wt% H_2SO_4 and without catalyst to compare the performance of solid acid catalyst in terms of the conversion of acids to esters. For 1wt% H_2SO_4, ester formation is 6.15 wt%. It would be possible to further enhance the conversion however by increasing the sulfuric acid concentration. However, as we know large amounts of sulfuric acid, result in problems such as difficulty in its separation and corrosion. Figure 30.3 shows performance of different catalysts in the production of 1-butyl acetate compared to heterogeneous catalyst Amberlyst-15. Without catalyst, reaction yield is very poor and 1-butyl acetate produced is as low as 1.76 wt%.

Esterified bio-oil using heterogonous and homogeneous catalyst is compared using the characteristics properties of bio-oil.

Figure 30.4 shows that the water content of the treated bio-oil reduces from 26.36 to 4.29 wt%. It can be further reduced by prolong heating to high temperatures but high temperatures causes polymerization reactions; moreover, catalyst thermal stability limit is 393 K [52–54]. Esterified bio-oil with sulfuric acid also shows significant reduction in the moisture content but sulfuric acid. We have found that the reactions take place even in the absence of catalyst though the extent is significantly lower than that in the presence of Amberlyst 15.

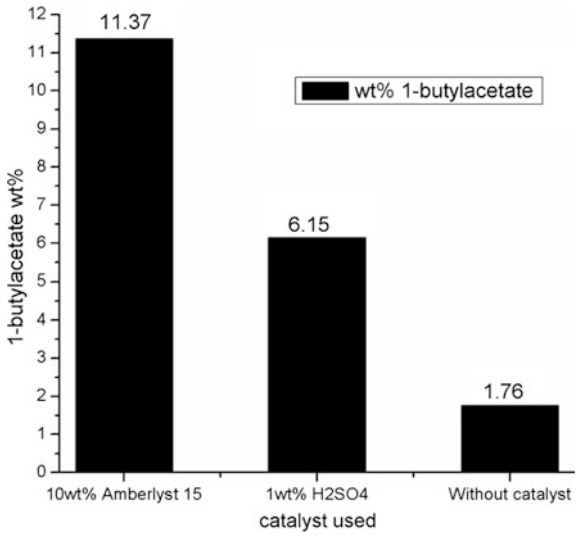

Fig. 30.3 Formation of 1-butyl acetate using different catalysts

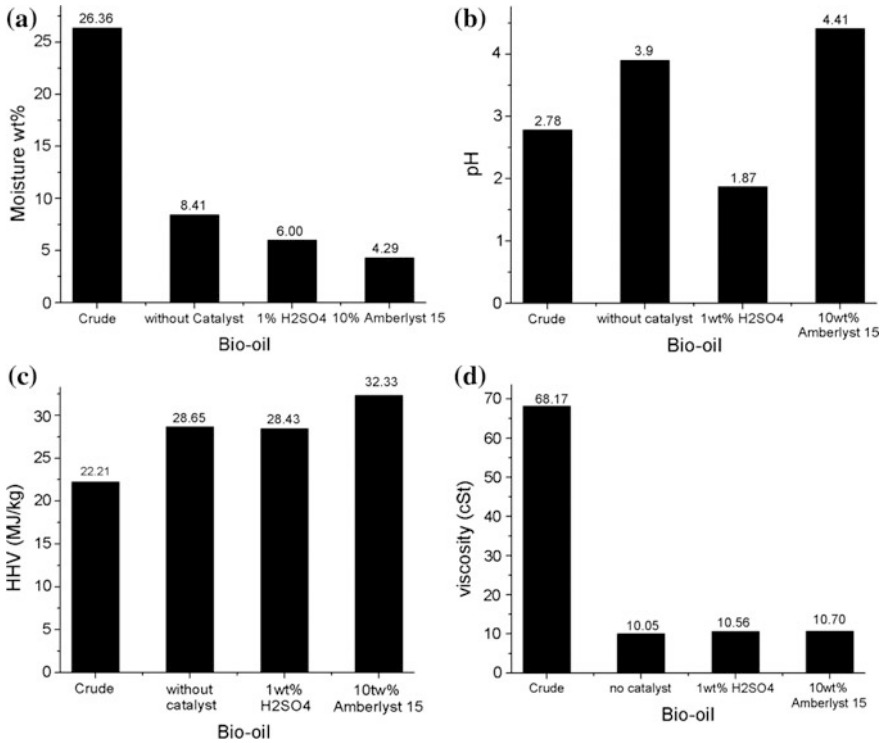

Fig. 30.4 Esterified Bio-oil product properties. **a** Moisture wt%, **b** pH Value, **c** HHV(MJ/kg), **d** viscosity (cSt)

The pH of the treated Bio-oil with sulfuric acid drops from 2.78 to 1.87 while with Amberlyst-15, it shows an improvement i.e., a rise from 2.78 to 4.41. The pH value of bio-oil products obtained without catalyst, improved to 3.9 as shown in the Fig. 30.4. The improvement in the pH value of the treated bio-oil with different catalysts is due to the dilution effect of 1-butanol as well as the occurrence of esterification reactions catalyzed by organic acids present in bio-oil.

30.3.3 Higher Heating Value

Higher heating value (HHV) of the crude Bio-oil is 22.21 MJ/kg, it is determined based on the Elemental analysis [32] of crude bio-oil and values are tabulated in Table 30.3. Bomb calorimeter could not be used to determine HHV due to high moisture content of the crude bio-oil. Hence for consistency, HHV of the esterified bio-oil is also determined by elemental analysis. It is found to increase to 32.33 MJ/kg after treating with 1-butanol in the presence of Amberlyst-15. Further, in the presence of sulfuric acid HHV is found to be 28.43 MJ/kg and that without catalyst it is 28.65 MJ/kg as shown in Fig. 30.4. Reasons for improving the HHV of bio-oil is water reduction in the product bio-oil as well as presence of large amount of 1-butanol (HHV: 37.5 MJ/kg).

30.3.4 Viscosity

Figure 30.4 shows the kinematic viscosity of different esterified bio-oils prepared using different methods. The kinematic viscosity of the crude bio-oil (moisture 26.36 wt%) is measured using Cannon-Fenske viscometer tube of size 300 (calibration constant is 0.25) at 40 °C and it is 68.17 cSt. The same after alcohol treatment in the presence of Amberlyst-15 is reduced to 10.7 cSt. This improvement in the viscosity is due to the dilution of 1-butanol. In the presence of sulfuric acid, viscosity is reduced to 10.56 cSt and without catalyst treatment viscosity reduced to 10.05 cSt.

Table 30.3 Elemental analysis of Bio-oil

Elements (wt%)	Crude bio-oil	No catalyst	1wt% H_2SO_4	10wt% Amberlyst-15
Carbon	50.92	56.83	55.05	60.93
Hydrogen	8.27	10.34	10.75	11.32
Nitrogen	2.23	2.39	2.55	2.16
Oxygen (by difference)	38.57	30.43	31.63	25.58
HHV (MJ/kg)	22.21	28.65	28.43	32.33

30.4 Catalyst Activity

To check the activity of the catalyst, the reaction is performed under otherwise similar conditions in the presence of the catalyst washed with isopropyl alcohol repeatedly and dried under vacuum for 8 h at 80 °C. The formation of 1-butyl ester is reduced from 11.37 to 7.32 wt%, which shows a decrease in the activity of the catalyst.

To identify the cause of deactivation, Amberlyst-15 was characterized for the surface area using BET apparatus; specific surface area of catalyst dropped from 43.97 to 16.94 m^2/g, in two reuses as shown in Fig. 30.5a, which is probably due to surface deposition and blockage of pores. To confirm this deposition TG Analysis of the re-used Amberlystp-15 is carried out and compared with the fresh catalyst. The weight loss of the used Amberlyst-15 is found to be more than fresh Amberlyst-15 as shown in Fig. 30.5b. It may be concluded that that used Amberlyst-15 suffers from surface depositions which leads to surface blockage and active sites of the catalyst.

An overview of the product properties of the esterified bio-oil obtained using Amberlyst-15, H_2SO_4 and no catalyst are summarized in Table 30.4 and compared

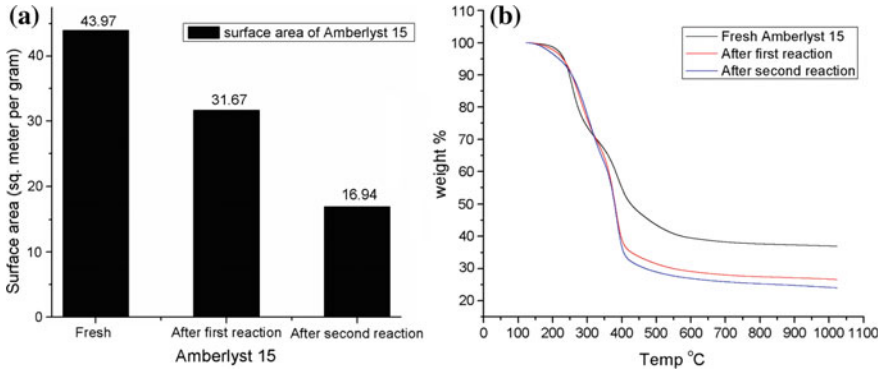

Fig. 30.5 **a** Surface area of Amberlyst-15. **b** Thermogravimetric profile of Amberlyst-15

Table 30.4 Product Properties of crude bio-oil, esterified bio-oil, and diesel

Physical properties	Crude bio-oil	Esterified bio-oil	Esterified bio-oil	Esterified bio-oil	Diesel
Catalyst	–	Amberlyst-15	H_2SO_4	No catalyst	–
Kinetic viscosity at 40 °C cSt	68.17	11.27	10.56	10.05	1.9–6.0
Water content wt%	26.36	4.29	6.00	8.41	<0.05 vol.%
Oxygen wt%	38.57	25.58	31.63	30.43	0.0
pH	2.78	4.41	1.87	3.90	7.00
HHV MJ kg^{-1}	22.21	32.33	28.43	28.65	44.8

with petroleum diesel. Some improvements are clearly shown when using Amberlyst-15. For example, the pH value improved considerably and the water content is reduced to 4.29%, leading to a considerable improvement of the HHV to 32.33 MJ kg^{-1}.

30.5 Conclusions

Esterification of wood pyrolysis oil with high boiling alcohol like n-butanol in the presence of Amberlyst-15 is investigated. In this process, using reactive distillation of bio-oil water content and acidity of bio-oil reduced significantly. With this catalyst, a subsequent neutralization step after treatment is avoided, however, it deactivates due to deposition of carbonaceous material formed by certain compounds present in the bio-oil. Systematic experimental studies will be required to investigate the cause of deactivation.

References

1. P.M. Mortensen, J.-D. Grunwaldt, P.A. Jensen, K. G. Knudsen, A.D. Jensen, Appl. Catal. A Gen. **407**, 1 (2011)
2. S. Sorrell, J. Speirs, R. Bentley, A. Brandt, R. Miller, Energy Policy **38**, 5290 (2010)
3. A. Demirbas, Appl. Energy **88**, 17 (2011)
4. A.V.V. Bridgwater, D. Meier, D. Radlein, Org. Geochem. **30**, 1479 (1999)
5. D. Mohan, C.U. Pittman Jr., P.H. Steele, Energy Fuels **20**, 848 (2006)
6. A. Oasmaa, Y. Solantausta, V. Arpiainen, E. Kuoppala, K. Sipilä, Energy Fuels, 1380 (2010)
7. A.V. Bridgwater, J. Anal. Appl. Pyrolysis **51**, 3 (1999)
8. H.B. Goyal, D. Seal, R.C. Saxena, Renew. Sustain. Energy Rev. **12**, 504 (2008)
9. C. Greenhalf, D. Nowakowski, (2011)
10. S. Arvelakis, E.G. Koukios, Biomass Bioenerg. **22**, 331 (2002)
11. A. Oasmaa, D.C. Elliott, S. Muller, Environ. Prog. Sustain. Energy **28** (2009)
12. Q. Yin, S. Wang, X. Li, Z. Guo, Y. Gu, in *International Conference on Optoelectronics and Image Processing* (2010)
13. A.V. Bridgwater, Biomass Bioenerg. **38**, 68 (2012)
14. W. Yu, Y. Tang, L. Mo, P. Chen, H. Lou, X. Zheng, Bioresour. Technol. **102**, 8241 (2011)
15. J. Wang, J. Chang, J. Fan, W. Jin-jiang, C. Jie, F.A.N. Juan, J. Fuel Chem. Technol. **38**, 560 (2010)
16. Q. Zhang, J. Chang, T. Wang, Y. Xu, Energy Convers. Manag. **48**, 87 (2007)
17. D.C. Elliott, G.G. Neuenschwander, in *Developments in Thermochemical and Biomass Conversion*, 1996, pp. 611–621
18. F.H. Mahfud, F. Ghijsen, H.J. Heeres, J. Mol. Catal. A: Chem. **264**, 227 (2007)
19. L.M. Yang Tang, W. Yu, Y. Tang, W. Yu, L. Mo, H. Lou, X. Zheng, Energy Fuels **22**, 3484 (2008)
20. A. Oasmaa, E. Kuoppala, A. Ardiyanti, R.H. Venderbosch, H.J. Heeres, Energy Fuels **24**, 5264 (2010)
21. J. Gagnon, S. Kaliaguine, Ind. Eng. Chem. Res. **27**, 1783 (1988)

22. S. Stephanidis, C. Nitsos, K. Kalogiannis, E.F. Iliopoulou, A.A. Lappas, K.S. Triantafyllidis, Catal. Today **167**, 37 (2011)
23. J. Wildschut, J. Arentz, C.B. Rasrendra, R.H. Venderbosch, H.J. Heeres, Environ. Prog. Sustain. Energy **28** (2009)
24. T.T. Viet, J.-H. Lee, J.W. Ryu, I.-S. Ahn, C.-H. Lee, Fuel **94**, 556 (2012)
25. R.V. Pindoria, A. Megaritis, A.A. Herod, R. Kandiyoti, Fuel **77**, 1715 (1998)
26. P.A. Horne, P.T. Williams, Fuel **75**, 1043 (1996)
27. P.T. Williams, P.A. Horne, Fuel **74**, 1839 (1995)
28. D.J. Mihalcik, C.A. Mullen, A.A. Boateng, J. Anal. Appl. Pyrolysis **92**, 224 (2011)
29. A. Aho, N. Kumar, A.V. Lashkul, K. Eränen, M. Ziolek, P. Decyk, T. Salmi, B. Holmbom, M. Hupa, D.Y. Murzin, Fuel **89**, 1992 (2010)
30. R.K. Sharma, N.N. Bakhshi, Bioresour. Technol. **45**, 195 (1993)
31. R.K.K. Sharma, N.N.N. Bakhshi, Bioresour. Technol. **35**, 57 (1991)
32. F.H. Mahfud, I. Melin-Cabrera, R. Manurung, H.J. Heeres, Process Saf. Environ. Prot. **85**, 466 (2007)
33. D.A. Bulushev, J.R.H. Ross, Catal. Today **171**, 1 (2011)
34. W. Li, C. Pan, Q. Zhang, Z. Liu, J. Peng, P. Chen, H. Lou, X. Zheng, Bioresour. Technol. **102**, 4884 (2011)
35. J. Xu, J. Jiang, Y. Sun, Y. Lu, X.U. Jun-ming, J. Jian-chun, S.U.N. Yun-juan, L.U. Yan-ju, J. Fuel Chem. Technol. **36**, 1 (2008)
36. J. Peng, P. Chen, H. Lou, X. Zheng, Energy Fuels **22**, 3489 (2008)
37. J.D. Adjaye, N.N. Bakhshi, Fuel Process. Technol. **45**, 161 (1995)
38. S. Zhang, Y. Yan, T. Li, Z. Ren, Bioresour. Technol. **96**, 545 (2005)
39. S.D. Stefanidis, K.G. Kalogiannis, E.F. Iliopoulou, A.A. Lappas, P.A. Pilavachi, Bioresour. Technol. **102**, 8261 (2011)
40. P. Bhattacharya, E.B. Hassan, P. Steele, J. Cooper, L. Ingram, BioResources **5**, 908 (2010)
41. P.A. Horne, N. Nugranad, P.T. Williams, J. Anal. Appl. Pyrolysis **34**, 87 (1995)
42. Z. Zhang, Q. Wang, P. Tripathi, C.U. Pittman Jr., Green Chem. **13**, 940 (2011)
43. X. Li, R. Gunawan, C. Lievens, Y. Wang, D. Mourant, S. Wang, H. Wu, M. Garcia-Perez, C.-Z. Li, Fuel **90**, 2530 (2011)
44. S. Miao, B.H. Shanks, Appl. Catal. A Gen. **359**, 113 (2009)
45. F.H. Mahfud, *Exploratory Studies on Fast Pyrolysis Oil Upgrading*, 2007
46. Z. Tang, Q. Lu, Y. Zhang, X. Zhu, Q.Q. Guo, Ind. Eng. Chem. Res. **48**, 6923 (2009)
47. N. Lohitharn, S. Miao, B.H. Shanks, *Upgrading of Bio-Oil via Acid Removal : Effect of Various Alcohols and Aldehydes on Esterification of Acetic Acid*, 2003
48. R.N. Hilten, B.P. Bibens, J.R. Kastner, K.C. Das, Energy Fuels **24**, 673 (2010)
49. L. Moens, S.K. Black, M.D. Myers, S. Czernik, Energy Fuels **23**, 2695 (2009)
50. D. Radlein, CA2165858 (1997)
51. T. Ezeji, N. Qureshi, H.P. Blaschek, Process Biochem. **42**, 34 (2007)
52. J.-Y. Park, D.-K. Kim, J.-S. Lee, Bioresour. Technol. **101**, S62 (2010)
53. J. Gangadwala, S. Mankar, S.M. Mahajani, A. Kienle, E. Stein, Ind. Eng. Chem. Res. **42**, 2146 (2003)
54. S. Talwalkar, P. Kumbhar, S.M. Mahajani, in *Situ Coating on Cation Exchange Resin Catalyst, Amberlyst-15, and Its Impact on the Hydration of Dicyclopentadiene* (n.d.)
55. J. Gangadwala, A. Kienle, E. Stein, S.M. Mahajani, Ind. Eng. Chem. Res. **43**, 136 (2004)

Chapter 31
Visible Frequency Plasmonic Metamaterial Perfect Absorber for Solar Energy Harvesting

P. Mandal, Mayank Ranakoti and Kapil K. Shukla

Abstract Plasmonic metamaterial perfect absorbers (PMPAs) are artificially designed metal-dielectric-metal structures to realize novel optical, electric and magnetic properties. In the recent years PPAs are seen to attract huge attention due to potential applications in optical properties manipulation, refractive index sensing, thermal imaging, solar photovoltaics and more. In solar photon harvesting PMPAs may play significant role in enhancing high absorption and generating more power. Due to perfect absorption the reflection loss can be minimized. In the present study, polarization insensitive subwavelength circular holes array on the top layer of a metal-dielectric-metal layers system has been modeled and investigated using finite difference time domain (FDTD) computation. Our result shows a broadband absorption in the range of 80–100% covering almost visible spectral range. In the report we have also shown the manipulation in spectral absorption by considering the hole depth, size and material filling. The studied structure may help in designing effective solar cell device.

Keywords Plasmonic metamaterials · Si solar cell · Modeling and simulation · Perfect absorber

31.1 Introduction

Solar photovoltaics have drawn considerable interests due to its potential as non-conventional electrical energy source, and have great market values. In this technique the endless sunshine can be converted to electrical power [1–5]. Thus, novel solar photon harvesting techniques have open up new domain of research. Not only active materials but proper choice of electrode geometry has great influence on the overall absorption enhancement and device efficiency. Recently it is observed that plasmonic metamaterial perfect absorbers (PMPAs) have great deal with broad

P. Mandal (✉) · M. Ranakoti · K.K. Shukla
Department of Physics, University of Petroleum and Energy Studies, Dehradun 248007, India
e-mail: pmandal@ddn.upes.ac.in

G. Anand et al. (eds.), *Nanotechnology for Energy and Water*,
Springer Proceedings in Energy, https://doi.org/10.1007/978-3-319-63085-4_31

band absorption [6] which can be manipulated to large extents of electromagnetic spectrum [7–9]. The structure primarily consists of metal-dielectric- metal layers sequentially placed on to each other. Top layer has periodic structuring to realize impedance matching. PMPAs help in enhancing absorption and hence, generation of more power. In the present study, polarization insensitive subwavelength circular holes array on the top layer of a metal-dielectric-metal layers system has been modeled and investigated using finite difference time domain (FDTD) computation. The cylindrical hole region is filled with Si and optical absorption is calculated. The results are compared with the bare Si layer absorption to show overall absorption enhancement. The study may help in designing future solar cells of improved device efficiency.

31.2 Design Parameters and Computations

Optical reflection (R(λ)), transmission (T(λ)) and absorption (A(λ)) spectra are obtained using finite difference time domain computation (OPTIWAVE commercial package, free version). The plasmonic perfect absorber is made of sequential layers (bottom to top) as follows: (a) a 200 nm thick substrate layer (SiO_2, RI: 1.5), (b) a 100 nm gold layer, (c) a 20 nm SiO_2 spacer layer of constant refractive index of 1.5, and finally, (d) a gold layer of 100 nm thick (until unless specified) on the top of the dielectric spacer layer. For impedance matching the top layer is perforated with periodic circular holes, typically of 300 nm diameter. The holes are arranged in a square lattice with period of 400–700 nm so as to realize densely or sparsely packed holes. To realize solar photovoltaic effect the cylindrical hole is filled with silicon (Si) and absorption is compared with the flat Si absorption. Gold layer is considered to follow Lorentz-Drude dispersion between 400 and 1500 nm. The unit cell simulation is performed using periodic boundary conditions (PBC) along X- and Y-directions, and, APML (anisotropic perfectly matched layers) along the growth direction (Z direction). A linearly polarized (for X-pol, E field along X, and for Y-pol, E field along Y) plane wave is launched normally.

31.3 Results and Discussions

From the FDTD computational analysis the reflection spectrum R(λ), transmission spectrum T(λ) and absorption spectrum A(λ) = 1 − R(λ) − T(λ)are obtained and plotted in the spectral range of 400–1500 nm as in Fig. 31.1. The stated spectral absorptions are shown in two parts (left and right). In the first part (left side) shows the spectra in the visible wavelengths ranging from 0.4 to 0.75 μm (Fig. 31.1), while, the second part (right side), the spectra are shown in the range of 0.75–1.5μm. The transmission spectra are not shown as the transmission values tend to zero in the spectral range of interests due to thicker blocking layer

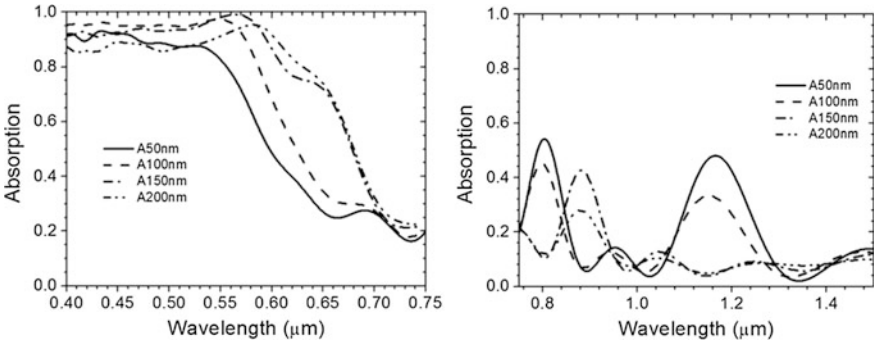

Fig. 31.1 Absorption and reflection spectra for the structure having holes of different depths at spectral range 0.4–0.75 microns (*left*) and 0.75–1.5 microns (*right*)

(of 100 nm thick gold layer)) on the quartz plate. Left panel represents the absorption spectra for four different holes' depths (50, 100, 150 and 200 nm) for a fixed period of 400 nm. For 50 nm hole depth the absorption spectrum shows absorption of about 90% below 0.54 μm. For 100 nm hole depth absorption spectrum shows about 95% absorption below 560 nm. By comparing these two spectra one can observe a significant absorption enhancement with the increased hole depth. For further increase in the hole depth (i.e. for 150 and 200 nm) the optical absorption, although, increases in the range beyond 560 nm the lower wavelength absorption falls. The spectra at higher wavelengths (right side) show overall decrease in spectral absorption.

We now concentrate on the period dependent optical absorption and reflection properties of PMPAs. Figure 31.1 of earlier section simply tells us that the structure may be effective for visible frequency absorption. However, for better photon harvesting the device must absorb NIR light too. Thus, tuning in overall optical absorption is required. We now set the structural period to different values, i.e. to 500, 600 and 700 nm while the hole size and depth are kept constant at 300 and 150 nm, respectively. The spectra are shown in Fig. 31.2. When the period is increased to 500 nm the broad absorption below 500 nm reduces. However, perfect absorption is seen at $\sim$630 nm. The overall absorption in the frequency range of interests is still significant and comparable to absorption in the case of 400 nm periodic structure. For further increase in the period (600 and 700 nm) the absorption becomes weak and very selective for perfect absorption, such as seen at 700 and 775 nm for 600 and 700 nm periodic structures, respectively. The period dependent characteristic absorption can be accounted using equation-1 (λ_{res} = resonating wavelength, a = period, m and n are integers, and ε_m is dispersive metal permittivity, air as dielectric medium [10]). The shaded area is the reflection of plasmon assisted high absorption due to excitation of plasmons by the top grating coupling at smaller periodic structure. The period dependent narrowing (see shaded area) is attributed to the weakening of interaction among the cavities.

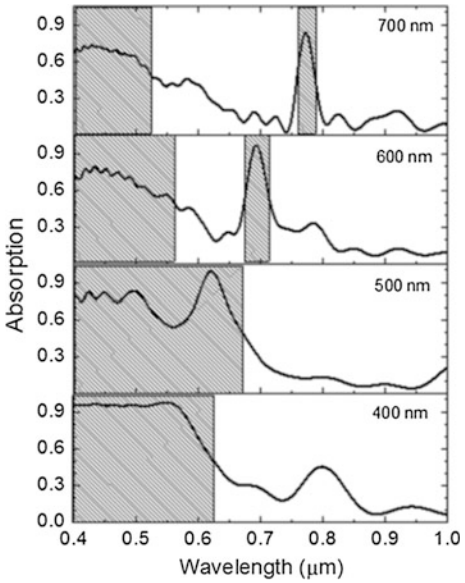

Fig. 31.2 Period dependent absorption and reflection spectra for the structure having holes of size 300 nm at spectral range 0.4–1.0 μm

$$\lambda_{res} = \frac{a}{\sqrt{m^2 + n^2}} \sqrt{\frac{\varepsilon_m}{\varepsilon_m + 1}} \tag{31.1}$$

To study the effect we filled the cylindrical air hole with crystalline Si and total absorption over the spectral range of 400–750 nm is calculated by integrating the area under the spectrum. The integrated areas for Si filled structure and bare Si layer (200 nm thick) are compared. Figure 31.3 shows the absorption spectra for the

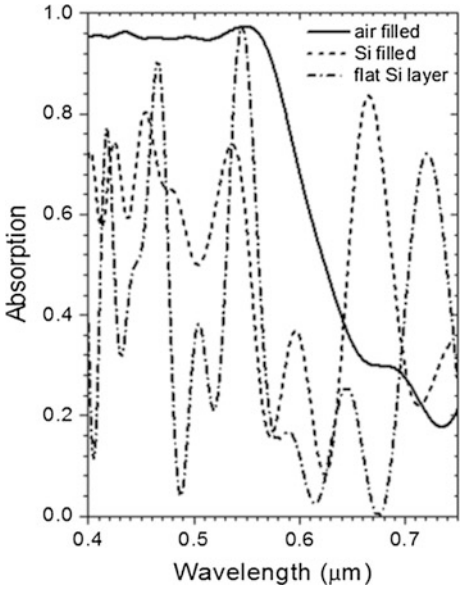

Fig. 31.3 Absorption spectra for the structure having hole size of 300 nm and depth 150 nm in the spectral range of 0.4–1.0 μm. The structural period is set to 600 nm

respective samples. The integrated area under the curves for Si filled and flat Si layer are calculated to be 17180 and 12980 square units, respectively. The percentage increase in absorption with respect to bare Si layer is about 32% which is considered to be significant. The enhanced absorption may increase solar cell efficiency.

31.4 Conclusions

We have investigated plasmonic metamaterial perfect absorbers (PMPAs) in view of solar cell applications. The present PMPA has subwavelength cylindrical holes array on the top layer of a metal-dielectric-metal layers system. The optical absorption properties on the modeled structure are investigated using finite difference time domain (FDTD) computation. The study shows significant influence of period and cavity holes depth on optical absorption in the visible frequency. Absorption enhancement of $\sim$32% is seen when the air holes are filled with Si. Our findings have potential implications in solar cell devices.

References

1. E. Rephaeli, S. Fan, Absorber and emitter for solar thermo-photovoltaic systems to achieve efficiency exceeding the Shockley-Queisser limit. Opt. Express **17**, 15145–15159 (2009)
2. M.K. Hedayati, F. Faupel, M. Elbahri, Review of plasmonic nanocomposite metamaterial absorber. Materials **7**, 1221 (2014)
3. Y. Wang, T. Sun, T. Paudel, Y. Zhang, Z. Ren, K. Kempa, Metamaterial-plasmonic absorber structure for high efficiency amorphous silicon solar cells. Nano Lett. **12**, 440–445 (2014)
4. V. Rinnerbauer et al., Metallic photonic crystal absorber-emitter for efficient spectral control in high-temperature solar thermophotovoltaics. Adv. Energy Mater. **4**, 1400334 (2014)
5. A. Lenert et al., A nanophotonic solar thermophotovoltaic device. Nat. Nanotechnol. **9**, 126–130 (2014)
6. P. Mandal, Plasmonic perfect absorber for refractive index sensing and SERS. Plasmonics **11**, 223 (2016)
7. K. Aydin, V.E. Ferry, R.M. Briggs, H.A. Atwater, Broadband polarization-independent resonant light absorption using ultrathin plasmonic super absorbers. Nat. Commun. **2**, 517 (2011)
8. M.K. Hedayati et al., Design of a perfect black absorber at visible frequencies using plasmonic metamaterials. Adv. Mater. **23**, 5410–5414 (2011)
9. T. Maier, H. Brückl, Wavelength-tunable microbolometers with metamaterial absorbers. Opt. Lett. **34**, 3012 (2009)
10. P.B. Johnson, R.W. Christy, Optical constants of the noble metals. Phys. Rev. B **6**, 4370 (1972)

Chapter 32
Derivatives of Extra Low Frequency on the Cardiovascular System

Anil Sirswal and Sonal Modi

Abstract Extremely low frequency (ELF) covers the frequency range of 3–300 Hz. Scientific Committee on Emerging and Newly Identified Health Risks (SCENIHR) has concluded that ELF magnetic fields are possibly carcinogenic. For breast cancer and cardiovascular disease, recent research has demonstrated that an association is unlikely and need more research. In this paper we have implanted the effect of ELF on the cardiovascular system (CVS). The frequency range of 30–50 Hz range, results in cyclonic resonance of human cell. It has non-thermal effect on body. It can result in fluctuation of blood pressure, asthenisation, fatigue, irritability, weakness, heart blood volume fluctuations and Electrocardiographic (ECG) changes. We have demonstrated the effects of the ELF on the CVS by modeling the CVS as nonlinear coupled oscillators having basic unit as Poincare oscillators and concluded that the blood flow is influenced by ELF.

Keywords Extremely low frequency · Nonlinear oscillators · Modeling · Cardiovascular system · Noise · Coupling · Non-thermal effects · Electromagnetic radiations · Directionality · Synchronization

32.1 Introduction

Today we live in a world that is increasingly "wired" and the entire population is affected by electromagnetic pollution. Proliferation of electrical and electronics devices, intelligence added to these devices, miniaturization, close packaging, etc. has resulted in exponential rise of electromagnetic (EM) pollution. Electromagnetic

A. Sirswal (✉)
Noida International University, Greater Noida, India
e-mail: anil_sirswal@yahoo.com

S. Modi
Department of Electrical Power and Energy, University of Petroleum and Energy Studies, Dehradun, India
e-mail: sonalmodi87@gmail.com

G. Anand et al. (eds.), *Nanotechnology for Energy and Water*,
Springer Proceedings in Energy, https://doi.org/10.1007/978-3-319-63085-4_32

Radiations (EMRs) have harmful effects on human beings. Even low level EMRs can cause biological damage [1–5].

The sources of EMRs are (Table 32.1):

The effects of EMRs on human beings largely depend on frequency, duration and power of the EMRs [1–5]. The effects of radiations can be broadly discussed under Thermal, Non-Thermal and Resonance Effects. The brief features of various effects of EMRs are tabulated below in Table 32.2.

Scientific Committee on Emerging and Newly Identified Health Risks (SCENIHR) has concluded that ELF magnetic fields are possibly carcinogenic and for breast cancer and cardiovascular disease an association is unlikely and need more research [1]. We have demonstrated the effects of ELF, in particular Cyclonic Resonance, on CVS. Cyclonic Resonance is due to lower frequencies (30–50 Hz range) and it builds up like cyclone as shown in Fig. 32.1.

The sources of ELF are High Tension overhead Power lines, TV sets, Video display terminals, industrial machinery, domestic distribution lines, home appliances, electric engines in cars/ train, welding devices, computer and TV screen, etc. We have modeled the CVS as a system of five linearly coupled autonomous Poincare oscillators (in presence of noise) [6, 7]. These oscillators represent heartbeat, respiration, myogenic activity of smooth muscles, neurogenic and endothelial activity respectively. Further due to ELF, Cyclonic Resonance of human cells occurs in the 30–50 Hz range. This will result into more activity of body cells, thus more exhaustion and increase in the requirement of oxygenated blood. The cardiac oscillator will receive corresponding action potential stimulus

Table 32.1 Sources of EMRs

Natural		Manmade
Terrestrial	Celestial	Electronics
Precipitatory	Solar system	Electrical
Atmospheric	Cosmic noise	Electro-mechanical
		Electro-optical

Table 32.2 Effects of EMRs

Effects of EMRs	Features/Reasons
Thermal	• High power • Short/medium/long duration • Permanent damage
Non-thermal	• Low power • Long duration • Damage may be reversible
Resonance	• Resonance principle • Frequency dependent • Cyclonic resonance (lower frequencies) • Oscillation resonance (higher frequencies) • Size of target organ is of the order of wavelength of the EMRs • Body parts may resonant from 30–3000 MHz [5].

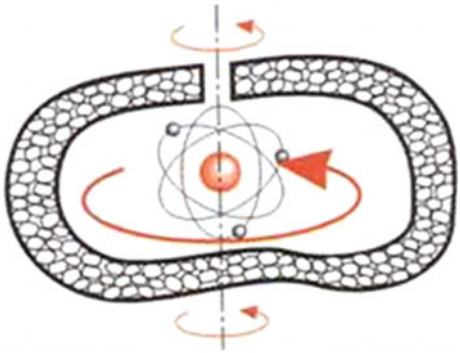

Fig. 32.1 Cyclonic resonance

from auto nervous system (ANS) which will affect heart rate, volume and resistance of blood vessels [8–12]. The cyclonic resonance of human cells affects the endothelial related metabolic activity thereby influencing CVS as follow:

- Blood pressure increase/ decrease/ fluctuation
- Asthenisation, fatigue, irritability, weakness
- heart blood volume fluctuations
- Electrocardiographic (ECG) changes

We have simulated the above results by altering the value of coupling constants and demonstrated that the blood flow is influenced due to ELF (cyclonic resonance of human body cells). Therefore, the model may be used to draw conclusions that the human CVS is affected by ELF, in particular due to cyclonic resonance effects. The data has been taken from Physionet website (www.physionet.org).

Finally, we have summarized the results and drawn conclusions.

32.2 Method

32.2.1 Modelling Coupling Among the Oscillators of CVS with the Basic Unit as the Poincare Oscillator

From the experimental observations of the CVS, we can conclude that there are five time scales involved having average frequencies of 1, 0.2, 0.1, 0.03 and 0.01 Hz due to heartbeat, respiration, myogenic, neurogenic and endothelial related metabolic activity respectively. These subsystems behave as autonomous oscillators [6, 7, 13, 14]. Analysis of cardio-respiratory synchrograms shows synchronization among the cardiorespiratory oscillators in the ratio of n: m. The blood flow of healthy individual always has one of the Lypunov exponents approximately equal to zero, suggesting that the CVS signal is deterministic and can be represented by differential equations. Thus each oscillation observed in the CVS signals can be

modeled as Poincare oscillator and the interactions between the subsystems as couplings between the oscillators [6, 7, 13, 14]. It can be represented by:

$$\dot{x}_i = -x_i q_i - y_i \omega_i + g_{x_i}(\mathbf{x}); \dot{y}_i = -y_i q_i + x_i \omega_i + g_{y_i}(\mathbf{y})$$

and

$$q_i = \propto_i \left(\sqrt{x_i^2 + y_i^2} - a_i \right) \tag{32.1}$$

Where, x (blood flow) and **y** (velocity of flow) are vectors of oscillator state variables. $\propto_i$, a_i and ω_i are constants and $g_{y_i}(\mathbf{y})$ and $g_{x_i}(\mathbf{x})$ are linear coupling vectors; i = 1, 2, 3, 4 and 5 corresponds to heart, respiration, myogenic, neurogenic and metabolic oscillators respectively.

32.2.2 Simplified Version of CVS

The simplified version can be represented by:

$$\dot{x}_1 = -x_1 q_1 - y_1 \omega_1 + \eta_2 x_2 - \eta_3 x_3 - \eta_4 x_4 + \eta_5 x_5 \tag{32.2}$$

$$\dot{y}_1 = -y_1 q_1 + x_1 \omega_1 + \eta_2 y_2 - \eta_3 y_3 - \eta_4 y_4 + \eta_5 y_5 \tag{32.3}$$

$$\dot{x}_2 = -x_2 q_2 - y_2 \omega_2 + \theta_4 x_4 - \theta_5 x_5 \tag{32.4}$$

$$\dot{y}_2 = -y_2 q_2 + x_2 \omega_2 + \theta_4 y_4 + \theta_5 y_5 \tag{32.5}$$

$$\dot{x}_3 = -x_3 q_3 - y_3 \omega_3 + \gamma_4 x_4 - \gamma_5 x_5 \tag{32.6}$$

$$\dot{y}_3 = -y_3 q_3 + x_3 \omega_3 + \gamma_4 y_4 - \gamma_5 y_5 \tag{32.7}$$

$$\dot{x}_4 = -x_4 q_4 - y_4 \omega_4 - \rho_2 x_2 + \rho_3 x_3 - \rho_5 x_5 \tag{32.8}$$

$$\dot{y}_4 = -y_4 q_4 + x_4 \omega_4 - \rho_2 y_2 + \rho_3 y_3 - \rho_5 y_5 \tag{32.9}$$

$$\dot{x}_5 = -x_5 q_5 - y_5 \omega_5 + \sigma_2 x_2 - \sigma_3 x_3 - \sigma_4 x_4 \tag{32.10}$$

$$\dot{y}_5 = -y_5 q_5 + x_5 \omega_5 + \sigma_2 y_2 - \sigma_3 y_3 - \sigma_4 y_4 \tag{32.11}$$

where η_i, θ_i, γ_i, ρ_i and σ_i are coupling terms.

Table 32.3 Quantification of interaction between heart and lung

Data	Synchronization index from phases	Directionality index
f1y01 m	0.082472	−0.18188
f1y02 m	0.11714	−0.29774
f1y03 m	0.10448	−0.28581
f1y04 m	0.074225	−0.46454
f1y05 m	0.074405	−0.76421
f1y06 m	0.18454	−0.044598
f1y07 m	0.15444	−0.024598
f1y08 m	0.082076	−0.76929
f1y09 m	0.070076	−0.78979
f1y10 m	0.170026	−0.58248

For simplification purpose and to reproduce the time series and power spectra to be similar to experimental data, the parameters were set as given below. These parameters were further altered to consider the effect of ELF (cyclonic resonance effect).

$$\alpha_1 = \alpha_2 = \alpha_3 = \alpha_4 = \alpha_5 = 1$$

$$a_1 = a_5 = 0.5;\ a_2 = a_3 = a_4 = 1$$

$$\eta_2 = -\eta_3 = -\eta_4 = \eta_5 = 0.5$$

$$\theta_4 = \theta_5 = 0.1$$

$$\gamma_4 = \gamma_5 = 0.1$$

$$\rho_2 = \rho_3 = \rho_5 = 0.1$$

$$\sigma_2 = \sigma_3 = \sigma_4 = 0.1$$

$$\eta_6 = \eta_7 = \theta_6 = \theta_7 = \gamma_6 = \rho_6 = \sigma_6 = 0$$

f_1, f_2, f_3, f_4 and f_5 varied but close to the average frequencies of the subsystem

A fluctuation term, ξ (t) such that $< \xi(t) > = 0$ as $< \xi(t)\xi(0) > = D\ \delta(t)$, was added to the cardiac oscillations while considering noise. Thus heart can be represented by:

$$\dot{x}_1 = -x_1 q_1 - y_1 \omega_1 + g_{x_1}(x) + \xi(t) \tag{32.12}$$

32.2.3 *Effect of ELF on CVS*

In the ELF frequency range, the cyclonic resonance affects the CVS. Cyclonic Resonance is due to lower frequencies (30-50 Hz range) and it builds up like cyclone. This will result into more activity of body cells, thus more exhaustion of body parts and increase in the requirement of oxygenated blood. The cardiac oscillator will receive action potential stimulus from auto nervous system (ANS) which will affect heart rate, volume and resistance of blood vessels [8–12]. We have simulated the above results by altering the value of coupling constants. This model allows for the variation of the frequency and the value of coupling constants of the oscillators.

32.3 Results and Discussions

32.3.1 *Results Obtained from Data*

- Quantification of interaction between heart and lung: The synchronization index from phases and directionality index for various subject data are calculated (see Table 32.3). There is phase synchronization between lung and heart. It is not perfect but epoch of synchronization is present. The directionality index is negative suggesting that there is directionality from lung to heart.

32.3.2 *Modeling Coupling Among the Oscillators of CVS*

Results of modeling the linear couplings in theabsence of noise, presence of noise and parametric coupling are shown below (see Fig. 32.2). It resembles the experimentally obtained data (Fig. 32.3).

- Cyclonic Resonance effect increases endothelial related metabolic activity, which in turn will alter the coupling term due to endothelial related metabolic activity. The altering of coupling term will affect the cardiac oscillator (Fig. 32.4) and respiratory oscillator (Fig. 32.5). Thus the fluctuating blood pressure, irregular heart beats are justified.

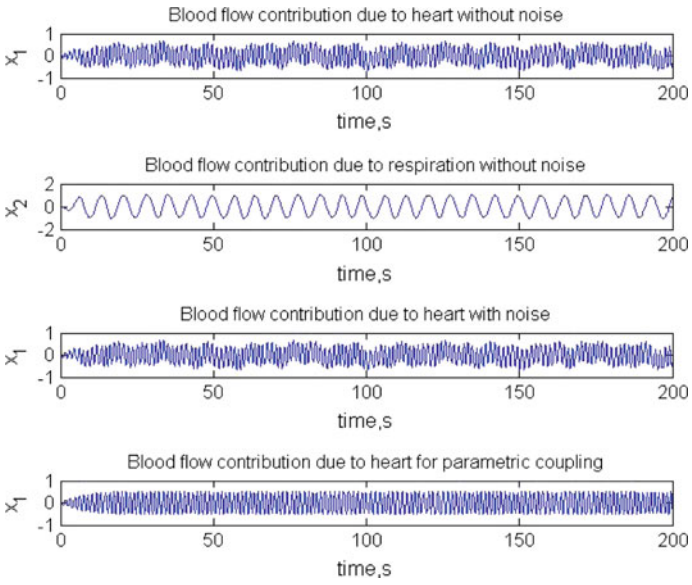

Fig. 32.2 First, third and fourth from *top*, shows cardiac oscillators for linear coupling without noise, with noise and parametric coupling respectively. Second from *top*, shows the respiratory oscillator

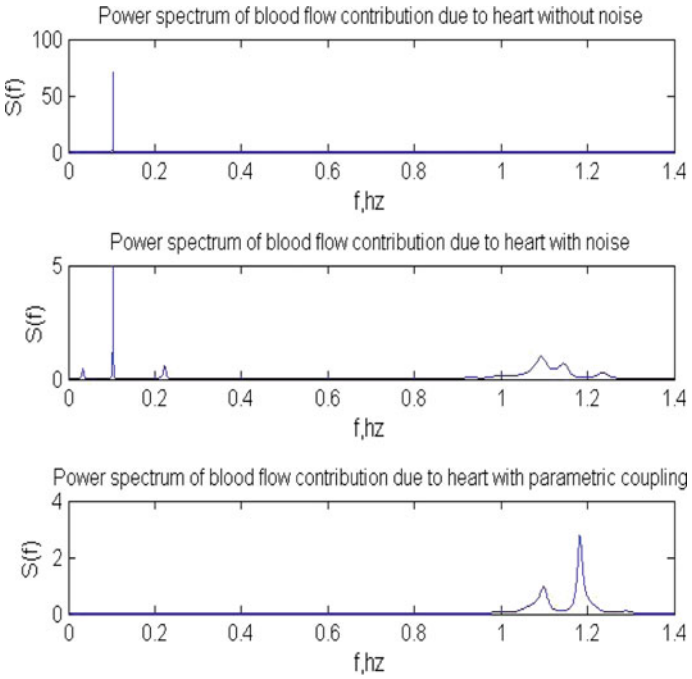

Fig. 32.3 Power spectrum of the time series for the flow generated by cardiac oscillator, x_1 for linear coupling without noise, with noise and parametric coupling respectively

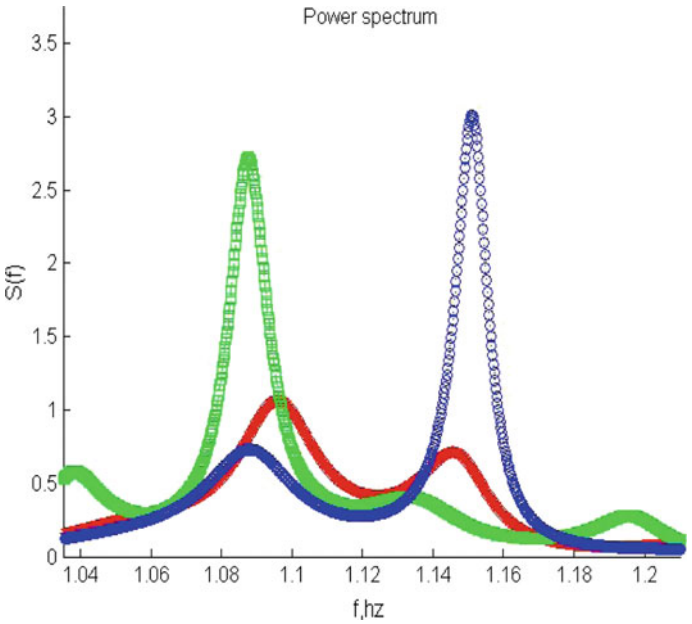

Fig. 32.4 Varying the coupling term due to endothelial related metabolic activity, results in prominent variations in the power spectrums of blood flow generated by cardiac oscillator

Fig. 32.5 Varying the coupling term due to endothelial related metabolic activity, result in promonent variations in the power spectrums of blood flow generated by respiratory oscillator

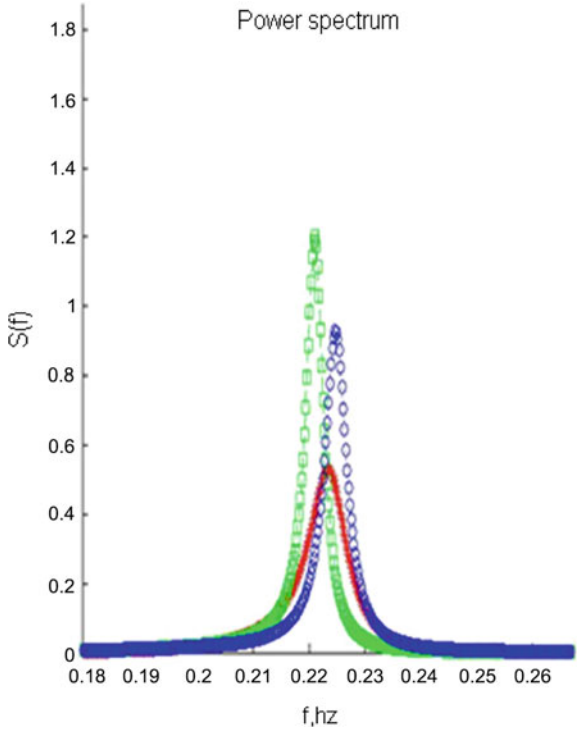

32.4 Conclusion

The time series of linearly coupled Poincare oscillators in presence of noise, modeled for CVS dynamics, resemble the experimentally obtained data. Due to Cyclonic resonance effects the normal functioning of CVS is influenced as follow:

- Blood pressure increase/ decrease/ fluctuation
- Asthenisation, fatigue, irritability,weakness
- Heart blood volume fluctuations
- Electrocardiographic (ECG) changes

32.5 Scope for Future Work

In future, the accurate heart signals and respiratory signals at various thresholds of ELF can be modeled and extrapolated to analyse the ELF effect, in particular the frequency at which cyclonic resonance takes place (30–50 MHz). The alteration of coupling constant due to ELF effect can be obtained experimentally and the limits of ELF can further be worked out and aligned based on this model. This will ascertain the effect of ELF on CVS and the safety limits can be worked out.

References

1. Possible effects of Electromagnetic Fields (EMF) on Human Health, Scientific Committee on Emerging and Newly Identified Health Risks (SCENIHR), Health and Consumer Protection DG, European Commission, 27 Jan 2015
2. Electromagnetic Environmental Effects Requirements for Systems, MIL Std 464 C, 01 Dec 2010, Department of Defense Interface Standard, United States of America
3. Protecting Personnel from Electromagnetic Fields, DoDI 6055.11, Department of Defense, United States of America
4. A. Sirswal, M.K. Dewan, Modeling effect of electromagnetic interference on cardiovascular system. Int. J. Res. Dev. Appl. Sci. Eng. (IJRDASE). **9**(1) (2016)
5. A. Sirswal, Modeling resonance effects of the electromagnetic radiations on the cardiovascular system, in *International Conference on ElectroMagnetic Interference & Compatibility (INCEMIC) 2016*, 21 Nov 2016
6. A. Stefanovska, D.G. Luchinsky, P.V.E. McClintock, Modelling couplings among the oscillators of the cardiovascular system. Physiol. Meas. **22**, 551–564 (2001)
7. A. Stefanovska, M. Braˇciˇc Lotriˇc, S. Strle, H. Haken, The cardiovascular system as coupled oscillators. Physiol. Meas. **22**, 545–550 (2001)
8. A.C. Guyton, J.E. Hall, *Textbook of Medical Physiology*, 11th edn. (Elsevier Saunders, Edinburgh, 2005
9. J.J. Batzel, D. Schneditz, T.H. Tran, *Cardiovascular and Respiratory Systems Modeling, Analysis, and Control* (Society for Industrial and Applied Mathematics, Philadelphia, 2007

10. D.M. Baekey, Y.I. Molkov, J.F.R. Paton, I.A. Rybak, T.E. Dick, Effect of baroreceptor stimulation on the respiratory pattern: Insights into respiratory-sympathetic interactions. Respir. Physiol. Neurobiol. **174**(1–2), 135–145 (2010)
11. Y.I. Molkov, A.P.L. Abdala, B.J. Bacak, J.C. Smith, J.F.R. Paton, I.A. Rybak, Late-expiratory activity: emergence and interactions with the respiratory CPG. J. Neurophysiol. **104**(5), 2713–2729 (2010)
12. I. Poliacek, K.F. Morris, B.G. Lindsey, L.S. Segers, M.J. Rose et al. Blood pressure changes alter tracheobronchial cough: computational model of the respiratory-cough network and in vivo experiments in anesthetized cats. J. Appl. Physiol. **111**(3), 861–873 (2011). (Bethesda, Md: 1985)
13. A. Stefanovska, Coupled oscillators. Complex but not complicated cardiovascular and brain interactions. IEEE Eng. Med. Biol. Mag. Q. Mag. Eng. Med. Biol. Soc. **26**(6), 25–29 (2007)
14. Y. Shiogai, A. Stefanovska, P.V.E. McClintock, Nonlinear dynamics of cardiovascular ageing. Phys. Rep. Rev. Sect. Phys. Lett. **488**(2–3), 51–110 (2010)